Star Formation in the Perseus Molecular Cloud: Observations of Dynamics and Comparison to Simulations

by

Helen M. Kirk
Hon.B.Sc., University of Toronto, 2003
M.Sc., University of Victoria, 2005

A Dissertation Submitted in Partial Fulfillment of the
Requirements for the Degree of

DOCTOR OF PHILOSOPHY

in the Department of Physics and Astronomy

Star Formation in the Perseus Molecular Cloud: Observations of Dynamics and Comparison to Simulations

by

Helen M. Kirk
Hon.B.Sc., University of Toronto, 2003
M.Sc., University of Victoria, 2005

Supervisory Committee

Dr. D. Johnstone, Supervisor
(Herzberg Institute of Astrophysics and Deptartment of Physics & Astronomy)

Dr. D. VandenBerg, Co-Supervisor
(Department of Physics & Astronomy)

Dr. S. Ellison, Departmental Member
(Department of Physics & Astronomy)

Dr. I. Putnam, Outside Member
(Department of Mathematics & Statistics)

Dr. J. Di Francesco, Additional Member
(Herzberg Institute of Astrophysics and Department of Physics & Astronomy)

Supervisory Committee

Dr. D. Johnstone, Supervisor
(Herzberg Institute of Astrophysics and Deptartment of Physics & Astronomy)

Dr. D. VandenBerg, Co-Supervisor
(Department of Physics & Astronomy)

Dr. S. Ellison, Departmental Member
(Department of Physics & Astronomy)

Dr. I. Putnam, Outside Member
(Department of Mathematics & Statistics)

Dr. J. Di Francesco, Additional Member
(Herzberg Institute of Astrophysics and Department of Physics & Astronomy)

ABSTRACT

The relative importance of physical processes occurring on the various scales within molecular clouds is strongly debated, partly due to the lack of systematic cloud-wide observations available until recently. My thesis characterizes the kinematics of star formation across the entire Perseus molecular cloud as well as in a suite of simulations, providing statistical measures that successful theories of star formation will have to explain. My thesis consists of three interconnected projects described below.

Dense core survey

The kinematics of the dense cores in Perseus were measured through single pointing observations of the N_2H^+(1–0) and $C^{18}O$(2–1) transitions, tracing the dense core gas and surrounding lower density gas respectively. The internal velocity dispersion of the dense cores was observed to be small – dominated by thermal motions, and roughly the size expected for the cores to be in virial equilibrium. The dense cores also have little motion with respect to the surrounding low density gas – usually much less than the ambient sound speed of the medium.

Comparison to cloud survey

The dense core observations were compared to a full spectral cube of ^{13}CO(1–0) emission from the COMPLETE Survey, tracing the lower-density cloud material. From this analysis, it was determined that the dense cores have little motion with respect to the larger structures that they inhabit – smaller than the typical velocity dispersion or the estimated virial velocity dispersion of the region.

Analysis of simulations

A suite of thin-sheet MHD simulations with varying levels of input magnetic field strengths and turbulence were analyzed in a manner to mimic the above observational surveys. While the small internal velocity dispersion of the dense cores could be reproduced by most of the simulations, the small motion between the core and its surrounding lower density gas could not be produced at the same time as the observed large-scale non-thermal motions.

Future directions

The kinematic measures presented here will be straightforward to apply to future multi-cloud surveys as well as other numerical simulations. This will allow the effect of environment on star formation to be better explored in both the observational and simulated domains.

Contents

List of Tables

List of Figures

ACKNOWLEDGEMENTS

First, I would like to acknowledge the support, boundless enthusiasm, and encouragement I have received over the years from my supervisor, Doug. I am also grateful for the opportunities I have had to work with and learn from astronomers both in Victoria (particularly James) and also from all around the world, and thank them for their generosity.

No thesis could be completed without the immeasurable support from family and friends. To my dear family and friends in Ontario, thank you for providing a good listening ear throughout this process. And to my wonderful adopted family, Ann and Jim, and my good friends in Victoria, thank you for all of your support, for sharing in my adventures and inspiring me to achieve more.

Somewhere, something incredible is waiting to be known.

– Carl Sagan

Chapter 1

Introduction

Stars are born within molecular clouds, large, cold complexes of gas and dust. Molecular clouds span tens of parsecs ($\sim 10^{19}$ cm), have temperatures of tens to hundreds of Kelvin, and have densities of a few hundred particles per cubic centimetre, which is extremely rarefied compared to the density of our atmosphere ($\sim 10^{19}$ particles per cubic centimetre), but dense compared to the vacuum of empty space. Molecular clouds are composed primarily of molecular hydrogen gas, H_2, with trace amounts of heavier molecular species such as CO. The dust within molecular clouds consists mostly of approximately micron-sized conglomerations of primarily carbon-bearing molecules that are coated in a layer of water, methane, and other volatile ices. The dust grains have an abundance of roughly 1/100th of the gas species by mass (Stahler & Palla, 2004). Within these large molecular cloud complexes, dense and compact sub-regions known as dense cores are observed; sometimes these cores are observed to undergo gravitational collapse to form either a single star or a small cluster of stars. These dense cores have sizes of roughly 0.1 pc ($\sim 10^{17}$ cm) and densities above 10^4 cm^{-3} (Stahler & Palla, 2004).

On the grand scale of the Universe, stars are important – they are responsible for a significant fraction of light from external galaxies and are one of the main tracers of the baryonic matter within the Universe. Through their lives and deaths, stars also provide the major pathway to the production of most elements heavier than the hydrogen and helium formed shortly after the Big Bang. On a much smaller scale, stars are the focal point of planetary systems such as our own Solar System; understanding the processes by which planets form requires a prior knowledge of how the central star evolved. Stars also provide the energy necessary for the survival of life as we know it. Understanding how stars form, and hence the processes regulating

the formation and evolution of molecular clouds and the dense cores within them is thus an integral part of astrophysics.

1.1 Theoretical Overview

Molecular clouds tend to contain upwards of 10,000 solar masses ($M_\odot$; 1 $M_\odot$ = 2×10^{33} g) of material. For typical cloud conditions, a temperature of a few tens of Kelvin and density of a few hundred particles per cubic centimetre, internal thermal pressure alone is unable to prevent the large-scale collapse of the entire cloud. This can be seen through the Jeans equation; the Jeans mass is the approximate maximum mass that thermal pressure can support against gravity. The Jeans mass can be written as:

$$M_{\rm J} = \left(\frac{\pi^{3/2}}{G^{3/2}\ \mu^{1/2}\ m_H^{1/2}} \right)\ c_s^3 n^{-1/2} \tag{1.1}$$

(from Hartmann, 1998), where G is the gravitational constant, μ is the mean molecular weight (~ 2.35), m_H is the mass of a proton, c_s is the sound speed, and n is the number density. Assuming a density of 10^2 cm^{-3} and a temperature of 100 K, the Jeans mass is 1700 $M_\odot$. Since molecular clouds contain ten to one hundred times more mass than the Jeans mass, they must either be undergoing global gravitational collapse, or additional processes must be occuring that prevent this. The timescale for global gravitational collapse is relatively short – faster than the sound-crossing time of the molecular cloud. The freefall time is given by

$$t_{\rm ff} = \frac{1}{\sqrt{G \mu m_H n}} \tag{1.2}$$

while the sound-crossing time of the cloud is given by

$$t_{\rm therm} = L / c_s \tag{1.3}$$

where L is the cloud length and c_s is the sound speed. For a cloud with a density of 10^2 cm^{-3}, size of 10 pc, and temperature of 100 K, the freefall time is roughly 6×10^6 years and the sound-crossing time is 10^7 years.

Global gravitational collapse of the molecular cloud is ruled out by observations showing that the fraction of the molecular cloud mass that ends up in stars is small, roughly a few percent (e.g., Myers et al., 1986; Evans et al., 2009). One or more

mechanisms must therefore be acting to prevent the gravitational collapse of the entire molecular cloud. This global support must still, however, allow for the formation and evolution of small, compact dense regions (dense cores) that are observed. Broadly, two different types of mechanisms have been proposed. The first mechanism, often referred to as the 'Standard Model', invokes strong magnetic fields that act to prevent the motion of ionized material perpendicular to the field lines and thus delay gravitational collapse. The second mechanism encompasses a variety of flavours of 'turbulent' scenarios, wherein large-scale supersonic motions within the molecular cloud act to prevent the gravitational collapse of the entire cloud.

1.1.1 Magnetic Fields

As early as the 1950's, magnetic fields were believed to be important in the evolution of molecular clouds. Mestel & Spitzer (1956) demonstrated that even in the presence of strong magnetic fields, dense material can eventually overcome the field and build up small-scale density condensations that are able to undergo gravitational collapse. In the standard magnetic picture, molecular clouds were generally considered to be long-lived, quasi-static entities; subsequent work focussed on the equilibrium structure of molecular clouds (e.g., Mouschovias, 1976). The study of the evolution of a single core within the larger cloud eventually culminated in the development of the 'Standard Model' (Shu, Adams, & Lizano, 1987). In the magnetic support scenario, magnetic fields are strong enough to prevent the flow of ionic material perpendicular to them. Uncharged particles are also prevented from fast gravitational infall due to frequent collisions with the ions that are tied to the field. Gradually, neutral particles are able to diffuse past the magnetic field lines and build up concentrations of mass in a process known as ambipolar diffusion. The mass of this dense region eventually becomes sufficiently large that the force of gravity overwhelms the magnetic field, and ionic particles then also partake in the gravitational collapse of the dense object, dragging the magnetic field lines in with them. The timescale for ambipolar diffusion is given by

$$t_{\rm AD} \simeq \frac{L^2}{v_{\rm A}^2 \ \tau_{ni}} \tag{1.4}$$

where L is the length scale of interest, τ_{ni} is the neutral-ion interaction timescale, and v_A is the Alfvèn speed, given by

$$v_{\rm A} = \frac{B}{\sqrt{4\pi\rho}} \tag{1.5}$$

where B is the magnetic field strength and ρ the gas density (Shu, 1992). The neutral-ion interaction timescale can be written as

$$\tau_{ni} = 1.4\Big(\frac{m_i + m_{\rm H_2}}{m_i}\Big)\frac{1}{n_i\langle\sigma w\rangle_{i\rm H_2}} \tag{1.6}$$

where m_i is the mass of the ion, m_{H_2} is the mass of molecular hydrogen, and $\langle\sigma w\rangle_{iH_2}$ is the neutral-ion collision rate (Ciolek & Basu, 2006). Using the values and relationship between neutral and ion densities adopted by Ciolek & Basu (2006), this yields a timescale of $\tau_{ni} = 10^4$ ($n_{\rm n}$ / 10^5 cm^{-3})$^{-1/2}$ years. For a 0.1 pc region with a mean density of 10^5 cm^{-3} and magnetic field strength of 10 μG, the ambipolar diffusion timescale is 10^6 years; due to the $n_n^{1.5}$ dependence from the various terms, this quickly becomes a much longer timescale for lower density (pre-dense core) material. The ambipolar diffusion timescale for larger scale cloud conditions is often quoted as being roughly ten times the free-fall timescale, although this value clearly depends on the magnetic field strength, as well as the density and size-scale of interest.

Observations of magnetic fields are tricky. Magnetic fields can be measured either through their line of sight (LOS) strength or via the polarization showing the field direction projected on the plane of the sky. The lack of information available in the third dimension in either case can severely complicate the interpretation of the measurements. The magnetic field strength is measured through the detection of the splitting of an emission or absorption line into multiple components through the Zeeman effect (this was first observed as a widening of emission lines in the presence of a magnetic field by Zeeman, 1897). The multiple components tend to be separated by a very small frequency difference (smaller than the line width except in the case of very strong magnetic fields), so that high resolution spectra and multiple polarization observations are required in order to accurately determine the magnetic field strength (e.g., Crutcher, 1988). Both of these requirements necessitate long observations in order to obtain sufficient signal to make a detection, hence these observations are rare. Despite this, a limited number of observations have been made; Crutcher (1999) summarizes all of the detections and upper limits measured up to 1999. These

observations appear to indicate that magnetic fields are dynamically important and are in fact approximately 'critical', i.e., the force exerted by the magnetic fields on the cloud mass is roughly equal to the gravitational force (Crutcher, 1999).

Polarization angle measurements indicate the orientation of the magnetic field on the plane of the sky. The dust grains present in molecular clouds are prolate spheroids which tend to carry a non-zero electric charge and are spinning. Interaction with the magnetic field in the cloud results in the dust grains spinning around their long axis (i.e., the direction with the maximum moment of inertia), with the spin axis aligned with the magnetic field of the cloud (Spitzer, 1978). Observations of absorbed starlight (e.g., in optical wavelengths) therefore reveal a polarization angle parallel to the magnetic field, since more of the radiation parallel to the long axis of the grain, or perpendicular to the field is absorbed. Observations of emission from dust grains (e.g., in submillimetre wavelengths), on the other hand, show a polarization angle perpendicular to the magnetic field, since dust grains radiate preferentially along their long axis. The total fraction of polarized emission is small, usually on the order of a few percent or less, so polarization measurements are tricky. In some cases where it has been possible to make polarization maps of dense cores, there is evidence for aligned magnetic fields that are pinched towards the dense core centre (e.g., Schleuning, 1998; Girart et al., 2006). This hourglass morphology is usually attributed to the magnetic field lines being partially dragged inwards as material is accreted onto the dense core, a manifestation of ambipolar diffusion and gravity.

Observations also indicate that the picture of quiescent molecular clouds with strong magnetic fields is not completely correct. Supersonic turbulent motions are observed within molecular clouds (e.g. Larson, 1981), with magnitudes similar to the Alfvèn speed (Eqn 1.5), arguing against the quasi-static picture. Significant non-thermal motions are in fact required to prevent the collapse of the molecular cloud even in a magnetically-supported regime. Magnetic fields can only prevent or slow the gravitational collapse of material perpendicular to the field lines, hence without some form of non-thermal motions (e.g., MHD waves in the form of nonlinear Alfvèn waves), molecular clouds would have a pancake-like geometry, which is not observed (Shu, Adams, & Lizano, 1987).

1.1.2 Turbulence

The term turbulence encompasses a large diversity of formation scenarios. Typically, these scenarios begin with supersonic turbulent motions within molecular clouds that eventually lead to the formation and evolution of dense cores. The molecular cloud itself is usually disrupted or dispersed during the formation of the dense cores, so there is rapid evolution on all size scales unlike the quasi-static evolution in the magnetic scenario.

Supersonic velocity dispersions have been observed in molecular clouds, with larger velocity dispersions present on larger scales, usually interpreted as a manifestation of turbulent motions (e.g., Larson, 1981). One major hurdle for the turbulent scenario is the origin of the supersonic turbulence, and whether the turbulent motions are maintained or decay. Without a continuous replenishment of the turbulence, the energy will decay in a short period of time (roughly the sound crossing time of the cloud; MacLow & Klessen, 2004).

If turbulent motions are not maintained on this timescale, the cloud rapidly becomes unstable to large-scale collapse, essentially reverting back to the original problem of how to prevent global gravitational collapse without additional support mechanisms, unless the bulk cloud has dissipated in this time. Some simulators allow the turbulence to dissipate ('decaying turbulence' simulations, e.g., Vázquez-Semadeni et al., 2007), while others continuously maintain it artificially ('driven turbulence' simulations, e.g., MacLow & Klessen, 2004). The origin of the initial (or maintained) turbulence has not yet been determined, although several ideas exist including the collision of atomic flows (e.g., Heitsch et al, 2008a) and supernova shocks (e.g., Elmegreen, 1998). Turbulent motions can also be generated through the collapse of non-uniform large-scale structure (e.g., Burkert & Hartmann, 2004). The importance of other physical proccesses, such as thermal and dynamical instabilities (e.g., Heitsch et al, 2008b), magnetic fields (e.g., Nakamura & Li, 2008), and even gravity (some simulations do not include self-gravity and many do not have global gravity) are under intense debate.

The mechanism by which cores accrete material also differs between simulations – in some, termed monolithic collapse, the cores accrete material from a fixed resevoir surrounding them (e.g., McKee & Tan, 2003), while in others, termed competitive accretion, cores accrete material from a variety of locations as they move about within their cluster gravitational potential (e.g. Bate et al., 2003).

Another major hurdle for turbulent simulations is the issue of timescales. Purely turbulent simulations usually predict the formation and evolution of dense cores within little more than a single free-fall time (and sometimes even faster than a single thermal crossing time!), while observations show that the value should be closer to 5 free-fall times (see Ward-Thompson et al., 2007, for a review).

One piece of support for the turbulent formation scenario is the ability to reproduce the observed distribution of dense core masses (the dense core mass function, discussed in more detail in §2.3.1). Nearly all turbulent simulations are currently able to reproduce the core mass function, however, so while this feat is a requirement of a successful simulation, it is not a sufficient test to prove the validity of a given set of initial conditions (e.g., Bonnell et al., 2007).

1.2 Observations

In order to determine which of the theoretical scenarios best matches reality (and particularly to distinguish between the various turbulent formation scenarios), observations are required. The dust present in star-forming regions extincts light from the region as it passes through the column of material towards the observer. Observations therefore tend to be performed at wavelengths longer than optical, where the extinction is less severe, or where the dust itself has significant thermal emission. Recently, technological advances have allowed for large-scale observations (spanning a significant fraction of a molecular cloud) to be made in a reasonable amount of time. This is beginning to allow for observations of dense cores to be made in a cloud-wide statistical manner, rather than on an individual basis, and for global cloud properties to be determined. These measurements allow for far greater discrimination between simulations than was previously possible. The different types of observations are outlined in more detail below, and their strengths towards gaining an understanding the global processes at work in star-forming regions are highlighted.

1.2.1 Dust Extinction

As mentioned above, dust present in star-forming regions extincts light, preferentially shorter wavelength light, which additionally leads to a reddening of any emission that does traverse the cloud. This property of dust can be used to determine the column density through a molecular cloud, since all molecular clouds in the galaxy will be

in front of some number of more distant stars. One of the more popular methods, Near Infrared Colour Excess (NICE; Lada et al., 1994) involves the observation of the reddening of background stars in the near infrared, where the intrinsic colour of main sequence and giant stars tend to be very similar (Lada et al., 1994). Figure 1.1 shows an example of a multi-wavelength observation of a well-known Bok globule (isolated small dense concentration of gas and dust). As can be seen from the left panel, bluer (shorter wavelength) light is preferentially extincted by dust grains, allowing only the redder (longer wavelength) light to pass through. The right hand panel shows the total column density inferrred from a detailed analysis of the star colours observed (further discussed below).

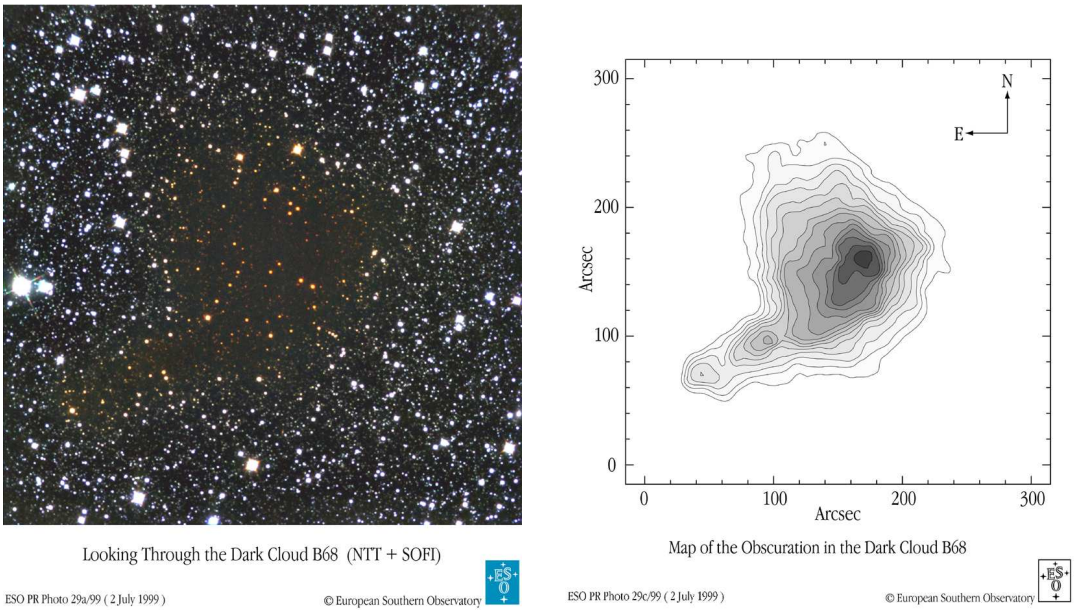

Figure 1.1 Left panel: A false-colour image of the B68 region combining three different near-infrared bands from the ESO 3.5 m telescope at La Silla. Right panel: The visual extinction (total column density) derived by analysis of star colours in the data presented in the left panel. These images are from the ESO press release available at `http://www.eso.org/public/outreach/press-rel/pr-1999/phot-29-99.html`. The full dataset and analysis appears in Alves, Lada & Lada (2001).

The NICE technique has now been improved and expanded to NICER (NICE-Revisited; Lombardi & Alves, 2001), relying on observations of two or more colours (three or more wavelengths) in order to better model the reddening. The basic premise of both these techniques is to assume that all stars have the same intrinsic colour (determined through observations of an 'un-extincted' region in the sky) and that dust

has similar scattering properties everywhere. The column density of dust can therefore be ascribed as the cause of the reddening of any stars redder than this value. Stars in front of and protostars within the molecular cloud are removed through multiple iterations determining outliers from the typical reddening derived for spatially close groups of stars. Smoothing of the individual reddening measurements is required to determine the dust column density between the stars, hence the final map resolution depends on the density of observed background stars and tends to be poor (e.g., several arcminutes for the Perseus and Ophiuchus molecular clouds using 2MASS data; Ridge et al., 2006). Higher resolution requires many background stars, which are found naturally in regions along the Galactic Plane (where there is higher intrinsic stellar density) or by obtaining very deep observations.

In general, dust extinction measurements have two advantages over other observations – fewer assumptions and larger coverage of scales. The process leading to the extinction and reddening is a relatively simple, well understood process, not influenced by many variables. The only major assumptions that must be made are that all dust grains tend to scatter light in the same manner (on the large scales probed by the observation) in order to convert the extinction measured to the total column density of dust and the value of the conversion factor. No assumptions about the temperature of the dust or other physical conditions are required. Extinction or reddening observations are also sensitive to large-scale density structures within molecular clouds, unlike that of dust emission, where large-scale structures are difficult to detect with ground-based observations (see discussion below). Given a large enough number of stars observed (deep enough observations), relatively small scales can be probed as well (e.g., the Pipe Nebula; Lombardi et al., 2006), and thus the (column) density structure can be determined consistently over a wide range of scales with a single tracer and method, a trait which distinguishes this method from the others discussed below.

Chapter 2 further discusses the analysis by Kirk, Johnstone, & Di Francesco (2006, hereafter KJD06) of the large-scale column density structure in the Perseus molecular cloud derived using the NICER technique.

1.2.2 Dust Emission

Dust grains emit radiation predominantly in the far infrared and (sub)millimetre since the temperature tends to be low. This submillimetre emission is usually described as

that of a modified blackbody, of the form

$$S(\nu) \propto \nu^{\beta} B_{\nu}(T_d) \tag{1.7}$$

where S is the emission as a function of frequency (ν), β is the spectral index of the dust emissivity function, B_ν is the blackbody emission at a frequency ν and (dust) temperature T_d (e.g., Johnstone et al., 2006). β thus describes the deviation from purely blackbody emission. This deviation is mostly ascribed to the difficulty of the dust grains emitting radiation at wavelengths of sizes larger than or comparable to their physical size, but can also be affected by optical depth (Ossenkopf & Henning, 1994).

Continuum observations of dust emission are commonly used to determine the structure of smaller-scale (column) density within molecular clouds. Several telescopes including the James Clerk Maxwell Telescope (JCMT), Caltech Submillimeter Observatory (CSO), Institut de Radioastronomie Millimétrique (IRAM) 30m, and Atacama Pathfinder Experiment (APEX) telescopes are equipped to map significant-size regions within molecular clouds. The Perseus molecular cloud, for example, has been mapped by both the JCMT and CSO telescope (Hatchell et al., 2005; Kirk, Johnstone, & Di Francesco, 2006; Enoch et al., 2006) with a resolution of $\sim$15″ at 850 μm at the JCMT and $\sim$31″ at 1100 μm at the CSO. These (sub)millimetre observations have the advantage of requiring much less time than the extinction method described above to obtain relatively high resolution. Resolutions on the order of 15″ are sufficient for studying nearby molecular clouds (within a few hundred parsecs), as this is roughly the Jeans length (the length scale associated with the Jeans mass introduced in eqn 1.1; see Hartmann 1998 for the Jeans length equation). The Jeans length represents the approximate size over which dense objects would be expected to fragment thermally. At a density of 10^5 cm^{-3} and temperature of 20 K, the Jeans length is roughly 0.1 pc, while 15″ corresponds to 0.15 pc at a distance of 200 pc. These dust emission measurements are thus ideally suited for efficiently revealing the location of dense cores that will potentially evolve into stars.

These observations do, however, require extra assumptions to fully interpret the data. In order to convert flux measurements into column densities, a dust temperature must be assumed, as well as the dust grain opacity. Since the dust grains may not be well-coupled with the gas present (except in the highest density regions), the two may not share a common temperature, hence the temperature cannot be determined

from measurements of gas phase species. Multi-wavelength observations of the same region can be used to attempt to constrain the temperature, although this can be complicated due to telescope beam patterns and other effects, so errors are often quite large (see, for example, Matthews et al., 2008). The dust grain opacity is also not well-constrained; the most popular models are those of Ossenkopf & Henning (1994), which show a variety of predictions depending on dust grain composition and the presence or absence of an icy mantle. The opacity is also thought to vary in warm regions, where icy mantles should melt, and the size distribution of dust grains could differ; the most extreme models predict opacities that differ by an order of magnitude (Di Francesco et al., 2007). Uncertainty of at least a factor of two is often assumed in the inferred dust column density (and mass), although this should scale all measurements in a region by roughly the same amount (for the majority of the molecular cloud, dust grain properties are thought to be the same), so the relative measurements should be more accurate.

One further complication with dust emission measurements mentioned earlier is that they do not provide information on the large-scale (column) density structure of the molecular cloud. To overcome both the brightness and variability of the earth's atmosphere at the wavelengths of interest (the Earth's atmosphere is orders of magnitude brighter than the astronomical sources of interest), as well as instabilities in the current detectors, dust emission measurements at millimetre and submillimetre wavelengths are usually made as difference measurements between two locations on the sky, described as 'chopping' the sky. This has the unfortunate consequence of also removing any information on structures the size of the chopping scale or larger from the maps (see, for example, Johnstone et al., 2000).

The easiest way to overcome the problems of chopping is to use telescopes in space, where there is no bright atmosphere to complicate observations. The *Herschel Space Observatory*, launched on May 14, 2009 will allow these measurements to be made in the submillimetre regime, although the angular resolution will only be moderate ($36''$ at 500 μm), since its primary mirror will only be 3.5 metres.

In the mid- to far- infrared regime, the *Spitzer Space Telescope* has already provided exquisite data spanning most nearby molecular clouds (e.g., Evans et al., 2003, 2009). These wavelengths are most sensitive to emission from warmer sources, i.e., protostars, hence *Spitzer* data has provided an excellent source of information for determining the evolutionary stage of the dense cores (e.g., has it already formed a protostar?). An analysis of both *Spitzer* and JCMT data for dense cores in the

Perseus molecular cloud (Jørgensen et al., 2007, 2008) is discussed in Chapter 2.

1.2.3 Gas Emission

A complementary way to observe molecular clouds is through the emission from molecular species. At the low temperatures and (relatively) high densities within molecular clouds, the majority of the material is found in molecular rather than atomic form. Indeed, molecular hydrogen is the most abundant species within molecular clouds. Due to its low mass, however, even its lowest energy levels above ground require high temperatures to excite. Therefore, H_2 emission cannot be used to probe the cold interiors of molecular clouds. Less abundant molecular species must therefore be used to trace the cloud material. The next most abundant molecule is CO, which has been found to have a number density of nearly 10^{-4} times that of H_2 in some regions (Stahler & Palla, 2004). CO, as well as a host of other (less abundant) carbon- and nitrogen-bearing molecules are commonly used to study molecular clouds. These molecules are heavier and their energy levels are easily populated in the typical conditions of molecular clouds.

The emission from a particular transition of a molecule depends on a variety of factors including the abundance of the molecule, the temperature and density of the medium (affecting how many molecules are in the desired state), and quantum mechanical properties (affecting how easily the particular transition can radiate). Spectral observations therefore have the power to reveal far more information about the properties of the emitting material, but disentangling the many factors involved can be challenging. The following sections outline a few basic cloud properties that have been revealed by spectral observations which are relevant to the subsequent chapters of this work.

1.2.3.1 Velocity

The kinematics of the gas is one of the easiest properties to determine, as it requires the least number of assumptions. For a Gaussian-like spectral profile, the centroid velocity of the emission is the mean velocity of the emitting material. Assuming that the molecular species is optically thin, then the linewidth of the emission indicates the velocity dispersion of the species. This velocity dispersion consists of both a thermal component (motions caused by the temperature of the material) as well as a non-thermal component (usually attributed to turbulent motions). The thermal

component of the lines is intrinsically narrow, several hundredths of a km s^{-1} for the typical molecules observed. Determination of the temperature is discussed in the following section; where an exact temperature determination is not possible, an estimate based on the typical conditions allows for an approximate separation of the thermal and non-thermal motions. In the case of optically thick emission, the linewidth measured becomes an upper limit for the true velocity dispersion of the gas.

Some molecular species, such as N_2H^+ and NH_3 emit multiple lines for the same transition, known as hyperfine components. These are due to either the nuclear quadrupole moment or the spin of an atom within the molecule coupling to the overall rotation, and are most commonly detected in molecules containing a ^{14}N or D atom (Schöier et al., 2005). These molecules have the advantage of requiring a larger column density in order to become optically thick (since some of the optical depth is 'taken up' in each of the hyperfine lines). Furthermore, the optical depth can be determined directly by the emission – each of the components has a different intrinsic opacity, thus the ratio in the peak intensities of each of the hyperfine components is a function of the total optical depth.

Chapter 3 presents the analysis of spectral observations of N_2H^+ and $C^{18}O$ for the dense cores in the Perseus molecular cloud. The bulk of this analysis relies on the determination of the centroid velocity and velocity dispersion of each molecular species using the considerations discussed above.

1.2.3.2 Temperature

In order to determine the temperature of the emitting material, two different transitions must be observed that originate from sufficiently different energy levels. Comparison of the number density in each of the two upper level energy states (determined through modelling each of the spectra) yields an estimate of the temperature through statistical equilibrium arguments. Usually, the wavelengths of these two different transitions are well-separated, requiring two separate observations in order to measure both. Ammonia (NH_3), however, is an exception, and the inversion transition for both the (1,1) and (2,2) states can be measured simultaneously, as the wavelengths are very similar. As further discussed in Chapter 2, Rosolowsky et al. (2008) use this technique to determine the temperatures of all of the dense cores in the Perseus molecular cloud.

1.2.3.3 Density

Molecular species can vary in their effectiveness in tracing the structure of a region depending, in part, on their fixed physical properties. The critical density is one important property, with species best tracing densities around their critical density[1] – a species with a critical density of 10^8 cm^{-3}, for example, would not be expected to emit efficiently in a region with a density of only 10^2 cm^{-3}. Note, however, that the critical density is only a coarse indicator of the density range probed by the molecular transition; the wavelength of the transition and optical depth are also factors that influence the density range traced. Emission profiles derived from molecules or dust can be used to determine the column density profile of a core (or the density profile through additional assumptions). Observations have shown that dense cores tend to have roughly flat ($N(r) \propto r^0$) column density profiles in the centre, turning over to a steeper power law relationship with $N(r) \propto r^{-2}$ at larger radii (Di Francesco et al., 2007).

1.2.3.4 Chemistry

An important factor implicit in interpreting any spectrum is what material within the cloud is responsible for the emission. This is partially governed by fixed physical constants and how these compare to the conditions present in the environment, as discussed above. Chemical processes add a significant complication to this, however. In cold, high density regions, molecules tend to "freeze-out" of the gas phase onto dust grains. The lack of detection or minimal detection of a species does not therefore necessarily imply a low total gas column density. Furthermore, some molecules cannot easily form in the presence of other species (due to, e.g., an alternate reaction pathway being energetically favourable). Careful comparisons of observations of many molecular species and dust continuum observations, coupled with chemical modelling, are required as a basis for interpreting spectral observations.

Comparisons between (sub)millimetre continuum and spectral observations have shown that carbon-bearing molecules, such as CO, tend to be depleted in the coldest and densest regions of molecular clouds (see Bergin & Tafalla, 2007, and the references therein). Nitrogen-bearing molecules, on the other hand, tend to continue to be present in the gas phase to a much higher density (Tafalla et al., 2002). Chemical

[1]The critical density is given by $A_{u,l}/C_{u,l}$ where A is the Einstein coefficient for spontaneous emission and C is the rate of collisionally induced de-excitiations (e.g., Stahler & Palla, 2004).

modelling suggests (Aikawa et al., 2001) that the reason for this is two-fold – carbon-bearing molecules tend to freeze-out slightly faster, and the formation of nitrogen-bearing molecules such as N_2H^+ and NH_3 is inhibited by the presence of CO, hence the formation rate increases as the CO freezes out onto the dust grains. At sufficiently high densities or a sufficiently long period of time, the rate of freeze-out for nitrogen-bearing molecules is predicted to overcome this enhancement from the disappearance of CO, and these nitrogen-bearing species should become significantly depleted as well. This freeze-out is rarely observed in dense cores, however, see Bergin et al. (2002) for one such example.

Coupled to the chemical reactions discussed above, some nitrogen-bearing molecules also tend to be good tracers of high density core gas due to their relatively high critical densities. N_2H^+ has a critical density of 10^5 cm^{-3} while NH_3, also observed to be a good dense gas tracer, has a critical density of 2×10^3 cm^{-3} (Schöier et al., 2005).[2] Therefore both due to the chemical reactions and the physical properties of N_2H^+ and NH_3, they are expected to be good tracers of the gas within dense cores.

As well as being depleted in the densest parts of cores, CO also has a lower critical density ($\sim 10^3$ cm^{-3} Ungerechts et al., 1997), and hence is observed throughout the larger scales of the molecular cloud. (Note also that the critical density is only a coarse approximation to the density regime well-traced by a molecule. While NH_3 and CO have similar critical densities, detailed modelling shows that NH_3 tends to be sensitive to 10^4 cm^{-3} density gas, while CO is sensitive to 10^3 cm^{-3} density gas; M. Tafalla, private communication, March 2009). In fact, so much CO is present on larger scales, that it is necessary to observe rarer isotopologues, such as ^{13}CO and C^{18}O rather than ^{12}CO in order to obtain optically thin (or less optically thick!) spectra. Furthermore, the process of freeze-out requires time to occur. Very young dense cores would be expected to have a much higher ratio of CO to N_2H^+, for example, than old dense cores. Chemistry unfortunately does not provide a clean "chemical clock" to age dense cores, as there are complications due to a variety of factors including the location and evolutionary history of each object (e.g., how long has the core had a high central density – did it form quasi-statically, or dynamically?); still, it can give some indication of the relative age of dense cores (e.g., Shirley, 2007).

[2]The molecular line database presented in Schöier et al. (2005), `www.strw.leidenuniv.nl/~moldata` provides the values of these constants most recently obtained in the laboratory. For the critical densities given above, a temperature of 10 to 15 K was assumed for C; the values change by at most 20% for the temperatures typical within molecular clouds.

One further chemical signature found in cold dense regions is a significant enhancement in the fraction of deuterium relative to hydrogen in the molecules present. Deuterium can replace an existant H atom on a molecule through a reaction of the original molecule with one of H_2D^+, D_2H^+, or D_3^+, as it is (slightly) energetically favourable for the molecule to bond with the slightly heavier deuterium than hydrogen. The reactive molecules H_2D^+, D_2H^+, and D_3^+ (along with H_3^+) all tend to be quickly destroyed in the presence of CO, and hence the "deuteration" reactions occur primarily once the CO has frozen out onto the dust grains (Bergin & Tafalla, 2007).

Chemistry is an integral part of the thesis implicit in all of the following chapters. Chapter 2 includes the summary of a comparative study of N_2H^+ and NH_3 in dense cores in the Perseus molecular cloud, while N_2H^+ and $C^{18}O$ observations of dense cores are presented and analyzed in Chapter 3. In Chapter 4, an analysis using the Chapter 3 data plus additional ^{13}CO data is performed. Chapter 5 shows a comparison between simulations and observations, and also implicitly relies on chemical considerations in order to convert the simulated quantities into observable ones.

1.3 Models

The previous sections have outlined the vast array of observations now available for molecular clouds and the information that each provides towards the physical conditions present. The following chapter highlights specific observational results that have been found for the Perseus molecular cloud, the star-forming environment which this thesis focusses on. The observations discussed in more detail in the following chapters are beginning to provide statistically significant contraints on the properties of dense cores and their environments across a variety of molecular cloud environments. Successful models and simulations of star formation are therefore now being challenged to reproduce these results. Simulations of particular relevance to the kinematic observations and analysis reported in Chapters 3 and 4 are the simulations of Klessen et al. (2005), Ayliffe et al. (2007), and Offner et al. (2008) which make predictions about the observable quantities analyzed in Chapters 3 and 4. These simulations will be discussed in more detail in the relevant sections. I contribute my own analysis of a suite of thin sheet magnetohydrodynamical (MHD) simulations from Basu, Ciolek & Wurster (2009) in Chapter 5.

1.4 Subsequent Chapters

The following chapters describe progress that has been made towards understanding the global physical processes in molecular clouds that lead to the formation of dense, star-forming cores with a particular focus on the nearby Perseus molecular cloud for which a wealth of data exists. Chapter 2 provides an overview of the existing large-scale observations in the Perseus molecular cloud, including the results of my MSc thesis (KJD06) and the collaborative effort with Jes Jørgensen (Jørgensen et al., 2007, 2008) for understanding core evolution in Perseus, as this data formed a key basis to the first component of my PhD project. Chapter 3 shows the results of the first component of my PhD project – a kinematic survey in N_2H^+ and $C^{18}O$ of the dense cores within the Perseus molecular cloud. These results are published in Kirk, Johnstone & Tafalla (2007, hereafter KJT07). Chapter 4 discusses the joint analysis of the N_2H^+ and $C^{18}O$ observations of Perseus in Chapter 3 with large-scale bulk gas velocity measurements in ^{13}CO. These results form the basis of Kirk, Pineda, Johnstone, & Goodman (in prep). In Chapter 5, the observational kinematic measures found in Chapters 3 and 4 are used in order to constrain simulations. I analyze a suite of thin-sheet magneto-hydrodynamical simulations of a star-forming region (roughly the size of an extinction region discussed in Chapter 2) with varying initial magnetic field strength and turbulence level. These simulations are "observed" in a way to mimic the measurements presented in Chapters 3 and 4, and the results compared. These results are published in Kirk, Johnstone & Basu (2009). A theoretical overview of this simulation setup and the physical relationships expected for various regimes of initial conditions is outlined in Appendix A. Finally, I conclude in Chapter 6 with a summary of the analysis presented in my thesis and a look toward future avenues to explore.

Chapter 2

Summary of Previous Work in Perseus

The Perseus molecular cloud is an ideal environment in which to study star formation. It is nearby, and despite the relatively large angular size it covers on the sky (roughly 6 square degrees), it has been observed over its entirety using a variety of the techniques outlined in the preceding chapter. Due to the wealth of pre-existing data, the Perseus molecular cloud is an ideal choice for detailed research – the observations done as part of this thesis have added value due to further interpretations that can be made from the complementary data. This chapter summarizes the complementary data in Perseus, focussing on previous work that I have done, including the results of my MSc thesis (Kirk, Johnstone, & Di Francesco, 2006), which formed the basis of the N_2H^+ survey of dense cores in this work (Chapter 3 and Kirk, Johnstone & Tafalla, 2007), and, in collaboration with Jes Jørgensen, the classification of the evolutionary status of the dense cores used in Chapter 3 (Jørgensen et al., 2007, 2008). Other related analysis involving the identification of outflow drivers in regions of Perseus that I was involved in (Walawender et al., 2005, 2006) are discussed briefly in Section 2.3.2.

2.1 Overview

The Perseus molecular cloud is part of the nearby ring of molecular clouds known as Gould's Belt; possibly all were formed as a result of swept up material following a supernova explosion (e.g., Olano, 1982). Perseus is relatively nearby, at a distance of ∼250 pc (Cernis, 1993), and is the closest molecular cloud currently forming both

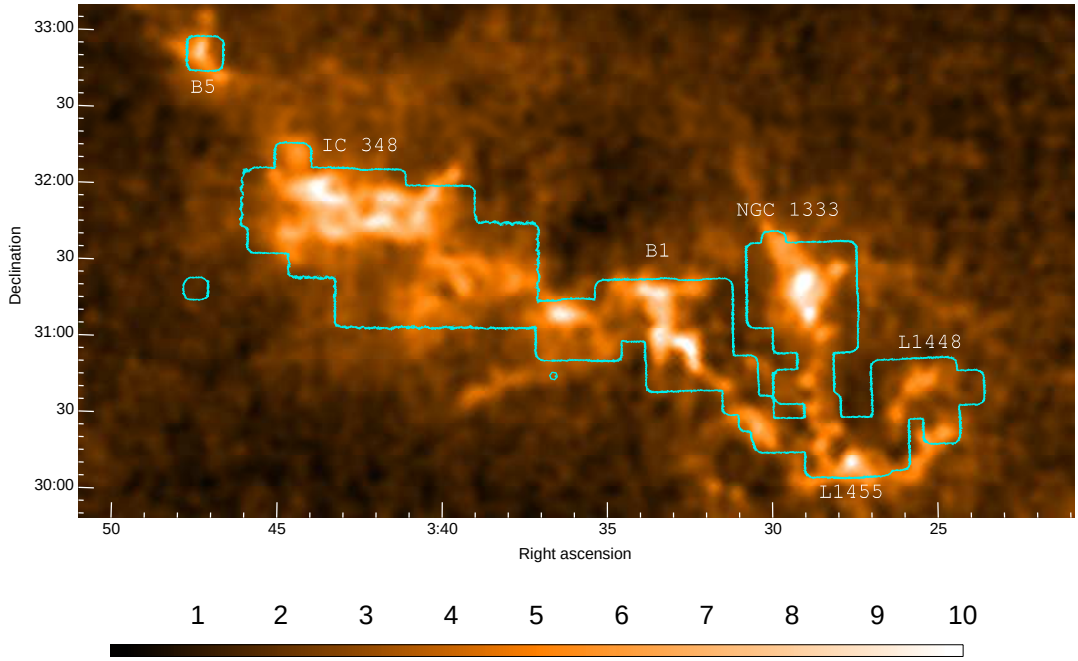

Figure 2.1 An extinction map of the Perseus molecular cloud, as derived from 2MASS data (greyscale). The colourbar indicates the image scale in magnitudes of visual extinction. The overlaid contour shows the region over which SCUBA submillimetre data exists, further discussed in Section 2.3. The common names of the various regions in the cloud are labelled.

low- and intermediate-mass stars (Bally et al., 2008). The cloud has a mass of a few thousand solar masses (e.g., KJD06), and consists of several smaller clustered regions which are actively forming stars (e.g., NGC 1333 and IC 348). Nearby young stellar OB associations may also be impacting the star formation process (e.g., Bally et al., 2008). Figure 2.1 shows the structures seen in the Perseus molecular cloud in extinction (see Section 2.2.1 for more details), with the contour indicating the region over which small-scale structure was observed using SCUBA submillimetre observations (see Section 2.3 for more details). The commonly used names of the various regions are also indicated.

A thorough review of recent observational surveys of the Perseus molecular cloud can be found in Bally et al. (2008), while detailed reviews of the NGC 1333 and IC 348 regions can be found in Walawender et al. (2008) and Herbst (2008), respectively.

2.2 Large-scale Structures

2.2.1 Extinction

As shown in Figure 2.1, the large-scale total column density structure of the Perseus molecular cloud is known from 2MASS dust reddening measurements. The technique used, NICER, is described in more detail in Section 1.2.1. The Perseus extinction data were first presented in KJD06, and are also discussed in Ridge et al. (2006). KJD06 identified structures within the extinction map on two different scales. The largest-scale structures were identified using the *clfind2d* algorithm (Williams, de Geus, & Blitz, 1994) on a slightly smoothed version of the map shown in Figure 2.1. The *clfind2d* algorithm essentially works by contouring the image at various intensities, and separating structures which appear as isolated regions at high contour levels. The smoothing was done to suppress fragmentation into smaller structures by *clfind2d*. These large-scale structures ('extinction regions') roughly correspond to the well-known star-forming regions denoted in Figure 2.1, and are shown in Figure 2.2. The derived properties including the peak visual extinction, size, and mass are given in Table 2.1. As well as being interesting in their own right, the extinction regions serve as a useful set of boundaries that subdivide the cloud, to search for an environmental variation in the properties of dense cores, for example. The extinction regions are used for this purpose in Chapters 3 and 4.

The smaller-scale structures visible within each well-known star-forming region were also identified in KJD06 by using a simple 2D Gaussian-fitting method. Figure 2.3 shows the extinction clump Gaussian fits. Derived properties of the extinction clumps including the peak visual extinction, radius, mass, and orientation are summarized in Table 2.2. These 'extinction clumps' were further used in the analysis discussed in Section 2.3.3 below.

Table 2.1. Properties of extinction regions in Perseus.[1]

Ref #	RA [a] (J2000.0)	Dec [a] (J2000.0)	Peak [b] A_V	Mass [b] ($M_\odot$)	R_{eff} [b] ($''$)	<n> [b] $10^3 cm^{-3}$
1	3:47:45.3	32:52:43.4	10.9	859.6	776.	7.1
2	3:43:57.1	31:59:28.7	10.1	1938.9	1119.	5.3
3	3:39:27.4	31:21:08.6	10.4	780.6	737.	7.5
4	3:36:28.9	31:11:13.1	9.3	560.5	670.	7.2
5	3:32:35.6	30:58:27.7	9.5	441.1	579.	8.8
6	3:30:28.7	30:26:30.2	7.6	257.6	454.	10.6
7	3:28:56.0	31:22:36.4	6.1	973.3	889.	5.3
8	3:28:53.3	30:44:00.5	7.0	246.2	453.	10.2
9	3:27:36.6	30:12:32.8	6.1	240.1	448.	10.3
10	3:25:22.8	30:43:19.2	5.9	173.7	386.	11.6
11	3:24:50.3	30:23:10.1	5.6	107.4	309.	14.0

[1]Table adapted from Kirk, Johnstone, & Di Francesco (2006).

[a]Position of peak extinction within core (accurate to $2.5'$).

[b]Peak visual extinction, mass, radius, and mean number density derived from *clfind2d* (Williams, de Geus, & Blitz, 1994).

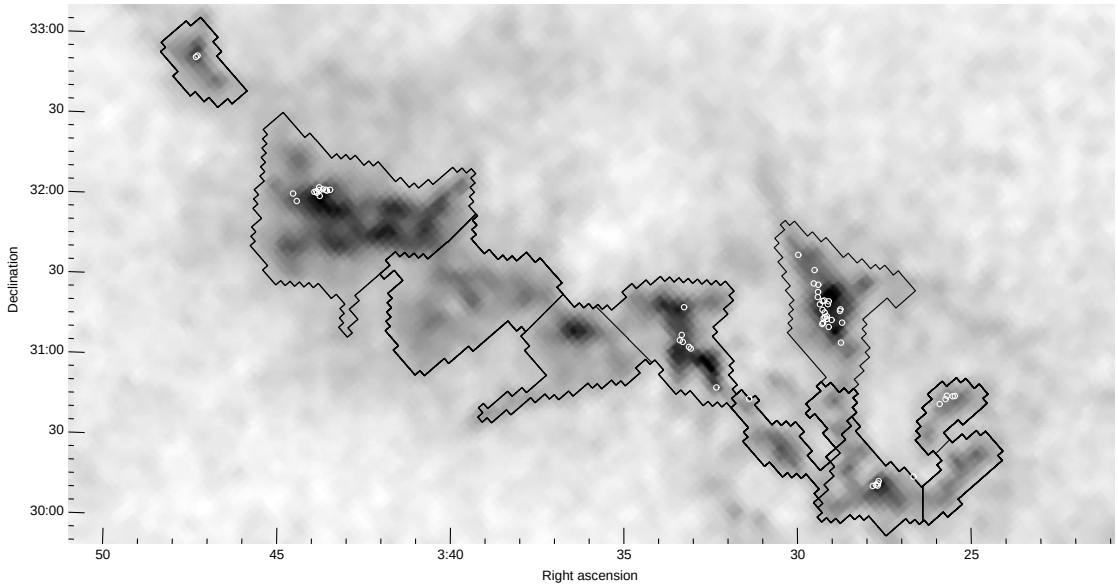

Figure 2.2 The extinction map (in A_V) of the Perseus molecular cloud (greyscale) with overlaid contours indicating the extinction regions identified by KJD06 using *clfind2d*. The white circles indicate the submillimetre cores identified in the SCUBA data (see Section 2.3 for more detail). Figure from Kirk, Johnstone, & Di Francesco (2006).

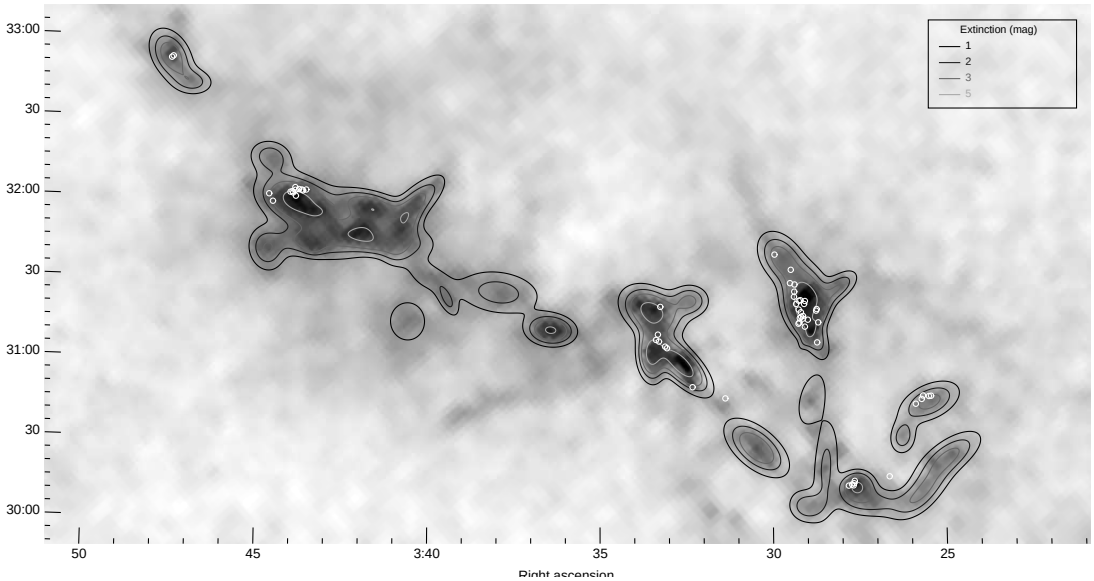

Figure 2.3 The extinction map (in A_V) of the Perseus molecular cloud (greyscale) with the overlaid contours indicating the result of the 2D Gaussian fits to the extinction clumps. The white circles indicate the submillimetre cores identified in the SCUBA data (see Section 2.3 for more detail). Figure from Kirk, Johnstone, & Di Francesco (2006).

Table 2.2. Properties of extinction clumps in Perseus.[1]

Ref #	RA [a] (J2000.0)	Dec [a] (J2000.0)	Peak [b] (A_V)	A_0 [b] (A_V)	Mass [b] ($M_\odot$)	σ_x [b] ($''$)	σ_y [b] ($''$)	<n> [b] ($10^3 cm^{-3}$)	Ext [c] Reg #
1	3:47:43.8	32:52:08.0	4.1	2.6	80.3	394.	253.	5.2	1
2	3:47:01.8	32:42:34.9	2.3	2.4	24.8	192.	291.	3.9	2
3	3:44:47.1	31:40:31.6	2.9	3.4	47.8	327.	258.	4.4	2
4	3:44:42.4	32:15:09.2	2.7	2.8	39.2	311.	237.	4.4	2
5	3:43:54.2	31:58:53.4	6.0	3.7	204.9	540.	324.	5.5	2
6	3:43:38.3	31:43:51.3	3.2	4.0	60.0	431.	227.	3.5	2
7	3:43:25.5	31:41:24.2	1.1	3.7	3.4	144.	115.	3.6	2
8	3:43:08.7	31:54:33.6	1.6	3.5	11.7	147.	252.	3.1	2
9	3:42:57.8	31:48:16.5	0.9	3.3	10.9	435.	138.	0.8	2
10	3:42:01.4	31:48:04.8	4.1	4.3	143.5	561.	321.	3.5	2
11	3:41:48.3	31:57:43.0	3.6	3.0	66.3	482.	198.	3.1	2
12	3:41:34.7	31:43:21.4	2.3	2.8	33.2	398.	184.	2.6	2
13	3:40:45.2	31:48:47.0	2.5	4.6	43.3	189.	469.	2.2	2
14	3:40:37.3	31:14:12.6	1.9	3.4	45.6	333.	364.	2.5	3
15	3:40:26.6	31:43:13.5	1.9	3.2	34.7	255.	362.	2.7	2
16	3:40:17.5	31:59:50.6	2.8	2.8	56.0	201.	502.	2.4	2
17	3:40:01.1	31:31:10.8	1.6	3.8	26.8	213.	403.	1.9	3
18	3:39:26.7	31:21:44.6	1.9	4.2	11.4	118.	264.	3.2	3
19	3:37:57.6	31:25:20.6	2.6	2.8	103.3	629.	327.	1.9	3
20	3:36:26.1	31:11:12.6	5.3	3.6	70.9	208.	332.	7.9	4
21	3:33:31.0	31:01:11.3	5.3	2.2	65.8	346.	185.	7.3	5
22	3:33:29.2	31:18:14.1	5.9	2.7	144.7	430.	292.	6.9	5
23	3:32:38.4	30:58:15.4	6.4	2.8	130.9	206.	505.	5.4	5
24	3:32:21.9	31:22:02.1	3.3	2.0	39.1	268.	226.	6.1	5
25	3:30:27.9	30:26:38.5	4.5	1.9	116.6	260.	511.	4.1	6
26	3:29:40.5	31:37:34.4	3.9	2.3	84.5	410.	273.	4.7	7
27	3:29:03.8	30:04:28.1	2.7	2.0	31.9	235.	260.	5.0	9
28	3:28:58.9	31:22:01.0	6.5	3.8	161.9	421.	304.	7.7	7
29	3:28:51.2	30:44:36.1	2.0	2.5	39.4	217.	474.	1.9	8

Table 2.2 (cont'd)

Ref #	RA [a] (J2000.0)	Dec [a] (J2000.0)	Peak [b] (A_V)	A_0 [b] (A_V)	Mass [b] ($M_\odot$)	σ_x [b] ($''$)	σ_y [b] ($''$)	<n> [b] ($10^3 cm^{-3}$)	Ext [c] Reg #
30	3:28:50.6	31:09:11.5	3.3	3.5	40.9	376.	170.	3.9	7
31	3:28:42.3	31:12:21.7	1.4	3.2	9.7	428.	81.	0.8	7
32	3:28:27.9	30:19:32.0	2.3	2.8	61.2	191.	723.	1.0	9
33	3:27:58.5	31:26:45.5	2.8	2.8	28.9	317.	167.	4.2	7
34	3:27:34.9	30:11:56.4	5.1	3.6	48.9	206.	238.	10.5	9
35	3:27:08.3	30:05:26.3	2.4	2.8	56.1	220.	537.	1.9	9
36	3:26:13.4	30:29:45.7	2.6	2.0	24.0	187.	249.	5.3	10
37	3:25:40.8	30:09:14.3	3.0	1.8	63.7	491.	220.	2.7	11
38	3:25:25.6	30:42:50.1	3.5	2.1	75.6	453.	244.	3.7	10
39	3:24:53.2	30:22:35.0	3.2	2.3	75.9	529.	228.	2.7	11

[1]Table adapted from Kirk, Johnstone, & Di Francesco (2006).

[a]Position of peak extinction within core (accurate to $2.5'$).

[b]Peak visual extinction, background visual extinction, mass, σ's, and mean density derived from Gaussian fitting.

[c]Associated extinction region.

2.2.1.1 Masses

The visual extinction inferred from the 2MASS stellar reddening data can be converted into mass estimates through several assumptions about standard dust properties (see KJD06, for more detail). The distribution of masses for both sets of structures identified in the extinction map were analyzed in KJD06. The distribution of masses is typically expressed as a power-law of the form

$$N(M) \propto M^{-\alpha} \tag{2.1}$$

where N is the cumulative number of objects of mass M or greater, and α is the slope.

Large-scale structures (typically observed using CO) are usually best fit with a shallow slope, e.g., $\alpha \sim 1$ (Kramer et al., 1998), which implies that most of the mass resides in the highest mass objects. Dense core mass distributions, on the other hand, typically have much steeper slopes, so that most of the mass resides in the smallest objects (e.g., Johnstone et al., 2000).

KJD06 found that the extinction regions had a mass distribution slope of $\alpha \sim 1$, similar to that observed for large-scale structure, while the extinction clumps had a steeper slope of $1.5 \leq \alpha \leq 2$, similar to that observed for the dense cores. Due to the small number of extinction regions and clumps identified, it was not clear whether this difference is due to physical processes or merely a manifestation of small number statistics or the manner in which objects were identified.

2.2.2 CO

^{12}CO and ^{13}CO observations have also been made of the entire Perseus molecular cloud; see Ridge et al. (2006) for the first analysis of this dataset. Pineda et al. (2008) compared the ^{12}CO and ^{13}CO emission with the 2MASS-derived visual extinction map in order to determine the abundance fraction of the two species. While the global result was similar to that found by previous work, they did find significant regional variation of up to 50%. This was attributed to photodissociation and / or chemical fractionation (the over-concentration of heavier isotopologues of molecular species versus their less heavy counterparts within a region), implying that the various regions in the cloud may have undergone a somewhat different chemical evolutionary history.

Structure identification in the ^{13}CO 3D (position, position, velocity) datacube using the three-dimensional version of the *clfind* routine (Williams, de Geus, & Blitz, 1994) is presented in Pineda et al. (2009). The main result of their analysis is that structure identification in three dimensions in this dataset is unreliable. In general, 3D structure identification is much more difficult than in the 2D maps – potential structures tend to span much of the 3D space, making the final identifications extremely reliant on the input parameters to the structure-identification algorithm. Pineda et al. (2009) showed that the resultant mass function of the structures they identified is highly dependent on the contouring levels chosen for *clfind* – the slope can vary from $\alpha \sim$1.6 to 2.4 simply by adjusting the contour level. This form of analysis of the structures found in the ^{13}CO dataset alone is thus not a useful prospect.

Despite the complexity, the ^{13}CO data is important for understanding the bulk motions of material within the molecular cloud. In Chapters 4 and 5, the ^{13}CO data are used to quantify the mean motion (centroid velocity) and velocity dispersion of the molecular cloud gas within specific regions analyzed, where the regions are determined from the extinction maps.

2.3 Dense Cores

Small-scale structure has been identified across the entire Perseus molecular cloud using both SCUBA submillimetre (Hatchell et al., 2005; KJD06) and Bolocam millimetre (Enoch et al., 2006) continuum observations. As described in the previous chapter, ground-based (sub)millimetre observations are sensitive only to smaller-scale structures due to several observational constraints. The SCUBA data analyzed in KJD06 included a substantial portion of data with integration times sufficiently long to allow the data to be binned to a resolution of 3″ (first reported and analyzed in Hatchell et al., 2005), plus an additional portion of data spanning less-studied regions of the Perseus cloud taken with shorter integration times (in order to allow a larger area to be mapped). A map binned to a resolution of 6″ was therefore used in order to include all of the data (note the intrinsic resolution of SCUBA is 15″, so the data still sub-samples the beam). We identified dense cores using the *clfind2d* algorithm. Additional properties of the dense cores such as the central concentration (or 'peakiness') were also derived, along with the results of Bonnor-Ebert sphere fitting. The Bonnor-Ebert sphere model is an isothermal sphere where thermal pressure balances gravity and the sphere edge is bounded by an external pressure (Bonnor, 1956; Ebert, 1955; Hartmann, 1998). Previous work (e.g., Johnstone et al., 2000; Alves, Lada & Lada, 2001) has shown that the BE sphere model can fit dense cores well and tends to provide model core properties that are physically reasonable (other similarly-shaped column density profiles can also provide good fits; see Dapp et al., 2009). Table 2.3 summarizes the dense core properties found in KJD06.

Table 2.3. Properties of submillimetre cores in Perseus.[1]

Name [a] (SMM J)	RA [b] (J2000.0)	Dec [b] (J2000.0)	f_0 [c] (Jy/bm)	S_{850} [c] (Jy)	R_{eff} [c] ($''$)	Mass[d] $M_\odot$	Conc[e]	Temp[e] (K)	M_{BE}[e] $M_\odot$	log n_{cent}[e] cm^{-3}	log P_{ext}/k[e] cm^3 K^{-1}	H05 [f] #	Extinction [g] Clump #
034769+32517	3:47:41.6	32:51:48.0	0.29	0.60	23.	0.3	0.45	12.	0.54	5.2	5.9	78	1
034764+32523	3:47:38.8	32:52:18.9	0.25	0.61	26.	0.3	0.48	10.	0.66	5.2	5.8	79	1
034472+32015	3:44:43.7	32:01:32.3	0.44	0.76	24.	0.4	0.56	10.	0.84	5.5	5.9	14	5
034461+31587	3:44:36.8	31:58:46.1	0.18	0.30	19.	0.2	0.31	14.	0.19	4.9	5.9	19	5
034410+32022	3:44:06.1	32:02:17.7	0.19	0.68	27.	0.4	0.30	17.	0.32	4.6	5.7	22	5
034404+32025	3:44:02.8	32:02:30.5	0.23	0.98	29.	0.6	0.29	18.	0.39	4.6	5.8	18	5
034402+32020	3:44:01.3	32:02:00.8	0.27	0.94	29.	0.5	0.41	14.	0.56	4.8	5.8	16	5
034396+32040	3:43:57.7	32:04:01.6	0.22	0.80	28.	0.4	0.36	17.	0.36	4.6	5.7	17	5
034395+32030	3:43:57.2	32:03:01.8	0.82	2.27	37.	1.3	0.71	12.	1.92	5.6	5.6	13	5
034394+32008	3:43:56.5	32:00:50.0	1.04	3.14	39.	1.7	0.72	13.	2.24	5.7	5.6	12	5
034385+32033	3:43:51.0	32:03:21.2	0.34	1.46	36.	0.8	0.52	12.	1.26	5.1	5.7	15	5
034376+32031	3:43:45.8	32:03:10.4	0.15	0.81	30.	0.4	0.17	17.	0.37	4.5	5.7	–	5
034373+32028	3:43:43.9	32:02:52.9	0.17	0.76	28.	0.4	0.22	17.	0.35	4.6	5.7	26	5
034363+32032	3:43:38.3	32:03:12.1	0.17	0.31	19.	0.2	0.29	14.	0.19	4.8	5.9	23	5
033335+31075	3:33:21.3	31:07:34.6	1.16	5.83	51.	3.2	0.72	15.	3.33	5.5	5.5	2	21
033329+31095	3:33:17.9	31:09:34.3	1.25	4.38	49.	2.4	0.79	13.	2.95	5.5	5.5	1	21
033326+31069	3:33:16.1	31:06:58.2	0.53	4.96	54.	2.8	0.54	15.	2.66	4.9	5.6	4	21
033322+31199	3:33:13.4	31:19:58.0	0.18	0.39	21.	0.2	0.29	15.	0.22	4.8	5.9	82	22
033309+31050	3:33:05.4	31:05:03.4	0.17	0.77	30.	0.4	0.26	17.	0.36	4.5	5.7	6	21
033303+31044	3:33:02.2	31:04:27.1	0.16	1.30	40.	0.7	0.26	18.	0.52	4.3	5.5	5	21
033229+30497	3:32:18.0	30:49:47.1	1.22	2.13	32.	1.2	0.76	12.	1.73	5.8	5.8	76	23
033134+30454	3:31:20.9	30:45:28.4	0.59	0.91	24.	0.5	0.62	10.	0.98	5.7	5.9	77	23
032986+31391	3:29:51.8	31:39:08.0	0.25	0.41	20.	0.2	0.42	12.	0.36	5.1	6.0	–	26
032942+31283	3:29:25.3	31:28:21.2	0.18	0.20	15.	0.1	0.28	13.	0.14	5.0	6.1	64	28
032939+31333	3:29:23.5	31:33:20.8	0.23	0.39	19.	0.2	0.36	15.	0.21	4.8	5.9	58	26
032931+31232	3:29:18.6	31:23:14.0	0.29	0.92	28.	0.5	0.44	12.	0.70	5.0	5.8	63	28
032930+31251	3:29:18.0	31:25:07.8	0.29	1.81	44.	1.0	0.55	11.	1.64	5.0	5.5	57	28
032928+31278	3:29:17.4	31:27:49.7	0.22	0.47	22.	0.3	0.40	13.	0.35	4.9	5.9	61	28
032925+31205	3:29:15.1	31:20:31.3	0.18	0.40	21.	0.2	0.29	15.	0.23	4.8	5.9	70	28

Table 2.3 (cont'd)

Name [a] (SMM J)	RA [b] (J2000.0)	Dec [b] (J2000.0)	f_0 [c] (Jy/bm)	S_{850} [c] (Jy)	R_{eff} [c] ($''$)	Mass[d] $M_\odot$	Conc[e]	Temp[e] (K)	M_{BE}[e] $M_\odot$	log n_{cent}[e] cm^{-3}	log P_{ext}/k[e] cm^3 K^{-1}	H05 [f] #	Extinction [g] Clump #
032919+31131	3:29:11.4	31:13:06.7	2.61	6.42	46.	3.6	0.83	16.	3.27	5.6	5.7	42	30
032917+31184	3:29:10.6	31:18:24.5	0.88	3.42	41.	1.9	0.68	13.	2.34	5.5	5.6	46	28
032917+31217	3:29:10.3	31:21:42.4	0.39	1.57	33.	0.9	0.46	14.	1.00	5.0	5.8	54	28
032916+31135	3:29:10.0	31:13:30.4	5.27	8.51	38.	4.7	0.84	19.	3.22	5.9	6.0	41	30
032914+31152	3:29:08.9	31:15:12.2	0.55	1.99	34.	1.1	0.56	13.	1.49	5.3	5.8	51	31
032912+31218	3:29:07.5	31:21:53.8	0.37	1.75	36.	1.0	0.50	13.	1.25	5.0	5.7	56	28
032911+31173	3:29:06.9	31:17:23.8	0.29	1.01	29.	0.6	0.41	15.	0.58	4.8	5.8	62	28
032910+31156	3:29:06.6	31:15:41.7	0.62	2.03	30.	1.1	0.49	15.	1.14	5.2	6.0	50	31
032905+31149	3:29:03.3	31:14:59.1	0.49	2.00	32.	1.1	0.45	16.	1.03	5.0	5.9	52	31
032905+31159	3:29:03.2	31:15:59.0	2.31	6.07	36.	3.4	0.70	17.	2.72	5.8	6.0	43	31
032901+31204	3:29:01.0	31:20:28.5	0.92	5.07	45.	2.8	0.61	16.	2.71	5.3	5.7	45	28
032900+31119	3:29:00.3	31:11:58.5	0.16	0.13	12.	0.1	0.24	12.	0.11	5.2	6.1	65	30
032899+31215	3:28:59.6	31:21:34.2	0.62	2.40	39.	1.3	0.63	12.	1.89	5.4	5.7	47	28
032891+31145	3:28:54.9	31:14:33.4	1.63	4.02	41.	2.2	0.79	14.	2.53	5.7	5.7	44	31
032866+31179	3:28:40.2	31:17:54.3	0.31	1.14	30.	0.6	0.42	14.	0.69	4.9	5.8	55	31
032865+31060	3:28:39.2	31:06:00.3	0.15	0.83	32.	0.5	0.25	17.	0.39	4.4	5.6	75	30
032865+31185	3:28:39.2	31:18:30.0	0.29	1.32	34.	0.7	0.44	14.	0.87	4.8	5.7	60	28
032861+31134	3:28:36.8	31:13:29.6	0.43	0.97	27.	0.5	0.57	11.	1.01	5.4	5.8	49	31
032780+30121	3:27:48.4	30:12:08.7	0.23	0.95	31.	0.5	0.39	15.	0.53	4.7	5.7	37	34
032771+30125	3:27:42.8	30:12:31.4	0.30	1.00	30.	0.6	0.45	12.	0.77	5.0	5.8	36	34
032766+30122	3:27:40.0	30:12:12.7	0.22	0.62	23.	0.3	0.27	17.	0.29	4.7	5.9	40	34
032765+30130	3:27:39.0	30:13:00.4	0.41	0.79	23.	0.4	0.50	11.	0.73	5.3	6.0	35	34
032763+30139	3:27:38.0	30:13:54.2	0.18	0.26	17.	0.2	0.30	14.	0.17	4.9	6.0	39	34
032662+30153	3:26:37.3	30:15:20.8	0.17	0.17	14.	0.1	0.23	13.	0.12	5.1	6.1	80	35
032581+30423	3:25:49.1	30:42:18.1	0.28	1.61	37.	0.9	0.41	16.	0.84	4.7	5.7	32	38
032564+30440	3:25:38.7	30:44:03.0	1.09	2.14	32.	1.2	0.72	12.	1.72	5.8	5.8	29	38
032560+30453	3:25:36.2	30:45:20.2	2.85	8.90	52.	4.9	0.84	17.	4.01	5.6	5.6	28	38
032543+30450	3:25:26.0	30:45:05.2	0.31	1.69	37.	0.9	0.42	16.	0.90	4.7	5.7	31	38
032537+30451	3:25:22.3	30:45:10.0	0.78	1.94	33.	1.1	0.68	12.	1.68	5.7	5.7	30	38

The SCUBA submillimetre data covers the bulk of the molecular cloud, as seen in Figure 2.1, and spans all of the regions of higher total column density. The dense core catalog therefore is particularly useful, as it summarizes the properties of the complete set of dense cores within the Perseus cloud. Spectral observations tend to require a much higher amount of observing time, hence complete continuum-mapped data can function as a guide as to where to focus spectral studies for maximum efficiency. Spectral observations in the dense gas tracers N_2H^+ (Chapter 3 and Kirk, Johnstone & Tafalla, 2007) and NH_3 (Rosolowsky et al., 2008) have now been performed using the dense core dataset, and the results will be discussed in later sections.

2.3.1 Masses

The observed (sub)millimetre continuum fluxes can be converted into mass estimates through the relationship

$$M_{core} = \frac{S_\lambda \ D^2}{\kappa_\lambda \ B_\lambda(T_d)} \tag{2.2}$$

following Reid & Wilson (2005) where S is the integrated intensity at wavelength λ, D is the distance, κ is the dust opacity (at wavelength λ), and B_λ is the Planck blackbody function at λ and dust temperature T_d. For the SCUBA observations of Perseus, this equation can be written as:

$$M_{core} = 0.23 \ S_{850} \left(\exp\left(\frac{17 \text{ K}}{T_d}\right) - 1 \right) \ \left(\frac{\kappa_{850}}{0.02 \text{ cm}^2 \text{ g}^{-1}}\right)^{-1} \ \left(\frac{D}{250 \text{ pc}}\right)^2 \ M_\odot \tag{2.3}$$

as in KJD06. Estimating the mass therefore requires assumptions about the distance, temperature, and dust opacity for the dense cores; the uncertainties are sizable for all of these quantities. In KJD06, we assumed a distance of 250 pc, a temperature of 15 K, and a dust opacity of 0.02 cm^2 g^{-1}, so that an observed flux of 1 Jy corresponds to 0.48 $M_\odot$. The Hatchell et al. (2005) core mass estimates differ by a factor of several compared to the KJD06 estimates due to these combined uncertainties.

Although the absolute calibration of the dense core masses has a very large uncertainty, the relative values are much more reliable. For example, given that all the cores lie at the same distance, any error in the assumed distance scales all of the masses by the same amount. The distribution of dense core masses, and in particular, the slope of the distribution, can thus be reasonably estimated despite the large uncertainties in the exact core masses. KJD06 find a mass distribution slope

Table 2.3 (cont'd)

Name [a] (SMM J)	RA [b] (J2000.0)	Dec [b] (J2000.0)	f_0 [c] (Jy/bm)	S_{850} [c] (Jy)	R_{eff} [c] ($''$)	Mass[d] $M_\odot$	Conc[e]	Temp[e] (K)	M_{BE}[e] $M_\odot$	log n_{cent}[e] cm^{-3}	log P_{ext}/k[e] cm^3 K^{-1}	H05 [f] #	Extinction [g] Clump #

[1]Table adapted from Kirk, Johnstone, & Di Francesco (2006).

[a]Name formed from J2000 positions (hhmm.mmdddmm.m)

[b]Position of peak flux within core (accurate to $6''$).

[c]Peak flux, total flux, and radius derived from *clfind2d* (Williams, de Geus, & Blitz, 1994). Note a beamsize of $19.9''$ is used for the peak flux.

[d]Mass derived from the total flux assuming $T_d = 15$ K, $\kappa_{850} = 0.02$ cm^2 g^{-1}, and D = 250 pc.

[e]Concentration, temperature, mass, central number density, and external pressure derived from Bonnor-Ebert modelling (see Kirk, Johnstone, & Di Francesco, 2006).

[f]Best corresponding submillimetre core in Hatchell et al. (2005). More cores were identified in their survey, as discussed in Kirk, Johnstone, & Di Francesco (2006), §4.1.

[g]Closest corresponding extinction clump.

of $\alpha \sim 2$ (where the slope is again defined by $N(M) \propto M^{-\alpha}$) from the SCUBA data (see Figure 2.4). Using the cores identified in the Bolocam data of Perseus, Enoch et al. (2006) find a similar slope. This slope is somewhat steeper than the slope of the initial stellar mass function found by Salpeter ($\alpha \sim 1.35$, Salpeter, 1955), but is consistent with the range of slopes found for dense cores in other molecular clouds (e.g., Motte et al., 1998; Johnstone et al., 2000, 2001; Reid & Wilson, 2005).

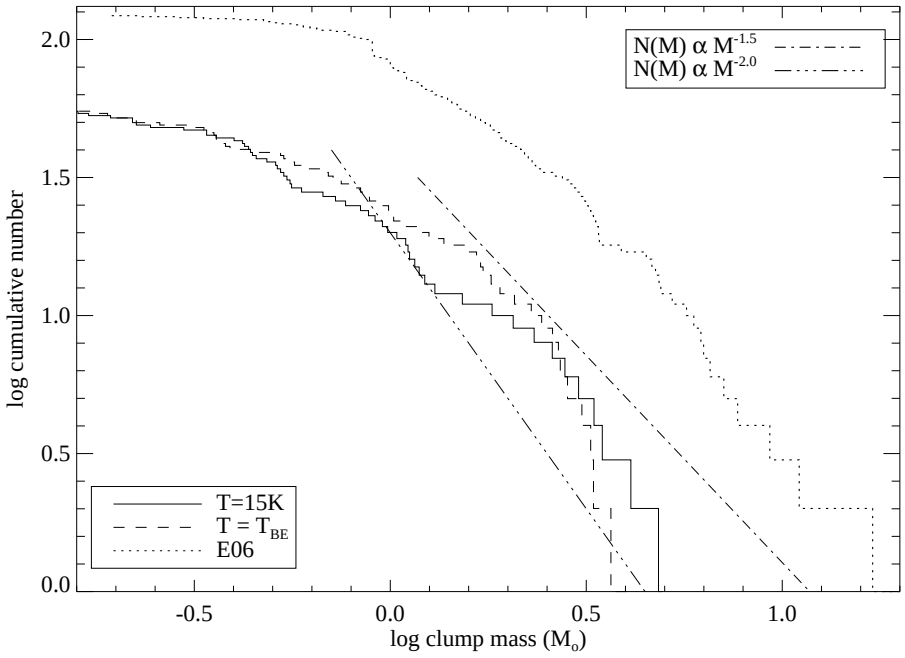

Figure 2.4 The distribution of masses of the dense cores identified in the SCUBA map. The solid line indicates the masses calculated assuming a global temperature of 15 K, while the dashed line shows the masses calculated assuming the temperature fit to the Bonnor-Ebert sphere model of each core. Both mass estimates yield similar-sloped distributions. The dotted line indicates the dense core mass function found by Enoch et al. (2006) in the Bolocom millimetre data, again, revealing a similar slope. Mass distribution slopes of -1.5 and -2 are shown to guide the eye. Figure from Kirk, Johnstone, & Di Francesco (2006).

2.3.2 Evolutionary Stage

2.3.2.1 Outflows

The evolutionary status of the submillimetre cores can be determined using a variety of techniques. Protostars are usually associated with outflows, hence one method to

determine whether the core is starless or protostellar is to search for indications of an outflow. Hatchell at al. (2007b) used ^{12}CO (3–2) maps around the submillimetre cores to search for outflow signatures. The ^{12}CO (3–2) spectral line is sensitive to warm material, hence a detection of large (many times the ambient sound speed) line-wings in a spectrum is a good indication of an outflow source. Hatchell at al. (2007b) identified 51 candidate outflow sources, of which 24 were definite detections. Confusion in the most clustered regions can lead to difficulty in determining the source and number of distinct outflows.

Outflows also shock ambient cloud gas as they move away from their central source; Hα and H_2 emission both trace hot (shocked) gas and can therefore be used to infer the presence of an outflow. In collaboration with Josh Walawender (Walawender et al., 2005, 2006), we used these shocked gas tracers to identify 21 submillimetre cores with large outflows in the B1 and IC 348 regions of Perseus respectively.

2.3.2.2 Infrared Colours

Alternatively, the evolutionary status of the submillimetre cores can be determined by the use of multi-wavelength continuum observations. Submillimetre cores that do not yet have a protostar formed in the centre emit primarily at very long wavelengths since their central temperatures are still cold ($\sim$ 10 K). Starless cores therefore have no emission in the shorter wavelength infrared bands detectable by the *Spitzer Space Telescope*. Protostars, on the other hand, have higher central temperatures ($\geq$ 1000 K), and despite the considerable extinction due to dust, some observable radiation at shorter wavelengths may be seen.

Two complementary studies have been performed using short wavelength continuum observations to classify the dense cores across Perseus as starless or protostellar. Hatchell et al. (2007a) used the continuum data available at all wavelengths (millimetre, submillimetre, and far- and mid- infrared) for the cores in Perseus to determine the spectral energy distribution (or SED). Hatchell et al. (2007a) then modelled the SED to determine the temperature of the emitting material. Based on the temperature inferred from the fit, the cores were classified as starless or protostellar. SED fitting in addition to colour cuts and other criteria were also used in the later study of Enoch et al. (2009) which includes analysis of cores in the Ophiuchus and Serpens clouds in addition to the Perseus data.

In collaboration with Jes Jorgensen (Jørgensen et al., 2007), we used a combination

of *Spitzer* and SCUBA data in order to identify the most deeply embedded (youngest) protostars. Dense cores and protostars were found to often be closely associated with each other and red *Spitzer* sources in particular were nearly always found in close proximity to a SCUBA core. Figure 2.5 illustrates these points – *Spitzer* sources and SCUBA cores are associated much more than would be expected from a random distribution (left panel), and the red *Spitzer* sources especially so. (Note that chance co-incidences have a probability of only a few percent for the entire population.) These associations between SCUBA cores and *Spitzer* sources are therefore expected to reveal young embedded protostars.

This finding led to the adoption two criteria for the identification of young protostars. The first criterion was the coincidence of a source detected in the longer wavelength *Spitzer* bands (24 or 70 μm) with a SCUBA core. An additional criterion was required in order to obtain a complete census of protostars – *Spitzer* sources that satisfied a colour range in the various *Spitzer* bands, without the requirement of a coincident SCUBA core. This second criterion allows for the inclusion of protostars that are sufficiently evolved such that their dusty envelopes become fainter than the sensitivity of the SCUBA data or missed due to source confusion. Young protostars are expected to have a particular range of red colours, unlike those of spurious objects that happen to lie in the foreground or background, as discussed in more detail by Jørgensen et al. (2006). The combination of the two criteria is essential, as either catalog is prone to incompleteness if used in isolation. The catalog of young YSOs identified in Perseus by Jørgensen et al. (2007) is shown in Table 2.4.

The Jørgensen et al. (2007) catalog is used as the basis for our subsequent analysis where a distinction between starless cores and protostars is required. As is discussed in Chapter 3 (Chapter 3), a comparison between the protostellar catalogs of Jørgensen et al. (2007) and Hatchell et al. (2007a) show that the majority ($\sim$ 90%) of the classifications are identical, and that there is not a significant impact on the results by using one catalog instead of the other.

2.3.3 Core Environment

2.3.3.1 Clustering

Visual inspection of the locations of the submillimetre cores indicates that the cores are clustered, mostly around the already-identified star-forming regions shown in Figure 2.1. The clustered nature of the cores can also be analyzed in a more quantitative

Table 2.4 List of embedded YSOs in Perseus. [1]

#	Position[a] RA (J2000)	DEC (J2000)	Mid-IR Colors [3.6] − [4.5]	[8.0] − [24]	Sep.[b] [″]	Conc.[c]	Code[d]	Other identifiers[e]
1	03 25 22.36	+30 45 13.6	2.9	6.5	0.2	0.70	ABC	L1448-IRS2 / IRAS 03222+3034
2	03 25 36.48	+30 45 23.2	2.8	6.0	7.0	0.87	ABC*	L1448-N(A)
3	03 25 38.87	+30 44 06.0	1.7	7.1	1.5	0.83	ABC	L1448-C(N)
4	03 26 37.46	+30 15 28.2	2.4	6.2	4.2	0.39	AB−	
5	03 27 38.27	+30 13 58.5	0.6	3.8	3.0	0.31	−B−*	L1455-FIR2
6	03 27 39.11	+30 13 02.8	3.3	7.0	1.9	0.59	AB−*	L1455-IRS1 / IRAS 03245+3002
7	03 27 43.25	+30 12 28.9	2.1	6.1	4.4	0.57	AB−	L1455-IRS4
8	03 27 47.69	+30 12 04.4	0.9	2.8	9.3	0.48	−B−*	
9	03 28 32.55	+31 11 04.8	-0.4	5.4	1.7	0.27	−B−	
10	03 28 34.53	+31 07 05.5	1.5	3.1	6.7	0.30	−B−*	
11	03 28 37.11	+31 13 28.3	2.8	...	...	0.66	−−C	IRAS 03255+3103
12	03 28 39.11	+31 06 01.6	1.3	6.0	8.0	0.32	AB−	(ass. HH 340)
13	03 28 40.62	+31 17 56.5	...	4.4	5.3	0.51	−B−	
14	03 28 45.31	+31 05 41.9	2.4	7.2	43.3	...	A−−	IRAS 03256+3055
15	03 28 55.59	+31 14 37.5	...	...	...	0.87	−−C	NGC1333-IRAS2A
16	03 28 57.36	+31 14 15.9	2.1	5.0	31.4	...	A−−*	NGC1333-IRSA2B
17	03 28 59.55	+31 21 46.7	0.6	2.8	13.6	0.67	−BC*	
18	03 29 00.61	+31 12 00.4	...	...	2.4	0.48	−B−	
19	03 29 01.66	+31 20 28.5	...	...	...	0.67	−−C	(ass. SVS12/ASR114)
20	03 29 03.30	+31 15 55.5	...	...	...	0.77	−−C	NGC1333-SVS13
21	03 29 04.09	+31 14 46.6	1.5	6.7	6.0	0.53	AB−	HH7-11 MMS6
22	03 29 10.53	+31 13 30.7	...	...	0.8	0.86	−BC	NGC1333-IRAS4A
23	03 29 10.72	+31 18 20.5	...	7.2	10.6	0.74	−BC2	
24	03 29 11.29	+31 18 31.3	...	8.2	2.8	0.74	−BC2	
25	03 29 12.07	+31 13 01.8	4.3	5.4	5.9	0.86	ABC	NGC1333-IRAS4B[f]
26	03 29 13.62	+31 13 57.9	3.1	...	2.4	0.58	−B−	NGC1333-IRAS4C
27	03 29 17.21	+31 27 46.2	1.1	7.8	5.9	0.54	AB−	(ass. Per 4)
28	03 29 18.25	+31 23 19.9	1.7	4.5	11.6	0.55	−B−*2	(ass. HH335)
29	03 29 18.73	+31 23 25.4	0.5	3.2	12.5	0.55	−B−*2	
30	03 29 23.50	+31 33 29.4	...	7.0	11.5	0.43	−B−	IRAS 03262+3123
31	03 29 51.89	+31 39 05.6	...	7.9	1.4	0.53	−B−	IRAS 03267+3128/([LMG94]Per 5)
32	03 31 21.01	+30 45 30.0	1.9	5.6	2.4	0.71	ABC	IRAS 03282+3035
33	03 32 18.03	+30 49 46.9	1.0	4.8	3.4	0.82	ABC	IRAS 03292+3039
34	03 33 13.81	+31 20 05.2	2.1	5.1	14.3	0.31	AB−	(ass. [LMG94] Per 9B)
35	03 33 14.41	+31 07 10.8	2.4	6.0	29.9	...	A−−*2	B1-SMM3
36	03 33 16.49	+31 06 52.3	...	...	2.7	0.55	−B−2	B1-d
37	03 33 16.67	+31 07 55.1	2.9	5.3	4.0	0.38	AB−	B1-a / IRAS 03301+3057
38	03 33 17.87	+31 09 31.8	4.5	4.5	2.2	0.84	ABC*	B1-c
39	03 33 20.34	+31 07 21.4	2.0	4.2	13.2	0.74	−BC*	B1-b
40	03 33 27.31	+31 07 10.2	2.5	7.7	1.2	0.32	AB−	(ass. HH789)
41	03 43 50.99	+32 03 24.7	1.3	5.5	2.7	0.65	ABC	
42	03 43 51.03	+32 03 08.0	1.2	5.7	17.8	...	A−−*	
43	03 43 56.91	+32 03 04.2	...	...	3.1	0.79	−BC	IC348-MMS
44	03 43 57.32	+32 00 47.6	...	...	8.3	0.78	−BC2	HH211-FIR (?)
45	03 43 57.64	+32 00 44.8	...	...	13.1	0.78	−BC2	(ass. HH211?)
46	03 43 59.41	+32 00 35.5	2.6	4.5	37.5	...	A−−	(ass. HH211?)
47	03 44 02.40	+32 02 04.7	1.5	5.4	18.3	...	A−−	
48	03 44 43.32	+32 01 31.6	0.9	3.8	7.2	0.62	−BC*	IRAS 03415+3152
49	03 47 41.61	+32 51 43.9	1.1	3.3	2.7	0.59	−B−*	B5-IRS1 / IRAS 03445+3242

[1] Adapted from Jørgensen et al. (2007), Table 3. Reproduced by permission of the AAS.

[a] Coordinates given in format of (hh mm ss.ss) for right ascension and (dd mm ss.s) for declination. Coordinates for sources selected on basis of the core concentration only (code "C") refer to position of SCUBA core.

[b] Separation between the mid-infrared source and the nearest submillimeter core.

[c] Concentration of submillimeter core from Kirk, Johnstone, & Di Francesco (2006).

[d] Code for selection of source according to which of the selection criteria (A, B, or C) applies (see Jørgensen et al., 2007, for further details). Asterisks indicate previously identified Spitzer embedded YSO candidates, while cores associated with multiple YSOs are indicated by a "2".

[e] Refers to main designation in the SIMBAD database, commonly used identifier or association (marked "ass.").

[f] c2d catalog refers to position of bright shock observed in the IRAC bands.

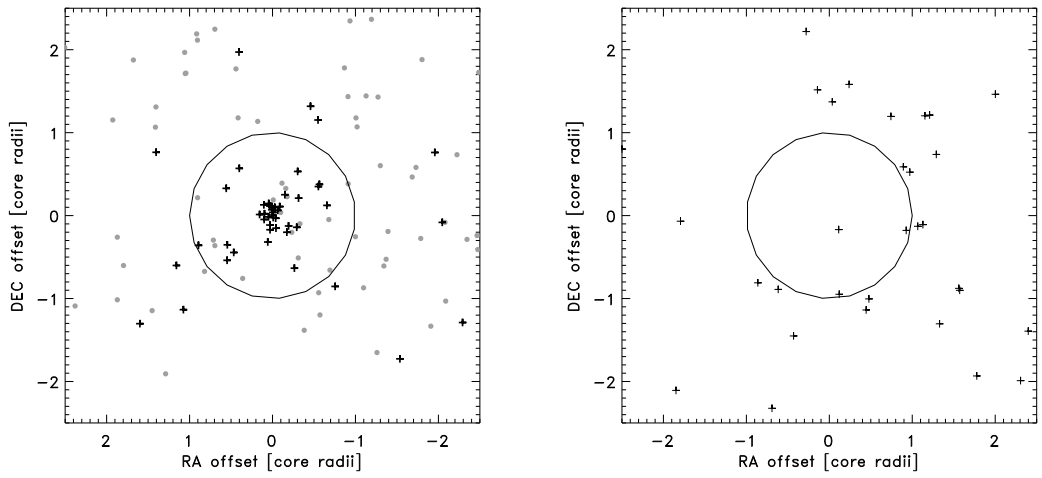

Figure 2.5 Left: The separation between *Spitzer* sources and the closest associated SCUBA core, in units of the SCUBA core radius and shifted to a common centre. Grey dots show *Spitzer* sources with 'blue' *Spitzer* colours in the shortest IRAC bands ([3.6]-[4.5]>1.0), while the black plusses show *Spitzer* sources with 'red' *Spitzer* colours in the shortest IRAC bands ([3.6]-[4.5]>1.0). Right: The result expected for a random distribution of the *Spitzer* sources over the SCUBA map. Figure from Jørgensen et al. (2007), Figure 2. Reproduced by permission of the AAS.

manner, however. Hatchell et al. (2005) and Jørgensen et al. (2008) both examine the clustering of cores within Perseus, with the former considering only the submillimetre cores and the latter additionally considering the protostars identified in the cloud (see Section 2.3.2). Clustered environments are typically defined by setting a threshold to the surface (or inferred volume) density of objects. Hatchell et al. (2005) use a single threshold of 1.2 $M_\odot$ pc^{-2} to define clustered versus non-clustered regions, and find 80% of cores are located within clustered regions. In Jørgensen et al. (2008), several thresholds are used to distinguish between loose and tight aggregations (with minimum densities of 1 and 25 $M_\odot$ pc^{-3} respectively), and groups and clusters (containing less than or more than 35 members respectively). We find that a significant fraction of the dense cores and protostars in Perseus are found within the loose aggregations and groups rather than the concentrated clusters. Another nearby molecular cloud that is also forming intermediate-mass stars, the Ophiuchus molecular cloud, was also studied by Jørgensen et al. (2008). Despite the bulk similarities of the two clouds, the two clouds display markedly different modes of star formation – in Ophiuchus, nearly all of the star formation is occuring within a single concentrated cluster. Figure 2.6 shows

the Jørgensen et al. (2008) results for the Perseus and Ophiuchus molecular clouds, highlighting the differences discussed. A comparative study also reveals additional intriguing differences between the two clouds including a different ratio of starless to protostellar cores and a different distribution of protostellar colours, indications that the evolutionary histories of the dense cores may vary significantly between these two environments. This variation underscores the importance of obtaining statistically significant observations of dense cores across multiple molecular cloud environments.

2.3.3.2 Extinction Threshold

The locations of the submillimetre cores can also be considered with respect to the large-scale cloud environment. We (KJD06) compared the positions of the submillimetre cores to the total dust column density at that location, as measured through the 2MASS reddening data. The dense cores were found to be located exclusively in the regions of high extinction ($A_V > 5$ mag), although the bulk of the cloud mass (58%) is at extinctions below 5 mag. KJD06 furthermore demonstrated that this was not an observational effect, using the Bonnor-Ebert sphere models of the cores discussed in Section 2.3. At lower extinctions (column densities), the surface pressure on the dense cores is expected to be lower (since there is less weight of cloud material pushing against them). Using the Bonnor-Ebert sphere model, KJD06 modelled the change in dense core properties in the lower extinction regions of the cloud (larger size, lower peak flux, and higher total flux due to the decrease in external pressure), and demonstrated that such dense cores would still be detectable in these environments. This result is shown in Figure 2.7.

An extinction threshold for core formation has been found by others in Perseus (Hatchell et al., 2005; Enoch et al., 2006), as well as in other clouds such as Taurus (Onishi et al., 1998) and Ophiuchus (Johnstone, Di Francesco, & Kirk, 2004). An extinction threshold for core formation has a natural explanation under a magnetically-dominated formation scenario. In this scenario, dense cores form via the gradual condensation of material. Initially, only neutral species can move perpendicular to the magnetic field lines, and their motion is slowed by collisions with ions that are tied to the field lines (ambipolar diffusion). Cores are therefore only expected to form in regions where the neutral-ion collision timescale is long enough (i.e., the ionization fraction is low enough) to allow for a significant amount material to collect within a reasonable timeframe. Due to photo-ionization, the outer regions of molecular clouds

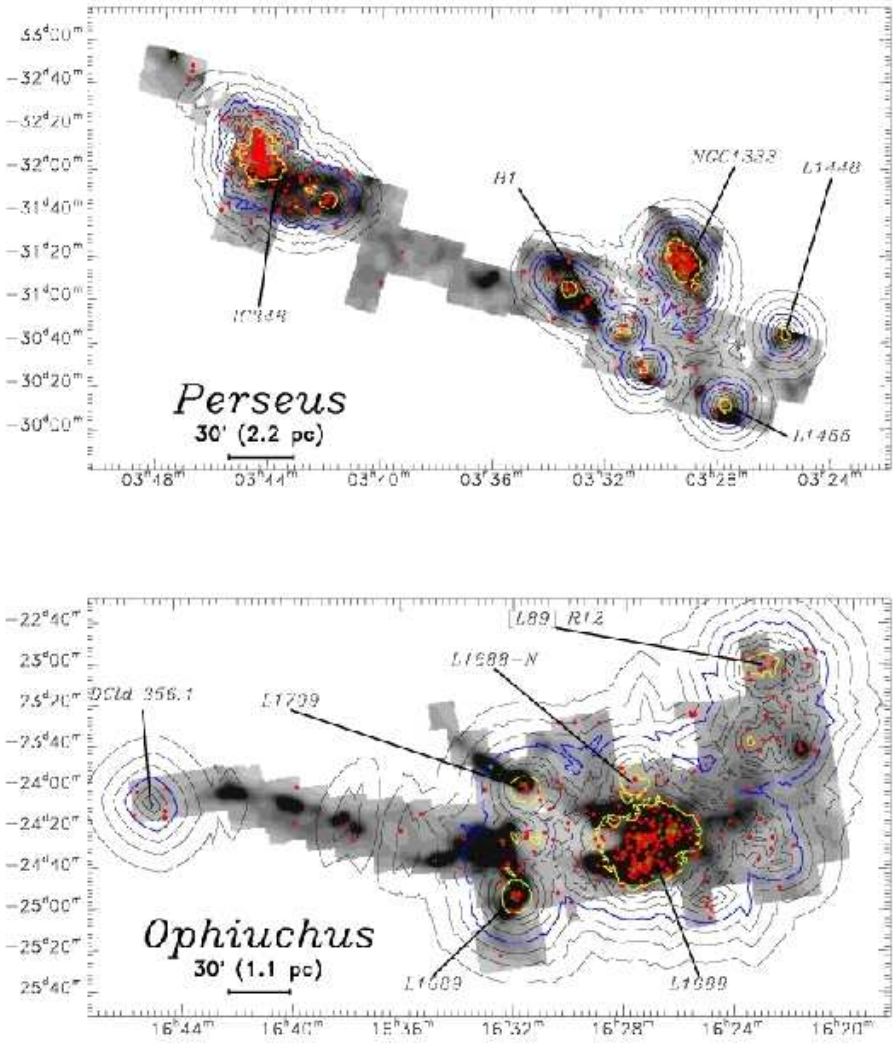

Figure 2.6 The volume density contours of YSOs identified in the Perseus (top) and Ophiuchus (bottom) molecular clouds. The contour levels correspond to derived densities of 0.125, 0.25, 0.5, 1.0 (blue) 2.0, 4.0, and 25.0 (yellow) $M_{\odot}$ pc^{-3}. The greyscale background image shows the 2MASS-derived extinction map of the clouds, while the red points show the locations of the YSOs and the green plus signs show the SCUBA cores. Figure from Jørgensen et al. (2008), Figure 13. Reproduced by permission of the AAS.

have too large an ionization fraction to allow dense cores to form; the ionization fraction is significantly reduced in the densest (highest extinction) portions of the molecular cloud where only cosmic rays are able to penetrate to create ions. McKee (1989) calculated that this condition occurs for a visual extinction of 4 to 8 mag. It

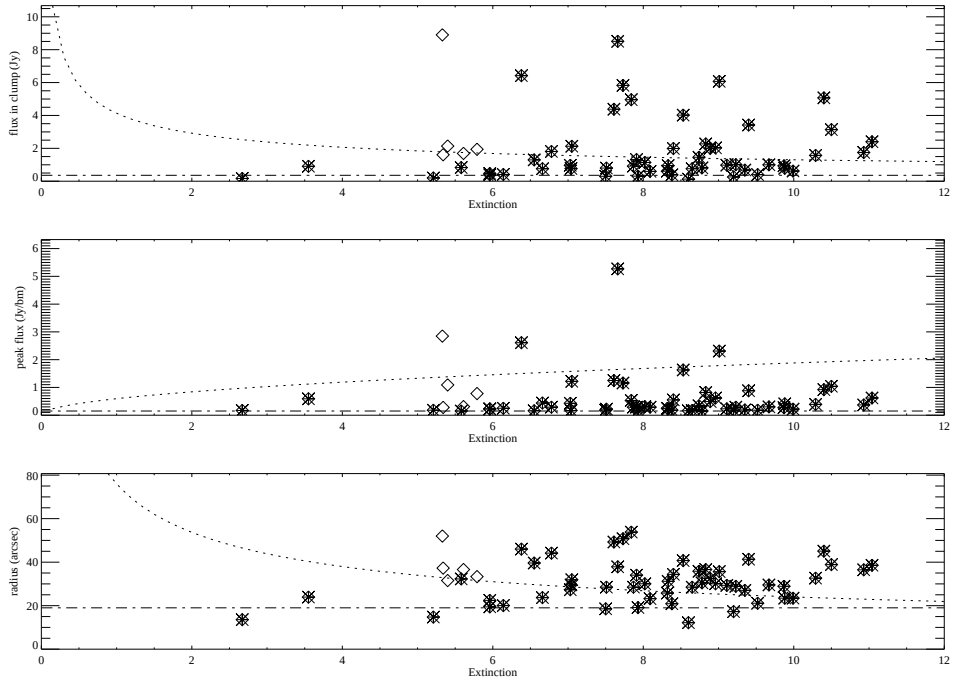

Figure 2.7 The total flux, peak flux, and radius (top, middle, and bottom panels respectively) of the dense cores identified in the SCUBA map versus the visual extinction measured at that location. The dash-dot line indicates the approximate observational sensitivity while the dotted line indicates the values expected for a critical Bonnor-Ebert sphere model. Diamonds denote the cores in the L1448 region, while asterisks denote the cores found in the rest of the cloud. Figure from Kirk, Johnstone, & Di Francesco (2006).

is not clear whether this extinction threshold is able to be similarly explained under turbulence-dominated formation scenarios.

2.3.4 Triggered Star Formation

The location of the dense cores can also be considered with respect to the large-scale structures visible in the extinction data. KJD06 compared the dense core positions with the Gaussian-modelled extinction clumps and found that the dense cores tended to lie offset from the peak of the extinction clumps, and preferentially toward one side of the clump, as illustrated in Figure 2.8. These offsets were correlated between each extinction clump in a manner suggestive of a triggering event driving the formation of the dense cores. The direction of the source of triggering suggested by the offsets was also found to be consistent with a young nearby bright B5 star, 40 Persei, which had

previously been suggested to be triggering star formation within the Perseus cloud (Walawender et al., 2004) in the L1451 region (slightly outside of Figure 2.1 below L1455). While not conclusive evidence, the observations do support the hypothesis that dense core formation in Perseus is driven by the heating and erosion of the larger Perseus molecular cloud structure preferentially on the side of the cloud impinged by the ultraviolet radiation emitted by 40 Persei (and other nearby stars in the same OB association).

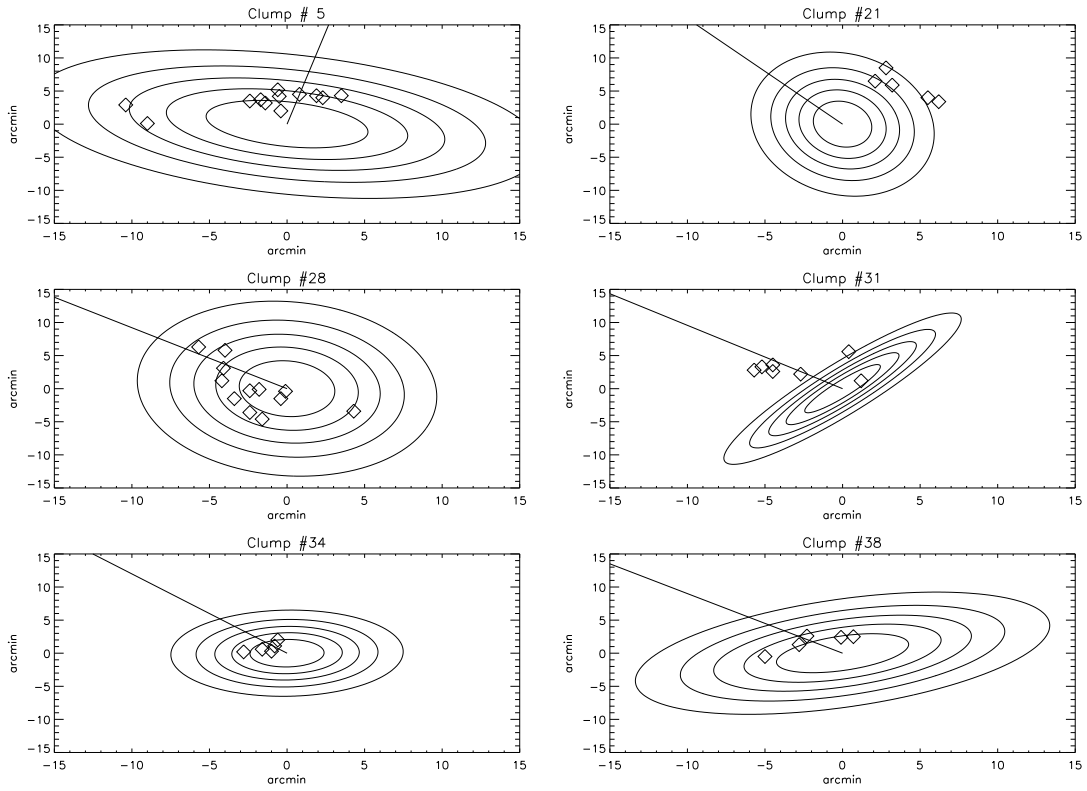

Figure 2.8 The distribution of SCUBA cores within the larger column density structures that they inhabit. The contours indicate the Gaussian model fit to each extinction clump, while the diamonds indicate the SCUBA core locations. The vectors indicate the direction to the ionizing B star 40 Per. Note that Clump# 21 is nearby and east of NGC 1333, which may be causing additional triggering to the westernmost (right) side of the clump. Figure from (Kirk, Johnstone, & Di Francesco, 2006).

2.3.5 Core Spectra

The spectra of dense cores have been observed in Perseus in both N_2H^+ (Chapter 3) and NH_3 (Rosolowsky et al., 2008). Core dynamics derived from the N_2H^+ observa-

tions are discussed in the following chapter; the NH_3 results are in good agreement with the N_2H^+ measurements.

The two spectral surveys also allow the physical conditions and chemical reactions affecting the dense cores to be investigated. The two surveys span a nearly identical set of objects, so in Johnstone et al. (in prep), we are comparing the two sets of observations to gain a better understanding of the two molecular species. Preliminary analysis indicates that emission from both of these molecules have similar centroid velocities and non-thermal linewidths, indicating that both trace similar material, providing more evidence that NH_3 is indeed a high density gas tracer.

2.4 Summary

Large-scale, systematic surveys of the Perseus molecular cloud already exist, providing a wealth of data with which to help build an understanding of the detailed processes occuring within it. The large-scale (column) density structure has been estimated from reddening of stars in the 2MASS catalog. Regions of higher mean total column density tend to correspond to well-known star-forming regions such as NGC 1333, and the local conditions (such as mean pressure) expected to affect dense core evolution within each region can be estimated from the extinction observations. Dense cores have been identified across the entire cloud in both submillimetre (Hatchell et al., 2005; Kirk, Johnstone, & Di Francesco, 2006) and millimetre (Enoch et al., 2006) observations, and properties of the cores such as size and mass determined. The dense cores tend to be found clustered in high column density regions within the molecular cloud, possibly indicating that magnetic fields influence the cores' formation and evolution. The correlated offset location of the cores from the highest column densities in the cloud suggests that photoionization from nearby OB stars may also be important. The dense cores have also been classified as starless or protostellar according to whether *Spitzer* mid- to near- infrared data indicates there is a central warm source present (Jørgensen et al., 2007; Hatchell et al., 2007a). All of this information will aid in the interpretation of the observations and simulation analysis presented in the following three chapters.

Chapter 3

Dynamics of Dense Cores in the Perseus Molecular Cloud

3.1 ABSTRACT

We survey the kinematics of over one hundred and fifty candidate (and potentially star-forming) dense cores in the Perseus molecular cloud with pointed N_2H^+(1-0) and simultaneous $C^{18}O$(2-1) observations. Our detection rate of N_2H^+ is 62%, rising to 84% for JCMT SCUBA-selected targets. In agreement with previous observations, we find that the dense N_2H^+ targets tend to display nearly thermal linewidths, particularly those which appear to be starless (using *Spitzer* data), indicating turbulent support on the small scales of molecular clouds is minimal. For those N_2H^+ targets which have an associated SCUBA dense core, we find their internal motions are more than sufficient to provide support against the gravitational force on the cores. Comparison of the N_2H^+ integrated intensity and SCUBA flux reveals fractional N_2H^+ abundances between 10^{-10} and 10^{-9}. We demonstrate that the relative motion of the dense N_2H^+ gas and the surrounding $C^{18}O$ gas is less than the sound speed in the vast majority of cases ($\sim$90%). The point-to-point motions we observe within larger extinction regions appear to be insufficient to provide support against gravity, although we sparsely sample these regions.

3.2 INTRODUCTION

Stars form in the densest regions of a hierarchy of structures that exist within a molecular cloud. Supersonic motions dominate on the largest scales (e.g., Larson, 1981) but appear to be much reduced on the smallest scale, that of a preprotostellar core (e.g., Benson & Myers, 1989). Understanding what physical processes are at play at each scale ranging from the largest to the smallest is a challenge that both observers and theorists face. The challenge is complicated by the fact that each molecular cloud possesses different properties – local environment has a strong effect on the star formation process. Some molecular clouds, such as Taurus, display isolated star-forming cores which are quiescent and have a low star formation efficiency, while others such as Orion display clustered star-forming cores and have more turbulent motions and a higher star formation efficiency (e.g., Cohen & Kuhi , 1979). While clustering increases the complexity of a region and hence the difficulty in understanding what processes are at play, the majority of stars appear to form in environments which are clustered to some degree, and hence it is important to study such regions to understand the impact of clustering. In this chapter, we examine the Perseus molecular cloud – a cloud which is less clustered and confused than structure in the Orion molecular cloud, but is not as isolated and quiescent as the Taurus molecular cloud. The Perseus molecular cloud consists of a chain of distinct, well-known small clustered environments in which stars are forming – e.g., NGC1333 and IC348 (Bally et al., 2008). There is a wealth of data uniformly spanning this cloud, courtesy of the *Spitzer* 'c2d' Survey (Evans et al., 2003) and the COMPLETE (Co-Ordinated Molecular Probe Line, Extinction, and Thermal Emission) Survey (see Ridge et al., 2006, for a summary of the publicly available data). The continuum data from the latter survey (SCUBA thermal dust emission and 2MASS near-IR extinction) allow for the determination of the (column) density structure of the cloud. In particular, we (Kirk, Johnstone, & Di Francesco, 2006, hereafter KJD06) characterized the environments in which dense cores (which could eventually evolve to form a star) were themselves able to form. In doing so, we determined a set of constraints, summarized in Chapter 2, on the dust column density structure of the cloud which simulations should match. The goal of the present work is to extend that set of density constraints to a set of dynamical constraints.

To sample the behaviour of the dense gas in cores across the molecular cloud, we performed pointed N_2H^+ observations on a set of locations including candidate

dense cores from submillimetre data, points of high visual extinction from the Palomar plates, and peaks of large-scale extinction from 2MASS data. With the addition of the *Spitzer* data (Jørgensen et al., 2007), we are able to differentiate between unevolved dense starless cores and their more evolved protostellar bretheren. We couple these data with the existing continuum data discussed above in order to determine the dynamical behaviour of the dense gas within the cloud on a variety of scales. Our data do not provide the resolution or full sampling of some other recent surveys (e.g., Walsh et al., 2007), but have the advantage of providing (sparse) sampling across a much larger area, and are thus complimentary to these other works.

3.3 SOURCE CATALOG

3.3.1 SCUBA submillimetre

The Perseus molecular cloud has been mapped over roughly ~ 3.5 square degrees in the submillimetre (sensitive to thermal radiation by dust grains) at 850 μm with the Submillimetre Common User Bolometer Array (SCUBA) at the James Clerk Maxwell Telescope in Hawaii. In KJD06, we identified approximately fifty cores in the SCUBA data using a $6''$ sampled map of all existing data in the cloud. The majority of these data were archival (see Hatchell et al., 2005), but also included some 'fast scan' maps (with insufficient integration time to allow for the typical $3''$ sampling) taken as part of the COMPLETE project (Ridge et al., 2006). KJD06 compared the properties of the SCUBA cores to the environment they inhabit through comparison to near IR extinction data with $2.5'$ resolution (see discussion of these data below), hence the consistent areal coverage was of greater importance than resolution. All of the submillimetre cores were found in regions of previously identified star-formation (e.g., B1, NGC1333), and none were found in the fast-scan mapped regions. For our current project, we utilize maps created with a finer $3''$ sampling which allows for better separation of close cores and determination of core properties such as radius. Appendix A discusses the re-reduction of the data we performed, and presents a full source catalog. We identify seventy two submillimetre cores above our usual S/N level (these cores are also used in Jørgensen et al., 2007), as well as 15 additional potential submillimetre cores which do not satisfy our S/N criteria.

The original $6''$ sampled map formed the basis of our target list of dense cores to observe in N_2H^+(1-0). We supplemented this with a list of potential SCUBA

cores which fell below the detection threshold of our core-identification procedure in order to have as complete a list as possible. This resulted in 89 dense core targets. These target positions are listed in Table 3.1 along with the associated better-defined SCUBA core from this chapter.

3.3.1.1 *Spitzer* and Young Protostars

The Perseus molecular cloud was also one of the clouds surveyed by the *Spitzer* 'c2d' project (Evans et al., 2003). While the submillimetre wavelengths covered by SCUBA are sensitive to the dusty envelopes of both starless cores and enshrouded protostars, the IR wavelengths probed by *Spitzer*, particularly the shorter wavelengths, are sensitive to the central accreting object and hence young protostars. Thus *Spitzer* observations are ideal in distinguishing between starless cores and their more evolved bretheren. The full *Spitzer* dataset is described in Jørgensen et al. (2006) and Rebull et al. (2007), while a catalogue identifying young protostellar candidates using a combination of *Spitzer* and SCUBA data is presented in Jørgensen et al. (2007). Note that the work of Jørgensen et al. (2007) utilizes the $3''$ sampled SCUBA core list included in Appendix A. Table 3.1 also shows whether the targets are associated with a young protostar as detected with *Spitzer*.

A second comprehensive catalog listing the protostellar and starless cores in Perseus has also recently been published by Hatchell et al. (2007a) where the sources were classified using SEDs fit to *IRAS*, *Spitzer*, SCUBA, and Bolocam observations. A significant difference between the two catalogs is that the Hatchell catalog used only the shorter wavelength *Spitzer* IRAC data, while the Jørgensen catalog relied primarily on the longer wavelength *Spitzer* MIPS data. The bulk of the two protostellar catalogs agree, but the Jørgensen catalog contains five protostars not in the Hatchell catalog and the Hatchell catalog contains seventeen protostars not in the Jørgensen catalog.

Of the five sources only in the Jørgensen catalog, one was outside the region included in the Hatchell catalog, two were classified as starless cores in the Hatchell catalog, and the remaining two had submillimetre emission below the threshold for identification. The Jørgensen catalog had three criteria for classification as a protostar – a set of colour criteria for a source across the IRAC (3.6, 4.5, 5.8 μm) and MIPS (24 μm) bands, spatial coincidence of a MIPS 24 μm source with a SCUBA core, or detection of a SCUBA core with a high central concentration (see Appendix A for

the definition of concentration). None of the seventeen protostars only identified in the Hatchell catalog are associated with a high submillimetre central concentration, therefore inclusion in the Jørgensen catalog would require a detection in the MIPS 24 μm band plus fulfilment of either the colour criteria or SCUBA core association. We searched the *Spitzer* data (Rebull et al., 2007; Jørgensen et al., 2006; Evans et al., 2003) around each of the seventeen protostars only in the Hatchell catalog. Twelve of the seventeen did not have MIPS detections with a signal to noise above five (seven of these had close SCUBA cores while five did not). Of the remaining five, none had close SCUBA cores or colours satisfying the colour criteria of the Jørgensen catalog. Of the sources only in the Jørgensen catalog, we observed four of the five and all had detections (our sources #21, 22, 74, and 95). Of the sources only in the Hatchell catalog, we observed ten of the seventeen and had detections for seven (our sources #92, 94, 101, 109, 110, 121, and 150).

A range of linewidths, centroid velocities, and peak intensities were found for these sources, therefore any potential mis-classification is unlikely to bias our results.

3.3.2 Extinction - 2MASS

From the COMPLETE Survey, we also have a map of the inferred total column density created from visual extinction measures derived using the NICER technique (Lombardi & Alves, 2001) on the 2MASS dataset (Ridge et al., 2006; Alves & Lombardi, in prep). This technique utilizes near infrared reddening of background stars in three wavelength bands (two colour indices) in order to determine the total column density of dust. The resolution of this map is $2.5'$ and spans the range of A_V =3 - 11 within the region mapped by SCUBA (Figure 2.1). KJD06 analyzed these extinction data and identified structures in the (dust) column density on two scales. We utilized the maxima in the smaller-scale structures (the 'extinction cores' of KJD06) to identify a further 24 targets for our N_2H^+ survey. In later sections of this chapter, we utilize the larger-scale structures ('extinction supercores' of KJD06) to define the environments in which the dense cores inhabit. The extinction target positions, along with the associated information from the extinction and submillimetre maps are given in Table 3.1.

3.3.3 Palomar Plates

The final extension to the dense core candidate target list was taken from visually-selected targets in the red POSS-II Palomar plates. We focussed on plates in regions devoid of SCUBA cores in order to maximize the extent of our coverage of environments within the cloud. This provided an additional 44 targets. The information on these targets is given in Table 3.1.

Figure 3.1 shows all of the targets we selected overlaid on the extinction map of the Perseus molecular cloud.

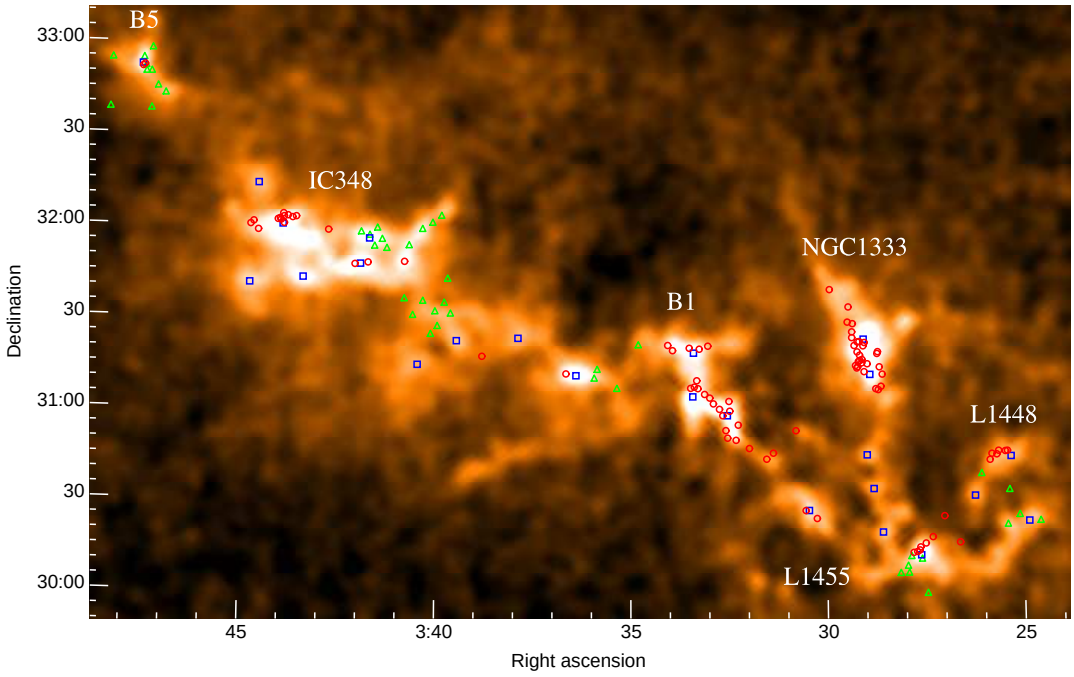

Figure 3.1 2MASS-derived visual extinction map of the Perseus molecular cloud overlaid with the positions of our IRAM survey targets. Red circles indicate the SCUBA-selected targets, green triangles indicate the Palomar plate-selected targets, and blue squares indicate the 2MASS-selected targets. Well-known star-formation regions are labelled.

3.4 OBSERVATIONS AND DATA REDUCTION

We made pointed observations of the 157 targets using the 30 m IRAM telescope in Pico Veleta, Spain. We observed N_2H^+(1-0) in both polarizations using the (AB)

100 GHz receivers and simultaneously observed $C^{18}O$(2-1) in both polarizations using the (CD) 230 GHz receivers, in both cases utilizing frequency switching. We used the VESPA correlator and smoothed to 0.05 km/s channels. The beamsize is $\sim 25''$ for N_2H^+ and $\sim 11''$ for $C^{18}O$. Each observation was made for 2 minutes and had an rms of $T_A^* \sim 0.1$ K. We made multiple pointings on some of the cores to better resolve spectral features or search for a signal to a higher sensitivity. We made four-point maps (offsets of $25''$ in RA and dec around the central pointing) around some of the targets in order to distinguish extended structures and search for cores offset from the assumed position. In the interests of minimizing observing time, this was done for only a subsample (62) of the cores.

We detected signal in N_2H^+ in 62% of our targets at the central position, with the rate rising to 84% for the SCUBA-selected targets. Since N_2H^+ is a 'late time' molecular ion, not attaining significant abundance until after $\sim 10^5$ yrs (Aikawa et al., 2003), this implies most of the SCUBA sources are at least this old.

Virtually every target had a $C^{18}O$ detection (96%). All but one of the spectra with signal in N_2H^+ had a corresponding detection in $C^{18}O$. Examination of the one rogue case revealed that higher than average noise in the $C^{18}O$ spectrum was likely responsible for the lack of a detection.

Table 3.2 shows the full break-down of the detection rates and numbers for the various target selection methods. There are several factors which likely go into the vast difference in success rates for the different selection criteria. Both the 2MASS and Palomar plate-selected targets have greater uncertainties attached to a potential core's position than the SCUBA-selected cores. The 2MASS map has a resolution of $2.5'$ and thus is insensitive to the small density peak of an individual core, rather, it represents a smoothed average of any large- plus small-scale dense structures along the line of sight. The Palomar plates have better resolution ($1''$) but are only sensitive to a few magnitudes of visual extinction. Our detection efficiency for this portion of the survey is similar to the NH_3 survey of Benson & Myers (1989) which used the original Palomar plates to identify candidate cores.

N_2H^+ has a critical density of $\sim 10^5$ cm^{-3} (Tafalla et al., 2002) and thus is sensitive to only the densest gas within molecular clouds. The SCUBA-selected and Palomar-selected targets were all chosen on the basis of apparent (column) density enhancements which would indicate the site of a dense core. While this was not the case for the 2MASS-selected targets (the resolution allowed only for the identification of peaks in the large-scale structure), those 2MASS-selected targets which had

detections all lie on or close to structure visible in the SCUBA observations. Hence all of the targets where we detected N_2H^+ are likely to be dense cores rather than less dense gas unassociated with any small-scale structure.

3.4.1 Fitting the Spectra

We reduced the N_2H^+ and $C^{18}O$ data from IRAM using CLASS [1]. First, we fit a baseline to each spectrum individually using a 4th order polynomial. The resultant spectra were then folded and summed where multiple pointings existed.

To fit the seven components of the N_2H^+(1-0) spectra, we used CLASS's HyperFine Split fitting routine, with the relative frequencies and optical depths for N_2H^+ taken from Caselli et al. (1995) and a frequency of 93176.258 MHz for the $N_2H^+(JF_1F=101\text{-}012)$ 'isolated' component (Lee, Myers & Tafalla, 2001).

In some cases (20 N_2H^+ spectra), two separate components were clearly required for a good fit. We interpret these spectra as belonging to two separate entities, rather than a central dip caused by self-absorption. Appendix B discusses the evidence for this interpretation of these cores.

Table 3.3 shows the best-fit line parameters found using CLASS for the N_2H^+ spectra – the centroid velocity, velocity dispersion (measured in terms of FWHM), the total optical depth, the baseline level (alternatively, the standard deviation in regions with no line emission), and the line rms (alternatively the standard deviation in the fitting residuals where there is line emission). All fits were visually inspected; those of poor reliability due to low S/N are noted in the final column – these have reasonable centroid velocities but poor dispersions since noise limits the determination of the extent of the line. We include the less secure fits only in the analysis of centroid velocities. The integrated intensities were also measured for each spectrum using the tdv function [2] in CLASS. We integrated over a range of -9 to +8 km/s around the centroid velocity fit (in order to include all hyperfine components), and take the error in the integrated intensity to be $B \times \delta V/\sqrt{N}$, where B is the spectrum's rms (baseline level), δV is the velocity range (17 km s^{-1}) and N the number of spectral channels summed over (541).

To fit the single-line $C^{18}O$(2-1) spectra, we used CLASS's Gaussian fitting routine, and assumed a rest frequency of 219560.354 MHz (Müller et al., 2001). These spectra

[1] See `http://www.iram.fr/IRAMFR/GILDAS`.

[2] The tdv function, a part of the spectral cube package, calculates the integrated intensity of individual spectra between two user-specified velocities, similar to the print area command.

often had complex shapes not well approximated by a single Gaussian. $C^{18}O$ traces less dense gas than N_2H^+ and thus could be expected to more often trace multiple structures along the line of sight. The Gaussian profile, however, is a simple approximation for the lines and provides a rough estimate on relevant properties. In cases where fitting a second Gaussian made a marked improvement to the fit, we did so (66 spectra). We fit a third component in only one case (a cross position) where three distinct and separate features were visible. Figure 3.2 shows three $C^{18}O$ spectra as an example of some of the types of profiles observed – the first displays an obvious single Gaussian profile, the second a clear double-Gaussian profile and the third a more complicated structure which we fit with a single Gaussian.

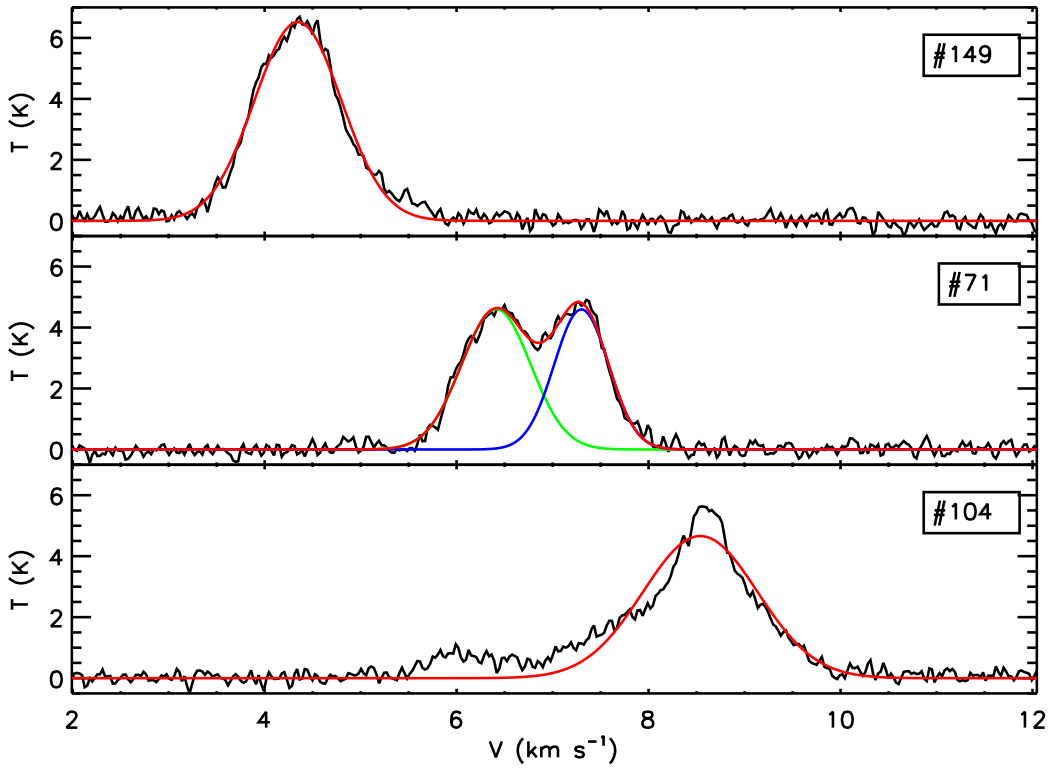

Figure 3.2 Three example $C^{18}O$ spectra showing differing spectral profiles. Black indicates the data while the red indicates the model fit. Blue and green indicate the components of a two Gaussian model. The vertical axis is in units of T_A^*.

Table 3.4 shows the best-fit parameters found by CLASS for the $C^{18}O$ spectra - the centroid velocity, velocity dispersion (measured in FWHM units), integrated intensity, peak intensity, baseline (the standard deviation where there is no line emission), and

line rms (the standard deviation of the fitting residuals where there is line emission). Similarly to our procedure for the N_2H^+ lines, we take the error in the integrated intensity (not included in the table) to be $B \times \delta V / \sqrt{N}$ where B is the baseline, δV is twice the FWHM and N the number of spectral channels summed over (each spectral channel is 0.0267 km s^{-1}).

3.4.2 Other Considerations – Pointing Accuracy

In the analysis below, we utilize only the measurements from the central pointing and ignore the offset cross pointings that we have on a subsample of the targets in order to treat the entire sample consistently. The observations of cross-positions are useful in allowing us to determine how accurately we determined the N_2H^+ core centres during target selection and how much error or bias might be introduced to our results from using only a single pointing. We leave a full discussion of these issues for Appendix C, but note the result that we find little evidence our results are affected by any errors or bias introduced by using a single pointing.

3.5 NON-THERMAL MOTIONS WITHIN DENSE N_2H^+ CORES

The one-dimensional thermal velocity dispersion expected for N_2H^+ is given by

$$\sigma_{T,n} = \sqrt{\frac{k_B\ T}{\mu_n\ m_H}} \tag{3.1}$$

where k_B is the Boltzmann constant, T is the temperature, μ_n is the molecular weight of N_2H^+ in atomic units (29) and m_H the mass of a hydrogen atom. We assume a temperature of 15 K, which lies within the range of temperatures we derived from Bonnor-Ebert modelling of SCUBA cores in the Perseus molecular cloud (KJD06). This corresponds to a thermal velocity dispersion of 0.065 km/s for N_2H^+. The non-thermal component of the velocity dispersion is then given by

$$\sigma_{NT,n} = \sqrt{\sigma^2_{obs,n} - \sigma^2_{T,n}} \tag{3.2}$$

where $\sigma_{obs,n}$ is the observed velocity dispersion. The level of internal turbulence, the ratio of non-thermal velocity dispersion to the mean thermal velocity dispersion of

the gas, is then :

$$f_{turb} = \frac{\sigma_{NT,n}}{c_s} \tag{3.3}$$

where we take a mean molecular weight of 2.33, which yields a sound speed of 0.23 km/s in the mean gas.

We use the same procedure to calculate the level of non-thermal motions observed in our $C^{18}O$ data, with $\mu_C = 30$ and a corresponding thermal velocity dispersion of 0.064 km/s.

The error in f_{turb} is small for either line since the linewidths are determined to better than 5% in most cases.

Recent ammonia observations (Rosolowsky et al, in prep), which include all of our targets, show a spread in temperatures between 10 and 15 K, with the mean near 12 K. The non-thermal motions we measure would only become ∼10% larger and the turbulent fraction ∼10 - 35% larger with the adoption of the ammonia temperatures. We maintain our use of 15 K for consistency with KJD06.

Maps of dense cores show that they are surrounded by a less dense envelope. In targets where we detected an N_2H^+ signal, we expect a surrounding envelope to also exist. Due to chemical effects, $C^{18}O$ is expected to trace a larger scale than N_2H^+ even with its smaller beamsize due to the higher frequency of the transition – $C^{18}O$ (with critical density $\sim 10^4$ cm^{-3}, e.g., Schöier et al., 2005) freezes out at densities of 10^5 cm^{-3} where N_2H^+ is detectable (e.g., Tafalla et al., 2002). Therefore, in a dense core, $C^{18}O$ measures are weighted to the outer parts while N_2H^+ measures are weighted to the denser inner parts. Hence in targets where we detect both N_2H^+ and $C^{18}O$, the $C^{18}O$ can be thought of as tracing the envelope of the dense N_2H^+ core. From our single pointing observations, we are unable to determine whether this surrounding less dense gas is found distinctly around each dense core (each core has a unique envelope) or on a larger scale (several cores sharing a common envelope). We therefore use the term envelope broadly in our discussion of results. In targets where we only detect $C^{18}O$, we do not have sufficient information to determine if the emission originates from an envelope-like region.

Previous observations of dense cores and their surroundings have shown that the dense gas (observed in N_2H^+ or NH_3) traces a 'coherent core' with a close-to-constant velocity dispersion of slightly above the thermal value (Benson & Myers, 1989; Barranco & Goodman, 1998; Goodman et al., 1998; Jijina et al., 1999; Caselli et al., 2002). Additionally, the dense core appears kinematically distinct from the surrounding less

dense gas (traced by OH or $C^{18}O$) which displays an increasing velocity dispersion with size (Barranco & Goodman, 1998; Goodman et al., 1998). We therefore expect that the velocity dispersion we measure in our N_2H^+ pointed observations represents the value that would be present across the entire coherence length of the core (∼0.1 pc for low-mass isolated cores in Goodman et al., 1998). Figure 3.3 which plots the distribution of the level of internal turbulence (f_{turb}) measured in N_2H^+, shows that indeed most of the dense cores have little non-thermal motion.

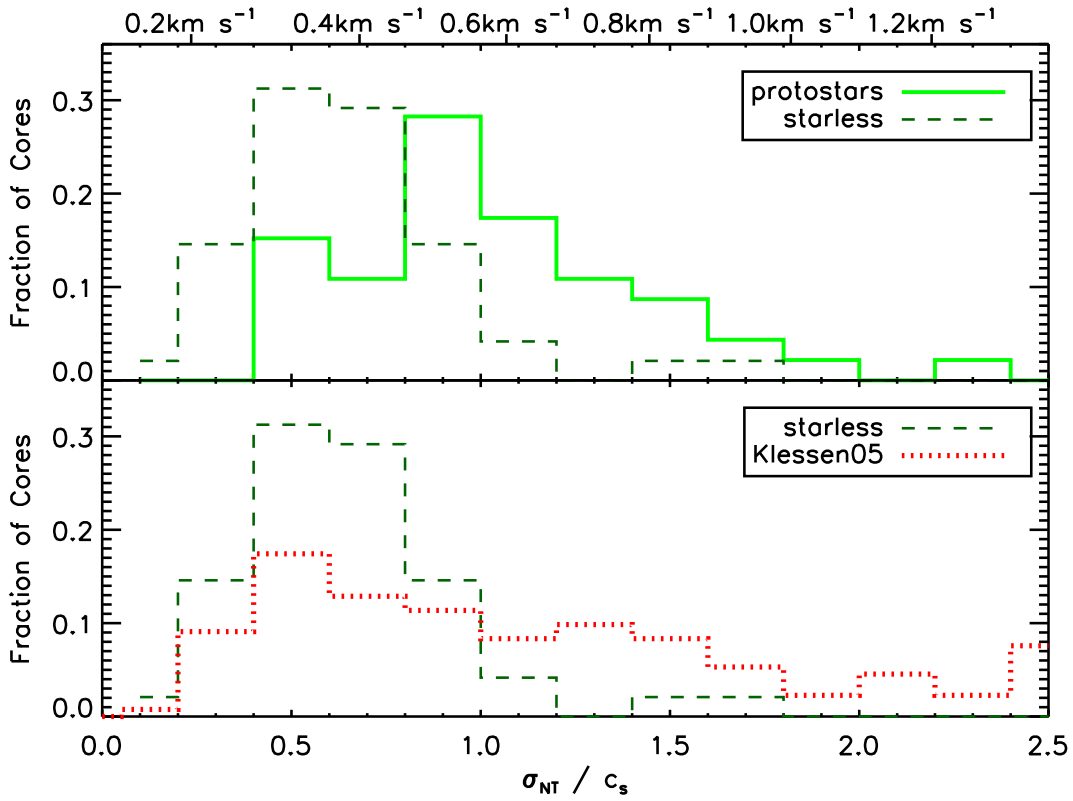

Figure 3.3 Relative level of non-thermal motions within the dense N_2H^+ cores. The top horizontal axis shows the observed FWHM linewidth in km/s while the bottom axis shows the turbulent fraction f_{turb} assuming a temperature of 15 K. The top panel shows the protostars (solid green line) and starless cores (dashed green line). The bottom panel shows the starless cores (dashed green line) versus the prediction from a gravoturbulent simulation by Klessen et al. (2005) for starless cores (dotted red line). Note that the final histogram bin for the Klessen et al. (2005) model includes all objects above this turbulent fraction (which extends to 4.3 in their model).

Any dense cores which have evolved to the protostellar phase might be expected to display a greater fraction of non-thermal motions – either infall our outflow motion

would be expected to broaden the line width observed. We analyze the subset of dense N_2H^+ cores which are not associated with protostars from the *Spitzer* catalog (also plotted in Figure 3.3) and find that, as expected, this subset does tend to display even less turbulent motions. The mean and standard deviation of the turbulent fraction is 0.6±0.3 and 1.0±0.4 for the starless cores and protostellar cores respectively.[3]

The turbulent fractions we find for starless cores and protostars are consistent with previous dense core surveys (e.g. Benson & Myers, 1989; Jijina et al., 1999). While Jijina et al. (1999) do observe higher turbulent fractions in cores belonging to more massive and turbulent molecular clouds such as Orion, the turbulent fractions we observe are consistent with the range Jijina et al. (1999) find in cores in molecular clouds with properties similar to Perseus.

The results are in contrast, however, to the simulation of Klessen et al. (2005) who find that their large-scale-driven turbulence model only has ∼50% of the cores with $f_{turb} \leq 1$; the small-scale-driven simulation has a much smaller fraction again. The distribution of cores in the Klessen et al. (2005) simulation are also plotted in Figure 3.3, displaying a significant tail to the distribution of f_{turb} of cores not found in our observations.

The turbulent fraction is also affected by association with young stellar clusters. Caselli & Myers (1995) analyzed ammonia cores in the Orion B molecular cloud and found an inverse relationship between core linewidth and distance to the nearest stellar cluster. There are three young star clusters near the Perseus molecular cloud – in NGC1333, IC348, and the Perseus OB association (e.g. Hatchell et al., 2005). We note our observations are consistent with a similar trend – the most turbulent cores are found in NGC1333 and IC348 (the Perseus OB association lies farther from the cores we observed).

We can perform a similar turbulent fraction analysis with the $C^{18}O$ observations (adapting the velocity dispersion equations above). The $C^{18}O$ observations are sensitive to a lower density regime and so trace larger structures which display a higher level of turbulent motion than the densest parts of the core displays (see Figure 3.4). This is also consistent with previous observations (e.g., Benson & Myers, 1989). The results from the Klessen et al. (2005) model are also plotted for reference. Although the model is a much closer match to these observations, the model 'observations' were

[3]Note that a KS test on the turbulent fractions for the starless and protostellar cores yields a maximum deviation of 0.5 between the two distributions and a probability of 6×10^{-7} that the two are drawn from the same parent distribution.

designed to match to a dense-gas tracer such as N_2H^+. The core boundaries used to define the 'observable area' of the cores in the simulation, the half-maximum column density contour (Klessen et al., 2005) better match the extent of densities traced by N_2H^+ than by $C^{18}O$. It is interesting to note that our $C^{18}O$ targets show much less variation in their distribution of f_{turb} between those which are and are not associated with a protostar than the dense N_2H^+ cores do. The mean and standard deviation are 1.2±0.6 and 1.8±0.7 for pointings not associated and associated with protostars respectively. This may indicate that at the early stages of protostellar evolution, protostars do not affect the bulk of their envelopes in a significant manner![4]

3.6 CORE VERSUS ENVELOPE MOTIONS

As discussed earlier, for the pointings which have both N_2H^+ and $C^{18}O$ detections, the N_2H^+ traces the dynamics of the dense core, while the $C^{18}O$ traces the dynamics of the surrounding less dense gas.

Previous studies using maps of N_2H^+ and $C^{18}O$ have shown that cores do not move ballistically within their envelopes (i.e. centroid velocity differences between N_2H^+ and $C^{18}O$ are smaller than the $C^{18}O$ linewidth) and most have subsonic core-to-envelope motions (e.g., Walsh et al., 2004, 2007). The Walsh et al. (2004) survey examined mostly single isolated cores, rather than those in clustered regions, while the Walsh et al. (2007) survey spanned a clustered region of dense cores (NGC1333, which is included in our larger-area sample although at lower resolution). Unfortunately, the Walsh et al. (2007) results are less certain since their $C^{18}O$ beamsize was significantly larger than their N_2H^+ beamsize. Thus our survey is ideal in providing a large statistical measure of core-envelope motions within a clustered environment.

We separately analyze the relative core to envelope motions of the starless and protostellar cores. In starless cores, the relative motions should be induced by the molecular cloud and the core formation process. In protostellar cores, the relative motions between core and envelope could be complicated by outflows or processes which decouple the core from its envelope. Figure 3.5 shows our results for the starless cores and protostars separately – both have a high fraction of relative velocities which are less than the sound speed.

[4]Note that a KS test of the turbulent distributions of the starless and protostellar cores yields a maximum deviation of 0.4 and a probability of 3×10^{-5} that the two are drawn from the same parent population.

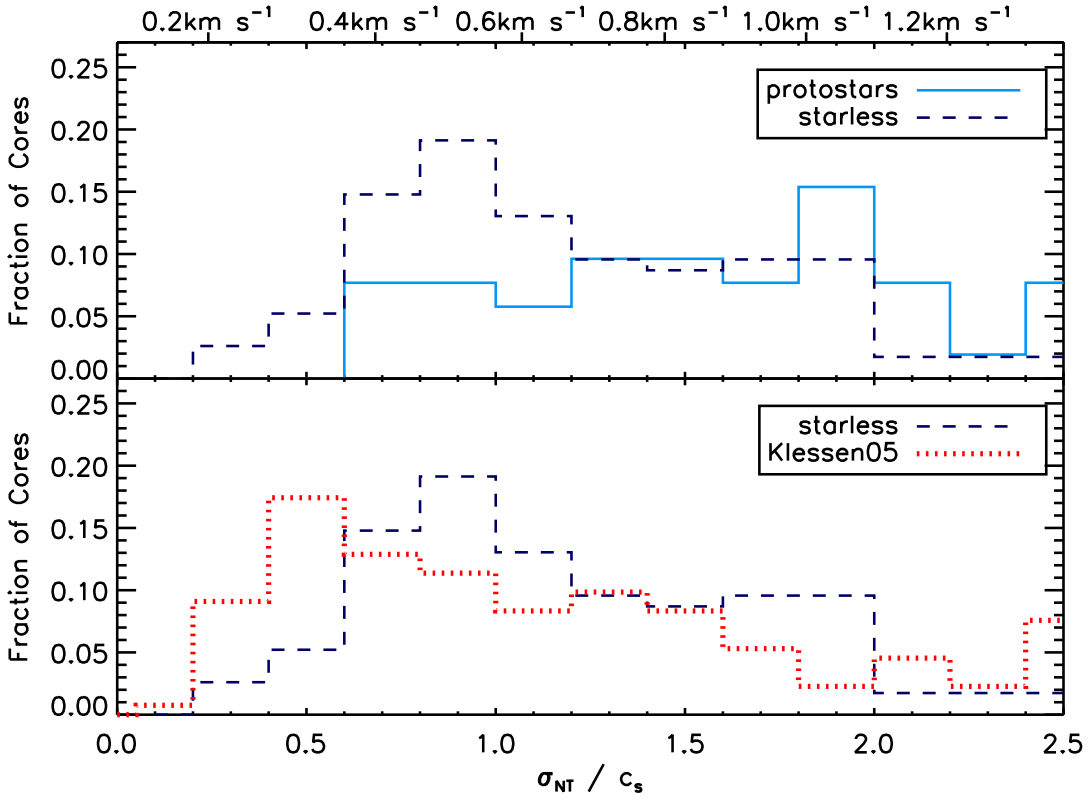

Figure 3.4 Relative level of non-thermal motions measured in $C^{18}O$. The top horizontal axis shows the observed FWHM linewidth in km/s while the bottom axis shows the turbulent fraction f_{turb} assuming a temperature of 15 K. The top panel shows the targets associated with protostars (solid blue line) and those not associated with protostars (dashed blue line). The bottom panel shows the targets not associated with protostars (dashed blue line) versus the prediction from a gravoturbulent simulation by Klessen et al. (2005) (dotted red line). Note that the final histogram bin for the Klessen et al. (2005) model includes all objects above this turbulent fraction (which extends to 4.3 in their model).

Ayliffe et al. (2007) has argued that the previous analyses of Walsh et al. (2004, 2007) biases results towards small velocity differences due to the method of analysis. In instances where multiple CO velocities were found along the line of sight, the velocity component closest to the N_2H^+ core velocity was assumed to be the one associated with the core. Here, we demonstrate that taking the closest CO velocity component is reasonable and does not introduce significant bias. Most of the cores in our observations had only a single velocity component fit. For these, we compared the difference in centroid velocity between the N_2H^+ and $C^{18}O$, as shown in Figure 3.5.

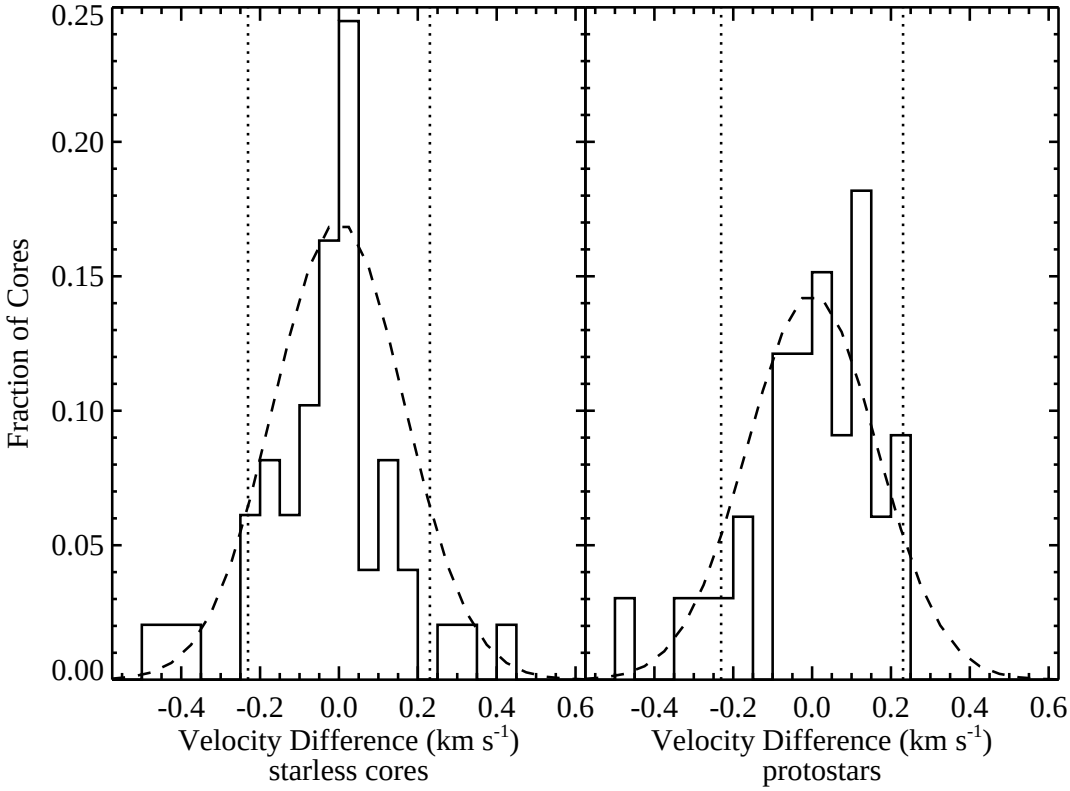

Figure 3.5 Difference in centroid veloicites of N_2H^+ to $C^{18}O$ for the starless cores (left) and protostars (right). The dotted lines indicate the sound speed of the ambient medium. The dashed lines indicate Gaussian fits to the distributions – the starless cores have $\sigma = 0.17$ km/s while the protostars have $\sigma = 0.16$ km/s.

This figure demonstrates that the vast majority of cores (nearly 90%) have differences less than the sound speed of the ambient medium (dotted lines), and the remaining cores have differences which are not much larger. Note that some of the N_2H^+ cores in this plot were fit to two velocity components; we considered these two velocity components as separate entities (i.e., plotted as two distinct cores). The velocity differences found for the two N_2H^+ velocity cores versus the surrounding $C^{18}O$ tend to be larger than for the other cores (since both N_2H^+ velocities are compared to the same $C^{18}O$ velocity). The CO linewidth for the two velocity N_2H^+ cores also tends to be broader than average. All of the cores have an error in the centroid velocity of around several hundredths of a km s^{-1}, indicating that the majority of the differences in velocities observed are real.

Figure 3.6 shows the absolute difference in N_2H^+ to $C^{18}O$ centroid velocity in

dense cores where two $C^{18}O$ velocity components were fit, again split into starless cores and protostars. The velocity differences here are ordered in terms of the largest-difference component (squares), while the smallest-difference component is denoted by diamonds or asterisks. Clearly the two CO velocity components are not correlated, as is expected since the second CO component merely lies along the same line of sight. The cores which happen to have a second $C^{18}O$ velocity component along the same line of sight should possess a similar distribution of core-to-envelope relative velocities as along lines of sight where only a single $C^{18}O$ velocity component was observed – i.e., velocity differences smaller than the sound speed in the vast majority of cases. As can be seen from Figure 3.6, in almost every case this implies the closer CO velocity component is the only sensible one to associate with the dense core; in the rare instance of ambiguity, the resultant number of cores with each velocity difference will be little affected.

Assuming in all cases that the closest velocity $C^{18}O$ component is the one associated with the N_2H^+ profile peak, we find that in the majority of dense cores, the core-to-envelope velocity tends to be smaller than thermal, (88% and 83% for the starless and protostellar cores respectively). In the Walsh et al. (2004) survey of mostly isolated cores, they find only one out of 35 cores (or 3%) with a core-to-envelope velocity exceeding the sound speed. The Walsh et al. (2007) survey of cores in NGC1333 found an rms core-to-envelope velocity of 0.53 km/s; nearly half of their cores have differences greater than the sound speed of the medium. Our survey includes the NGC1333 cores but finds much lower differences (we have rms velocity differences of 0.16 km/s for the starless cores and 0.18 km/s for the protostars when both the one- and two- velocity component CO spectra are included). This may indicate that the Walsh et al. (2007) survey results were biased by the much larger beamsize for $C^{18}O$ ($50''$) than N_2H^+ ($10''$) which could have sampled a large fraction of material not associated with the individual dense core's envelope.

As discussed in Walsh et al. (2004), small relative motions between cores and envelopes could be interpreted as an indication of quiescence on small scales, and as such would appear to argue against a competitive accretion scenario for star formation, where dense cores gain most of their mass by sweeping up material as they move through the cloud. Recent analysis of simulations by Ayliffe et al. (2007), however, show that the competitive accretion scenario is not necessarily incompatible with the observations. Ayliffe et al. (2007) analyzed the competitive accretion simulations of Bate et al. (2003) and demonstrated that the simulated observations also show core

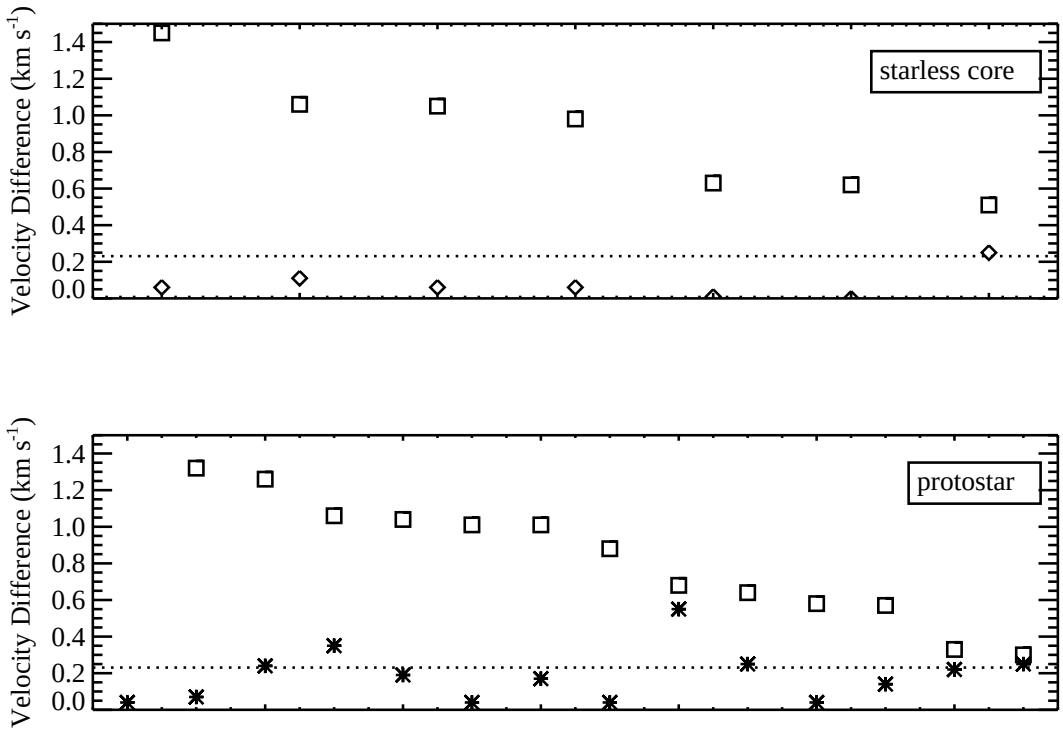

Figure 3.6 Difference in centroid velocities of N_2H^+ and $C^{18}O$ for starless cores (top) and protostars (bottom). The closest $C^{18}O$ velocity components are denoted by diamonds or asterisks while the farther $C^{18}O$ velocity components are denoted by squares. In each instance, the cores are ordered from largest to smallest difference in velocity using the farther $C^{18}O$ velocity component. The dotted line indicates the sound speed in the ambient medium.

to envelope motions are not ballistic. There were, however, differences between the simulated observations and the Walsh et al. (2004) results at later times in the simulation (such as the N_2H^+ linewidth becoming larger than the $C^{18}O$ linewidth), which were attributed to the clustered environment of the simulation, versus the isolated cores observed. Since our observations probe cores forming in a clustered environment (and include protostars), we can make a stronger comparison with the Ayliffe et al. (2007) results at later times. Ayliffe et al. (2007) do find the majority of their sources have velocity differences less than the sound speed at all time steps, however, they have a more significant tail out to large velocity differences (around 0.5 km/s or higher). They find the dispersion in the velocity difference ranges from 0.25 to 0.27 km/s, or 0.18 to 0.24 km/s after smoothing to the Walsh et al. (2004) resolu-

tion. It should also be noted that the N_2H^+ linewidth becomes equal to or larger than the $C^{18}O$ linewidth at 1.1 times the free-fall time and beyond, contradicting our observations (§4) and that of many previous studies. Thus while the simulation of competitive accretion analyzed by Ayliffe et al. (2007) has promise in reproducing core-to-envelope dynamics it does not simultaneously reproduce all observations.

Our results show no indication that the core-to-envelope motions significantly change between the starless and protostellar stages of evolution.

On an even smaller scale, Jørgensen et al. (2007) examined the location of YSOs within SCUBA cores and showed that they lie within 15″of the SCUBA core centre. These small separations, in combination with dense core lifetimes of a few 10^5 years (e.g. Enoch et al., 2008), imply that the YSOs have motions smaller than the thermal velocity relative to the SCUBA core they were born in. The picture that emerges from the combination of these results is that the central source, core, and envelope are quiescent.

3.7 CORE-TO-CORE MOTIONS

We next examine how the N_2H^+ cores move with respect to each other to gain an understanding of the dynamics on larger scales within the cloud.

We can use our visual extinction map of the Perseus molecular cloud to define the larger regions in which the dense N_2H^+ cores inhabit. In KJD06, we identify large-scale structure in the extinction map which we will term 'extinction regions' here to prevent confusion (the regions are referred to as 'extinction super cores' in KJD06). Starless cores within each extinction region should be coupled to the surrounding gas in the region, and hence the motion of the starless cores should reflect the motion of the ambient material. Protostellar cores may have become decoupled from their parental material, and hence are a less reliable tracer of the dynamics occuring in the region.

We analyze the motions within each extinction region and determine whether the regions appear to have sufficient velocity dispersion to provide support against gravity. We adopt the commonly used formulation of

$$\sigma_{grav} = \sqrt{GM_{ext}/5R_{ext}} \tag{3.4}$$

as the velocity dispersion required in 1-D to prevent collapse (see for example Bertoldi

& McKee, 1992). We estimate the total mass and size of each region from the extinction data (KJD06); these data are provided in Table 3.5. The above formula technically only applies to a uniform density sphere, but different density structures and object shapes change the required velocity dispersion by factors of order unity (Walsh et al., 2007; Bertoldi & McKee, 1992). Regions which display $\sigma_{obs} = \sigma_{grav}$ are often said to be in approximate virial equilibrium, although to have true virial equilibrium, the 'surface terms' of the virial equation must be included (e.g., Dib et al., 2007).

Motions providing support for the extinction region could originate on either the small or large scale. The former would be measurable through internal core motions, while the latter through core-to-core motions. In the case of the densest material probed by N_2H^+, the internal core motions are of order the thermal motions of a gas at ∼15 K. If the extinction regions were in virial equilibrium, they would require effective temperatures of up to several hundred Kelvin to prevent gravitational collapse (KJD06); therefore, internal thermal motions cannot provide the bulk of the support required and hence most of the support must originate in large scale motions. We measure the dispersion in centroid velocities of the N_2H^+ starless cores within each extinction region to determine the amount of support that can be provided by large scale motions traced by the cores. We add the contribution of thermal motions (which has little effect except for the smallest core-to-core velocity dispersions). This total support is plotted in Figure 3.7 in terms of the ratio of observed velocity dispersion to that which is required for virial equilibrium. The horizontal axis plots the mass within each extinction region.

In the case of the material probed by $C^{18}O$, small-scale motions could provide a larger contribution to overall support, since the internal velocity dispersions are often several times larger than the sound speed and are closer in magnitude to the point-to-point velocity differences. In order to account for both of these contributions and also to decrease potential errors from the difficulty in fitting each $C^{18}O$ spectrum, we sum all of the spectra within an extinction region and fit the sum with a single Gaussian thus measuring the total velocity dispersion within each region. We correct the thermal component of the velocity dispersion to be that of the mean gas, rather than $C^{18}O$. These results are shown in the plot as blue open diamonds.

Table 3.5 also summarizes the relevant information for each extinction region – the number of non-protostellar cores detected in N_2H^+ and $C^{18}O$ in each region and the velocity dispersions measured with both molecules.

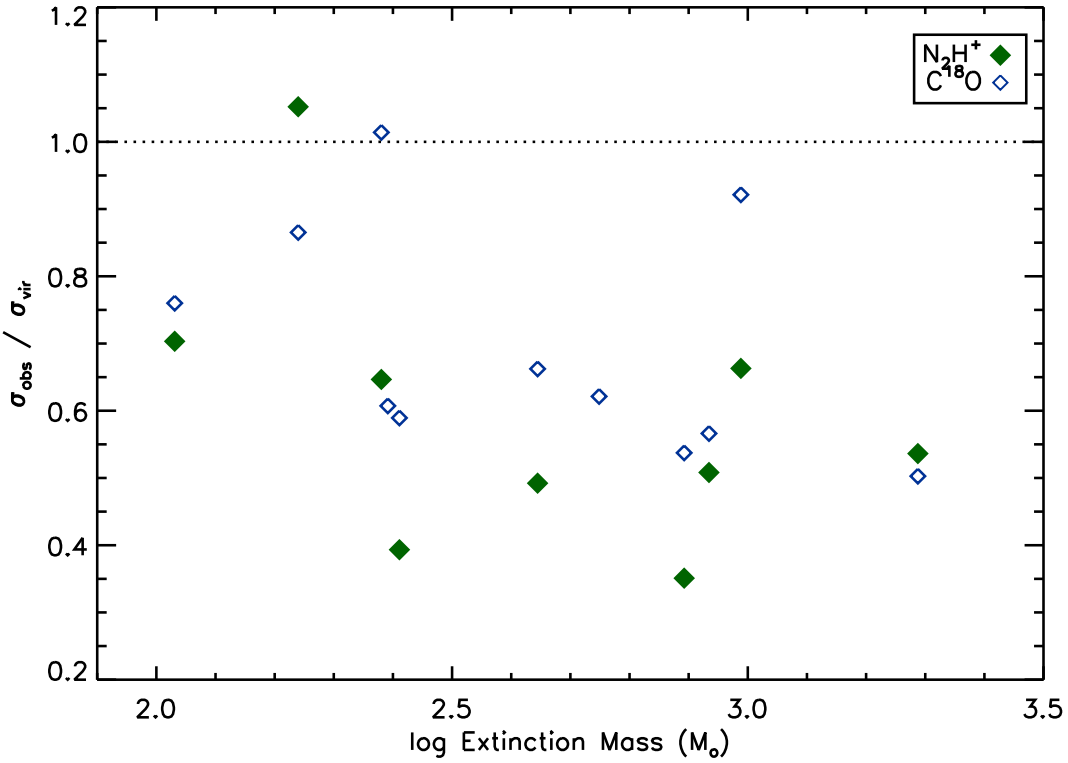

Figure 3.7 Ratio of the measured velocity dispersion to that required to counteract gravity ($\sqrt{GM_{ext}/5R_{ext}}$) versus the mass in the extinction region. The dotted line shows the expected relationship for virial equilibrium. The green filled diamonds denote the dispersion in centroid velocity for N_2H^+ starless cores. The blue open diamonds denote the dispersion of the summed $C^{18}O$ spectra for all starless cores in the extinction region. Two extinction regions have no N_2H^+ dispersion measured since less than two N_2H^+ cores were detected.

Variations by a factor on the order of one could be expected between the estimated and true velocity dispersion required for gravitational support – the extinction regions do not have a spherical geometry, several extinction regions have a small number of cores to calculate the velocity dispersion from, the cores do not span the entire extent of the extinction regions, and the conversion between extinction and mass has some uncertainty. It should also be noted that there is a velocity gradient across the Perseus molecular cloud – we leave a detailed analysis of the core motions relative to the overall cloud gradient for a future paper, and do not attempt to correct for it when calculating the velocity dispersions used here. With these considerations in mind, we find that the extinction regions tend to display velocity dispersions lower than

required for 'virial equilibrium', with the starless cores possessing lower dispersions in N_2H^+ than in $C^{18}O$, but the measurements do not rule out 'virial equilibrium'.

3.8 ENVIRONMENTAL EFFECT ON DENSE CORES

Most (84%) of the SCUBA cores have associated N_2H^+. For these cores, we can examine whether the SCUBA core properties have an effect on their internal dynamics. Since N_2H^+ requires $\sim 10^5$ years to form (Aikawa et al., 2003), the SCUBA cores must be at least this old, and hence are at an advanced stage of evolution, consistent with the results of Jørgensen et al. (2007).

3.8.1 Concentration

The 'peakiness' or central concentration of a core gives an indication of the importance of self-gravity of the core. The concentration is defined in terms of observable measures in equation (A1). Concentration can be thought of as an approximate proxy for evolutionary state with high concentration objects being more evolved (Walawender et al., 2005, 2006; Johnstone & Bally, 2006; Jørgensen et al., 2007) – in the framework of a Bonnor Ebert sphere model, any object with concentration above 0.72 is unstable to gravitational collapse, furthermore, heating from a central source also leads to an increase in concentration. Figure 3.8 shows the variation in observed core velocity dispersion with SCUBA concentration for both protostellar and starless cores. The mean concentration and velocity dispersion are lower in the starless cores than the protostars, with protostars of higher velocity dispersion also possessing high concentrations. The mean and standard deviation of the concentration is C = 0.4±0.1 and C = 0.6±0.2 for the starless and protostellar cores respectively. The velocity dispersion observed for cores associated with a SCUBA source is 0.20±0.08 km/s for the starless cores and 0.25±0.09 km/s for the protostars. The scatter in the velocity dispersion of the starless cores is mostly due to two starless cores with unusually high internal turbulence levels (> 1.5); excluding these two cores, the velocity dispersion becomes 0.18±0.04 km/s. These two starless cores are in NGC1333 where the region is highly clustered, making it more difficult to determine accurate core properties as well as determine if there is an associated protostar. The velocity dispersion for those cores which are not associated with a SCUBA source (primarily targets selected

from the Palomar plates) tend to be even lower – the mean and standard deviation is 0.14±0.04 km/s.

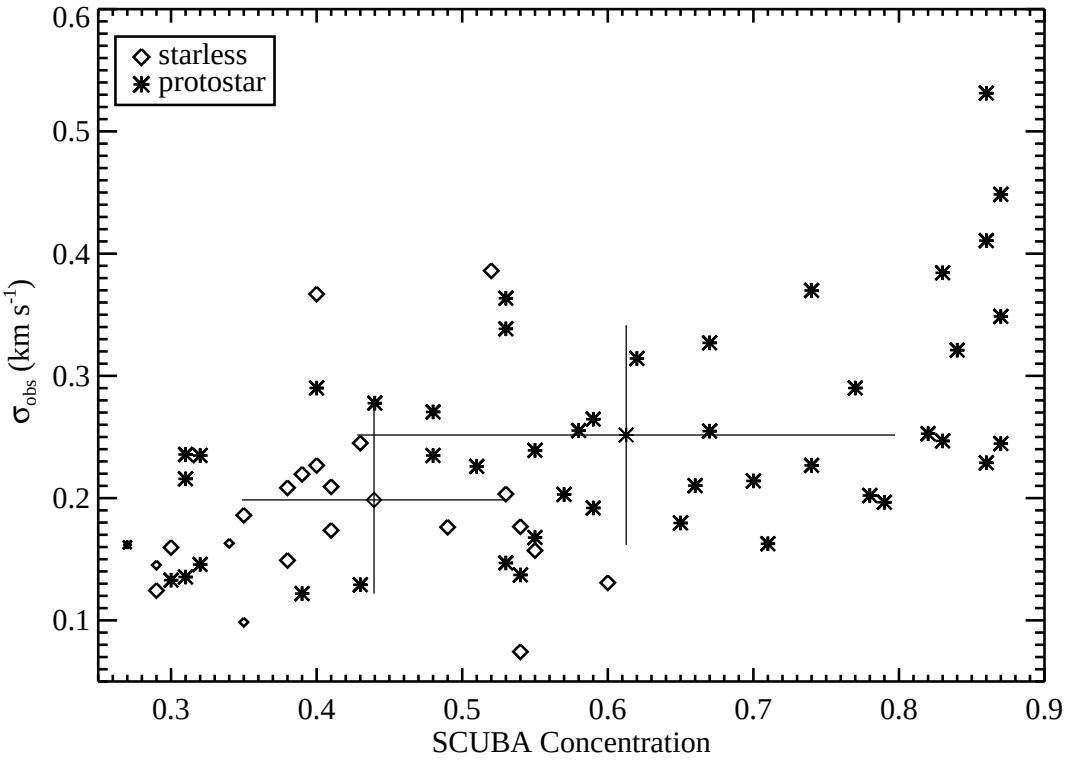

Figure 3.8 Variation of observed velocity dispersion in N_2H^+ cores versus concentration for starless cores (diamonds) and protostellar cores (asterisks). The large bold crosses indicate the mean and standard deviation for each of the two samples. The smaller symbols indicate SCUBA sources for which the properties derived from clumpfind are less secure (see discussion in Appendix A). These sources were not used in any of the calcuations.

3.8.2 Total Flux

We next examine the relationship between internal turbulence level with the total flux of the SCUBA core. Figure 3.9 shows SCUBA core total flux versus the velocity dispersion for both the starless and protostellar cores. No trend is apparent for the starless cores (diamonds), while there appears to be a weak trend of higher flux corresponding to higher velocity dispersion in the protostars (asterisks). If we split the protostars into those with fluxes greater than 5 Jy and less than 5 Jy, we find the

mean and standard deviation are 0.31±0.10 km/s and 0.23±0.07 km/s respectively. The symbols intersected by crosses show the mean and standard deviation for the protostars and starless cores, indicating that the protostars tend to have higher flux than the starless cores. This could be the result of slightly higher central temperatures in the protostellar cores.

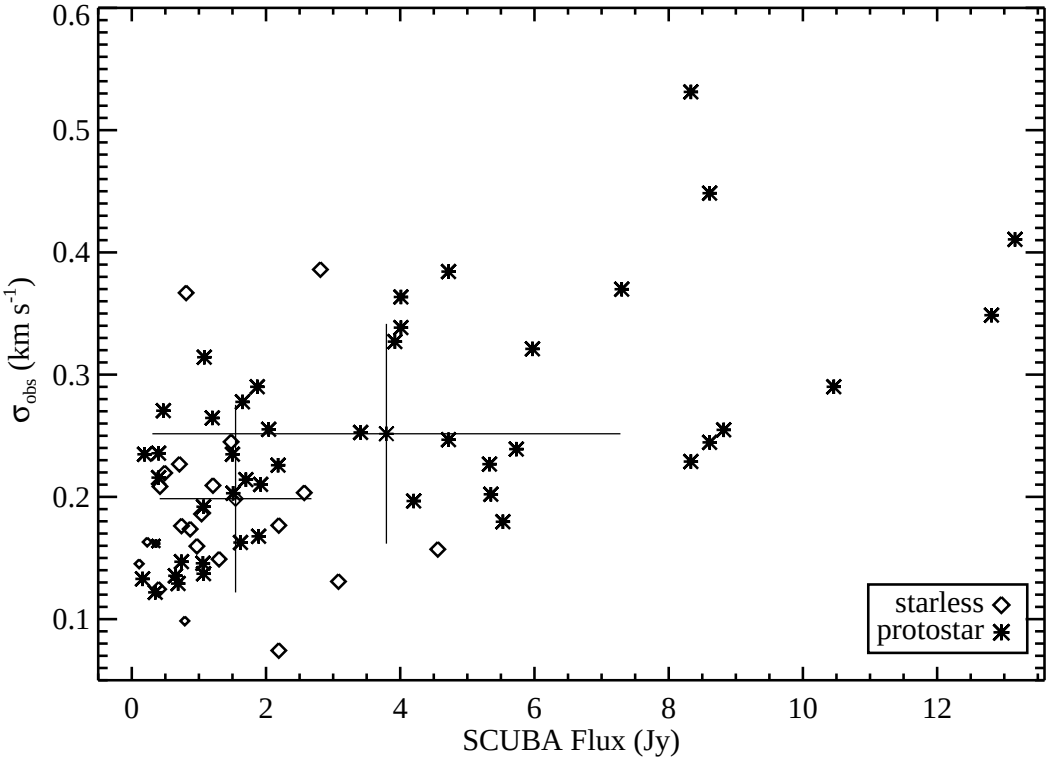

Figure 3.9 Variation of core velocity dispersion with the total flux within a SCUBA core for both protostars and starless cores. The same plotting convention is used as in Figure 3.8.

If we assume a constant temperature of 15 K, a dust opacity of 0.02 $g^{-1}cm^2$ at 850 μm and a distance to the Perseus molecular cloud of 250 pc (e.g., Cernis, 1993), we can convert the observed SCUBA flux into mass as 1 Jy = 0.48 $M_\odot$ (see KJD06). Note that due to the non-negligible uncertainties in all of the above quantities, the mass is only accurate to a factor of roughly 6. Even with the large uncertainty, we can use the mass and radius measured for each SCUBA core to estimate the internal velocity dispersion required to provide support against gravity, which we again take to be $\sigma_{grav} = \sqrt{GM_C/5R_C}$ (c.f. eq. [4]).

The velocity dispersion of the mean gas can be calculated by correcting for a thermal component with a molecular weight of 2.33 rather than 29 for N_2H^+. We can then compare the total gas velocity dispersion to that predicted for virial equilibrium (from the SCUBA observations). Figure 3.10 shows the square of the ratio of the observed velocity dispersion to the virial velocity versus SCUBA flux for the starless cores and protostars. 'Virial equilibrium' would occur for a ratio of 1 (dotted line). All of the N_2H^+ cores have higher velocity dispersions than predicted by the virial equation, with those at small SCUBA fluxes displaying the largest difference. The cores farthest from 'virial equilibrium' would require the SCUBA mass to be underestimated by a factor of ten or more if they were truly in virial equilibrium, far larger than our uncertainties allow. [5] Many of the cores would be far from virial equilibrium even if their observed velocity dispersion were purely thermal – the dashed and dot-dashed lines show the relationships for a 15 K thermal core velocity dispersion and assuming core radii of 10″ and 60″ respectively (bounding the observed range of SCUBA core radii).

The above analysis ignores the contribution of external pressure in the virial equilibrium calculation which for sub-Jeans mass objects keeps the internal motions thermal even though gravity alone does not require internal motions of this magnitude. In KJD06, we find that the SCUBA cores in Perseus are well fit by Bonnor-Ebert spheres with external pressures in the range of $5.5 \leq \log_{10}\mathrm{P}_{ext}/\mathrm{k}_B \leq 6.0$. For a 'typical' core of roughly one solar mass and 50″ in extent, when the external pressure is included in calculating virial equilibrium, the square of the virial velocity rises by a factor of approximately 1.3 to 2 of what it was without considering the external pressure, which would make most of the higher flux cores in approximate virial equilibrium. Similarly, a critical BE sphere, which has $\mathrm{R}_{crit}=0.41GM/c_s^2$ (Hartmann, 1998), requires $\sqrt{5 \times 0.41}$, or roughly 1.4, times the velocity dispersion one would naively assume. Note that observing a line width and converting to mass using the virial equation without accounting for surface pressure will overestimate the enclosed mass of an equilibrium core. See also Dib et al. (2007).

Our results thus show that while we observe velocity dispersions that are several times larger than what is predicted by the traditional 'virial equilibrium' measures,

[5] Note that this result is in contrast with some previous studies which have found that the majority of cores are gravitationally bound (e.g. Enoch et al., 2008). It is possible that this difference is primarily due to uncertainties in the flux to mass conversion; the majority of the dense cores in our survey are consistent with being gravitationally bound within the factor of six uncertainty in our conversion factor.

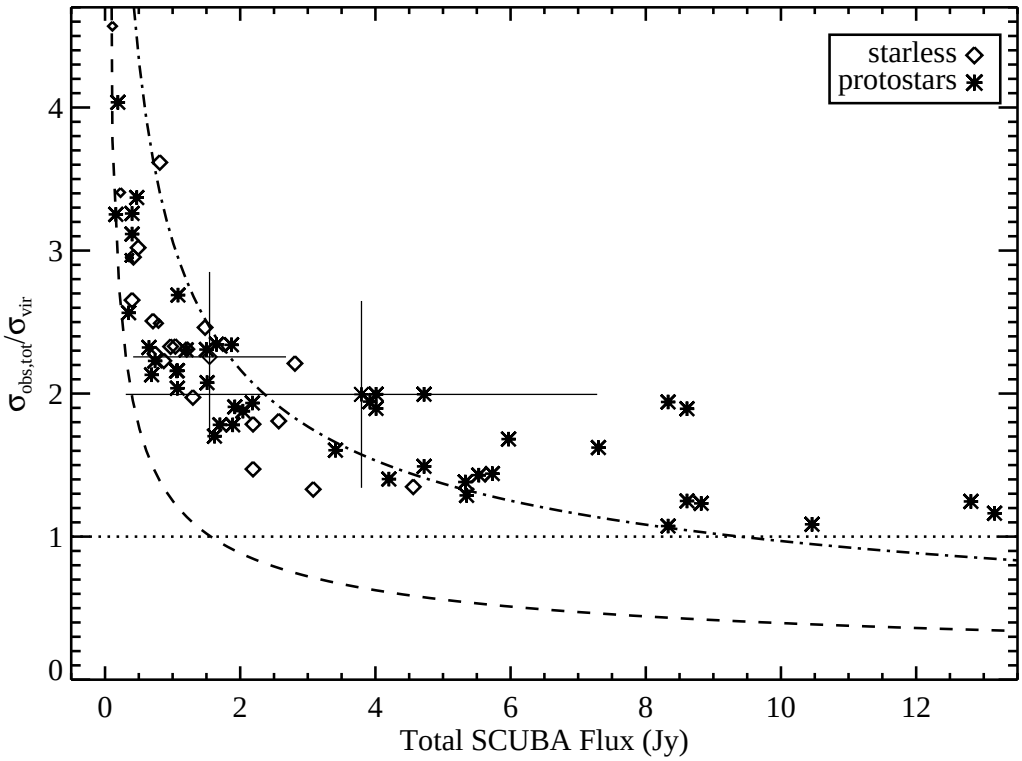

Figure 3.10 Ratio of the mean gas velocity dispersion to the virial velocity dispersion (calculated from SCUBA core flux and radius) squared, versus the observed SCUBA flux. The same plotting conventions are used as in Figure 3.8. The dotted line shows the expected relationship for virial equilibrium. The dashed and dot-dashed lines show the relationship for thermal 15 K cores assuming core radii of 10″ and 60″ respectively.

when the external pressure on the dense cores from the ambient cloud is accounted for, the agreement is reasonable for the higher flux cores. This is in contrast with some previous observations which tend to find velocity dispersions which are consistent with 'virial equilibrium' without accounting for any external pressure – for example, the low mass dense core survey of Caselli et al. (2002). Some previous studies, however, have shown that external pressure is required for virial equilibrium, e.g., in the Horsehead nebula (Ward-Thompson et al., 2006).

The turbulent simulations of Klessen et al. (2005) predict a relationship between virial and observed mass – their large-scale-driven simulation (which more closely matches our other observations) shows that the starless cores have virial masses which are greater by up to a factor of thirty than the actual mass. Unlike our observations,

however, the simulation shows that protostars have virial masses which are several times less than the actual mass. Klessen et al. (2005) points out that the virial mass estimates for protostars are underestimated due to the lack of velocity resolution of the gas in the central sink cell, but that this will have a small effect on the measured velocity dispersion since a small fraction of the core mass is contained within the sink cell.

3.8.3 Variation of Line Intensity

N_2H^+ and $C^{18}O$ observations can also serve as a probe of the chemistry of the dense cores. N_2H^+ is only able to form in significant amounts after $C^{18}O$ freezeout has occurred, as the two molecules form via competing reactions. While N_2H^+ is observed to be a good dense gas tracer for densities of $10^5 - 10^6$ cm^{-3} (Tafalla et al., 2002), it may freeze out onto dust grains at densities above this (Crapsi et al., 2005). $C^{18}O$ on the other hand, should be depleted at high densities. At later stages of evolution once a central protostar has formed, the situation is expected to reverse, with the central region heating, causing the liberation of CO and destruction of N_2H^+. Our SCUBA observations allow us to estimate the (column) density of the dense cores independently of our IRAM observations which may be affected by chemistry. Using the same flux to mass conversion factors discussed above, we can convert the SCUBA flux into a column density – 1 Jy beam^{-1} corresponds to 0.24 g cm^{-2} or $\sim 10^{22}$ cm^{-2}. Making the further assumption that the cores are roughly spherical and have a diameter of $\sim 50''$ in the plane of the sky, this corresponds to a density of $\sim 10^6$ cm^{-3}.

Figure 3.11 shows the total SCUBA flux within the IRAM N_2H^+ beam for each observation versus the integrated intensity measured in both N_2H^+ and $C^{18}O$. The N_2H^+ integrated intensity shows some correlation with the total SCUBA flux for both the starless and protostellar cores. The $C^{18}O$ integrated intensity possibly shows a very weak correlation with SCUBA flux below ∼1Jy and no correlation above this. This is consistent with denser cores being dominated by central freeze out (i.e., even with increasing column density, the $C^{18}O$ integrated intensity remains constant).

We also examine the ratio between the $C^{18}O$ and N_2H^+ integrated intensities – a low ratio, for example, would be indicative of freezeout. Figure 3.12 shows the total SCUBA flux observed in each IRAM beam versus the ratio of integrated intensity measured in $C^{18}O$ and N_2H^+. This figure shows that high $C^{18}O$ to N_2H^+ ratios mostly occur for starless cores, and only at smaller SCUBA fluxes, i.e., where the

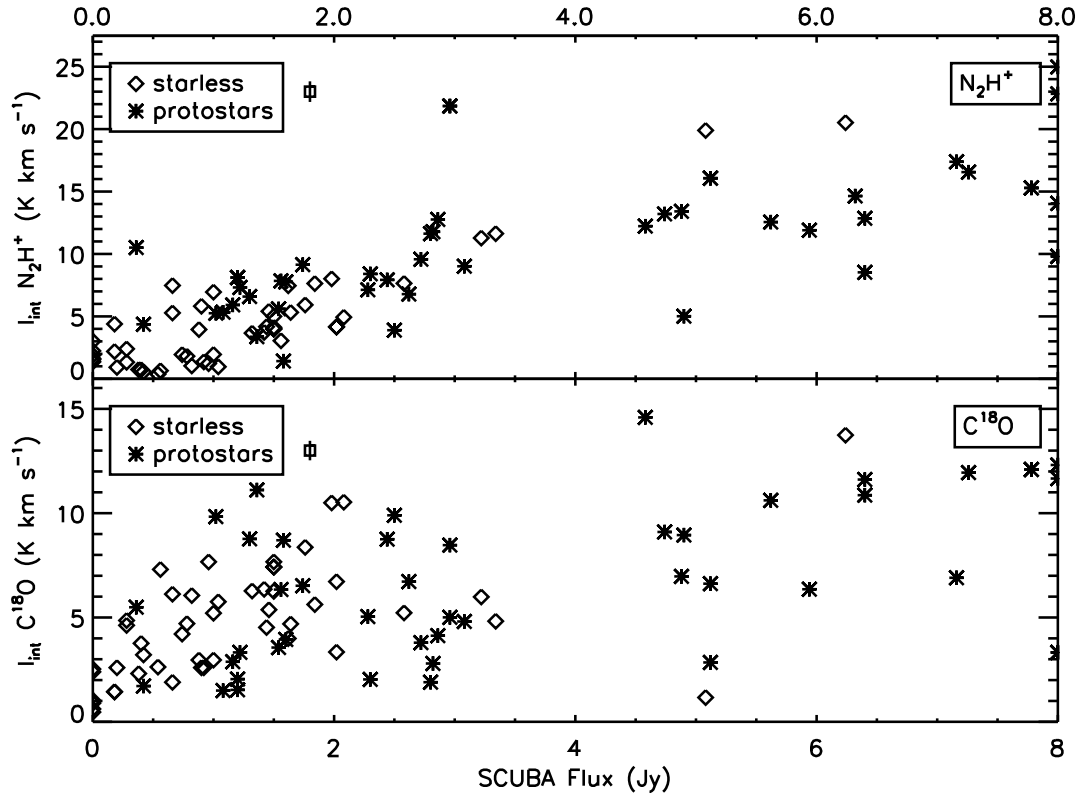

Figure 3.11 Variation in integrated intensity for $C^{18}O$ and N_2H^+ with total SCUBA flux over the region observed by IRAM. Note that cores associated with total SCUBA fluxes of over 8 Jy were included in the plot as having SCUBA fluxes of 8 Jy $beam^{-1}$. The same plotting conventions are used as in Figure 3.8. The squares with vertical lines indicate the mean size of the error in the integrated intensity. The error bar for the $C^{18}O$ integrated intensity has been enlarged by a factor of two.

density is lowest and hence there is little to no freeze out. All high flux SCUBA cores have low $C^{18}O$ to N_2H^+ ratios. Due to the large relative error in the N_2H^+ integrated intensity for these cores, the error in the ratio is often greater than 100%. Note that following the results of §5, in the few cases where two $C^{18}O$ components were associated with an N_2H^+ dense core, the integrated intensity of the component with the closest velocity is plotted.

We can also calculate the N_2H^+ column density from the integrated intensity, assuming an excitation temperature of 15 K and correcting for the optical depth. We use eq. (10) of Shirley et al. (2005), and find a column density of

$$N_{N_2H^+} = 1.47 \times 10^7 \frac{\langle \tau \rangle}{1 - e^{-\langle \tau \rangle}} \int T_A^* dV \times \frac{F_{eff}}{B_{eff}} \, cm^{-2} \tag{3.5}$$

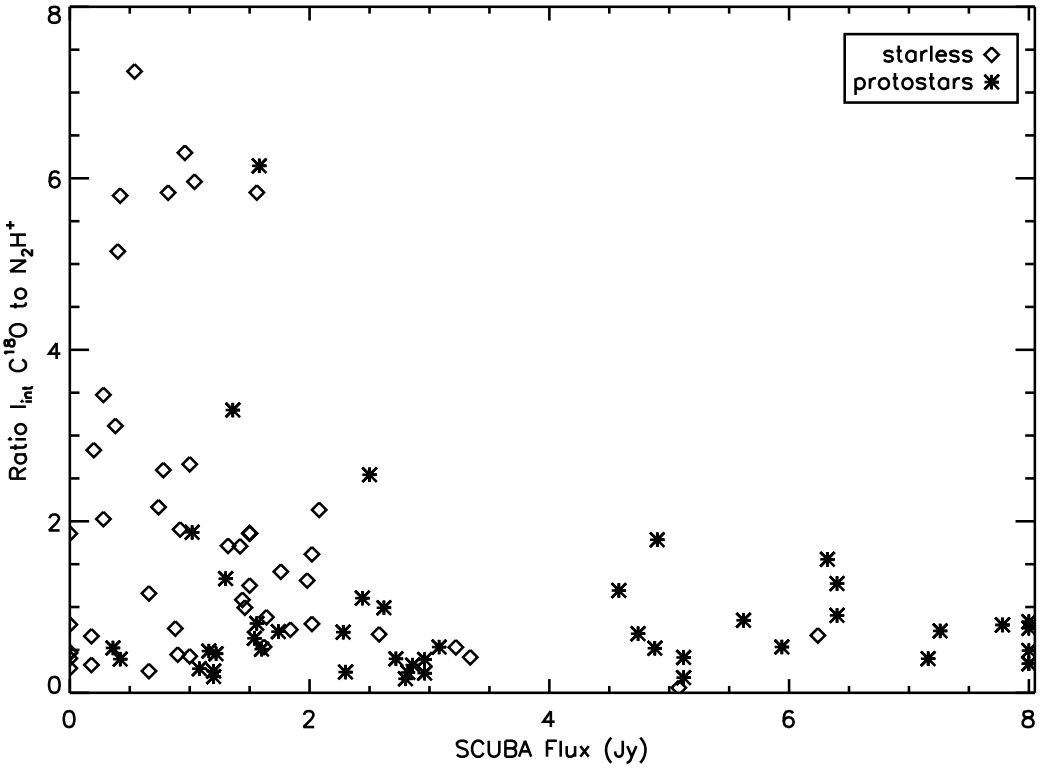

Figure 3.12 Ratio in $C^{18}O$ to N_2H^+ integrated intensity versus total SCUBA flux over the IRAM beam. Note that all cores associated with SCUBA fluxes of over 8 Jy have been included in the plot as having values of 8 Jy. The diamonds denote starless cores while the asterisks denote the protostars.

where $\langle\tau\rangle$ is the mean optical depth of the hyperfine transitions (CLASS's hfs fitting routine fits $\tau_{tot} = 7\langle\tau\rangle$), $\int T_A^* dV$ is the integrated intensity in K m s^{-1}, and $F_{eff} = 0.95$ and $B_{eff} = 0.77$ are beam efficiency parameters available from the IRAM 30m website. Our minimum observable total (gas) column density is $\sim 10^{11}$ cm^{-2}.

Figure 3.13 shows the N_2H^+ column density derived versus the total column density derived from the total SCUBA flux measured in the IRAM beam. The relative error in the total column densities is ∼30% (the calibration error of SCUBA data), with an absolute error close to a factor of six due to uncertainties in constants used to convert flux to mass.[6] The errors in the N_2H^+ column density vary substantially, mostly due to errors in the optical depth determined; the median error is 30%. The noise in the SCUBA map is ∼10 mJy beam^{-1}, which translates to a minimum ob-

[6]The factor of six is due to the combination of uncertainties in the distance, temperature, and dust grain opacity.

servable total column density of $\sim 10^{21}$ cm^{-2}.

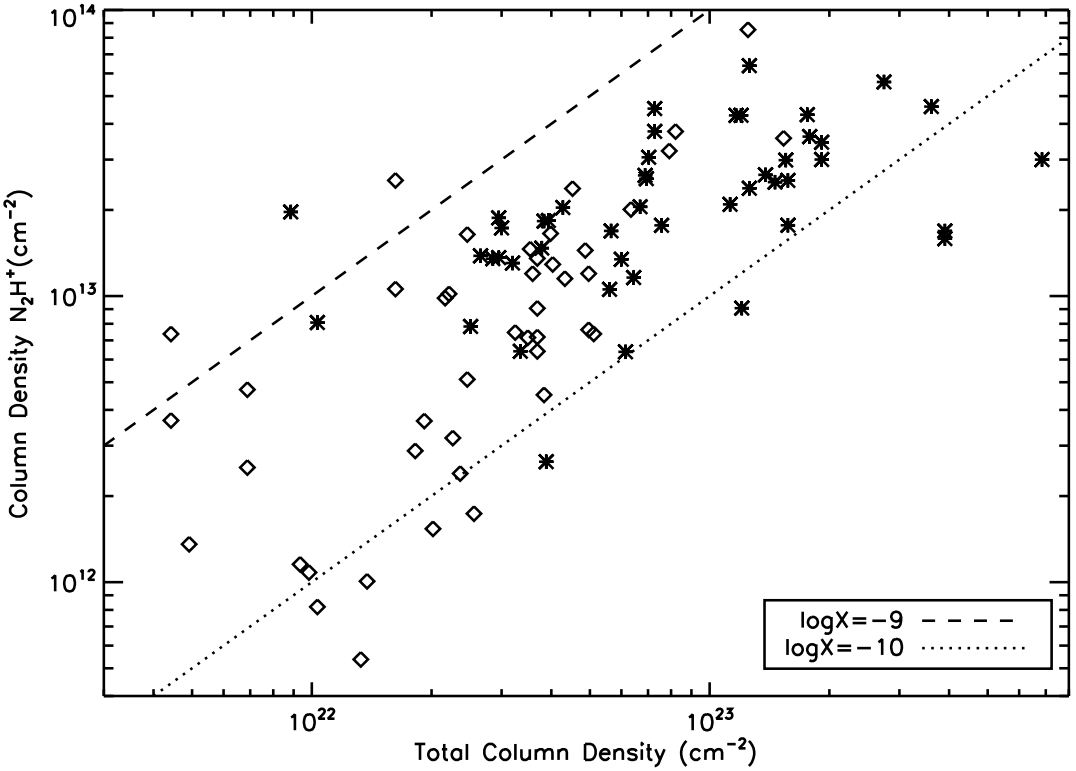

Figure 3.13 Column density of N_2H^+ versus the total column density (calculated using the SCUBA flux within the IRAM beam). The diagonal lines indicate fractional abundances of N_2H^+. Starless cores are diamonds while protostars are asterisks.

Overplotted on Figure 3.13 are lines of constant N_2H^+ abundance. The cores lie between approximately $N_{N_2H^+}$ / $N_{H_2} = 10^{-9}$ and 10^{-10}, consistent with what has been more accurately derived from detailed mapping and analysis of single cores (e.g., Shirley et al., 2005; Tafalla et al., 2004).

3.9 CONCLUSIONS

We present results from a survey of N_2H^+(1-0) and $C^{18}O$(2-1) of 157 dense core candidates in the Perseus molecular cloud. We detect N_2H^+ in 62% of our targets, and 84% of our SCUBA-selected targets. N_2H^+ is a 'late-time' molecular ion which does not become abundant until $\sim 10^5$ years (Aikawa et al., 2003). Since we detect N_2H^+ in the vast majority of SCUBA cores, this argues that objects which attain

sufficient density to be detectable with SCUBA are not short-lived, transient objects. This is in agreement with the findings of Jørgensen et al. (2007) and Enoch et al. (2008) who argue that starless dense cores have roughly equal lifetimes to that of deeply embedded protostars, which is on the order of 10^5 years (Ward-Thompson et al., 2007).[7]

We differentiated between starless cores and protostars on the basis of *Spitzer* data (Jørgensen et al., 2007). In N_2H^+, the starless cores have linewidths which are dominated by thermal broadening, while the protostars have slightly larger linewidths, consistent with many previous surveys including Benson & Myers (1989) and Jijina et al. (1999). We find fewer N_2H^+ cores dominated by non-thermal motions than predicted by the turbulent simulations of Klessen et al. (2005). For the starless cores, the mean ratio of non-thermal to thermal motions ($f_{turb} \sim 0.6$) implies the ratio of non-thermal to thermal pressure, f_{turb}^2, is less than 40%. Naively, this runs counter to turbulent models where cores as well as transient density peaks form at the convergence of supersonic flows. Simulations must therefore demonstrate that turbulent pressure does not dominate in the high density regime probed by N_2H^+.

The $C^{18}O$ observations, sensitive to lower density material, reveal much more non-thermal motions, as previous surveys have shown. There is less difference in non-thermal motions between targets associated with protostars and those that are not associated with protostars, implying that protostars have little effect on the bulk dynamics of their envelopes at the earlier stages of evolution.

We find the relative motions of the dense N_2H^+ cores and their envelopes (measured in $C^{18}O$) tend to be less than thermal in the majority of cases, confirming and strengthening the results of Walsh et al. (2004, 2007) for clustered star forming environments.

Within large scale structure, defined through 2MASS extinction observations, the core-to-core motions of starless cores are not sufficient to provide support against gravity, however, the sparse sampling of each extinction region leads to large errors associated with the core-to-core velocity dispersions we measure. The total velocity dispersion tends to be smaller when measured in N_2H^+ than $C^{18}O$ due to the smaller linewidths seen in N_2H^+.

The N_2H^+ cores which have an associated submillimetre source detected with

[7]Note that this lifetime applies only to the cores once they have attained sufficient density to be detected by these methods, i.e., above roughly 10^4 cm^{-3}. The time spent in lower density phases is not constrained by these observations.

SCUBA have internal motions several times larger than is required to provide support against gravity. Inclusion of external pressure shows the cores to be in approximate virial equilibrium. The protostars tended to have higher SCUBA concentrations, and total fluxes. High ratios of $C^{18}O$ to N_2H^+ integrated intensity, possibly indicating chemically young gas, were found for some cores which had a low flux measured with SCUBA. At higher SCUBA fluxes, only low ratios of $C^{18}O$ to N_2H^+ integrated intensity were observed. Column densities derived for N_2H^+ were consistent with abundance ratios between 10^{-9} and 10^{-10}, in agreement with what has been previously derived for cores with more accurate observations.

Our survey utilized single pointings on most of our dense core candidates, rather than using the traditional route of mapping. We show that the lack of a full map around each source has a minimal effect on our dynamical analysis. High resolution maps are, however, quite helpful in disentagling the motions in complex regions such as NGC1333 where multiple objects along the line of sight could otherwise lead to confusion in interpretation of results. Our method is an efficient and effective way to survey the dynamics of dense cores over the full extent of a molecular cloud. In the future, this method can be applied to other molecular clouds in order to determine whether the dynamical properties of the cores observed in the Perseus molecular cloud are universal or are dependent on the cloud environment.

3.10 ACKNOWLEDGEMENTS

We thank the IRAM 30 m staff for their hospitality and support during our observations.

The Second Palomar Observatory Sky Survey (POSS-II) was made by the California Institute of Technology with funds from the National Science Foundation, the National Geographic Society, the Sloan Foundation, the Samuel Oschin Foundation, and the Eastman Kodak Corporation.

HK[8] is supported by a Natural Sciences and Engineering Research Council of Canada CGS Award and a National Research Council of Canada GSSSP Award. DJ is supported by a Natural Sciences and Engineering Research Council of Canada grant.

HK would like to acknowledge valuable discussions with people at the CfA –

[8]Guest User, Canadian Astronomy Data Centre, which is operated by the Herzberg Institute of Astrophysics, National Research Council of Canada

other members of the COMPLETE collaboration, in particular Alyssa Goodman, Jens Kauffman, and Erik Rosolowsky, as well as Phil Myers and Charles Lada. Additionally, HK thanks Matthew Bate for a sending a preprint of his work.

3.11 APPENDIX A: SCUBA OBSERVATIONS

In this chapter, we utilize newly created 850 μm SCUBA maps with a finer sampling size of 3″ to better determine SCUBA source properties. We used our full 6″ sampled map of KJD06 to define regions in which to create 3″ sampled maps. As in KJD06, we combined all of the scan- and jiggle- map data in the JCMT archive[9] and used the same reduction procedure as in KJD06, making modifications only for the smaller sampling size. We first use the normal SCUBA software (Holland et al., 1999) to flat-field and atmospheric-extinction correct the raw data. We then used the matrix inversion technique of Johnstone et al. (2000) to produce the images. The matrix inversion technique has been shown to produce better images than the standard procedure used at the JCMT, particularly when combining data of different qualities (Johnstone et al., 2000), as is the case for the archival data used here. In order to correct for atmospheric fluctuations and other effects, SCUBA data are in the form of a series of difference measures (chops). Any image-reconstruction technique is thus insensitive to real structures which have sizes several times larger than the chop throw (Johnstone et al., 2000). We remove this structure by subtracting a large-scale smoothed version of the map from the original (we smooth with a Gaussian of σ =90″). In order to prevent the introduction of negative 'bowls' around bright sources (and similarly diffuse positive regions around deep compact 'holes'), we first create a map where all values outside of $\pm$0.1 Jy beam^{-1} per pixel were replaced with those values before smoothing to create the large-scale smoothed map (0.1 Jy beam^{-1} corresponds to roughly five times the rms value). We also smoothed pixel-to-pixel noise using a Gaussian with $\sigma = 3''$. Figure 3.14 shows our map of B1 as an example of the 3″ SCUBA maps.

To identify SCUBA cores in the maps, we utilized the object-identifying algorithm of Williams, de Geus, & Blitz (1994), 'Clumpfind 2D'. In this algorithm, objects

[9]Based on observations obtained with the James Clerk Maxwell Telescope, which is operated by the Joint Astronomy Centre in Hilo, Hawaii on behalf of the parent organizations PPARC in the United Kingdom, the National Research Council of Canada and The Netherlands Organization for Scientific Research.

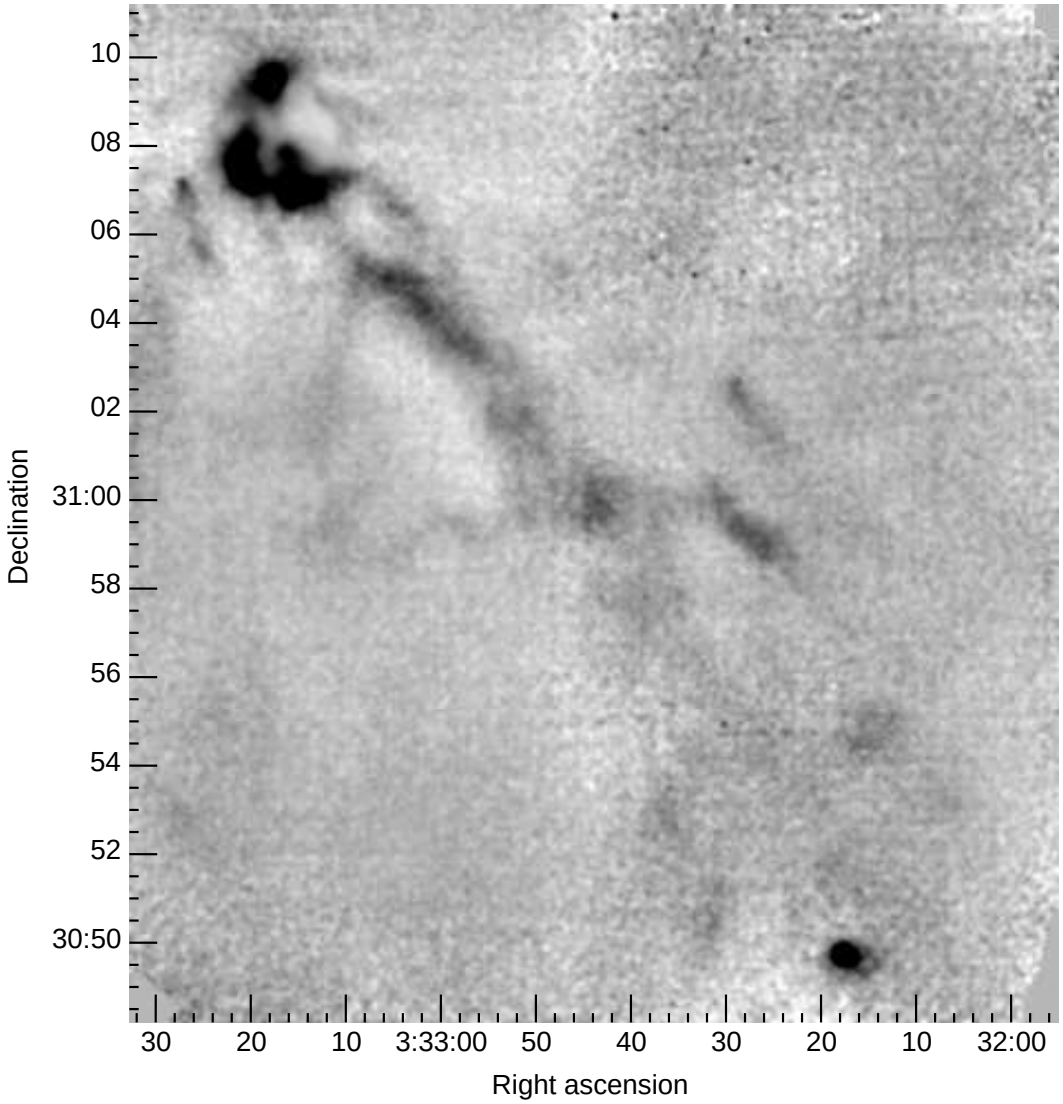

Figure 3.14 The 3″ SCUBA map of the B1 star forming region. The image is scaled such that white corresponds to ∼0 Jy beam^{-1}and black to ∼0.25 Jy beam^{-1}.

are identified as peaks at 2 'σ_C' intervals and extended until they either encounter another object or the lowest allowed 'σ_C' level. Normally, σ_C is the noise level in the map, however, in order to have a consistent core-identification threshold in all of the 3″ mapped regions, we used $\sigma_C = 0.03$ Jy beam^{-1} per pixel, which corresponds to approximately the same level in which we identified SCUBA cores in our previous work KJD06. Accurate noise levels for each 3″ sampled map were difficult to determine in some cases due to the small map sizes.

In addition, several regions had no cores identified but displayed hints of structures

with peaks below the object-identification theshold of $5\sigma_C$. In order to put some constraints / upper limits on the submillimetre properties of potential cores in these regions, we ran clumpfind to a lower identification threshold ($\sigma_C = 0.01$ Jy beam^{-1} per pixel) in these regions only. It should be noted that properties derived for these objects are not as reliable as the originally identified cores. We term these objects as having 'less secure fits' throughout the chapter and do not include these in our quantitative analysis. Table 3.6 below denotes the properties of the SCUBA cores identified.

Finally, as discussed in Appendix C, SCUBA observations in the region of NGC1333 appear to have a shift of $6''$ in RA relative to data at other wavelengths, apparently due to an unusually large pointing error at the JCMT. Here, we apply a global shift of $6''$ to the NGC1333 observations to compensate for this.

3.11.1 Comparison to Previous Results

While Clumpfind does a reasonable job of identifying structures in two dimensional maps where the filling factor is low, the cores identified in the $3''$ sampled maps used here are different from the set we identified previously in the $6''$ sampled map of KJD06, even though the same data are used and the reduction procedure is almost identical, albeit with a different smoothing scale. This is because Clumpfind relies on contours for determining object edges, so that slight variations in flux per pixel can change the size of core boundaries, which then affects the measured size and total flux, although the peak flux would be unchanged. In clustered regions, the slight variation in flux per pixel can also change where or when cores are either separated from or merged with close neighbours. Clumpfind identifies distinct clumps where two regions are isolated at a given search contour (every $2\sigma_C$). For example, a peak at $6.9\sigma_C$ surrounded by pixels at $6.1\sigma_C$ and near a peak at $11\sigma_C$ would be identified as a single object (at the 7 and $5\sigma_C$ contours, all of the flux is connected). If the $6.9\sigma_C$ peak were instead a peak at $7.1\sigma_C$, it would be identified as a separate object from the $11\sigma_C$ peak (the flux is in two unconnected regions at the $7\sigma_C$ contour). Thus individual core properties are difficult to compare between maps reduced under even slightly different schemes or resolutions. We do not show a comparison of the cores identified here with those identified in the $6''$ sampled map of KJD06, but note that given variations in core boundaries and potential merging of cores, the list of cores we identify in the $3''$ sampled map spans the cores identified in the $6''$ sampled map

and also includes an additional four cores (#4, 28, 72, 73).

3.11.2 Core Properties

The properties of the cores identified in the 3″ sampled map are shown in Table 3.6. The core radius, peak flux, and total flux are found with Clumpfind. We also calculate the concentration of each core – previous work has shown this to be an indicator of the evolutionary state of the core, with higher concentrations corresponding to later stages of evolution (Walawender et al., 2005, 2006; Johnstone & Bally, 2006). Following Johnstone et al. (2001), the concentration can be calculated from observational quantities as:

$$C = 1 - \frac{1.13 B^2 S_{850}}{(\pi R_{obs}^2) f_0} \tag{3.6}$$

where B is the beamsize, S_{850} the total flux, R_{obs} the radius, and f_0 the peak flux. As in KJD06, we can also model the cores as Bonnor Ebert (BE) spheres – spherically symmetric isothermal objects where thermal pressure balances gravity and an external pressure. The best fit BE sphere model properties are also included in Table 3.6.

3.12 APPENDIX B: TWO-COMPONENT N_2H^+ CORES

In this section we discuss the N_2H^+ spectra which we found required two velocity components for a good model fit. We treated these two velocity components as originating from independent objects along the line of sight, rather that a single core whose spectrum shows self-absorption. The optimal method for distinguishing between self-absorption and two distinct cores would be to observe the region with an optically thinner tracer. Since this is not available to us, we instead examine the data we do have for these cores (e.g. spectra at cross positions, SCUBA observations, and other N_2H^+ survey data) and discuss how well they support our interpretation.

Most of the cores for which we fit two components lie in regions where complex motions are seen on smaller scales, such as NGC1333, where it is not surprising to find two cores along the line of sight. In instances where we found a common velocity component between two close pointings, we excluded this common velocity component from the second source in our subsequent analysis in order to avoid counting the same core twice.

In NGC1333, we found six cores with two velocity components – #99, 103, 106, 107, 111, and 118. All of these except #99 fall within the survey region of Walsh et al. (2007) which in every instance identifies a distinct object at each velocity that we fit to our data. Source #99, which falls outside of the Walsh et al. (2007) survey region, was observed at cross positions (see Figure 3.15). The two components show varying relative intensities across the five positions mapped, supporting the hypothesis of two distinct cores.

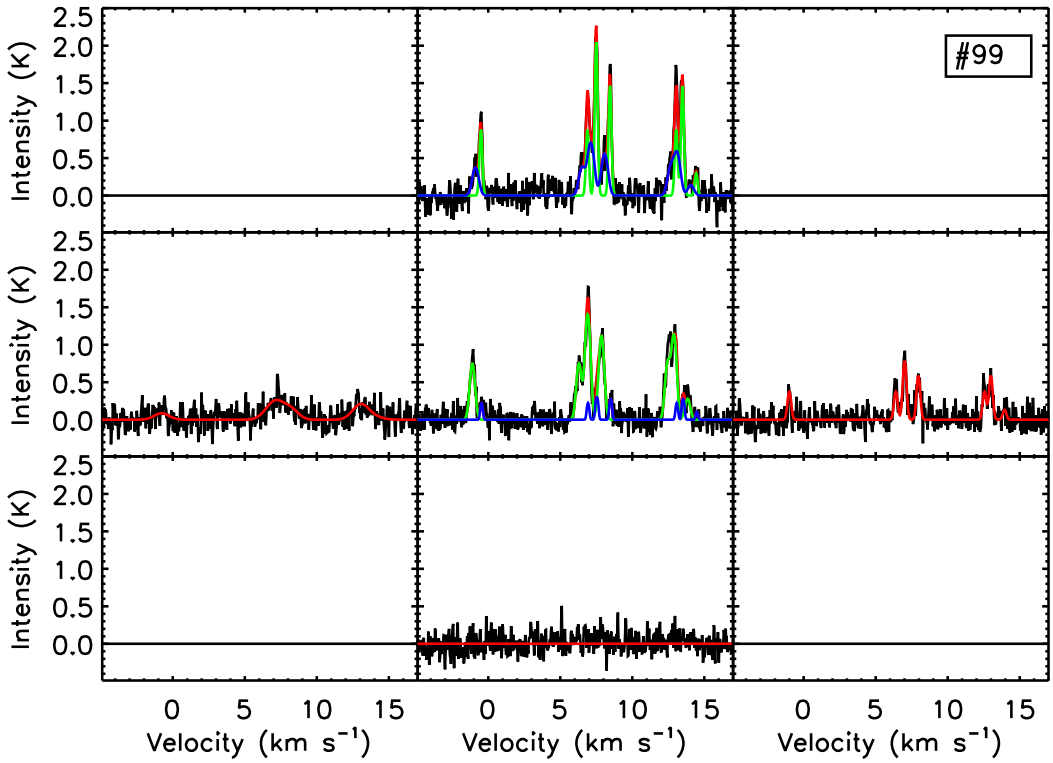

Figure 3.15 Spectrum for source #99 in NGC1333. The vertical axis is in units of T_A^*. Red indicates the summed fit while blue and green indicate the two different components fit (where applicable).

In IC348, we fit two cores with two velocity components, #22 and 27. While there is no high resolution N_2H^+ map of IC348, Tafalla et al. (2006) provide a 50″ resolution map. Our core #22 corresponds to Tafalla et al. (2006)'s source C in IC348-SW1 which they show appears to be related to outflow structure seen in CO. Tafalla et al. (2006) identify two velocity components in N_2H^+ which correspond to the velocities we found. Our core #27 corresponds to source A in IC348-SW1 which

Tafalla et al. (2006) associate with a single broad (∼1.6 km/s) velocity component. Our observations (Figure 3.16) clearly show two distinct velocity components, perhaps resolvable due to the smaller beamsize of our observations.

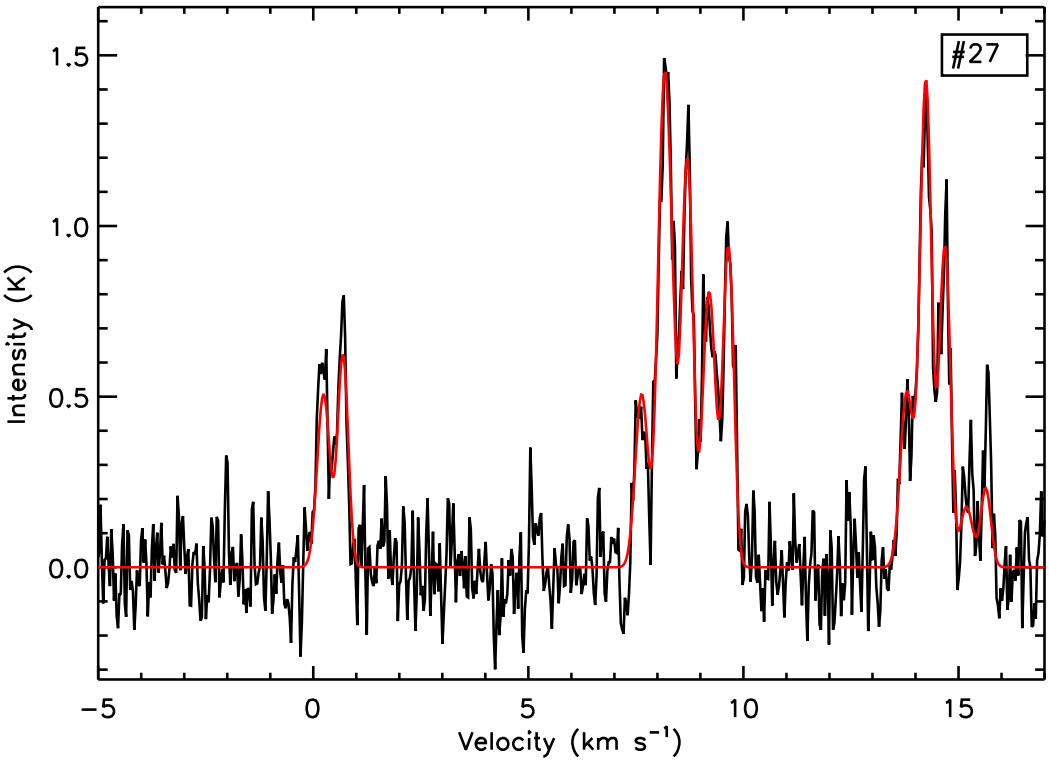

Figure 3.16 Spectrum for source #27 in IC348. The same plotting convention is used as in Figure 3.15.

In L1455, one core (#136) was fit with two velocity components. Cross positions were also observed, and where the S/N is high enough, the two components are clearly quite separate (see Figure 3.17).

North of B1, one core (#76) was fit with two velocity components at one cross position only. This observation has low S/N and is designated as being of poor quality, and therefore was not used in any of the analysis.

The core with the poorest two velocity component fit is #148 in L1448. In this instance, the model does not well fit the data in several places (see Figure 3.18), making the interpretation of two distinct cores uncertain. The SCUBA map suggests the core is isolated – the nearest SCUBA core is roughly an arcminute away. Without additional observations, no firm interpretation can be made.

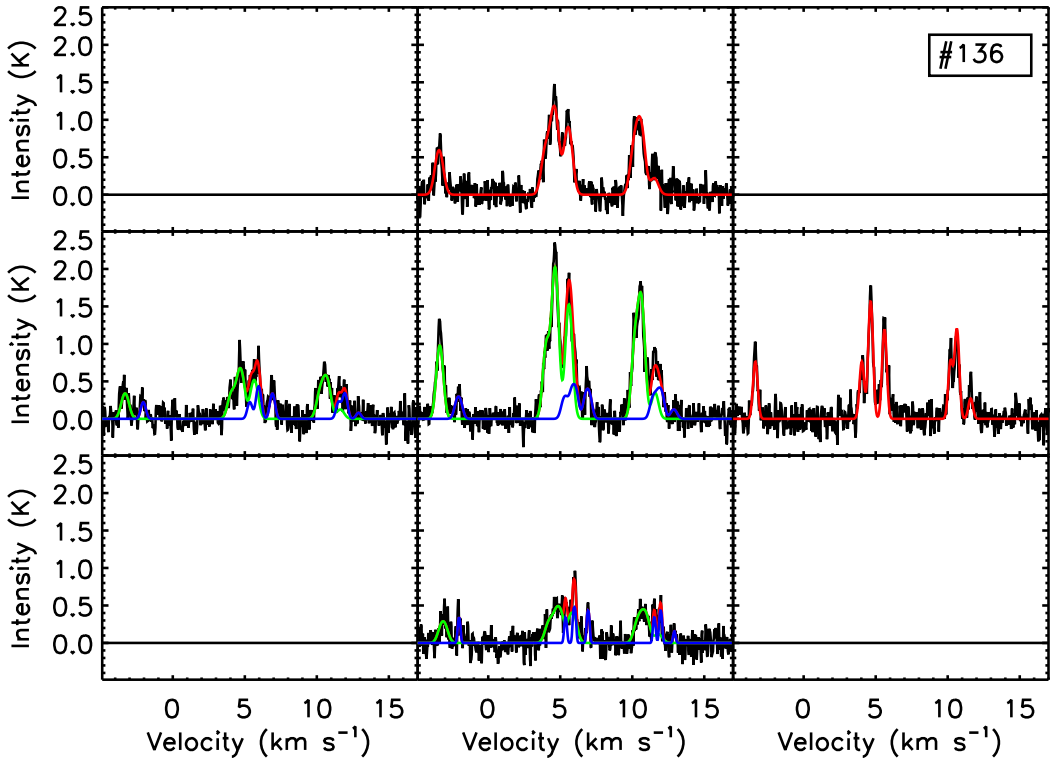

Figure 3.17 Spectrum for source #136 in L1544. The same plotting convention is used as in Figure 3.15.

3.13 APPENDIX C: EFFECT OF UTILIZING SINGLE POINTINGS

For the analysis in the chapter, we utilized only the data from the central pointing on each target in order to have a consistent dataset. Since we have four-point cross data around some of our targets, we can ask two additional questions – how accurate were the target centre positions that we used and does our utilization of only the central point bias or change any of our results. Here we address these questions in turn.

3.13.1 Accuracy of Dense Core Pointings

We first note one occurence that led to small offsets between some positions in the SCUBA catalog we used for determining our target positions and the catalog of Appendix A. After the publication of KJD06, we discovered an offset of $\sim 6''$ in RA in

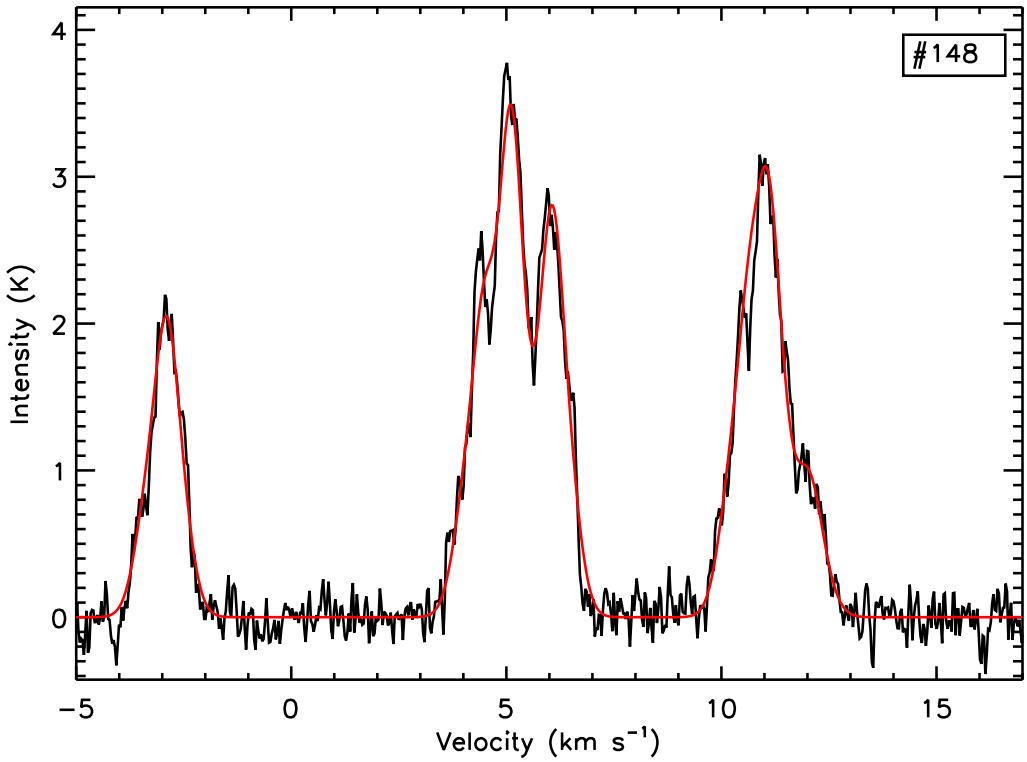

Figure 3.18 Spectrum of source #148, the two velocity component core in L1448. The same plotting convention is used as in Figure 3.15.

the region of NGC1333 in the SCUBA data compared with data at other wavelengths. This is intrinsic to the data (not caused by an analysis error) and is apparently caused by an unusually large pointing error with SCUBA. This offset is further discussed in Di Francesco et al. (2008). This offset was not known at the time of our IRAM observations, hence was not accounted for when the SCUBA target list was created. This 6″ offset is much smaller than the IRAM N_2H^+ beamsize (25″) and hence should not have a large effect on the results, but is noted here for completeness.

We expect the N_2H^+ cores to have extents of order one or two IRAM beams (25″) in N_2H^+, the typical size of the SCUBA cores. SCUBA is sensitive to a similar range of densities, $\sim 10^4 - 10^6$ cm^{-3} using the approximation in §7. If we chose our target positions well, we expect the central position to show more signal than offset positions, although the cores should extend past the central pointing.

Figure 3.19 shows the fractional difference between the integrated intensity at the central position and largest value at an offset position (pluses) as well as the difference

with the average value of all offset positions (squares). The vertical lines indicate the error in the difference measure for the maximum difference. Nearly half of the cores plotted have highest integrated intensities at the central pointing, while another third have integrated intensities which are slightly larger at a single cross position. Only about one fifth of the cores show significantly larger integrated intensities at a single offset position. An additional thirteen positions where offset observations were made are not plotted due to a lack of a good central detection. Of these, ten also had no detections at any offset positions.

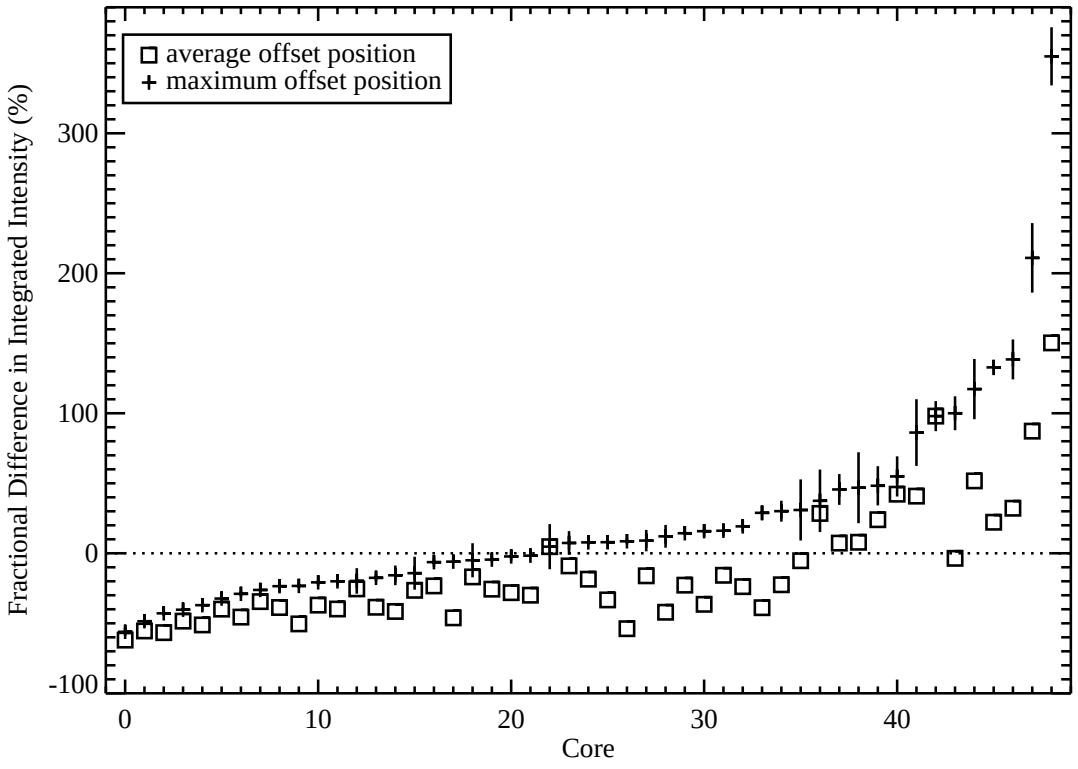

Figure 3.19 Fractional difference in integrated intensity between centre and offset positions in dense N_2H^+ cores. The pluses denote the maximum difference with the vertical lines indicating the error in this measurement. The squares denote the average difference for all four offset positions versus the centre. The cores are ordered according to the maximum difference.

It should be noted that we utilized two different set of criteria to determine which targets to map crosses around. Approximately half (thirty of sixty-two) of the cross targets had strong central detections – we observed at offsets to search for extended structure. The remaining half of the targets were chosen based on a very weak or non-

existent central detection in order to search for a stronger signal nearby (2MASS or Palomar plate - selected targets). The first of these cross-map criteria biases towards targets where the centre was well chosen, while the second biases towards poorly chosen centres. The former set of cross maps were mostly based on SCUBA cores where we had a high detection probability and it was easiest to determine precise core centres. Nearly all of the SCUBA-selected cores with crosses are consistent with having their strongest integrated intensity at the central position. The latter-chosen cross targets account for the largest integrated intensity differences at cross positions as well as the targets with insufficient signal to noise to obtain a fit and thus be included in the plot. Not surprisingly, our position selection was less accurate for these latter targets – many of the detections are not consistent with the central position having the highest integrated intensity. Since these latter crossed observations are biased to the worst-determined centre positions, we expect that our overall determination of centres was more successful.

We can therefore conclude that the pointings were quite accurate for the SCUBA-selected targets and reasonably accurate for the targets selected using the other methods, especially given the difficulties in determining precise centres in the latter case. As we shall see in the following section, the question of accuracy of the centre positions does not play an important role in the kinematical results presented earlier – these change very little between centre and cross positions.

3.13.2 Impact on Results

Now we examine whether our utilization of a single pointing of each dense N_2H^+ core introduces significant bias or error in the core properties measured.

3.13.2.1 Line Widths

We calculated the difference in N_2H^+ linewidth between each centre position and the surrounding cross and found this difference to be very small. Most (93%) of the N_2H^+ cores have mean differences less than one or two spectral channels (0.05 km/s in FWHM units), i.e., consistent with measuring the same value. The mean absolute difference of the entire sample was 0.018 km/s and none had differences close to the sound speed (FWHM of 0.15 km/s for N_2H^+) and the mean difference was approximately zero. Therefore, we expect that our analysis utilizing only central pointings does not introduce significant error or bias to our measurement of core linewidth.

3.13.2.2 Centroid Velocities

The difference in centroid velocity for the N_2H^+ cores at centre and cross positions is also small, as shown in Figure 3.20. In Figure 3.20, the vertical lines indicate the range in differences over the four cross positions. Note that the six sources with two velocity components fit at either centre or cross position have not been included in this plot. All but one of the N_2H^+ cores have a difference between the central and average cross velocity that is less than the thermal velocity dispersion; the mean difference is approximately zero and the standard deviation is 0.04 km s^{-1}. The N_2H^+ cores which have the largest centroid velocity differences have less secure fits where there is greater uncertainty in the centroid velocity determined. On the other hand, in the majority of cases the difference in velocities between cross and central positions are larger than the the fitting errors of those velocities, indicating that there is real variation in the centroid velocity between locations. This variation is much smaller than the core-to-core variations analyzed in the §6, however, where extinction regions require support against gravity with core-to-core motions many times larger than the sound speed. We thus find that little error or bias is introduced into our results by using data from a central pointing only.

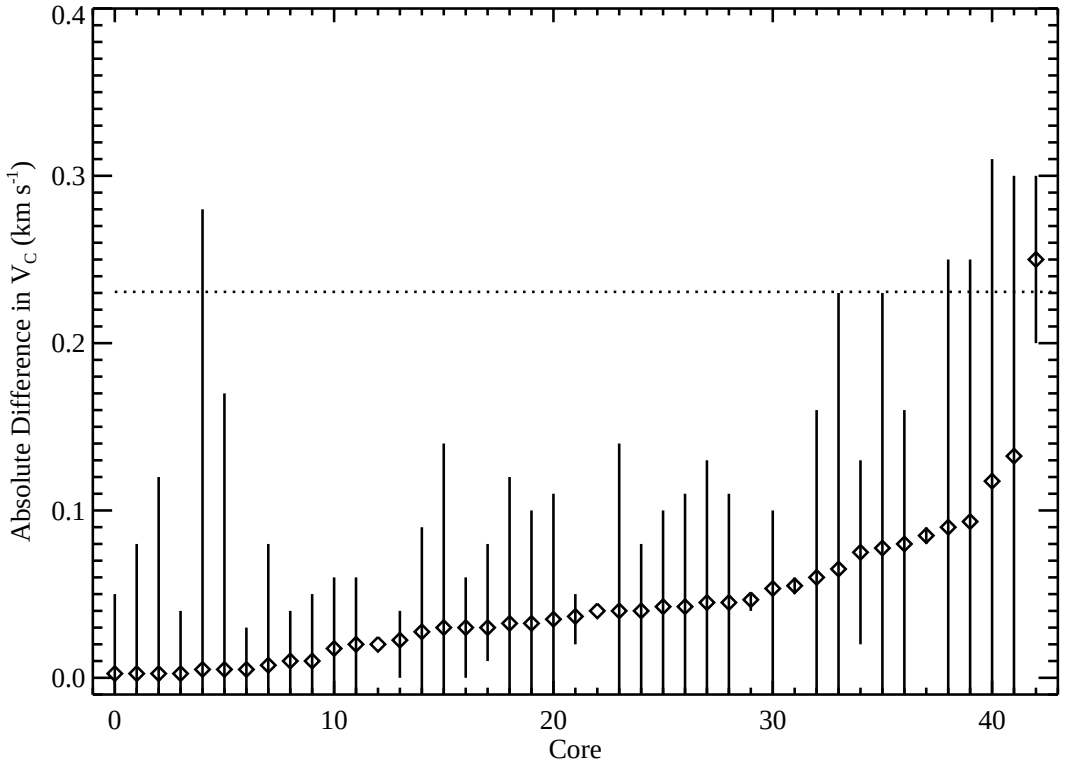

Figure 3.20 Difference in centroid velocity between the cross and central positions, with N_2H^+ cores ordered in increasing average difference. The diamonds indicate the average cross velocity difference while the vertical lines indicate the range in centroid velocity difference at all cross positions. Cores with two velocity components fit have not been included. The dotted line indicates the sound speed.

Table 3.1. Target Properties

#	RA (J2000.0)	Dec (J2000.0)	Sel. [a] Method	Cross? [b]	SCUBA [c] core	SCUBA [d] flux (Jy)	Spitzer [e] protostar	Ext. [f] Region	Mean Ext. [g] (A_V)
1	3:48:31.1	32:38:21.0	P	no	..	0	..	...	1.9
2	3:48:29.1	32:54:33.0	P	no	..	0	..	1	4.2
3	3:47:42.3	32:52:28.1	E	yes	..	0.88	..	1	8.1
4	3:47:41.8	32:51:40.3	S	no	1	1.74	49	1	8.0
5	3:47:40.4	32:54:39.0	P	yes	..	0.28	..	1	8.2
6	3:47:39.0	32:52:11.2	S	no	3	1.46	..	1	8.1
7	3:47:37.0	32:52:03.0	P	yes	..	0.28	..	1	7.8
8	3:47:36.1	32:50:11.0	P	yes	..	0	..	1	7.1
9	3:47:28.1	32:50:13.0	P	no	..	0.32	..	1	6.0
10	3:47:27.2	32:57:56.0	P	no	..	1.18	..	1	5.1
11	3:47:27.1	32:38:08.0	P	no	..	0	..	1	3.3
12	3:47:17.7	32:45:26.0	P	yes	..	0	..	1	5.3
13	3:47:05.6	32:43:12.0	P	yes	..	0	..	1	6.0
14	3:44:49.0	31:41:20.2	E	no	..	0.08	..	2	7.2
15	3:44:48.9	32:00:31.8	S	no	4	1.32	..	2	6.5
16	3:44:44.2	32:01:26.9	S	yes	5	2.50	48	2	6.6
17	3:44:37.3	32:14:04.3	E	no	..	0	..	2	6.0
18	3:44:36.9	31:58:40.7	S	yes	6	1.42	..	2	7.2
19	3:44:06.6	32:02:05.6	S	no	8	1.76	..	2	9.5
20	3:44:03.3	32:02:24.3	S	no	9	2.62	47	2	9.5
21	3:44:01.8	32:01:54.6	S	no	10	2.44	47	2	9.9
22	3:43:58.9	32:00:37.3	E	yes	..	1.58	46	2	10.4
23	3:43:58.2	32:04:01.4	S	no	11	2.08	..	2	8.0
24	3:43:57.2	32:03:01.6	S	no	12	4.90	43	2	9.3
25	3:43:57.0	32:00:49.7	S	no	13	6.40	44	2	10.5
26	3:43:51.1	32:03:20.9	S	no	15	3.08	41	2	9.1
27	3:43:44.0	32:02:46.4	S	no	..	1.50	..	2	9.3
28	3:43:38.3	32:03:05.6	S	no	16	1.50	..	2	8.3
29	3:43:26.5	31:43:14.3	E	no	..	0	..	2	8.5
30	3:42:48.1	31:58:51.0	S	yes	..	1.04	..	2	5.7
31	3:42:06.4	31:47:41.0	S	no	..	1.08	..	2	9.5
32	3:41:57.9	31:47:48.1	E	no	..	0	..	2	9.6
33	3:41:57.1	31:58:27.0	P	yes	..	0.38	..	2	8.1
34	3:41:46.2	31:48:14.0	S	yes	18	0.56	..	2	9.1
35	3:41:44.3	31:56:08.1	E	no	..	0.04	..	2	8.8
36	3:41:43.8	31:57:22.0	P	yes	..	0.36	..	2	8.9
37	3:41:36.2	31:53:48.0	P	no	..	0	..	2	7.4
38	3:41:32.0	31:59:46.0	P	no	..	0.20	..	2	6.5
39	3:41:24.5	31:56:04.0	P	no	..	0	..	2	8.1
40	3:41:17.2	31:53:07.0	P	no	..	0.18	..	2	6.4
41	3:40:49.7	31:48:34.0	S	yes	22	0.78	..	2	8.3
42	3:40:49.6	31:36:35.0	P	yes	..	0.38	..	3	3.4
43	3:40:42.7	31:54:05.0	P	no	..	0.36	..	2	7.7

Table 3.1 (cont'd)

#	RA (J2000.0)	Dec (J2000.0)	Sel. [a] Method	Cross? [b]	SCUBA [c] core	SCUBA [d] flux (Jy)	Spitzer [e] protostar	Ext. [f] Region	Mean Ext. [g] (A_V)
44	3:40:36.4	31:31:08.0	P	yes	..	0.34	..	3	4.5
45	3:40:28.6	31:14:42.3	E	no	..	0	..	3	5.6
46	3:40:22.0	31:59:29.0	P	yes	..	0.16	..	2	7.9
47	3:40:20.9	31:35:50.0	P	no	..	0.38	..	3	5.1
48	3:40:08.7	31:24:57.0	P	no	..	0.14	..	3	4.1
49	3:40:06.3	32:01:33.0	P	yes	..	0.42	..	2	5.7
50	3:40:02.0	31:32:24.0	P	no	..	0	..	3	5.9
51	3:39:58.3	31:27:34.0	P	yes	..	0.44	..	3	4.7
52	3:39:52.6	32:03:52.0	P	yes	..	0	..	2	5.7
53	3:39:47.7	31:35:16.0	P	no	23	0.40	..	3	3.6
54	3:39:42.6	31:43:11.0	P	no	..	0.12	..	3	3.4
55	3:39:38.0	31:31:42.0	P	yes	25	0.42	..	3	5.7
56	3:39:28.5	31:22:36.2	E	no	..	0	..	3	6.4
57	3:38:49.0	31:17:31.0	S	no	..	0	..	3	4.0
58	3:37:53.4	31:23:29.9	E	no	..	0.38	..	3	6.0
59	3:36:39.3	31:11:49.0	S	no	..	0.52	..	4	8.5
60	3:36:23.9	31:11:13.2	E	no	..	0.02	..	4	9.5
61	3:35:55.7	31:10:28.0	P	yes	..	0	..	4	7.1
62	3:35:51.2	31:13:21.0	P	yes	..	0	..	4	5.9
63	3:35:20.8	31:07:05.0	P	yes	..	0.54	..	4	4.4
64	3:34:47.8	31:21:25.0	P	yes	..	0.36	..	5	4.6
65	3:34:02.4	31:21:08.0	S	yes	..	0.76	..	5	7.3
66	3:33:55.0	31:19:25.0	S	no	..	0.64	..	5	7.3
67	3:33:29.2	31:20:11.0	S	yes	..	0.82	..	5	9.2
68	3:33:27.3	31:06:58.7	S	no	28	1.02	40	5	7.5
69	3:33:24.1	31:04:10.4	E	no	..	0	..	5	9.4
70	3:33:22.7	31:18:34.2	E	no	..	0	..	5	9.2
71	3:33:21.7	31:07:22.2	S	no	29	7.16	39	5	7.8
72	3:33:17.9	31:09:27.8	S	yes	30	7.26	38	5	7.6
73	3:33:16.1	31:06:51.6	S	no	32	4.74	36	5	8.4
74	3:33:13.8	31:19:51.3	S	yes	33	1.54	34	5	8.9
75	3:33:05.9	31:04:56.6	S	yes	34	1.84	..	5	7.6
76	3:33:00.6	31:20:50.0	S	yes	..	1.00	..	5	6.4
77	3:32:58.0	31:03:44.0	S	yes	..	1.64	..	5	7.0
78	3:32:52.5	31:01:49.0	S	yes	..	0.96	..	5	9.0
79	3:32:43.2	30:59:60.0	S	yes	..	1.50	..	5	10.8
80	3:32:38.2	30:57:53.0	S	yes	..	0.60	..	5	8.8
81	3:32:33.6	30:52:59.0	S	no	..	0.28	..	5	5.8
82	3:32:31.2	30:57:52.9	E	no	..	0	..	5	10.7
83	3:32:31.0	30:50:29.0	S	yes	..	0.50	..	5	5.0
84	3:32:28.6	31:02:35.0	S	yes	..	0.74	..	5	7.2
85	3:32:27.4	30:59:22.0	S	yes	..	1.44	..	5	11.0
86	3:32:18.0	30:49:45.4	S	yes	37	5.94	33	5	7.2

Table 3.1 (cont'd)

#	RA (J2000.0)	Dec (J2000.0)	Sel. [a] Method	Cross? [b]	SCUBA [c] core	SCUBA [d] flux (Jy)	Spitzer [e] protostar	Ext. [f] Region	Mean Ext. [g] (A_V)
87	3:32:14.5	30:54:45.0	S	yes	..	0.92	..	5	6.9
88	3:31:57.7	30:47:01.0	S	no	..	0.90	..	5	4.0
89	3:31:31.3	30:43:27.2	S	no	..	0.92	..	6	4.9
90	3:31:21.0	30:45:25.6	S	yes	38	2.72	32	6	4.0
91	3:30:46.1	30:52:44.0	S	yes	..	0.88	..	...	3.5
92	3:30:32.0	30:26:24.0	S	yes	..	0.66	..	6	6.6
93	3:30:26.9	30:26:25.2	E	no	..	0	..	6	7.1
94	3:30:15.0	30:23:45.0	S	yes	39	0.90	..	6	6.0
95	3:29:52.0	31:39:03.4	S	yes	40	1.60	31	7	5.9
96	3:29:25.1	31:28:16.1	S	no	41	1.00	..	7	5.1
97	3:29:23.4	31:33:15.7	S	yes	42	1.22	30	7	6.1
98	3:29:18.5	31:23:08.8	S	no	44	1.36	28	7	7.9
99	3:29:18.4	31:25:02.7	S	yes	45	2.02	..	7	7.0
100	3:29:17.2	31:27:44.4	S	no	46	1.30	27	7	5.8
101	3:29:15.0	31:20:32.1	S	no	47	1.56	..	7	9.0
102	3:29:13.2	31:13:55.8	S	no	48	5.62	26	7	6.7
103	3:29:11.3	31:13:07.4	S	no	49	15.88	25	7	6.6
104	3:29:10.5	31:18:25.1	S	no	50	6.40	23	7	9.4
105	3:29:10.2	31:21:43.0	S	no	51	4.14	..	7	10.0
106	3:29:09.9	31:13:31.1	S	yes	52	27.86	22	7	7.0
107	3:29:08.8	31:15:12.8	S	no	53	5.08	..	7	8.1
108	3:29:07.4	31:21:48.4	S	no	55	3.90	..	7	10.5
109	3:29:06.8	31:17:18.3	S	no	56	1.98	..	7	9.2
110	3:29:06.5	31:15:36.3	S	no	57	6.24	..	7	8.6
111	3:29:03.7	31:14:47.7	S	no	60	2.96	21	7	8.5
112	3:29:03.2	31:15:53.6	S	no	61	14.68	20	7	9.0
113	3:29:01.4	31:20:23.1	S	no	62	6.32	19	7	10.3
114	3:29:00.8	31:22:34.9	E	no	..	0	..	7	11.5
115	3:29:00.2	31:11:53.0	S	no	64	0.36	18	7	8.2
116	3:28:59.5	31:21:28.7	S	no	65	4.58	17	7	10.7
117	3:28:57.3	30:44:28.9	E	no	..	0.48	..	8	5.9
118	3:28:55.3	31:14:27.9	S	yes	66	7.78	15	7	8.8
119	3:28:51.4	31:10:57.0	E	no	..	0	..	7	10.1
120	3:28:47.6	30:33:21.1	E	no	..	0	..	8	5.6
121	3:28:42.5	31:06:13.1	S	no	67	1.62	..	7	5.8
122	3:28:40.1	31:17:48.4	S	no	68	2.86	13	7	8.1
123	3:28:39.1	31:18:24.1	S	no	69	3.22	..	7	8.1
124	3:28:38.8	31:05:54.3	S	no	70	1.56	12	7	5.4
125	3:28:36.7	31:13:23.6	S	yes	71	2.28	11	7	8.0
126	3:28:34.5	31:06:59.3	S	no	72	0.42	10	7	5.2
127	3:28:34.4	30:18:59.9	E	yes	..	0.18	..	9	6.3
128	3:28:32.3	31:10:58.7	S	yes	73	1.16	9	7	6.3
129	3:28:08.4	30:05:37.0	P	yes	..	0	..	9	4.5

Table 3.1 (cont'd)

#	RA (J2000.0)	Dec (J2000.0)	Sel. [a] Method	Cross? [b]	SCUBA [c] core	SCUBA [d] flux (Jy)	Spitzer [e] protostar	Ext. [f] Region	Mean Ext. [g] (A_V)
130	3:27:57.1	30:07:57.0	P	yes	..	0.36	..	9	6.6
131	3:27:55.6	30:05:40.0	P	yes	..	0	..	9	4.9
132	3:27:51.7	30:11:06.0	P	yes	..	0.18	..	9	7.0
133	3:27:48.3	30:12:08.0	S	yes	75	2.30	8	9	7.7
134	3:27:42.7	30:12:24.5	S	no	76	2.82	7	9	9.3
135	3:27:39.0	30:12:53.6	S	no	78	2.80	6	9	10.1
136	3:27:37.9	30:13:53.2	S	yes	79	1.20	5	9	9.5
137	3:27:36.8	30:11:17.1	E	no	..	0	..	9	9.9
138	3:27:35.6	30:10:12.0	P	yes	..	0	..	9	8.5
139	3:27:29.5	30:15:09.0	S	no	..	0.84	..	9	7.9
140	3:27:27.6	29:58:54.0	P	yes	..	0	..	9	3.3
141	3:27:18.7	30:17:12.0	S	no	..	0.86	..	9	4.1
142	3:27:00.4	30:24:01.0	S	no	..	0.82	..	...	2.0
143	3:26:37.2	30:15:18.7	S	yes	80	1.08	4	9	3.0
144	3:26:12.9	30:30:34.8	E	no	..	0.16	..	10	5.2
145	3:26:02.5	30:37:58.0	P	no	..	0.20	..	10	3.7
146	3:25:49.3	30:42:15.1	S	no	82	2.58	..	10	5.4
147	3:25:46.3	30:44:14.1	S	no	..	0.66	..	10	5.0
148	3:25:38.9	30:43:59.8	S	no	83	5.12	3	10	5.4
149	3:25:36.0	30:45:10.8	S	no	84	11.16	2	10	5.4
150	3:25:25.7	30:45:01.6	S	no	85	3.34	..	10	5.8
151	3:25:23.7	30:21:07.0	P	no	..	0	..	11	6.1
152	3:25:22.5	30:45:06.5	S	no	86	4.88	1	10	5.9
153	3:25:20.2	30:32:31.0	P	yes	..	0	..	...	2.2
154	3:25:17.1	30:43:20.7	E	no	..	0	..	10	5.9
155	3:25:05.4	30:24:13.0	P	no	..	0	..	11	4.2
156	3:24:51.0	30:21:57.3	E	no	..	0	..	11	6.2
157	3:24:33.7	30:22:07.0	P	no	..	0.10	..	11	5.1

[a]Target selection was based on SCUBA cores (S), potential SCUBA cores (SA), Palomar plate candidates (P), and 2MASS extinction structures (E).

[b]Were offset positions observed?

[c]SCUBA core reference number (see Appendix)

[d]Total SCUBA flux within the IRAM beam (derived from the 6″ map of Kirk, Johnstone, & Di Francesco, 2006).

[e]Spitzer reference number (from Jørgensen et al., 2007)

[f]Extinction region number (from Kirk, Johnstone, & Di Francesco, 2006)

[g]Mean extinction within the IRAM beam.

Table 3.2. Detection rates for the target selection methods.

Tracer	SCUBA	Palomar	2MASS	Total[a]
N_2H^+ (1-0)	84% (75/89)	42% (18/43)	14% (3/22)	62% (96/154)
$C^{18}O$ (2-1)	98% (87/89)	93% (40/43)	95% (21/22)	96% (148/154)

[a]Several targets in the Palomar- and 2MASS- selected lists lie close to a SCUBA-selected target and appear to sample the same object (one and two targets respectively). We only count these targets once for both these statistics and the subsequent analysis.

Table 3.3. Parameters of Spectral Fitting for N_2H^+

#[a]	RA[b] off.	dec[b] off.	V_C[c,d] (km s^{-1})	ΔV[c] (km s^{-1})	error[c] (m s^{-1})	opt.[c] depth	error[c]	rms[c] base(K)	rms[c] fit(K)	$\int$ I [e] (K km s^{-1})	sec.[f] fit ?
1	0	0	...	...	...	...	...	0.15	...	...	...
2	0	0	...	...	...	...	...	0.15	...	...	...
3	0	0	10.22	0.25	5	6.53	0.64	0.08	0.10	2.38	yes
3	0	-1	10.26	0.40	6	5.41	0.48	0.12	0.15	5.54	yes
3	0	1	10.21	0.28	12	1.75	1.19	0.12	0.11	1.40	yes
3	-1	0	10.23	0.36	7	5.29	0.60	0.12	0.17	3.71	yes
3	1	0	10.22	0.28	8	0.88	0.50	0.12	0.11	0.98	yes
4	0	0	10.24	0.45	5	6.30	0.33	0.10	0.18	7.39	yes
5	0	0	10.20	0.26	11	4.28	1.24	0.15	0.17	1.94	yes
5	0	-1	10.10	0.31	12	2.86	1.20	0.14	0.13	1.64	yes
5	0	1	10.22	0.23	5	6.27	0.75	0.13	0.16	2.11	yes
5	-1	0	10.10	0.27	23	7.97	3.62	0.13	0.14	0.64	yes
5	1	0	10.25	0.25	7	4.34	0.98	0.14	0.14	2.11	yes
6	0	0	10.37	0.41	7	6.19	0.55	0.10	0.11	4.38	yes
7	0	0	10.43	0.38	30	3.69	2.20	0.14	0.15	1.08	no
7	0	-1	...	...	...	...	...	0.14	...	...	...
7	0	1	10.34	0.42	48	7.78	3.81	0.13	0.12	0.68	no
7	-1	0	...	...	...	...	...	0.13	...	...	...
7	1	0	10.35	0.42	11	6.21	0.93	0.14	0.14	3.35	yes
8	0	0	10.07	0.27	14	0.38	0.04	0.14	0.14	1.07	yes
8	0	-1	...	...	...	...	...	0.14	...	...	...
8	0	1	10.07	0.23	8	3.96	1.07	0.13	0.14	1.66	yes
8	-1	0	...	...	...	...	...	0.14	...	...	...
8	1	0	10.01	0.18	5	2.29	0.86	0.14	0.15	1.39	yes
9	0	0	...	...	...	...	...	0.23	...	...	...
10	0	0	...	...	...	...	...	0.14	...	...	...
11	0	0	...	...	...	...	...	0.15	...	...	...
12	0	0	10.76	0.21	10	0.58	1.08	0.14	0.14	1.10	yes
12	0	-1	10.81	0.18	8	1.80	1.30	0.11	0.11	0.89	yes
12	0	1	10.72	0.20	9	0.16	2.77	0.11	0.12	0.81	yes
12	-1	0	...	...	...	...	...	0.11	...	...	...
12	1	0	10.72	0.19	8	3.63	1.27	0.12	0.10	1.05	yes
13	0	0	10.99	0.29	9	4.08	0.93	0.14	0.16	2.43	yes
13	0	-1	10.83	0.26	5	3.67	0.54	0.11	0.16	3.14	yes
13	0	1	11.05	0.20	13	4.82	2.16	0.11	0.11	0.67	yes
13	-1	0	10.84	0.25	19	1.25	0.77	0.11	0.10	0.54	yes
13	1	0	11.00	0.31	9	0.10	0.61	0.11	0.13	1.60	yes
14	0	0	...	...	...	...	...	0.12	...	...	...
15	0	0	8.94	0.29	6	4.87	0.67	0.11	0.12	2.96	yes
16	0	0	9.87	0.74	32	1.56	0.65	0.11	0.13	3.15	yes
16	0	-1	9.57	0.39	22	0.32	1.64	0.12	0.13	1.62	yes
16	0	1	...	...	...	...	...	0.13	...	...	...
16	-1	0	...	...	...	...	...	0.13	...	...	...

Table 3.3 (cont'd)

#[a]	RA[b] off.	dec[b] off.	V_C[c,d] (km s^{-1})	ΔV[c] (km s^{-1})	error[c] (m s^{-1})	opt.[c] depth	error[c]	rms[c] base(K)	rms[c] fit(K)	$\int$ I [e] (K km s^{-1})	sec.[f] fit ?
16	1	0	9.67	0.49	53	3.47	2.07	0.12	0.13	1.18	no
17	0	0	...	...	...	...	...	0.11	...	...	...
18	0	0	9.92	0.52	13	3.96	0.63	0.10	0.15	3.01	yes
18	0	-1	9.99	0.37	17	2.03	1.12	0.13	0.14	1.89	yes
18	0	1	9.87	0.46	23	3.05	1.36	0.13	0.13	1.83	yes
18	-1	0	9.61	0.66	48	0.10	1.56	0.13	0.12	1.22	yes
18	1	0	9.74	0.59	105	0.25	0.10	0.12	0.13	0.93	no
19	0	0	8.55	0.35	4	4.11	0.36	0.10	0.13	4.79	yes
20	0	0	8.57	0.68	19	2.19	0.40	0.11	0.27	5.48	yes
21	0	0	9.02	0.65	9	2.05	0.29	0.10	0.13	6.41	yes
22	0	0	8.88	0.65	53	6.69	1.74	0.08	0.08	1.15	no
22	0	0	8.11	0.24	23	3.45	1.13	0.08	0.08	1.15	no
22	0	-1	8.16	0.28	8	0.54	0.01	0.12	0.14	1.97	yes
22	0	1	9.28	0.24	14	3.88	1.71	0.12	0.13	1.42	yes
22	-1	0	8.95	0.57	12	2.26	0.52	0.14	0.19	5.21	yes
22	1	0	...	...	...	...	...	0.12	...	...	...
23	0	0	8.27	0.41	0	0.23	0.00	0.10	0.15	3.99	yes
24	0	0	8.74	0.46	8	3.02	0.48	0.10	0.11	4.06	yes
25	0	0	9.06	0.48	6	5.13	0.38	0.11	0.13	6.90	yes
26	0	0	8.56	0.42	4	4.24	0.26	0.10	0.14	7.29	yes
27	0	0	8.24	0.34	12	1.27	0.01	0.10	0.11	3.23	yes
27	0	0	8.70	0.27	6	2.97	0.36	0.10	0.11	3.23	yes
28	0	0	8.46	0.58	15	6.07	0.91	0.11	0.16	3.33	yes
29	0	0	...	...	...	...	...	0.12	...	...	...
30	0	0	8.84	0.22	14	2.92	1.86	0.13	0.13	0.78	yes
30	0	-1	...	...	...	...	...	0.13	...	...	...
30	0	1	...	...	...	...	...	0.13	...	...	...
30	-1	0	8.86	0.19	13	3.37	1.77	0.12	0.11	0.82	yes
30	1	0	...	...	...	...	...	0.12	...	...	...
31	0	0	...	...	...	...	...	0.12	...	...	...
32	0	0	...	...	...	...	...	0.08	...	...	...
33	0	0	9.45	0.35	105	0.79	0.10	0.14	0.15	0.60	no
33	0	-1	...	...	...	...	...	0.12	...	...	...
33	0	1	9.40	0.21	11	12.04	2.87	0.11	0.10	0.79	yes
33	-1	0	9.41	0.23	25	0.24	19.08	0.11	0.10	0.28	no
33	1	0	9.40	0.35	2	1.17	1.28	0.11	0.13	0.64	yes
34	0	0	8.21	0.25	5	0.81	0.00	0.12	0.12	0.52	no
34	0	-1	8.19	0.22	21	0.10	1.10	0.12	0.12	0.36	no
34	0	1	...	...	...	...	...	0.12	...	...	...
34	-1	0	...	...	...	...	...	0.12	...	...	...
34	1	0	8.24	0.20	11	3.44	1.62	0.12	0.10	0.77	no
35	0	0	...	...	...	...	...	0.11	...	...	...
36	0	0	9.39	0.20	5	4.32	0.76	0.14	0.15	2.59	yes

Table 3.3 (cont'd)

#[a]	RA[b] off.	dec[b] off.	V_C[c,d] (km s^{-1})	ΔV[c] (km s^{-1})	error[c] (m s^{-1})	opt.[c] depth	error[c]	rms[c] base(K)	rms[c] fit(K)	$\int$ I [e] (K km s^{-1})	sec.[f] fit ?
36	0	-1	9.39	0.18	10	2.19	1.55	0.12	0.13	0.68	yes
36	0	1	9.43	0.19	5	4.21	0.75	0.11	0.12	1.95	yes
36	-1	0	9.42	0.19	6	3.91	0.98	0.12	0.14	1.49	yes
36	1	0	9.41	0.22	4	6.70	0.66	0.11	0.12	2.80	yes
37	0	0	...	...	...	...	...	0.14	...	...	...
38	0	0	...	...	...	...	...	0.15	...	...	...
39	0	0	...	...	...	...	...	0.14	...	...	...
40	0	0	...	...	...	...	...	0.14	...	...	...
41	0	0	8.45	0.23	9	4.71	1.16	0.12	0.16	1.47	yes
41	0	-1	...	...	...	...	...	0.15	...	...	...
41	0	1	8.40	0.28	18	4.62	2.09	0.14	0.14	1.18	yes
41	-1	0	...	...	...	...	...	0.14	...	...	...
41	1	0	8.39	0.20	12	1.17	1.60	0.13	0.16	1.01	yes
42	0	0	...	...	...	...	...	0.14	...	...	...
42	0	-1	...	...	...	...	...	0.11	...	...	...
42	0	1	...	...	...	...	...	0.13	...	...	...
42	-1	0	...	...	...	...	...	0.12	...	...	...
42	1	0	...	...	...	...	...	0.12	...	...	...
43	0	0	...	...	...	...	...	0.14	...	...	...
44	0	0	...	...	...	...	...	0.14	...	...	...
44	0	-1	...	...	...	...	...	0.12	...	...	...
44	0	1	...	...	...	...	...	0.13	...	...	...
44	-1	0	...	...	...	...	...	0.12	...	...	...
44	1	0	...	...	...	...	...	0.13	...	...	...
45	0	0	...	...	...	...	...	0.12	...	...	...
46	0	0	...	...	...	...	...	0.07	...	...	...
46	0	-1	...	...	...	...	...	0.07	...	...	...
46	0	1	...	...	...	...	...	0.07	...	...	...
46	-1	0	...	...	...	...	...	0.08	...	...	...
46	1	0	...	...	...	...	...	0.07	...	...	...
47	0	0	...	...	...	...	...	0.13	...	...	...
48	0	0	...	...	...	...	...	0.13	...	...	...
49	0	0	...	...	...	...	...	0.14	...	...	...
49	0	-1	...	...	...	...	...	0.12	...	...	...
49	0	1	7.90	0.22	10	5.13	1.47	0.11	0.11	1.14	yes
49	-1	0	...	...	...	...	...	0.12	...	...	...
49	1	0	7.87	0.20	17	0.74	0.78	0.12	0.10	0.68	no
50	0	0	...	...	...	...	...	0.13	...	...	...
51	0	0	...	...	...	...	...	0.09	...	...	...
51	0	-1	...	...	...	...	...	0.08	...	...	...
51	0	1	...	...	...	...	...	0.08	...	...	...
51	-1	0	...	...	...	...	...	0.08	...	...	...
51	1	0	...	...	...	...	...	0.08	...	...	...

Table 3.3 (cont'd)

#[a]	RA[b] off.	dec[b] off.	V_C[c,d] (km s^{-1})	ΔV[c] (km s^{-1})	error[c] (m s^{-1})	opt.[c] depth	error[c]	rms[c] base(K)	rms[c] fit(K)	$\int$ I [e] (K km s^{-1})	sec.[f] fit ?
52	0	0	...	...	...	...	...	0.14	...	...	...
52	0	-1	...	...	...	...	...	0.12	...	...	...
52	0	1	...	...	...	...	...	0.12	...	...	...
52	-1	0	...	...	...	...	...	0.12	...	...	...
52	1	0	...	...	...	...	...	0.12	...	...	...
53	0	0	10.05	0.34	39	0.10	1.93	0.13	0.13	0.59	no
54	0	0	...	...	...	...	...	0.12	...	...	...
55	0	0	9.77	0.34	21	0.10	1.25	0.09	0.09	0.45	yes
55	0	-1	9.79	0.37	29	0.10	1.55	0.09	0.07	0.39	no
55	0	1	9.82	0.28	16	0.41	1.43	0.08	0.08	0.66	yes
55	-1	0	...	...	...	...	...	0.09	...	...	...
55	1	0	9.81	0.35	19	1.52	1.49	0.09	0.09	0.83	yes
56	0	0	...	...	...	...	...	0.12	...	...	...
57	0	0	...	...	...	...	...	0.13	...	...	...
58	0	0	...	...	...	...	...	0.11	...	...	...
59	0	0	...	...	...	...	...	0.13	...	...	...
60	0	0	...	...	...	...	...	0.08	...	...	...
61	0	0	...	...	...	...	...	0.14	...	...	...
61	0	-1	...	...	...	...	...	0.12	...	...	...
61	0	1	...	...	...	...	...	0.12	...	...	...
61	-1	0	...	...	...	...	...	0.12	...	...	...
61	1	0	...	...	...	...	...	0.13	...	...	...
62	0	0	...	...	...	...	...	0.13	...	...	...
62	0	-1	...	...	...	...	...	0.12	...	...	...
62	0	1	...	...	...	...	...	0.12	...	...	...
62	-1	0	...	...	...	...	...	0.12	...	...	...
62	1	0	...	...	...	...	...	0.12	...	...	...
63	0	0	7.01	0.33	29	0.10	20.01	0.06	0.06	0.29	no
63	0	-1	6.99	0.25	18	0.10	4.71	0.06	0.06	0.40	yes
63	0	1	7.07	0.26	22	3.36	2.18	0.06	0.06	0.35	no
63	-1	0	...	...	...	...	...	0.06	...	...	...
63	1	0	...	...	...	...	...	0.07	...	...	...
64	0	0	...	...	...	...	...	0.13	...	...	...
64	0	-1	...	...	...	...	...	0.11	...	...	...
64	0	1	...	...	...	...	...	0.12	...	...	...
64	-1	0	...	...	...	...	...	0.11	...	...	...
64	1	0	...	...	...	...	...	0.06	...	...	...
65	0	0	...	...	...	...	...	0.13	...	...	...
65	0	-1	...	...	...	...	...	0.12	...	...	...
65	0	1	...	...	...	...	...	0.13	...	...	...
65	-1	0	...	...	...	...	...	0.13	...	...	...
65	1	0	...	...	...	...	...	0.13	...	...	...
66	0	0	...	...	...	...	...	0.13	...	...	...

Table 3.3 (cont'd)

#[a]	RA[b] off.	dec[b] off.	V_C[c,d] (km s^{-1})	ΔV[c] (km s^{-1})	error[c] (m s^{-1})	opt.[c] depth	error[c]	rms[c] base(K)	rms[c] fit(K)	$\int$ I [e] (K km s^{-1})	sec.[f] fit ?
67	0	0	6.23	0.37	24	0.10	0.52	0.13	0.11	0.84	yes
67	0	-1	...	...	...	...	...	0.15	...	...	...
67	0	1	6.32	0.27	13	0.10	1.78	0.13	0.12	1.15	yes
67	-1	0	6.39	0.42	52	0.10	2.66	0.14	0.13	0.85	no
67	1	0	6.22	0.34	17	1.22	1.26	0.14	0.13	1.82	yes
68	0	0	6.92	0.55	8	0.19	0.01	0.11	0.15	4.25	yes
69	0	0	...	...	...	...	...	0.12	...	...	...
70	0	0	...	...	...	...	...	0.09	...	...	...
71	0	0	6.66	0.87	8	8.07	0.23	0.11	0.19	14.06	yes
72	0	0	6.27	0.76	6	5.93	0.20	0.11	0.21	13.39	yes
72	0	-1	6.55	0.56	8	8.79	0.50	0.12	0.16	7.32	yes
72	0	1	6.05	0.63	9	5.34	0.35	0.13	0.16	8.00	yes
72	-1	0	6.29	0.77	15	1.75	0.39	0.12	0.14	5.79	yes
72	1	0	6.21	0.72	14	4.70	0.44	0.12	0.19	6.51	yes
73	0	0	6.43	0.56	3	13.04	0.09	0.11	0.19	10.68	yes
74	0	0	6.84	0.32	4	9.10	0.46	0.10	0.17	4.53	yes
74	0	-1	6.77	0.34	7	0.26	0.01	0.12	0.17	2.92	yes
74	0	1	6.88	0.38	8	4.99	0.73	0.12	0.16	3.47	yes
74	-1	0	6.79	0.35	7	4.71	0.64	0.12	0.15	3.74	yes
74	1	0	6.76	0.33	30	4.14	3.06	0.13	0.13	1.01	no
75	0	0	6.63	0.44	5	12.25	0.68	0.10	0.20	6.17	yes
75	0	-1	6.65	0.35	9	4.97	0.81	0.12	0.12	2.91	yes
75	0	1	6.57	0.49	9	7.39	0.73	0.12	0.22	4.88	yes
75	-1	0	6.59	0.42	4	13.48	0.18	0.12	0.20	5.90	yes
75	1	0	6.64	0.32	5	6.12	0.59	0.12	0.18	4.69	yes
76	0	0	6.51	0.49	37	9.05	3.49	0.13	0.14	1.58	yes
76	0	-1	6.74	0.28	19	0.10	0.17	0.13	0.15	1.63	no
76	0	-1	6.22	0.34	35	1.89	0.82	0.13	0.15	1.63	no
76	0	1	...	...	...	...	...	0.14	...	...	...
76	-1	0	6.50	0.67	65	0.10	1.08	0.13	0.12	0.80	no
76	1	0	6.66	0.44	25	2.43	1.39	0.13	0.13	1.70	yes
77	0	0	6.64	0.32	6	7.72	0.72	0.13	0.20	4.30	yes
77	0	-1	6.65	0.31	7	10.65	1.02	0.13	0.18	3.36	yes
77	0	1	6.62	0.28	6	4.98	0.72	0.13	0.14	2.89	yes
77	-1	0	6.68	0.26	6	9.73	1.05	0.13	0.13	2.91	yes
77	1	0	6.62	0.39	8	9.22	0.91	0.13	0.16	4.03	yes
78	0	0	6.67	0.27	22	4.31	1.73	0.13	0.13	0.99	no
78	0	-1	6.70	0.25	26	0.10	3.48	0.13	0.15	0.81	no
78	0	1	6.58	0.32	105	1.03	0.10	0.12	0.13	1.46	yes
78	-1	0	6.57	0.43	24	2.72	1.23	0.12	0.13	1.39	yes
78	1	0	...	...	...	...	...	0.14	...	...	...
79	0	0	6.82	0.38	9	9.65	1.05	0.13	0.17	4.04	yes
79	0	-1	6.84	0.41	8	13.79	1.29	0.09	0.13	2.93	yes

Table 3.3 (cont'd)

#[a]	RA[b] off.	dec[b] off.	V_C[c,d] (km s^{-1})	ΔV[c] (km s^{-1})	error[c] (m s^{-1})	opt.[c] depth	error[c]	rms[c] base(K)	rms[c] fit(K)	$\int$ I [e] (K km s^{-1})	sec.[f] fit ?
79	0	1	6.79	0.34	9	6.16	0.94	0.10	0.12	2.45	yes
79	-1	0	6.59	0.42	14	5.08	0.92	0.09	0.09	1.11	yes
79	1	0	6.80	0.29	5	9.17	0.74	0.10	0.13	3.23	yes
80	0	0	...	...	...	...	...	0.14	...	...	...
80	0	-1	6.10	0.32	24	0.10	1.09	0.13	0.14	0.88	no
80	0	1	...	...	...	...	...	0.13	...	...	...
80	-1	0	6.24	0.33	33	4.86	2.88	0.12	0.12	0.99	yes
80	1	0	6.99	0.31	26	0.95	2.13	0.13	0.13	1.08	no
81	0	0	...	...	...	...	...	0.14	...	...	...
82	0	0	...	...	...	...	...	0.08	...	...	...
83	0	0	...	...	...	...	...	0.14	...	...	...
83	0	-1	...	...	...	...	...	0.12	...	...	...
83	0	1	6.60	0.32	105	0.87	0.10	0.13	0.12	0.42	no
83	-1	0	...	...	...	...	...	0.13	...	...	...
83	1	0	6.56	0.31	15	0.10	2.79	0.13	0.12	1.17	yes
84	0	0	6.61	0.30	6	0.10	0.45	0.13	0.11	1.57	yes
84	0	-1	6.65	0.27	7	4.61	0.72	0.14	0.19	3.11	yes
84	0	1	...	...	...	...	...	0.12	...	...	...
84	-1	0	...	...	...	...	...	0.13	...	...	...
84	1	0	...	...	...	...	...	0.14	...	...	...
85	0	0	6.41	0.41	6	14.60	0.32	0.12	0.15	3.37	yes
85	0	-1	6.43	0.39	8	13.14	0.39	0.13	0.15	2.67	yes
85	0	1	6.33	0.51	47	5.89	3.33	0.13	0.14	0.71	no
85	-1	0	6.43	0.39	20	3.82	1.67	0.13	0.14	1.29	yes
85	1	0	6.44	0.39	5	15.56	0.35	0.13	0.18	3.91	yes
86	0	0	6.90	0.60	5	5.35	0.25	0.11	0.16	9.62	yes
86	0	-1	6.89	0.44	8	5.08	0.51	0.12	0.17	5.05	yes
86	0	1	7.01	0.56	16	3.27	0.76	0.13	0.14	3.72	yes
86	-1	0	6.78	0.52	5	8.14	0.37	0.12	0.18	9.05	yes
86	1	0	6.91	0.58	21	1.76	0.85	0.13	0.13	2.91	yes
87	0	0	5.90	0.31	24	7.13	2.86	0.13	0.14	1.10	no
87	0	-1	5.77	0.34	26	0.10	0.94	0.12	0.13	0.68	no
87	0	1	...	...	...	...	...	0.13	...	...	...
87	-1	0	...	...	...	...	...	0.14	...	...	...
87	1	0	5.88	0.21	13	8.10	2.35	0.12	0.12	0.94	yes
88	0	0	...	...	...	...	...	0.14	...	...	...
89	0	0	...	...	...	...	...	0.11	...	...	...
90	0	0	6.93	0.38	4	5.65	0.31	0.11	0.18	7.75	yes
90	0	-1	6.76	0.42	2	0.26	0.07	0.12	0.12	3.17	yes
90	0	1	6.96	0.44	8	4.06	0.47	0.12	0.16	5.94	yes
90	-1	0	7.01	0.60	12	2.06	0.45	0.12	0.16	4.60	yes
90	1	0	6.97	0.31	14	3.78	1.29	0.12	0.12	1.64	yes
91	0	0	7.83	0.37	11	8.17	1.17	0.14	0.15	3.19	yes

Table 3.3 (cont'd)

#[a]	RA[b] off.	dec[b] off.	V_C[c,d] (km s^{-1})	ΔV[c] (km s^{-1})	error[c] (m s^{-1})	opt.[c] depth	error[c]	rms[c] base(K)	rms[c] fit(K)	$\int$ I [e] (K km s^{-1})	sec.[f] fit ?
91	0	-1	7.72	0.47	15	0.29	0.13	0.12	0.13	2.15	yes
91	0	1	7.84	0.37	1	0.12	0.00	0.13	0.13	1.70	yes
91	-1	0	7.72	0.44	16	4.72	1.17	0.12	0.13	2.44	yes
91	1	0	7.86	0.37	22	2.63	1.46	0.12	0.11	1.54	yes
92	0	0	6.08	0.37	3	13.96	0.17	0.13	0.21	6.05	yes
92	0	-1	6.00	0.36	7	3.60	0.62	0.12	0.18	3.57	yes
92	0	1	6.06	0.37	8	4.67	0.71	0.13	0.14	3.71	yes
92	-1	0	5.95	0.46	8	5.79	0.69	0.12	0.18	4.10	yes
92	1	0	6.13	0.31	6	9.53	0.85	0.13	0.19	4.46	yes
93	0	0	5.94	0.57	48	0.10	0.81	0.08	0.08	0.44	no
94	0	0	5.90	0.38	8	2.51	0.50	0.13	0.20	4.71	yes
94	0	-1	5.79	0.30	5	5.11	0.51	0.13	0.16	4.60	yes
94	0	1	5.94	0.25	6	2.21	0.60	0.13	0.15	3.21	yes
94	-1	0	5.76	0.34	15	1.50	1.23	0.12	0.12	1.46	yes
94	1	0	5.95	0.33	6	3.03	0.48	0.13	0.18	4.26	yes
95	0	0	8.15	0.35	4	7.30	0.43	0.11	0.24	6.28	yes
95	0	-1	8.17	0.24	4	5.25	0.57	0.12	0.17	3.35	yes
95	0	1	8.23	0.27	5	3.26	0.52	0.12	0.14	3.86	yes
95	-1	0	8.16	0.38	8	3.57	0.59	0.12	0.21	4.25	yes
95	1	0	8.16	0.32	0	0.12	0.00	0.12	0.16	3.63	yes
96	0	0	7.54	0.49	6	7.27	0.50	0.10	0.22	5.62	yes
97	0	0	7.50	0.30	3	7.27	0.41	0.11	0.15	5.92	yes
97	0	-1	7.51	0.30	13	5.69	1.38	0.12	0.13	1.79	yes
97	0	1	7.54	0.30	4	3.04	0.38	0.12	0.16	3.36	yes
97	-1	0	7.49	0.29	5	4.46	0.50	0.12	0.13	3.53	yes
97	1	0	7.45	0.31	5	7.32	0.63	0.12	0.14	4.20	yes
98	0	0	7.47	0.40	9	3.78	0.62	0.10	0.14	2.73	yes
99	0	0	7.54	0.17	16	10.79	4.34	0.10	0.12	3.36	yes
99	0	0	6.91	0.42	6	3.22	0.18	0.10	0.12	3.36	yes
99	0	-1	...	...	...	...	...	0.13	...	...	...
99	0	1	7.12	0.50	25	3.21	0.40	0.12	0.11	4.01	yes
99	0	1	7.50	0.24	7	0.10	3.18	0.12	0.11	4.01	yes
99	-1	0	7.01	0.30	18	1.58	1.51	0.11	0.13	1.21	yes
99	1	0	7.23	1.22	165	0.10	1.41	0.12	0.11	1.02	no
100	0	0	7.52	0.32	4	4.40	0.38	0.11	0.13	5.33	yes
101	0	0	8.21	0.86	21	0.10	0.15	0.09	0.11	2.47	yes
102	0	0	7.84	0.60	5	5.44	0.25	0.11	0.15	10.15	yes
103	0	0	7.15	1.25	36	2.27	0.37	0.11	0.12	7.93	yes
103	0	0	6.79	0.54	32	1.37	0.01	0.11	0.12	7.93	yes
104	0	0	8.59	0.53	5	4.34	0.24	0.11	0.21	10.40	yes
105	0	0	...	...	...	...	...	0.11	...	...	...
106	0	0	7.49	0.97	4	5.59	0.01	0.05	0.09	11.37	yes
106	0	0	6.73	0.70	8	1.82	0.20	0.05	0.09	11.37	yes

Table 3.3 (cont'd)

#[a]	RA[b] off.	dec[b] off.	V_C[c,d] (km s^{-1})	ΔV[c] (km s^{-1})	error[c] (m s^{-1})	opt.[c] depth	error[c]	rms[c] base(K)	rms[c] fit(K)	$\int$ I [e] (K km s^{-1})	sec.[f] fit ?
106	0	-1	7.59	0.92	105	0.19	0.10	0.12	0.13	3.84	yes
106	0	-1	6.73	0.55	105	1.70	0.10	0.12	0.13	3.84	yes
106	0	1	7.81	0.60	12	8.71	0.50	0.13	0.17	12.99	yes
106	0	1	6.94	0.70	18	3.56	0.52	0.13	0.17	12.99	yes
106	-1	0	7.71	0.52	7	5.28	0.01	0.12	0.14	5.80	yes
106	-1	0	6.55	0.51	1	0.10	0.00	0.12	0.14	5.80	yes
106	1	0	6.93	0.75	105	1.97	0.10	0.12	0.15	12.49	yes
106	1	0	7.75	0.59	105	6.98	0.10	0.12	0.15	12.49	yes
107	0	0	7.93	0.74	6	5.11	0.07	0.11	0.20	16.10	yes
107	0	0	7.24	0.31	7	19.08	1.05	0.11	0.20	16.10	yes
108	0	0	...	...	...	...	...	0.11	...	...	...
109	0	0	8.48	0.53	7	2.97	0.31	0.11	0.18	6.48	yes
110	0	0	7.97	0.91	7	2.40	0.13	0.12	0.22	16.60	yes
111	0	0	6.82	0.80	105	2.28	0.10	0.10	0.16	17.67	yes
111	0	0	7.74	0.86	105	5.10	0.10	0.10	0.16	17.67	yes
112	0	0	8.40	0.68	4	4.66	0.14	0.12	0.17	18.46	yes
113	0	0	7.97	0.60	5	4.87	0.20	0.11	0.18	11.84	yes
114	0	0	...	...	...	...	...	0.09	...	...	...
115	0	0	7.16	0.64	7	3.54	0.26	0.11	0.19	8.50	yes
116	0	0	7.83	0.77	9	2.18	0.23	0.12	0.14	9.89	yes
117	0	0	...	...	...	...	...	0.12	...	...	...
118	0	0	7.34	0.58	9	4.26	0.36	0.11	0.15	12.37	yes
118	0	0	7.74	1.06	17	6.49	0.18	0.11	0.15	12.37	yes
118	0	-1	7.22	0.39	3	3.93	0.24	0.13	0.26	9.29	yes
118	0	1	7.39	0.74	11	5.74	0.23	0.12	0.16	12.16	yes
118	0	1	8.20	0.74	37	7.43	0.41	0.12	0.16	12.16	yes
118	-1	0	7.66	0.78	14	5.10	0.38	0.12	0.15	8.37	yes
118	1	0	7.17	0.58	17	3.77	0.39	0.12	0.12	5.02	yes
118	1	0	8.11	0.58	31	8.42	1.53	0.12	0.12	5.02	yes
119	0	0	...	...	...	...	...	0.08	...	...	...
120	0	0	...	...	...	...	...	0.11	...	...	...
121	0	0	7.22	0.38	4	6.22	0.36	0.10	0.14	6.03	yes
122	0	0	7.98	0.53	4	7.49	0.27	0.10	0.18	10.32	yes
123	0	0	8.19	0.48	4	10.59	0.37	0.10	0.19	9.12	yes
124	0	0	7.04	0.34	4	7.05	0.40	0.11	0.17	6.34	yes
125	0	0	7.28	0.50	105	0.10	0.10	0.10	0.21	5.76	yes
125	0	-1	7.29	0.46	19	0.62	1.03	0.11	0.13	1.80	yes
125	0	1	7.25	0.44	9	0.10	0.63	0.12	0.12	1.91	yes
125	-1	0	7.39	0.47	7	9.14	0.63	0.12	0.17	6.26	yes
125	1	0	7.36	0.39	40	1.04	2.45	0.12	0.12	0.67	no
126	0	0	6.84	0.31	7	3.37	0.57	0.11	0.12	3.53	yes
127	0	0	5.54	0.32	11	1.89	0.95	0.12	0.12	1.77	yes
127	0	-1	5.47	0.26	13	0.10	1.27	0.12	0.11	0.84	yes

Table 3.3 (cont'd)

#[a]	RA[b] off.	dec[b] off.	V_C[c,d] (km s^{-1})	ΔV[c] (km s^{-1})	error[c] (m s^{-1})	opt.[c] depth	error[c]	rms[c] base(K)	rms[c] fit(K)	$\int$ I [e] (K km s^{-1})	sec.[f] fit ?
127	0	1	5.51	0.37	10	0.97	0.79	0.12	0.14	2.31	yes
127	-1	0	5.57	0.22	19	3.51	2.84	0.17	0.16	0.92	no
127	1	0	5.44	0.29	12	3.67	1.23	0.12	0.13	1.42	yes
128	0	0	7.21	0.38	5	6.69	0.51	0.11	0.14	4.79	yes
128	0	-1	7.23	0.44	26	2.57	1.42	0.11	0.12	1.38	yes
128	0	1	7.25	0.39	7	5.61	0.69	0.11	0.14	3.79	yes
128	-1	0	7.26	0.29	5	5.09	0.52	0.11	0.17	3.73	yes
128	1	0	7.13	0.31	6	2.99	0.58	0.12	0.14	3.15	yes
129	0	0	4.56	0.30	16	3.94	1.66	0.13	0.12	1.31	yes
129	0	-1	4.78	0.40	7	0.11	0.00	0.11	0.15	2.07	yes
129	0	1	4.63	0.28	14	1.77	1.42	0.12	0.12	1.13	yes
129	-1	0	4.86	0.45	11	4.33	0.81	0.12	0.14	3.13	yes
129	1	0	4.50	0.30	31	1.32	2.30	0.12	0.12	0.61	no
130	0	0	4.85	0.39	26	2.77	1.73	0.13	0.12	1.39	yes
130	0	-1	...	...	...	...	...	0.14	...	...	...
130	0	1	4.77	0.54	68	2.05	2.26	0.13	0.15	0.83	no
130	-1	0	4.60	0.31	33	1.86	3.11	0.13	0.14	0.41	no
130	1	0	4.90	0.28	7	4.26	0.79	0.15	0.14	2.78	yes
131	0	0	4.78	0.25	10	0.10	0.44	0.13	0.12	1.24	yes
131	0	-1	4.90	0.29	12	0.52	0.99	0.11	0.12	1.20	yes
131	0	1	4.72	0.19	5	3.73	0.78	0.12	0.13	1.81	yes
131	-1	0	4.85	0.21	8	2.66	1.04	0.11	0.11	1.33	yes
131	1	0	4.78	0.31	15	0.10	2.50	0.12	0.11	0.99	yes
132	0	0	4.77	0.67	9	1.91	0.54	0.12	0.13	3.55	yes
132	0	-1	4.77	0.52	0	0.12	0.00	0.13	0.16	2.01	yes
132	0	1	4.88	0.71	7	0.20	0.00	0.13	0.14	4.12	yes
132	-1	0	4.74	0.58	13	0.26	0.51	0.13	0.16	3.73	yes
132	1	0	5.00	0.61	25	0.98	0.96	0.14	0.15	2.11	yes
133	0	0	5.06	0.55	7	4.64	0.35	0.11	0.15	6.80	yes
133	0	-1	4.81	0.61	10	3.15	0.39	0.12	0.14	6.38	yes
133	0	1	5.11	0.73	49	4.39	1.38	0.12	0.14	2.19	yes
133	-1	0	4.85	0.64	9	4.07	0.36	0.12	0.14	7.32	yes
133	1	0	5.11	0.57	8	4.11	0.42	0.12	0.17	6.26	yes
134	0	0	4.87	0.48	3	5.96	0.08	0.13	0.36	9.53	yes
135	0	0	4.72	0.62	5	6.61	0.28	0.11	0.24	9.41	yes
136	0	0	5.94	0.51	105	6.92	0.10	0.11	0.16	6.56	yes
136	0	0	4.64	0.56	105	1.91	0.10	0.11	0.16	6.56	yes
136	0	-1	4.87	0.64	46	5.38	1.79	0.11	0.12	2.29	yes
136	0	-1	5.98	0.19	23	9.67	4.46	0.11	0.12	2.29	yes
136	0	1	4.59	0.65	19	2.75	0.62	0.12	0.14	3.75	yes
136	-1	0	4.65	0.37	11	1.84	0.69	0.12	0.15	3.00	yes
136	1	0	5.96	0.39	42	2.65	2.70	0.12	0.13	2.86	yes
136	1	0	4.70	0.60	33	2.60	1.26	0.12	0.13	2.86	yes

Table 3.3 (cont'd)

#[a]	RA[b] off.	dec[b] off.	V_C[c,d] (km s^{-1})	ΔV[c] (km s^{-1})	error[c] (m s^{-1})	opt.[c] depth	error[c]	rms[c] base(K)	rms[c] fit(K)	$\int$ I [e] (K km s^{-1})	sec.[f] fit ?
137	0	0	...	...	...	...	...	0.09	...	...	...
138	0	0	5.07	0.30	11	2.75	1.10	0.12	0.14	1.75	yes
138	0	-1	5.10	0.32	17	0.71	1.28	0.12	0.12	1.06	yes
138	0	1	5.09	0.30	15	0.10	2.16	0.11	0.12	0.76	yes
138	-1	0	5.04	0.26	9	3.10	1.02	0.12	0.10	1.47	yes
138	1	0	5.16	0.30	20	0.10	1.75	0.11	0.11	0.79	yes
139	0	0	5.09	0.40	17	2.48	0.98	0.14	0.18	2.61	yes
140	0	0	5.34	0.25	10	3.35	1.20	0.13	0.14	1.53	yes
140	0	-1	5.41	0.28	2	0.82	0.00	0.11	0.13	1.13	yes
140	0	1	5.34	0.21	22	1.81	2.91	0.11	0.11	0.22	no
140	-1	0	5.45	0.22	20	1.20	2.31	0.11	0.12	0.48	no
140	1	0	5.30	0.21	5	2.61	0.43	0.11	0.14	1.72	yes
141	0	0	...	...	...	...	...	0.14	...	...	...
142	0	0	...	...	...	...	...	0.14	...	...	...
143	0	0	5.09	0.29	5	8.88	0.67	0.11	0.20	4.31	yes
143	0	-1	5.07	0.31	19	1.53	1.65	0.12	0.11	1.10	yes
143	0	1	5.23	0.37	8	19.48	0.65	0.11	0.14	1.89	yes
143	-1	0	5.10	0.28	11	3.06	1.14	0.11	0.14	1.72	yes
143	1	0	5.08	0.33	15	8.26	1.71	0.12	0.11	1.84	yes
144	0	0	...	...	...	...	...	0.12	...	...	...
145	0	0	3.42	0.24	28	0.10	4.57	0.12	0.12	0.74	no
146	0	0	4.49	0.37	6	9.10	0.56	0.12	0.28	6.18	yes
147	0	0	4.64	0.47	8	4.61	0.52	0.10	0.14	4.27	yes
148	0	0	5.03	0.90	105	17.34	0.10	0.11	0.20	13.00	yes
148	0	0	5.11	0.58	105	0.11	0.10	0.11	0.20	13.00	yes
149	0	0	4.51	0.82	5	6.40	0.14	0.12	0.21	20.20	yes
150	0	0	4.05	0.49	3	12.99	0.11	0.12	0.20	9.41	yes
151	0	0	4.52	0.34	1	0.44	0.00	0.12	0.14	1.80	yes
152	0	0	4.08	0.50	5	12.75	0.44	0.12	0.18	10.85	yes
153	0	0	...	...	...	...	...	0.13	...	...	...
153	0	-1	...	...	...	...	...	0.14	...	...	...
153	0	1	...	...	...	...	...	0.14	...	...	...
153	-1	0	...	...	...	...	...	0.14	...	...	...
153	1	0	...	...	...	...	...	0.14	...	...	...
154	0	0	...	...	...	...	...	0.12	...	...	...
155	0	0	4.15	0.33	11	4.47	1.05	0.12	0.11	2.16	yes
156	0	0	...	...	...	...	...	0.12	...	...	...
157	0	0	...	...	...	...	...	0.13	...	...	...

[a]See Table 3.1 for the locations of the targets.

[b]measured in units of the beam (25″)

[c]Centroid velocity, velocity dispersion (FWHM), optical depth, baseline rms, model rms, and the corresponding errors where appropriate determined using CLASS

[d]The error was similar in all cases with a mean and standard deviation of 8±8 m/s.

[e]Integrated intensity computed using the tdv function in CLASS. See §3.1 for further details.

[f]Was the fit judged to be good?

Table 3.4. Parameters of Spectral Fitting for $C^{18}O$

#[a]	RA[b] off.	dec[b] off.	V_C[c,d] (km s^{-1})	ΔV[c] (km s^{-1})	error[c] (m s^{-1})	$T^*_{A,peak}$[c] (K)	$\int$ I[c] (K km s^{-1})	rms[c] base(K)	rms[c] fit(K)	sec.[e] fit ?
1	0	0	...	...	...	...	...	0.47	...	...
2	0	0	10.42	0.46	51	2.32	1.14	0.42	0.36	yes
2	0	0	9.61	0.72	103	1.50	1.15	0.42	0.36	yes
3	0	0	10.20	0.53	11	3.92	2.21	0.18	0.35	yes
3	0	-1	10.13	0.84	19	3.00	2.68	0.23	0.46	yes
3	0	1	10.16	0.50	10	4.68	2.49	0.25	0.27	yes
3	0	1	9.21	0.40	38	1.54	0.65	0.25	0.27	yes
3	-1	0	10.21	0.58	12	4.86	3.02	0.27	0.38	yes
3	1	0	10.17	0.61	30	2.38	1.54	0.26	0.35	yes
4	0	0	10.11	0.91	8	4.05	3.92	0.15	0.28	yes
5	0	0	10.19	1.00	39	2.73	2.92	0.42	0.49	yes
5	0	-1	10.06	0.81	30	3.03	2.61	0.36	0.55	yes
5	0	1	9.97	1.25	32	2.64	3.50	0.34	0.56	yes
5	-1	0	10.07	1.12	33	3.14	3.74	0.37	0.45	yes
5	1	0	10.16	0.96	36	3.00	3.05	0.37	0.40	yes
6	0	0	10.18	0.86	13	3.53	3.23	0.19	0.31	yes
7	0	0	10.10	0.82	31	3.21	2.78	0.43	0.47	yes
7	0	-1	9.93	0.83	28	3.10	2.75	0.36	0.38	yes
7	0	1	9.98	1.11	40	2.83	3.34	0.38	0.46	yes
7	-1	0	9.98	0.91	30	3.07	2.96	0.36	0.50	yes
7	1	0	10.11	0.92	30	3.28	3.20	0.38	0.42	yes
8	0	0	10.20	0.53	27	3.11	1.76	0.40	0.37	yes
8	0	-1	10.29	0.65	25	3.02	2.08	0.40	0.55	yes
8	0	1	10.12	0.52	22	3.45	1.89	0.37	0.38	yes
8	-1	0	10.22	0.51	20	3.93	2.14	0.37	0.36	yes
8	1	0	9.99	0.23	25	2.85	0.70	0.38	0.36	yes
8	1	0	10.48	0.65	97	1.82	1.26	0.38	0.36	yes
9	0	0	10.16	0.60	36	2.74	1.74	0.37	0.53	yes
10	0	0	9.61	0.52	36	2.79	1.55	0.37	0.40	yes
11	0	0	...	...	...	...	...	0.38	...	...
12	0	0	10.86	0.40	20	3.54	1.52	0.43	0.38	yes
12	0	-1	10.88	0.23	5	4.35	1.07	0.22	0.24	yes
12	0	-1	10.14	0.39	32	1.49	0.62	0.22	0.24	yes
12	0	1	10.78	0.34	14	3.43	1.24	0.27	0.28	yes
12	-1	0	10.75	0.26	25	1.57	0.44	0.25	0.20	yes
12	1	0	10.19	0.92	26	1.00	0.98	0.23	0.34	yes
12	1	0	10.74	0.31	26	2.83	0.93	0.23	0.34	yes
13	0	0	10.98	0.41	20	3.26	1.44	0.37	0.44	yes
13	0	-1	10.84	0.38	16	3.23	1.31	0.27	0.36	yes
13	0	1	11.01	0.32	18	2.82	0.95	0.28	0.29	yes
13	-1	0	10.88	0.32	12	3.99	1.35	0.27	0.33	yes
13	1	0	11.05	0.49	22	2.86	1.50	0.25	0.49	yes
14	0	0	8.10	1.06	81	0.76	0.86	0.20	0.19	yes

Table 3.4 (cont'd)

#[a]	RA[b] off.	dec[b] off.	V_C[c,d] (km s^{-1})	ΔV[c] (km s^{-1})	error[c] (m s^{-1})	$T^*_{A,peak}$[c] (K)	$\int$ I[c] (K km s^{-1})	rms[c] base(K)	rms[c] fit(K)	sec.[e] fit ?
15	0	0	9.11	0.86	11	4.12	3.77	0.21	0.36	yes
16	0	0	9.81	1.36	13	4.10	5.95	0.17	0.18	yes
16	0	-1	9.48	0.69	16	4.69	3.43	0.30	0.30	yes
16	0	1	9.70	0.89	20	4.14	3.93	0.29	0.38	yes
16	-1	0	9.36	0.85	23	5.28	4.80	0.38	0.52	yes
16	1	0	9.38	0.89	17	4.59	4.35	0.29	0.44	yes
17	0	0	7.73	0.48	21	1.62	0.82	0.20	0.23	yes
18	0	0	9.59	1.23	17	2.91	3.82	0.17	0.29	yes
18	0	-1	8.72	1.02	140	1.46	1.59	0.29	0.35	yes
18	0	-1	9.91	0.91	61	3.10	2.98	0.29	0.35	yes
18	0	1	9.40	1.07	17	4.09	4.66	0.26	0.41	yes
18	-1	0	9.36	0.80	15	4.44	3.80	0.26	0.24	yes
18	-1	0	8.31	0.52	54	1.18	0.65	0.26	0.24	yes
18	1	0	9.52	0.62	18	4.02	2.65	0.30	0.36	yes
19	0	0	8.56	0.67	6	7.03	5.03	0.19	0.33	yes
20	0	0	8.55	0.62	8	6.17	4.04	0.21	0.52	yes
21	0	0	8.82	1.00	10	4.95	5.26	0.17	0.28	yes
22	0	0	8.60	1.13	8	4.35	5.23	0.15	0.44	yes
22	0	-1	8.37	0.94	18	4.08	4.08	0.25	0.66	yes
22	0	1	8.82	0.92	12	4.96	4.83	0.23	0.37	yes
22	-1	0	8.87	0.60	26	5.17	3.29	0.22	0.32	yes
22	-1	0	8.18	0.51	26	2.98	1.63	0.22	0.32	yes
22	1	0	8.28	0.63	17	5.18	3.46	0.33	0.47	yes
23	0	0	8.25	0.75	11	7.93	6.33	0.32	0.80	yes
24	0	0	8.76	0.85	8	5.91	5.38	0.18	0.31	yes
25	0	0	8.94	0.81	6	7.59	6.53	0.18	0.58	yes
26	0	0	8.52	0.57	26	4.73	2.89	0.18	0.29	yes
26	0	0	9.14	0.55	26	2.46	1.44	0.18	0.29	yes
27	0	0	8.72	0.57	5	7.31	4.46	0.19	0.51	yes
28	0	0	8.67	0.98	10	4.40	4.61	0.18	0.30	yes
29	0	0	9.59	0.38	31	1.48	0.60	0.23	0.24	yes
30	0	0	8.74	0.44	8	7.32	3.46	0.29	0.56	yes
30	0	-1	8.67	0.50	8	7.13	3.77	0.31	0.47	yes
30	0	1	8.80	0.44	9	6.74	3.18	0.34	0.49	yes
30	-1	0	8.78	0.46	8	7.61	3.73	0.32	0.74	yes
30	1	0	8.72	0.51	8	6.84	3.68	0.30	0.53	yes
31	0	0	8.42	0.69	13	4.92	3.62	0.29	0.29	yes
32	0	0	8.31	1.04	57	0.69	0.76	0.13	0.13	yes
33	0	0	9.34	0.50	28	2.60	1.39	0.32	0.27	yes
33	0	0	8.39	0.62	89	0.91	0.60	0.32	0.27	yes
33	0	-1	8.31	0.63	73	0.65	0.43	0.23	0.24	yes
33	0	-1	9.29	0.34	12	3.32	1.20	0.23	0.24	yes
33	0	1	9.38	0.41	16	2.90	1.28	0.25	0.30	yes

Table 3.4 (cont'd)

#[a]	RA[b] off.	dec[b] off.	V_C[c,d] (km s^{-1})	ΔV[c] (km s^{-1})	error[c] (m s^{-1})	$T^*_{A,peak}$[c] (K)	$\int$ I[c] (K km s^{-1})	rms[c] base(K)	rms[c] fit(K)	sec.[e] fit ?
33	-1	0	9.38	0.39	15	3.14	1.31	0.28	0.28	yes
33	1	0	9.29	0.56	18	3.03	1.81	0.27	0.25	yes
34	0	0	8.24	0.58	7	7.11	4.39	0.27	0.72	yes
34	0	-1	8.65	0.51	64	1.83	1.00	0.31	0.29	yes
34	0	-1	8.13	0.39	18	5.12	2.12	0.31	0.29	yes
34	0	1	8.36	0.68	20	3.27	2.38	0.34	0.65	yes
34	-1	0	8.17	0.44	8	6.99	3.30	0.31	0.48	yes
34	1	0	8.28	0.61	12	6.07	3.92	0.33	0.71	yes
35	0	0	8.80	0.51	95	0.72	0.39	0.22	0.21	yes
35	0	0	9.32	0.25	13	2.88	0.77	0.22	0.21	yes
36	0	0	9.36	0.35	20	3.34	1.25	0.41	0.28	yes
36	0	-1	9.35	0.31	15	3.30	1.10	0.27	0.36	yes
36	0	1	9.44	0.36	14	2.93	1.13	0.21	0.24	yes
36	0	1	8.72	0.70	135	0.62	0.47	0.21	0.24	yes
36	-1	0	9.40	0.38	28	2.85	1.17	0.29	0.45	yes
36	1	0	9.36	0.33	13	3.00	1.06	0.22	0.17	yes
36	1	0	8.64	0.57	64	0.75	0.45	0.22	0.17	yes
37	0	0	9.20	0.25	37	1.52	0.40	0.35	0.30	yes
37	0	0	9.70	0.37	53	1.28	0.50	0.35	0.30	yes
38	0	0	9.50	0.48	50	1.92	0.97	0.38	0.33	yes
39	0	0	9.30	0.31	27	2.60	0.85	0.38	0.37	yes
40	0	0	8.99	0.55	27	2.75	1.61	0.34	0.46	yes
41	0	0	8.39	0.39	7	6.89	2.83	0.29	0.27	yes
41	0	0	7.40	0.54	28	2.38	1.37	0.29	0.27	yes
41	0	-1	7.44	0.58	35	2.93	1.80	0.41	0.53	yes
41	0	-1	8.26	0.47	12	6.35	3.17	0.41	0.53	yes
41	0	1	8.41	0.48	8	8.71	4.42	0.43	0.65	yes
41	0	1	7.47	0.50	50	1.92	1.03	0.43	0.65	yes
41	-1	0	7.32	0.64	48	2.48	1.70	0.47	0.46	yes
41	-1	0	8.38	0.36	9	8.83	3.42	0.47	0.46	yes
41	1	0	8.37	0.32	7	9.44	3.17	0.42	0.46	yes
41	1	0	7.46	0.64	46	2.16	1.48	0.42	0.46	yes
42	0	0	8.89	0.74	38	1.92	1.50	0.33	0.38	yes
42	0	-1	8.86	0.78	44	1.85	1.55	0.28	0.33	yes
42	0	1	8.98	0.60	18	2.97	1.88	0.27	0.30	yes
42	-1	0	9.00	0.65	56	1.27	0.89	0.29	0.32	yes
42	1	0	8.98	0.55	48	1.30	0.76	0.29	0.22	yes
43	0	0	8.70	0.53	25	2.47	1.38	0.35	0.43	yes
44	0	0	9.16	0.71	59	0.89	0.68	0.32	0.35	no
44	0	-1	...	...	...	...	...	0.37	...	...
44	0	1	8.98	0.44	61	1.13	0.53	0.30	0.31	yes
44	0	1	9.62	0.39	24	3.01	1.26	0.30	0.31	yes
44	-1	0	...	...	...	...	...	0.32	...	...

Table 3.4 (cont'd)

#[a]	RA[b] off.	dec[b] off.	V_C[c,d] (km s^{-1})	ΔV[c] (km s^{-1})	error[c] (m s^{-1})	$T^*_{A,peak}$[c] (K)	$\int$ I[c] (K km s^{-1})	rms[c] base(K)	rms[c] fit(K)	sec.[e] fit ?
44	1	0	9.32	0.92	54	1.16	1.13	0.27	0.34	yes
45	0	0	...	...	...	...	...	0.22	...	...
46	0	0	8.35	0.61	13	3.00	1.95	0.19	0.19	yes
46	0	-1	8.29	0.59	11	3.01	1.90	0.17	0.25	yes
46	0	1	8.34	0.49	9	3.61	1.89	0.17	0.17	yes
46	-1	0	8.28	0.47	9	3.01	1.50	0.16	0.17	yes
46	1	0	8.41	0.61	12	2.97	1.92	0.18	0.17	yes
47	0	0	10.09	0.57	15	3.53	2.15	0.28	0.30	yes
48	0	0	9.15	0.30	11	3.40	1.10	0.29	0.29	yes
49	0	0	7.88	0.39	23	3.14	1.30	0.37	0.31	yes
49	0	-1	8.02	0.83	38	1.75	1.55	0.26	0.28	yes
49	0	1	7.91	0.56	28	2.51	1.49	0.27	0.35	yes
49	-1	0	7.95	0.42	17	2.99	1.35	0.26	0.26	yes
49	1	0	7.93	0.56	19	2.94	1.76	0.24	0.36	yes
50	0	0	9.49	0.46	47	1.42	0.70	0.34	0.26	yes
51	0	0	9.40	0.41	17	2.46	1.08	0.22	0.24	yes
51	0	-1	9.35	0.35	21	2.16	0.79	0.26	0.20	yes
51	0	1	9.71	0.54	33	2.56	1.47	0.30	0.33	yes
51	-1	0	9.51	0.37	22	2.03	0.79	0.26	0.23	yes
51	1	0	9.37	0.39	15	3.18	1.32	0.25	0.29	yes
52	0	0	8.22	0.69	50	1.62	1.19	0.35	0.32	yes
52	0	-1	8.11	0.43	17	2.75	1.26	0.27	0.35	yes
52	0	1	8.34	0.57	42	1.65	1.01	0.30	0.27	yes
52	-1	0	7.98	0.44	20	3.59	1.70	0.33	0.40	yes
52	1	0	8.27	0.59	39	1.71	1.07	0.29	0.27	yes
53	0	0	9.95	0.50	15	4.20	2.26	0.33	0.34	yes
54	0	0	9.63	0.52	20	3.01	1.67	0.32	0.28	yes
55	0	0	9.71	0.50	13	3.60	1.93	0.24	0.24	yes
55	0	0	8.32	0.47	64	0.96	0.48	0.24	0.24	yes
55	0	-1	9.65	0.46	8	3.53	1.72	0.17	0.18	yes
55	0	-1	8.42	0.60	59	0.59	0.37	0.17	0.18	yes
55	0	1	8.32	0.41	36	0.92	0.40	0.20	0.23	yes
55	0	1	9.72	0.48	10	3.80	1.95	0.20	0.23	yes
55	-1	0	9.66	0.42	10	3.23	1.46	0.18	0.19	yes
55	1	0	9.72	0.45	10	3.37	1.62	0.20	0.22	yes
56	0	0	9.59	0.52	30	1.55	0.86	0.21	0.32	yes
57	0	0	...	...	...	...	...	0.31	...	...
58	0	0	4.78	0.67	99	0.40	0.28	0.21	0.16	no
59	0	0	7.67	0.95	38	2.18	2.20	0.31	0.28	yes
60	0	0	8.17	0.31	38	0.61	0.20	0.15	0.13	yes
60	0	0	7.13	0.90	45	0.87	0.83	0.15	0.13	yes
61	0	0	7.36	1.00	77	1.21	1.29	0.29	0.32	yes
61	0	-1	7.28	0.90	54	1.35	1.29	0.28	0.30	yes

Table 3.4 (cont'd)

#[a]	RA[b] off.	dec[b] off.	V_C[c,d] (km s^{-1})	ΔV[c] (km s^{-1})	error[c] (m s^{-1})	$T^*_{A,peak}$[c] (K)	$\int$ I[c] (K km s^{-1})	rms[c] base(K)	rms[c] fit(K)	sec.[e] fit ?
61	0	1	7.38	0.64	53	1.15	0.79	0.25	0.25	yes
61	-1	0	7.39	0.79	45	1.46	1.23	0.28	0.34	yes
61	1	0	7.34	1.07	88	1.02	1.16	0.30	0.33	yes
62	0	0	7.53	0.79	44	1.81	1.51	0.29	0.31	yes
62	0	-1	7.81	0.75	36	2.16	1.74	0.28	0.37	yes
62	0	1	7.49	1.14	63	1.62	1.98	0.28	0.34	yes
62	-1	0	7.47	0.73	61	1.53	1.19	0.31	0.30	yes
62	1	0	7.44	1.02	40	1.67	1.81	0.26	0.36	yes
63	0	0	7.07	0.64	16	2.31	1.58	0.17	0.13	yes
63	0	-1	7.02	0.60	26	1.48	0.95	0.15	0.17	yes
63	0	1	7.12	0.46	8	3.26	1.59	0.15	0.16	yes
63	-1	0	7.03	0.86	61	0.77	0.70	0.16	0.17	yes
63	1	0	7.13	0.43	7	3.48	1.58	0.14	0.19	yes
64	0	0	7.28	1.22	158	0.48	0.62	0.29	0.25	no
64	0	-1	...	...	...	...	...	0.32	...	...
64	0	1	7.47	1.03	151	0.61	0.67	0.30	0.24	no
64	-1	0	...	...	...	...	...	0.31	...	...
64	1	0	7.42	1.62	139	0.44	0.76	0.15	0.13	yes
65	0	0	6.91	0.34	17	3.32	1.20	0.34	0.26	yes
65	0	-1	6.77	0.44	22	3.15	1.48	0.34	0.31	yes
65	0	1	7.09	0.88	61	1.59	1.48	0.30	0.36	yes
65	-1	0	6.78	0.52	41	1.85	1.02	0.34	0.32	yes
65	1	0	7.34	1.38	122	0.78	1.16	0.29	0.31	yes
65	1	0	6.90	0.23	17	2.19	0.54	0.29	0.31	yes
66	0	0	6.61	0.54	35	2.07	1.20	0.30	0.38	yes
67	0	0	6.63	1.00	21	3.43	3.64	0.30	0.44	yes
67	0	-1	6.69	0.97	35	3.44	3.55	0.38	0.47	yes
67	0	1	6.58	1.22	53	1.97	2.57	0.37	0.52	yes
67	-1	0	6.36	0.40	31	3.40	1.45	0.40	0.43	yes
67	-1	0	6.95	0.54	40	3.88	2.21	0.40	0.43	yes
67	1	0	6.29	0.54	40	3.08	1.78	0.41	0.30	yes
67	1	0	6.95	0.47	34	3.33	1.68	0.41	0.30	yes
68	0	0	6.81	1.04	12	5.35	5.91	0.20	0.47	yes
69	0	0	6.65	1.09	55	1.06	1.23	0.23	0.22	yes
70	0	0	6.61	0.92	19	2.16	2.11	0.14	0.27	yes
71	0	0	6.41	0.85	16	4.60	4.15	0.18	0.20	yes
71	0	0	7.30	0.67	14	4.60	3.27	0.18	0.20	yes
72	0	0	6.47	1.20	8	5.64	7.18	0.17	0.22	yes
72	0	-1	6.68	1.02	19	4.63	5.02	0.29	0.43	yes
72	0	1	6.43	1.01	12	5.51	5.90	0.25	0.32	yes
72	-1	0	6.54	1.27	20	3.67	4.94	0.25	0.31	yes
72	1	0	6.41	1.09	11	6.93	8.01	0.27	0.38	yes
73	0	0	6.65	0.95	6	5.41	5.47	0.16	0.23	yes

Table 3.4 (cont'd)

#[a]	RA[b] off.	dec[b] off.	V_C[c,d] (km s^{-1})	ΔV[c] (km s^{-1})	error[c] (m s^{-1})	$T^*_{A,peak}$[c] (K)	$\int$ I[c] (K km s^{-1})	rms[c] base(K)	rms[c] fit(K)	sec.[e] fit ?
74	0	0	6.93	0.86	18	2.33	2.14	0.17	0.22	yes
74	0	-1	6.99	0.93	25	2.69	2.67	0.26	0.26	yes
74	0	1	6.92	0.59	18	2.84	1.79	0.25	0.29	yes
74	-1	0	6.82	0.67	25	2.45	1.74	0.25	0.28	yes
74	1	0	6.78	0.87	53	2.17	2.01	0.27	0.26	yes
74	1	0	7.46	0.29	25	1.84	0.57	0.27	0.26	yes
75	0	0	6.70	0.89	15	3.57	3.38	0.20	0.40	yes
75	0	-1	6.71	0.69	17	4.10	3.00	0.29	0.47	yes
75	0	1	6.69	0.82	17	3.54	3.11	0.25	0.29	yes
75	-1	0	6.68	0.81	18	3.88	3.33	0.27	0.32	yes
75	1	0	6.77	0.83	12	4.49	3.95	0.24	0.37	yes
76	0	0	6.63	0.73	17	4.04	3.13	0.31	0.37	yes
76	0	-1	6.79	0.54	26	3.96	2.28	0.38	0.44	yes
76	0	-1	6.09	0.33	47	2.06	0.72	0.38	0.44	yes
76	0	1	6.61	0.65	25	3.23	2.22	0.38	0.37	yes
76	-1	0	6.49	0.67	24	3.67	2.60	0.39	0.42	yes
76	1	0	6.71	0.54	16	4.68	2.67	0.37	0.40	yes
77	0	0	6.68	0.79	26	3.37	2.82	0.34	0.32	yes
77	0	-1	6.70	0.56	22	4.34	2.61	0.42	0.29	yes
77	0	1	6.62	0.74	43	3.48	2.73	0.45	0.53	yes
77	-1	0	6.63	0.73	27	3.53	2.74	0.35	0.35	yes
77	1	0	6.71	0.67	22	4.15	2.94	0.38	0.37	yes
78	0	0	6.68	1.09	33	3.98	4.61	0.36	0.54	yes
78	0	-1	6.66	0.83	21	4.24	3.76	0.34	0.42	yes
78	0	1	6.72	0.98	33	3.07	3.21	0.33	0.38	yes
78	-1	0	6.65	0.75	20	4.03	3.22	0.33	0.36	yes
78	1	0	6.89	0.86	20	4.14	3.80	0.32	0.46	yes
79	0	0	6.57	1.02	30	3.46	3.76	0.35	0.33	yes
79	0	-1	6.50	0.94	18	3.78	3.80	0.26	0.28	yes
79	0	1	6.68	0.77	24	4.09	3.36	0.36	0.30	yes
79	-1	0	6.47	0.72	15	4.42	3.41	0.29	0.38	yes
79	1	0	6.62	0.82	18	3.85	3.35	0.28	0.32	yes
80	0	0	6.74	0.63	42	2.91	1.94	0.33	0.33	yes
80	0	0	5.93	0.72	55	2.74	2.10	0.33	0.33	yes
80	0	-1	6.87	0.46	45	2.36	1.16	0.38	0.27	yes
80	0	-1	6.20	0.69	46	3.30	2.44	0.38	0.27	yes
80	0	1	6.59	0.62	47	3.19	2.10	0.34	0.26	yes
80	0	1	5.89	0.60	66	2.26	1.45	0.34	0.26	yes
80	-1	0	6.39	0.88	26	3.12	2.93	0.34	0.37	yes
80	1	0	6.03	0.61	17	2.93	1.89	0.36	0.46	yes
80	1	0	6.82	0.90	9	1.91	1.84	0.36	0.46	yes
81	0	0	6.67	1.26	133	0.84	1.12	0.34	0.30	no
82	0	0	6.47	1.01	27	1.38	1.48	0.15	0.15	yes

Table 3.4 (cont'd)

#[a]	RA[b] off.	dec[b] off.	V_C[c,d] (km s^{-1})	ΔV[c] (km s^{-1})	error[c] (m s^{-1})	$T^*_{A,peak}$[c] (K)	$\int$ I[c] (K km s^{-1})	rms[c] base(K)	rms[c] fit(K)	sec.[e] fit ?
83	0	0	6.72	0.65	31	2.39	1.66	0.32	0.38	yes
83	0	-1	6.72	0.51	33	1.85	1.01	0.32	0.35	yes
83	0	1	6.71	0.58	25	2.56	1.57	0.31	0.45	yes
83	-1	0	6.63	0.56	36	1.57	0.94	0.31	0.32	yes
83	1	0	6.52	0.39	16	3.33	1.37	0.31	0.34	yes
84	0	0	6.82	0.79	29	3.01	2.53	0.35	0.42	yes
84	0	-1	6.77	0.68	23	2.97	2.13	0.31	0.43	yes
84	0	1	6.47	0.56	67	1.51	0.90	0.34	0.28	yes
84	-1	0	6.75	0.64	80	1.28	0.87	0.34	0.32	yes
84	1	0	6.77	0.75	24	3.02	2.40	0.33	0.53	yes
85	0	0	6.50	0.98	32	2.60	2.72	0.30	0.40	yes
85	0	-1	6.43	0.67	21	3.20	2.30	0.32	0.35	yes
85	0	1	6.30	0.74	45	1.90	1.51	0.32	0.36	yes
85	-1	0	6.43	0.71	31	2.77	2.09	0.35	0.34	yes
85	1	0	6.49	0.77	23	2.90	2.39	0.31	0.34	yes
86	0	0	6.89	0.96	13	3.73	3.82	0.18	0.28	yes
86	0	-1	6.90	0.75	22	2.72	2.16	0.25	0.25	yes
86	0	1	6.98	0.83	26	2.09	1.85	0.23	0.27	yes
86	-1	0	6.78	0.61	20	2.84	1.85	0.26	0.23	yes
86	1	0	6.78	0.54	13	3.93	2.26	0.26	0.28	yes
87	0	0	5.90	0.41	19	3.60	1.56	0.37	0.27	yes
87	0	-1	5.83	0.41	17	3.41	1.50	0.33	0.31	yes
87	0	1	5.96	0.56	18	3.56	2.12	0.31	0.37	yes
87	-1	0	5.92	0.39	25	2.69	1.12	0.35	0.26	yes
87	1	0	5.94	0.45	23	3.03	1.46	0.34	0.45	yes
88	0	0	6.95	0.66	26	3.14	2.22	0.34	0.35	yes
89	0	0	7.26	1.23	197	0.56	0.73	0.19	0.20	no
90	0	0	7.00	1.08	27	1.98	2.28	0.16	0.25	yes
90	0	-1	7.55	0.80	52	1.62	1.38	0.26	0.23	yes
90	0	-1	6.68	0.51	56	1.27	0.69	0.26	0.23	yes
90	0	1	7.17	1.19	62	1.01	1.28	0.23	0.25	yes
90	-1	0	7.08	1.57	79	1.19	1.99	0.25	0.21	yes
90	1	0	7.11	1.14	104	0.86	1.04	0.25	0.26	yes
91	0	0	7.78	0.56	30	2.98	1.78	0.36	0.53	yes
91	0	-1	7.63	0.59	20	3.08	1.94	0.32	0.32	yes
91	0	1	7.70	0.51	25	2.49	1.36	0.34	0.47	yes
91	-1	0	7.80	0.43	24	2.28	1.04	0.31	0.36	yes
91	1	0	7.53	0.78	31	2.16	1.79	0.33	0.44	yes
92	0	0	6.06	0.57	54	1.88	1.14	0.39	0.49	yes
92	0	-1	6.02	0.42	26	2.24	1.01	0.30	0.34	yes
92	0	1	6.02	0.46	29	2.08	1.02	0.30	0.28	yes
92	-1	0	6.06	0.65	63	1.20	0.83	0.33	0.23	yes
92	1	0	5.98	0.58	27	2.33	1.44	0.32	0.47	yes

Table 3.4 (cont'd)

#[a]	RA[b] off.	dec[b] off.	V_C[c,d] (km s^{-1})	ΔV[c] (km s^{-1})	error[c] (m s^{-1})	$T^*_{A,peak}$[c] (K)	$\int$ I [c] (K km s^{-1})	rms[c] base(K)	rms[c] fit(K)	sec.[e] fit ?
93	0	0	6.17	0.60	20	1.51	0.96	0.14	0.15	yes
94	0	0	5.98	0.67	37	2.20	1.56	0.38	0.35	yes
94	0	-1	5.90	0.58	47	1.33	0.83	0.31	0.32	yes
94	0	1	5.87	0.64	59	1.31	0.90	0.29	0.26	yes
94	-1	0	5.66	0.42	47	1.11	0.50	0.31	0.29	yes
94	1	0	5.99	0.65	42	1.69	1.17	0.29	0.29	yes
95	0	0	8.10	0.52	8	4.27	2.37	0.18	0.25	yes
95	0	-1	8.18	0.35	14	2.99	1.10	0.25	0.38	yes
95	0	1	8.21	0.39	25	1.86	0.77	0.23	0.22	yes
95	-1	0	8.20	0.37	32	1.73	0.68	0.28	0.25	yes
95	1	0	8.10	0.39	13	3.47	1.45	0.26	0.28	yes
96	0	0	7.53	0.71	16	2.35	1.78	0.19	0.30	yes
97	0	0	7.51	0.49	7	3.82	2.00	0.16	0.19	yes
97	0	-1	7.51	0.42	11	3.73	1.67	0.23	0.27	yes
97	0	1	7.48	0.49	21	2.74	1.42	0.26	0.35	yes
97	-1	0	7.41	0.53	20	2.43	1.36	0.25	0.29	yes
97	1	0	7.49	0.39	10	4.57	1.89	0.26	0.32	yes
98	0	0	7.39	1.05	8	6.00	6.68	0.19	0.40	yes
99	0	0	7.53	0.39	5	9.76	4.04	0.21	0.35	yes
99	0	0	6.91	0.46	9	4.07	2.01	0.21	0.35	yes
99	0	-1	7.56	0.51	7	10.40	5.59	0.35	0.70	yes
99	0	1	7.41	0.58	8	9.40	5.80	0.36	1.04	yes
99	-1	0	7.30	0.82	16	3.96	3.46	0.27	0.46	yes
99	1	0	7.44	0.52	7	7.96	4.41	0.27	0.51	yes
100	0	0	7.55	0.71	6	7.01	5.27	0.19	0.29	yes
101	0	0	8.35	1.42	9	7.09	10.70	0.20	0.73	yes
102	0	0	7.72	1.11	10	5.40	6.38	0.19	0.25	yes
103	0	0	6.60	0.86	28	2.19	2.00	0.18	0.20	yes
103	0	0	7.83	1.06	31	2.71	3.06	0.18	0.20	yes
104	0	0	8.54	1.41	28	4.66	6.98	0.33	0.51	yes
105	0	0	8.49	0.88	18	3.61	3.40	0.17	0.26	yes
105	0	0	7.43	0.85	6	10.30	9.27	0.17	0.26	yes
106	0	0	7.30	1.92	10	3.42	7.01	0.11	0.28	yes
106	0	-1	6.48	0.78	36	2.17	1.80	0.29	0.31	yes
106	0	-1	7.84	1.18	40	2.84	3.57	0.29	0.31	yes
106	0	1	6.69	0.44	21	2.85	1.35	0.29	0.31	yes
106	0	1	7.70	1.00	27	4.03	4.30	0.29	0.31	yes
106	-1	0	7.81	0.83	19	4.52	3.98	0.29	0.39	yes
106	-1	0	6.45	0.78	49	1.59	1.32	0.29	0.39	yes
106	1	0	6.79	0.74	85	1.28	1.01	0.30	0.34	yes
106	1	0	7.69	0.98	40	4.58	4.80	0.30	0.34	yes
107	0	0	7.75	1.59	35	2.75	4.65	0.18	0.23	yes
107	0	0	6.99	0.41	23	1.58	0.70	0.18	0.23	yes

Table 3.4 (cont'd)

#[a]	RA[b] off.	dec[b] off.	V_C[c,d] (km s^{-1})	ΔV[c] (km s^{-1})	error[c] (m s^{-1})	$T^*_{A,peak}$[c] (K)	$\int$ I [c] (K km s^{-1})	rms[c] base(K)	rms[c] fit(K)	sec.[e] fit ?
108	0	0	7.46	1.06	6	9.74	10.99	0.17	0.25	yes
108	0	0	8.79	0.78	16	3.24	2.70	0.17	0.25	yes
109	0	0	8.52	1.49	25	3.98	6.31	0.26	0.40	yes
110	0	0	7.56	1.88	18	4.13	8.26	0.19	0.27	yes
111	0	0	6.68	1.59	0	1.78	3.01	0.18	0.37	yes
111	0	0	7.39	2.13	1	2.24	5.09	0.18	0.37	yes
112	0	0	8.18	1.51	14	6.44	10.32	0.24	0.45	yes
113	0	0	7.73	1.46	8	8.83	13.70	0.22	0.64	yes
114	0	0	7.89	1.66	14	4.54	8.02	0.14	0.23	yes
114	0	0	7.15	0.45	10	3.14	1.49	0.14	0.23	yes
115	0	0	7.46	1.53	30	2.03	3.30	0.17	0.23	yes
116	0	0	8.00	1.53	26	5.38	8.77	0.16	0.48	yes
116	0	0	6.82	1.49	26	0.58	0.92	0.16	0.48	yes
117	0	0	5.75	0.42	13	3.25	1.46	0.24	0.20	yes
118	0	0	7.62	1.31	16	5.22	7.27	0.23	0.35	yes
118	0	-1	7.67	1.71	25	3.40	6.18	0.25	0.43	yes
118	0	1	7.62	1.23	15	5.70	7.46	0.28	0.35	yes
118	-1	0	7.72	1.16	28	3.26	4.04	0.26	0.32	yes
118	1	0	7.64	2.07	24	4.06	8.94	0.27	0.38	yes
119	0	0	6.82	1.15	74	1.24	1.51	0.15	0.23	yes
119	0	0	8.08	0.87	31	1.58	1.47	0.15	0.23	yes
120	0	0	5.37	0.44	17	2.47	1.16	0.22	0.30	yes
121	0	0	7.28	0.92	26	2.46	2.40	0.20	0.22	yes
121	0	0	6.24	0.36	23	1.81	0.70	0.20	0.22	yes
122	0	0	8.06	0.96	24	2.43	2.48	0.18	0.28	yes
123	0	0	8.34	0.94	12	3.61	3.60	0.17	0.24	yes
124	0	0	6.91	1.57	27	2.29	3.81	0.19	0.36	yes
125	0	0	7.35	0.70	15	4.07	3.03	0.22	0.41	yes
125	0	-1	7.34	0.52	19	3.06	1.68	0.29	0.26	yes
125	0	1	7.98	1.46	97	1.25	1.95	0.23	0.21	yes
125	0	1	7.36	0.50	29	2.39	1.27	0.23	0.21	yes
125	-1	0	7.67	1.45	106	0.79	1.21	0.24	0.25	yes
125	-1	0	7.36	0.39	18	2.82	1.16	0.24	0.25	yes
125	1	0	7.56	1.17	42	2.12	2.63	0.26	0.40	yes
126	0	0	6.86	1.64	112	0.59	1.03	0.19	0.19	yes
127	0	0	5.50	0.43	20	1.92	0.87	0.22	0.28	yes
127	0	-1	5.43	0.41	31	1.29	0.56	0.26	0.29	yes
127	0	1	5.52	0.46	20	2.24	1.10	0.25	0.39	yes
127	-1	0	5.46	0.55	47	1.30	0.76	0.34	0.22	yes
127	1	0	5.47	0.40	24	1.49	0.63	0.26	0.17	yes
128	0	0	7.14	1.40	75	1.16	1.73	0.21	0.19	yes
128	0	0	8.53	0.46	45	0.97	0.47	0.21	0.19	yes
128	0	-1	8.48	0.50	82	1.00	0.53	0.25	0.28	yes

Table 3.4 (cont'd)

#[a]	RA[b] off.	dec[b] off.	V_C[c,d] (km s^{-1})	ΔV[c] (km s^{-1})	error[c] (m s^{-1})	$T^*_{A,peak}$[c] (K)	$\int$ I [c] (K km s^{-1})	rms[c] base(K)	rms[c] fit(K)	sec.[e] fit ?
128	0	-1	7.12	1.37	88	1.29	1.89	0.25	0.28	yes
128	0	1	8.36	0.74	137	0.90	0.71	0.26	0.29	no
128	0	1	7.38	0.51	53	1.52	0.83	0.26	0.29	no
128	-1	0	7.30	0.76	155	0.75	0.61	0.23	0.20	yes
128	-1	0	8.29	0.66	78	0.83	0.58	0.23	0.20	yes
128	1	0	8.22	0.62	44	1.15	0.76	0.23	0.25	yes
128	1	0	6.58	0.57	39	1.73	1.04	0.23	0.25	yes
128	1	0	7.24	0.44	39	1.40	0.66	0.23	0.25	yes
129	0	0	4.55	0.23	28	1.15	0.28	0.28	0.21	yes
129	0	-1	4.75	0.41	42	0.96	0.42	0.23	0.23	yes
129	0	1	4.65	0.38	35	1.04	0.43	0.23	0.18	yes
129	-1	0	4.91	0.46	38	0.95	0.47	0.21	0.21	yes
129	1	0	4.57	0.53	95	0.72	0.41	0.25	0.22	yes
130	0	0	4.86	0.67	101	0.51	0.36	0.27	0.21	no
130	0	-1	...	...	...	...	...	0.40	...	...
130	0	1	5.20	2.10	252	0.61	1.37	0.36	0.36	no
130	-1	0	...	...	...	...	...	0.39	...	...
130	1	0	4.90	0.57	56	1.62	0.98	0.37	0.35	yes
131	0	0	4.73	0.38	58	0.93	0.37	0.28	0.16	yes
131	0	-1	4.81	0.54	55	1.02	0.58	0.25	0.23	yes
131	0	1	4.89	0.78	87	0.54	0.45	0.23	0.23	yes
131	-1	0	4.93	0.83	119	0.52	0.46	0.27	0.17	no
131	1	0	4.74	0.61	233	0.65	0.42	0.24	0.29	no
132	0	0	5.14	1.01	99	0.79	0.86	0.26	0.30	yes
132	0	-1	5.05	1.09	224	0.64	0.74	0.37	0.32	no
132	0	1	5.07	1.10	151	0.79	0.92	0.37	0.36	no
132	-1	0	5.01	1.54	204	0.67	1.10	0.35	0.29	no
132	1	0	5.17	1.16	104	1.00	1.23	0.34	0.32	no
133	0	0	5.22	1.07	48	1.07	1.22	0.17	0.14	yes
133	0	-1	5.01	0.94	44	1.35	1.35	0.21	0.26	yes
133	0	1	5.15	2.49	307	0.41	1.09	0.26	0.25	no
133	-1	0	4.94	1.57	110	0.69	1.15	0.24	0.25	no
133	1	0	5.24	0.72	39	1.57	1.20	0.23	0.20	yes
134	0	0	5.75	0.43	21	1.64	0.74	0.17	0.15	yes
134	0	0	4.91	0.70	20	2.25	1.68	0.17	0.15	yes
135	0	0	4.68	0.70	35	1.53	1.14	0.17	0.14	yes
135	0	0	5.73	1.14	124	0.80	0.98	0.17	0.14	yes
136	0	0	5.90	0.45	19	1.93	0.92	0.18	0.17	yes
136	0	0	4.40	1.34	75	0.86	1.23	0.18	0.17	yes
136	0	-1	5.94	0.90	55	1.70	1.64	0.27	0.31	yes
136	0	1	5.96	0.39	28	1.56	0.65	0.24	0.20	yes
136	0	1	4.48	1.38	126	0.65	0.96	0.24	0.20	yes
136	-1	0	4.58	1.02	149	0.69	0.75	0.24	0.26	no

Table 3.4 (cont'd)

#[a]	RA[b] off.	dec[b] off.	V_C[c,d] (km s^{-1})	ΔV[c] (km s^{-1})	error[c] (m s^{-1})	$T^*_{A,peak}$[c] (K)	$\int$ I[c] (K km s^{-1})	rms[c] base(K)	rms[c] fit(K)	sec.[e] fit ?
136	-1	0	5.80	0.52	48	1.26	0.70	0.24	0.26	no
136	1	0	5.93	1.00	26	0.83	0.88	0.24	0.29	yes
136	1	0	4.27	1.14	26	0.67	0.82	0.24	0.29	yes
137	0	0	5.73	0.68	68	1.20	0.87	0.15	0.16	yes
137	0	0	4.70	0.93	112	0.79	0.78	0.15	0.16	yes
138	0	0	5.24	0.90	68	0.99	0.95	0.27	0.27	yes
138	0	-1	5.34	0.92	76	0.93	0.90	0.23	0.26	yes
138	0	1	5.34	0.67	52	0.94	0.67	0.24	0.28	yes
138	-1	0	5.14	0.91	110	0.67	0.65	0.24	0.22	no
138	1	0	5.59	0.56	34	1.80	1.07	0.25	0.25	yes
139	0	0	4.92	0.97	123	0.76	0.78	0.39	0.47	no
140	0	0	5.34	0.27	19	1.85	0.54	0.25	0.21	yes
140	0	-1	5.43	0.36	28	2.07	0.79	0.24	0.33	yes
140	0	1	5.37	0.27	12	2.58	0.74	0.22	0.17	yes
140	-1	0	5.42	0.36	24	1.42	0.54	0.25	0.28	yes
140	1	0	5.27	0.34	19	2.25	0.82	0.25	0.15	yes
141	0	0	4.76	1.34	160	0.83	1.19	0.33	0.27	yes
142	0	0	...	...	...	...	...	0.39	...	...
143	0	0	5.09	0.46	18	1.85	0.90	0.18	0.18	yes
143	0	-1	5.09	0.46	64	0.96	0.47	0.26	0.21	yes
143	0	1	5.28	0.49	30	1.57	0.82	0.26	0.23	yes
143	-1	0	5.12	0.34	23	1.58	0.58	0.26	0.14	yes
143	1	0	5.00	0.58	55	0.89	0.55	0.25	0.28	yes
144	0	0	3.85	0.67	35	1.00	0.71	0.20	0.22	yes
145	0	0	3.60	1.31	264	1.12	1.56	0.25	0.44	yes
146	0	0	4.34	0.88	11	3.37	3.14	0.16	0.24	yes
147	0	0	4.55	0.86	10	4.01	3.68	0.18	0.32	yes
148	0	0	5.36	0.53	7	3.03	1.71	0.20	0.27	yes
148	0	0	4.81	1.02	15	3.67	3.98	0.20	0.27	yes
149	0	0	4.35	1.07	8	6.52	7.40	0.19	0.30	yes
150	0	0	4.09	0.68	10	4.00	2.90	0.19	0.21	yes
151	0	0	4.41	0.56	49	1.04	0.62	0.25	0.25	yes
152	0	0	4.05	0.74	7	5.32	4.19	0.16	0.21	yes
153	0	0	...	...	...	...	...	0.27	...	...
153	0	-1	...	...	...	...	...	0.53	...	...
153	0	1	...	...	...	...	...	0.36	...	...
153	-1	0	...	...	...	...	...	0.41	...	...
153	1	0	...	...	...	...	...	0.39	...	...
154	0	0	3.95	0.51	14	3.21	1.75	0.21	0.28	yes
155	0	0	4.11	0.49	25	1.80	0.94	0.24	0.26	yes
156	0	0	4.45	1.12	122	0.38	0.45	0.23	0.25	yes
157	0	0	4.26	0.64	28	1.91	1.31	0.24	0.28	yes

[a]See Table 3.1 for the locations of the targets.

[b]measured in units of the beam (25″)

[c]Centroid velocity, velocity dispersion (FWHM), peak intensity, integrated intensity, baseline rms, model rms, and the corresponding errors where appropriate determined using CLASS

[d]The error was similar in all cases with a mean and standard deviation of 16±15 m/s.

[e]Was the fit judged to be good?

Table 3.5. Properties of Extinction Regions.

Number [a]	RA[a] (J2000.0)	Dec[a] (J2000.0)	Mass[a] ($M_\odot$)	Radius[a] ($''$)	σV_{grav} [b] (km s^{-1})	N_N [c]	σV_N [d] (km s^{-1})	N_C [e]	σV_C [f] (km s^{-1})	Notes [g]
1	3:47:45.3	32:52:43.4	859.6	776	0.89	7	0.39	9	0.46	B5
2	3:43:57.1	31:59:28.7	1938.9	1119	1.11	11	0.55	25	0.51	IC348
3	3:39:27.4	31:21:08.6	780.6	737	0.87	2	0.20	11	0.41	SW of IC348
4	3:36:28.9	31:11:13.1	560.5	670	0.77	1	0	5	0.42	E of B1
5	3:32:35.6	30:58:27.7	441.1	579	0.73	9	0.28	19	0.43	B1
6	3:30:28.7	30:26:30.2	257.6	454	0.63	3	0.09	4	0.30	SW of B1
7	3:28:56.0	31:22:36.4	973.3	889	0.88	8	0.54	12	0.78	NGC1333
8	3:28:53.3	30:44:00.5	246.2	453	0.62	0	0	2	0.30	S of NGC1333
9	3:27:36.6	30:12:32.8	240.1	448	0.62	8	0.32	10	0.58	L1455
10	3:25:22.8	30:43:19.2	173.7	386	0.56	4	0.55	6	0.44	L1448
11	3:24:50.3	30:23:10.1	107.4	309	0.50	2	0.26	4	0.30	S of L1448

[a]Extinction region information from KJD06

[b]Velocity dispersion required to support the region

[c]Number of starless cores detected in N_2H^+ within the extinction region

[d]Velocity dispersion of the N_2H^+ starless cores in the region (uncorrected for the thermal motion of the mean gas)

[e]Number of non-protostars detected in $C^{18}O$ within the extinction region

[f]Velocity dispersion of the non-protostellar $C^{18}O$ detections in the extinction region (uncorrected for the thermal motion of the mean gas)

[g]Descriptive location of extinction region

Table 3.6. Properties of the submillimetre cores identified in the Perseus SCUBA map with 3″ pixels.

Name [a] (SMM J)	# [b]	RA [c] (J2000.0)	Dec [c] (J2000.0)	f_0 [d] (Jy/bm)	S_{850} [d] (Jy)	R_{eff} [d] (″)	Conc [e]	T_{BE} [e] (K)	log n_{cent} [e] (cm^{-3})	P_{ext}/k [e] (cm^3 K^{-1})	Secure [f] Fit?	Assoc [g] Protostar
034769+32517	1	3:47:41.5	32:51:46.5	0.4	1.07	22.9	0.59	11.	5.68	6.00	yes	49
034765+32530	2	3:47:39.2	32:53:01.5	0.2	0.26	13.7	0.20	15.	5.14	6.20	yes	–
034765+32522	3	3:47:39.2	32:52:16.5	0.4	0.74	18.9	0.49	12.	5.54	6.20	yes	–
034481+32005	4	3:44:48.8	32:00:30.5	0.2	0.40	17.2	0.29	16.	4.99	6.10	yes	–
034473+32015	5	3:44:43.9	32:01:33.7	0.6	1.08	20.8	0.62	12.	5.88	6.10	yes	48
034461+31588	6	3:44:36.8	31:58:48.8	0.2	0.49	18.1	0.39	14.	5.11	6.10	yes	–
034438+32100	7	3:44:23.1	32:10:01.3	0.1	0.30	18.6	0.32	14.	4.85	5.90	no	–
034410+32022	8	3:44:06.1	32:02:16.4	0.2	1.30	28.0	0.38	18.	4.79	5.90	yes	–
034404+32024	9	3:44:02.8	32:02:25.4	0.3	1.87	30.3	0.40	19.	4.85	6.00	yes	–
034401+32019	10	3:44:01.2	32:01:55.4	0.3	1.65	28.3	0.44	16.	5.10	6.00	yes	–
034396+32040	11	3:43:58.1	32:04:04.5	0.3	0.87	21.5	0.41	16.	5.12	6.10	yes	–
034395+32030	12	3:43:57.2	32:03:04.5	1.3	4.20	37.1	0.79	15.	5.77	5.80	yes	43
034394+32008	13	3:43:56.7	32:00:49.5	1.4	5.35	38.9	0.78	16.	5.76	5.80	yes	44
034394+32038	14	3:43:56.7	32:03:52.5	0.2	0.87	23.2	0.35	19.	4.80	6.00	yes	–
034384+32034	15	3:43:50.8	32:03:25.5	0.5	5.53	54.8	0.65	14.	5.22	5.50	yes	41
034363+32031	16	3:43:38.0	32:03:07.5	0.2	1.48	32.4	0.43	15.	4.89	5.80	yes	–
034180+31574	17	3:41:48.0	31:57:27.3	0.1	0.08	10.8	0.34	11.	5.21	6.10	no	–
034178+31482	18	3:41:46.8	31:48:15.4	0.1	0.29	20.9	0.34	13.	4.73	5.80	no	–
034176+31574	19	3:41:46.2	31:57:24.4	0.1	0.18	15.6	0.44	9.	5.37	6.00	no	–
034167+31503	20	3:41:40.5	31:50:21.4	0.1	0.21	18.4	0.32	12.	4.81	5.80	no	–
034160+31499	21	3:41:36.2	31:49:54.4	0.1	0.20	18.2	0.34	12.	4.81	5.80	no	–
034081+31488	22	3:40:49.2	31:48:48.2	0.1	0.79	32.9	0.35	16.	4.43	5.50	no	–
033979+31349	23	3:39:47.5	31:34:59.5	0.1	0.07	8.8	0.23	11.	5.39	6.30	no	–
033966+31320	24	3:39:39.9	31:32:05.5	0.1	0.07	9.9	0.27	11.	5.29	6.20	no	–
033965+31318	25	3:39:39.0	31:31:53.5	0.1	0.11	12.9	0.29	11.	5.07	6.00	no	–
033963+31312	26	3:39:38.1	31:31:17.5	0.1	0.09	11.9	0.31	11.	5.13	6.10	no	–
033960+31320	27	3:39:36.4	31:32:02.5	0.1	0.06	9.7	0.26	10.	5.28	6.20	no	–
033345+31071	28	3:33:27.3	31:07:09.0	0.2	0.19	11.7	0.32	14.	5.26	6.30	yes	40
033335+31074	29	3:33:21.3	31:07:27.2	1.5	7.30	40.7	0.74	18.	5.77	5.90	yes	39

Table 3.6 (cont'd)

Name [a] (SMM J)	# [b]	RA [c] (J2000.0)	Dec [c] (J2000.0)	f_0 [d] (Jy/bm)	S_{850} [d] (Jy)	R_{eff} [d] ($''$)	Conc [e]	T_{BE} [e] (K)	log n_{cent} [e] (cm^{-3})	P_{ext}/k [e] (cm^3 K^{-1})	Secure [f] Fit?	Assoc [g] Protostar
033330+31095	30	3:33:18.0	31:09:33.2	1.8	5.97	43.7	0.84	16.	5.66	5.70	yes	38
033327+31078	31	3:33:16.6	31:07:51.2	0.3	2.27	33.9	0.38	23.	4.62	5.90	yes	37
033327+31069	32	3:33:16.3	31:06:54.2	0.6	5.73	44.1	0.55	17.	5.17	5.80	yes	36
033321+31198	33	3:33:13.2	31:19:53.5	0.2	0.65	20.5	0.31	18.	4.88	6.00	yes	34
033309+31050	34	3:33:05.6	31:05:00.4	0.2	1.04	26.6	0.35	20.	4.69	5.90	yes	–
033307+31047	35	3:33:04.7	31:04:45.4	0.2	0.46	18.0	0.16	17.	4.96	6.10	yes	–
033303+31043	36	3:33:01.9	31:04:18.4	0.2	1.83	36.9	0.34	22.	4.45	5.70	yes	–
033229+30498	37	3:32:17.8	30:49:48.3	1.8	3.41	30.6	0.82	14.	5.94	6.00	yes	33
033134+30454	38	3:31:20.8	30:45:29.4	0.8	1.62	24.5	0.71	12.	6.02	6.00	yes	32
033025+30237	39	3:30:15.3	30:23:43.5	0.2	0.23	13.9	0.34	14.	5.11	6.20	no	–
032986+31391	40	3:29:51.9	31:39:07.0	0.3	0.74	20.5	0.53	11.	5.56	6.10	yes	31
032942+31282	41	3:29:25.6	31:28:16.4	0.2	0.42	15.6	0.38	15.	5.19	6.30	yes	–
032939+31333	42	3:29:24.0	31:33:19.4	0.3	0.69	18.8	0.43	14.	5.29	6.20	yes	30
032935+31255	43	3:29:21.4	31:25:34.4	0.2	1.59	35.0	0.36	21.	4.48	5.70	yes	–
032931+31232	44	3:29:19.0	31:23:13.5	0.4	1.89	30.6	0.55	13.	5.37	5.90	yes	29
032930+31251	45	3:29:18.5	31:25:10.5	0.4	2.19	34.3	0.54	13.	5.25	5.80	yes	–
032929+31278	46	3:29:17.6	31:27:49.5	0.3	1.07	25.8	0.54	12.	5.42	5.90	yes	27
032925+31205	47	3:29:15.5	31:20:31.5	0.2	0.81	22.7	0.40	16.	5.00	6.00	yes	–
032922+31139	48	3:29:13.6	31:13:55.5	0.7	2.04	24.8	0.58	14.	5.67	6.20	yes	26
032920+31131	49	3:29:12.2	31:13:07.5	3.7	8.33	37.3	0.86	19.	5.88	6.00	yes	25
032918+31184	50	3:29:11.3	31:18:28.5	1.1	5.33	39.9	0.74	16.	5.74	5.80	yes	24
032918+31217	51	3:29:10.8	31:21:43.5	0.5	2.77	32.8	0.51	16.	5.22	6.00	yes	–
032917+31135	52	3:29:10.6	31:13:31.5	8.0	13.16	32.2	0.86	24.	6.11	6.40	yes	22
032914+31152	53	3:29:08.9	31:15:16.5	0.6	3.08	32.5	0.60	15.	5.50	6.00	yes	–
032914+31170	54	3:29:08.7	31:17:04.5	0.3	0.73	19.0	0.36	19.	4.98	6.20	yes	–
032913+31219	55	3:29:08.0	31:21:55.5	0.5	1.99	28.1	0.54	14.	5.42	6.00	yes	–
032912+31173	56	3:29:07.3	31:17:22.5	0.3	0.71	17.5	0.40	16.	5.25	6.30	yes	–
032911+31156	57	3:29:06.8	31:15:37.5	0.7	2.81	27.3	0.52	16.	5.47	6.20	yes	–
032909+31221	58	3:29:05.4	31:22:07.5	0.3	1.66	28.6	0.36	23.	4.70	6.00	yes	–

Table 3.6 (cont'd)

Name [a] (SMM J)	# [b]	RA [c] (J2000.0)	Dec [c] (J2000.0)	f_0 [d] (Jy/bm)	S_{850} [d] (Jy)	R_{eff} [d] ($''$)	Conc [e]	T_{BE} [e] (K)	log n_{cent} [e] (cm^{-3})	P_{ext}/k [e] (cm^3 K^{-1})	Secure [f] Fit?	Assoc [g] Protostar
032908+31187	59	3:29:05.2	31:18:43.5	0.2	0.22	12.8	0.26	14.	5.19	6.30	yes	–
032906+31148	60	3:29:04.0	31:14:52.5	0.6	4.01	34.7	0.53	17.	5.31	6.00	yes	21
032905+31159	61	3:29:03.3	31:15:55.5	3.0	10.46	36.5	0.77	21.	5.94	6.10	yes	20
032902+31204	62	3:29:01.7	31:20:28.5	1.1	8.82	46.3	0.67	18.	5.52	5.80	yes	19
032901+31143	63	3:29:01.0	31:14:22.5	0.2	0.79	24.2	0.37	18.	4.75	5.90	yes	–
032901+31119	64	3:29:00.7	31:11:58.5	0.3	0.47	17.2	0.48	11.	5.54	6.20	yes	18
032900+31215	65	3:29:00.0	31:21:34.5	0.8	3.92	37.4	0.67	14.	5.60	5.80	yes	17
032892+31146	66	3:28:55.6	31:14:37.5	2.5	8.61	48.6	0.87	17.	5.61	5.70	yes	15
032871+31062	67	3:28:43.0	31:06:13.4	0.2	0.97	27.8	0.30	19.	4.64	5.80	yes	–
032867+31178	68	3:28:40.4	31:17:52.3	0.4	2.18	32.1	0.51	14.	5.21	5.90	yes	13
032866+31184	69	3:28:39.7	31:18:25.3	0.4	2.57	36.6	0.53	14.	5.17	5.80	yes	–
032865+31059	70	3:28:39.5	31:05:55.3	0.2	1.06	27.7	0.32	19.	4.65	5.90	yes	12
032861+31134	71	3:28:37.1	31:13:28.3	0.6	1.92	29.5	0.66	12.	5.70	5.90	yes	11
032858+31070	72	3:28:35.0	31:07:04.3	0.2	0.16	10.0	0.30	14.	5.39	6.40	yes	10
032854+31110	73	3:28:32.7	31:11:04.2	0.2	0.36	16.4	0.27	16.	5.02	6.10	yes	9
032785+30241	74	3:27:51.5	30:24:09.3	0.1	0.24	15.6	0.27	14.	5.00	6.00	no	–
032780+30121	75	3:27:48.2	30:12:10.5	0.3	1.50	30.2	0.48	13.	5.13	5.90	yes	8
032771+30124	76	3:27:42.9	30:12:28.5	0.4	1.51	28.4	0.57	12.	5.47	5.90	yes	7
032766+30122	77	3:27:39.7	30:12:13.5	0.2	1.00	23.3	0.35	20.	4.82	6.00	yes	–
032765+30130	78	3:27:39.2	30:13:01.5	0.6	1.20	21.1	0.59	12.	5.79	6.20	yes	6
032763+30139	79	3:27:38.3	30:13:55.5	0.2	0.40	16.0	0.31	16.	5.06	6.20	yes	5
032662+30154	80	3:26:37.6	30:15:24.7	0.2	0.35	14.2	0.39	14.	5.32	6.30	yes	4
032584+30419	81	3:25:51.0	30:41:55.5	0.5	4.03	36.3	0.44	20.	4.95	6.00	yes	–
032581+30423	82	3:25:48.9	30:42:19.5	0.5	4.56	44.3	0.55	16.	5.13	5.80	yes	–
032564+30440	83	3:25:38.9	30:44:04.5	1.7	4.72	37.6	0.83	15.	5.78	5.80	yes	3
032560+30452	84	3:25:36.3	30:45:16.5	4.1	12.81	45.9	0.87	21.	5.74	5.90	yes	2
032543+30450	85	3:25:25.8	30:45:04.4	0.2	1.21	27.4	0.41	16.	4.91	5.90	yes	–
032537+30452	86	3:25:22.4	30:45:13.4	1.0	1.70	22.4	0.70	13.	6.08	6.10	yes	1
032516+30238	87	3:25:10.2	30:23:51.0	0.2	0.17	11.1	0.28	14.	5.30	6.30	no	–

Table 3.6 (cont'd)

Name [a] (SMM J)	# [b]	RA [c] (J2000.0)	Dec [c] (J2000.0)	f_0 [d] (Jy/bm)	S_{850} [d] (Jy)	R_{eff} [d] ($''$)	Conc [e]	T_{BE} [e] (K)	log n_{cent} [e] (cm^{-3})	P_{ext}/k [e] (cm^3 K^{-1})	Secure [f] Fit?	Assoc [g] Protostar

[a]Name formed from J2000 positions (hhmm.mmddddmm.m)

[b]Reference number used in the text of this paper

[c]Position of peak flux within core (accurate to $3''$).

[d]Peak flux, total flux, and radius derived from *clfind* (Williams, de Geus, & Blitz, 1994). The beamsize is $15.7''$ for the peak flux.

[e]Concentration, temperature, central number density, and external pressure derived from Bonnor-Ebert modelling (see text).

[f]See text for description of which submillimetre core identificationsare considered to be secure.

[g]The reference number of any associated Spitzer protostar from the catalog of Jørgensen et al. (2007). Note that if more than one protostar is considered to be associated (within $15''$), only the closest one is listed.

Chapter 4

The Dynamics of Dense Cores in the Perseus Molecular Cloud II: The Relationship Between Dense Cores and the Cloud

4.1 INTRODUCTION

Star formation is entering an era where the properties of dense, star-forming cores and their environs can be described in a statistical manner across many molecular cloud environments. Existing multi-cloud surveys include the COMPLETE Survey (Ridge et al., 2006), *Spitzer* c2d Survey (Evans et al., 2003), and *Spitzer* Gould Belt Surveys, while surveys that are in progress or starting soon include the JCMT and *Herschel* Gould Belt surveys (Ward-Thompson et al., 2007; André & Saraceno, 2005). These surveys will characterize dense core properties with sufficient detail to allow for the measurement of both global properties as well as the variation due to molecular cloud environment. Numerical simulations have also begun to make explicit predictions about a variety of observable dense core properties, going beyond global statistics such as the mass function.

As previously discussed in Chapter 2, one nearby molecular cloud that has been particularly well-studied already is Perseus. The Perseus molecular cloud is located relatively close-by at a distance of 250 pc (Cernis, 1993) and is an intermediate-mass star-forming region with protostars and dense cores found primarily within small

clustered environments (e.g., NGC 1333 and IC 348). To study the dense cores in an unbiassed manner, dust column density observations have been undertaken in the (sub)millimetre continuum (Hatchell et al. 2005; Kirk, Johnstone, & Di Francesco 2006, hereafter KJD06 and also summarized in Chapter 2; Enoch et al. 2006) and the large-scale structure of the cloud has been determined through visual extinction inferred via reddening of stars in the 2MASS dataset (KJD06; Chapter 2; Ridge et al. 2006). The young protostellar content of the cloud has been measured using *Spitzer* data (Rebull et al., 2007; Jørgensen et al., 2007; Hatchell et al., 2007a). Molecular line data also exists on multiple scales within the cloud. The kinematics of the dense cores have been traced by pointed observations in N_2H^+ (Chapter 3) and NH_3 (Rosolowsky et al., 2008), and their immediate less-dense surroundings in $C^{18}O$ (Chapter 3) and CCS (Rosolowsky et al., 2008). Note that carbon-bearing molecules tend to freeze out quickly onto dust grains in the centres of cold, dense cores, while nitrogen-bearing molecules do not (see, for example, Tafalla et al., 2002). Hence in dense cores, nitrogen-based molecules tend to trace the dense parts of the cores, while carbon-bearing molecules tend to trace the lower density envelopes of the cores. The less-dense gas in Perseus has been mapped in its entirety at lower resolution in ^{12}CO(1–0) and ^{13}CO (1–0) (Ridge et al., 2006; Pineda et al., 2008), with outflows identified across the entire cloud in an unbiassed manner using the ^{12}CO(1–0) dataset (Borkin et al, in prep), and outflows around the dense cores mapped in ^{12}CO(3–2) (Hatchell at al., 2007b).

Since a wealth of data exists for the Perseus molecular cloud, it is possible to move beyond characterizing properties of structures in the cloud based on a single tracer, and advance to a study of the kinematic relationship between the structures on different scales within the cloud.

Several studies have already been carried out which compare the dust column density measurements on various scales in Perseus (and have been summarized in Chapter 2). Jørgensen et al. (2007) related the young embedded protostars to the SCUBA dense cores that they inhabit and showed that the protostars have little, if any, motion within the dense core they form out of. In turn, the SCUBA dense cores are found only within high extinction zones within the molecular cloud, suggesting an extinction threshold of $A_V \sim 5$ mag for dense core formation (KJD06). Such a threshold is consistent with predictions from a magnetically-dominated formation scenario, wherein dense core formation is only possible in the highest column density regions, where the ionization fraction is low enough to allow for a fast ambipolar

diffusion timescale (McKee, 1989). The dense cores also tend to be offset from the peaks of the larger extinction regions that they inhabit in a pattern suggestive of a triggered formation scenario. A nearby B0 star, 40 Persei, previously suggested as a trigger for star formation in the nearby L1451 region (Walawender et al., 2004), is located in a position to be consistent with this scenario (KJD06 and Chapter 2).

A similar multi-scale kinematic analysis has not yet been performed, although the previous single-scale analyses reveal information which already places constraints on the star formation scenario. The pointed N_2H^+(1–0) and $C^{18}O$(2–1) observations (Chapter 3) of the dense cores showed that the dense cores in Perseus are intimately tied to their surrounding envelope of material. The internal velocity dispersion of the N_2H^+ gas tends to be thermally-dominated, while the internal velocity dispersion of the $C^{18}O$ gas tends to be much more non-thermal. Despite this, the difference in centroid velocities is typically less than the sound speed, and much less than the velocity dispersion of the $C^{18}O$ gas. Similar results were found from the pointed NH_3(1,1) and (2,2) and CCS(2–1) survey (Rosolowsky et al., 2008). In a survey of isolated dense cores in a variety of star-forming regions, Walsh et al. (2004) found similarly small velocity differences and argued that this is evidence against the competitive accretion scenario. Ayliffe et al. (2007) analyzed a simulation where cores undergo competitive accretion and produced mock observations to match the Walsh et al. (2004) survey. Ayliffe et al. (2007) found they could match the small velocity differences at later times in the simulation, however, the dense core line width at later times greatly exceeded that found in observations. This illustrates that 'observations' of simulations are necessary for comparisons, as they can produce unexpected results. The Perseus observations of Chapter 3 extend this result to a more clustered star formation environment, where competitive accretion is predicted to be more effective (see, for example, Ayliffe et al., 2007).

Using estimates of the mass and size of the dense cores from the SCUBA observations and the internal velocity dispersion from the N_2H^+ survey, Chapter 3 furthermore showed that the dense cores appear to be in virial equilibrium, so long as the surface pressure on the cores (from the overlying mass of the cloud) is considered.

Simulators have started to 'observe' similar kinematic measures in their simulations, such as the internal velocity dispersion of cores (Klessen et al. 2005; Ayliffe et al. 2007; Offner et al. 2008; Chapter 5) and the core-to-envelope velocity difference (Ayliffe et al. 2007, Chapter 5). These measurements allow for a direct comparison between the observational kinematic surveys and the simulations. In this chapter,

we use the multi-scale kinematic data available in the Perseus molecular cloud to determine the relationship between the dense cores and the lower-density cloud gas. These measurements provide an additional avenue by which to test future models of star formation.

4.2 OBSERVATIONS

Our analysis here is based primarily on two datasets - a survey of the kinematics of the dense cores (N_2H^+) and their surrounding envelopes ($C^{18}O$) in Perseus (Chapter 3), and a survey of the less-dense gas (^{13}CO) spanning the entire Perseus cloud (Ridge et al., 2006; Pineda et al., 2008). Additionally, we make use of the large structures (termed 'extinction regions' here) identified in an extinction map of Perseus based on analysis of the 2MASS dataset ('extinction super cores' in KJD06, or Chapter 2). Here, we summarize the relevant information for each of these datasets.

4.2.1 Pointed N_2H^+ and $C^{18}O$ Observations

Using the IRAM 30 m telescope, Chapter 3 made single pointing observations in frequency-switching mode of N_2H^+(1–0) and $C^{18}O$(2–1) in 157 candidate dense cores in Perseus. The beamsize was 25″ for N_2H^+ and 11″ for $C^{18}O$. The positions observed were selected primarily based on the SCUBA submillimetre analysis of KJD06, with additional targets selected based on a visual inspection of the Palomar plates and the location of the maxima of large-scale structures seen in the 2MASS-based visual extinction map of Perseus (KJD06, also shown in Chapter 2). N_2H^+ emission was detected in the majority of pointings (97), with the highest fraction of detections belonging to the SCUBA dense core list and lower fractions for the others. $C^{18}O$ emission was detected in all but one of the pointings. Linewidths, centroid velocities, and integrated intensities were measured for all of the spectra with detected signal. N_2H^+(1–0) has seven hyperfine components in its spectrum and these were simultaneously fit using CLASS's hyperfine fitting program. The vast majority of the N_2H^+ spectra required a single component (Gaussian) velocity fit, and of the few cases where a second velocity component was required, the two components were usually discernible in the spectrum. The $C^{18}O$ spectra were fit with a single Gaussian where appropriate, but more frequently required a two-component Gaussian fit. When N_2H^+ spectra are plotted in this chapter, the single Gaussian profile derived

from the model fit is shown for simplicity.

The N_2H^+ dense cores were further divided into protostellar and starless, based on associations with the Perseus embedded YSO catalog of Jørgensen et al. (2007). This YSO catalog uses two criteria of which protostars must satisfy at least one. The first criterion is the spatial coincidence of a *Spitzer* source and a SCUBA core, and the second criterion is colours that satisfy [3.6] - [4.5] $>$ 1 and [8.0] - [24] $>$ 4.5 in the *Spitzer* bands, i.e., colours that have been previously shown to select YSOs (see Jørgensen et al., 2007, for more details).

4.2.2 ^{13}CO Map

The ^{13}CO(1–0) data were obtained by the COMPLETE team[1] using the SEQUOIA focal plane array at the FCRAO telescope (Ridge et al., 2006). The region mapped covers $\sim$20 deg^2, with a 46″ angular resolution and 0.066 km s^{-1} velocity channels. The data were baselined and convolved onto a 23″ grid; the average noise is 0.1 K (in T_a^* scale). A detailed comparison between the molecular line data and extinction is presented by Pineda et al. (2008).

4.2.3 2MASS Extinction

In addition to the above datasets, a map of the visual extinction throughout the Perseus cloud has been produced based on reddening of stars in the 2MASS catalog (Ridge et al. 2006; KJD06 and Chapter 2). This map was created using the NICER technique (Lombardi & Alves, 2001), and was first presented in KJD06. The extinction map provides a useful dataset for defining the large-scale structures in Perseus. While this is not the only way to classify the large-scale column density structures, it has the advantage of being simpler than disentangling structures in a spectral cube. In datasets with clustered emission features, which are particularly prevalent in ^{13}CO maps of molecular clouds, the emergent properties of the structures identified are particularly sensitive to the precise structure-identifying algorithm and parameters used (see, for example, Pineda et al., 2009). For our analysis here, we use the large-scale structures identified in KJD06, and summarized in Chapter 2 using the 2D version of *clfind* (Williams, de Geus, & Blitz, 1994) algorithm with a threshold of 3 mag and a stepsize of 1 mag on the extinction map smoothed to 5′ resolution. The relevant

[1]All of the COordinated Molecular Probe Line Extinction Thermal Emission (COMPLETE) Survey data are publicly available at `http://www.cfa.harvard.edu/COMPLETE/`

properties of these extinction regions are summarized in KJD06 (Table 3, reproduced here in Table 2.2) and Chapter 3 (Table 3.5).

Figure 4.1 summarizes the data analyzed in this chapter. The greyscale image shows the integrated intensity of the ^{13}CO data, while the triangles show the N_2H^+ and $C^{18}O$ pointings. The total column density, as measured by the extinction observed in the 2MASS dataset is overlaid as contours.

4.3 RELATIVE MOTIONS AT THE DENSE CORE POSITIONS

In Chapter 3, we showed that there is little motion between the dense cores (N_2H^+) and their surrounding envelopes ($C^{18}O$) in Perseus – the motion is always much less than the envelope velocity dispersion and for 90% of the cores, is less than the sound speed. This implies that the dense core is dynamically coupled to its surrounding envelope, and appears to argue against the competitive accretion scenario (Chapter 3; Walsh et al 2004, but see also Ayliffe et al 2007). Since ^{13}CO(1–0) is sensitive to lower density material than $C^{18}O$(2–1), we can additionally compare the N_2H^+ and $C^{18}O$ centroid velocities to that of the ^{13}CO to determine whether the tight correlation in velocities extends to the less dense material. (Note that the beamsize of the ^{13}CO observations is several times larger than that of the other tracers, so a larger physical volume of material is being traced.)

Figure 4.2 shows the difference in centroid velocity between the three species at the same location; these data are also provided in Table 4.1. (Note that in the figure and accompanying analysis, only the ^{13}CO Gaussian fits deemed 'good', roughly 87%, were used.) As can be seen from the figure, the spread in velocity difference is much smaller between N_2H^+ and $C^{18}O$ than between N_2H^+ and ^{13}CO. The standard deviation of the centroid velocity differences are 0.19 km s^{-1} (N_2H^+ - $C^{18}O$) and 0.33 km s^{-1} (N_2H^+ - ^{13}CO), while the sound speed is 0.23 km s^{-1} for the mean gas (assuming a temperature of 15 K and a mean molecular weight of $\mu = 2.33$). The thermal velocity dispersion in ^{13}CO gas at the same temperature is 0.07 km s^{-1}.

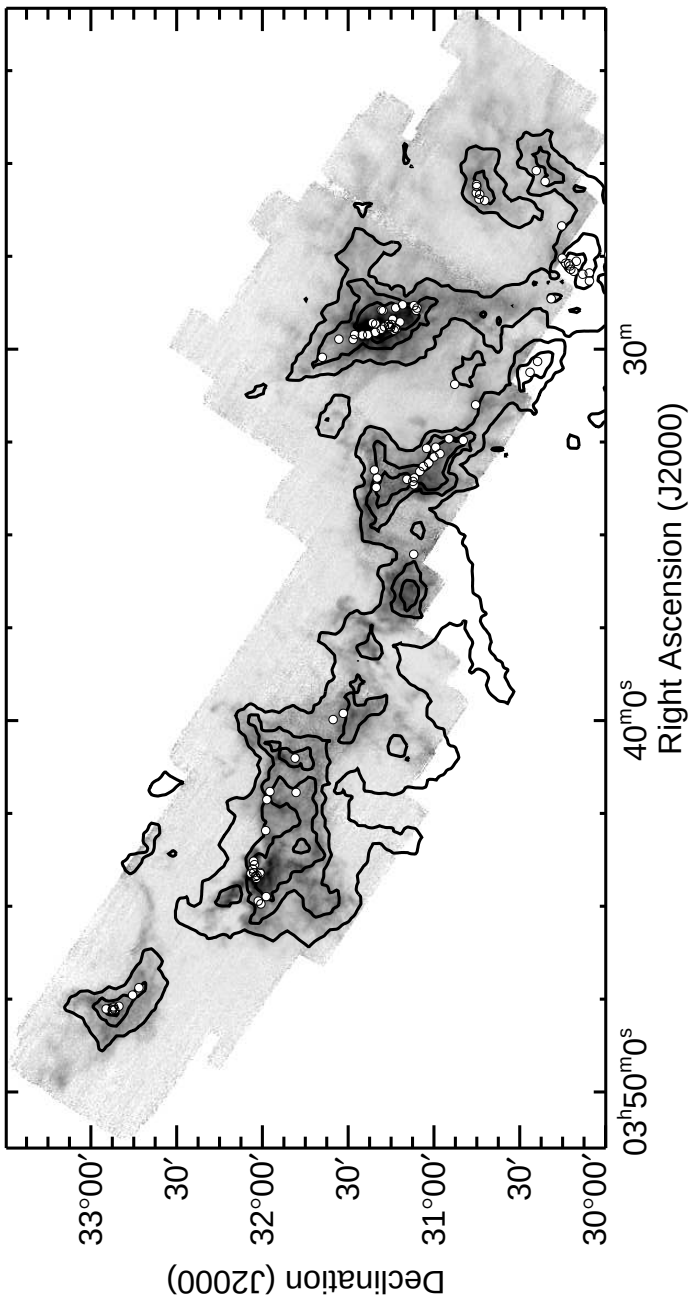

Figure 4.1 The greyscale image shows the ^{13}CO integrated intensity map from the FCRAO telescope. The overlaid contours show extinction measurements derived from 2MASS data. The white circles show the locations of all of the IRAM 30 m N_2H^+ observations. See text for details.

Table 4.1. N_2H^+ to ^{13}CO Relative Motions

N_2H^+ [a] #	N_2H^+ - $C^{18}O$ [a] Δ V (km s^{-1})	N_2H^+ - $C^{18}O$ [a] σ V (km s^{-1})	N_2H^+ - ^{13}CO point [b] Δ V (km s^{-1})	N_2H^+ - ^{13}CO point [b] σ V (km s^{-1})	Good Fit?	Region[c] #	N_2H^+ - ^{13}CO region [d] Δ V (km s^{-1})	N_2H^+ - ^{13}CO region [d] σ V (km s^{-1})	Good Fit?
4	0.13	0.91	0.11	0.58	Y	1	0.19	0.64	Y
5	0.01	1.00	0.21	0.64	Y	1	0.15	0.64	Y
6	0.19	0.86	0.35	0.67	Y	1	0.32	0.64	Y
8	-0.13	0.53	-0.19	0.50	Y	1	0.02	0.64	Y
12	-0.10	0.40	0.32	0.69	Y	1	0.71	0.64	Y
13	0.01	0.41	0.44	0.67	Y	1	0.94	0.64	Y
15	-0.17	0.86	-0.09	0.61	Y	2	0.14	0.91	Y
16	0.06	1.36	0.50	0.78	Y	2	1.07	0.91	Y
18	0.33	1.23	0.54	0.83	Y	2	1.12	0.91	Y
19	-0.01	0.67	0.03	0.64	Y	2	-0.25	0.91	Y
20	0.02	0.62	0.14	0.65	Y	2	-0.23	0.91	Y
21	0.20	1.00	0.41	0.71	Y	2	0.22	0.91	Y
22	-0.49	1.13	-0.55	0.68	Y	2	-0.69	0.91	Y
23	0.02	0.75	-0.19	0.82	Y	2	-0.53	0.91	Y
24	-0.02	0.85	0.17	0.75	Y	2	-0.06	0.91	Y
25	0.12	0.81	0.32	0.64	Y	2	0.26	0.91	Y
26	0.04	0.57	-0.22	0.67	Y	2	-0.24	0.91	Y
27	-0.48	0.57	-0.54	0.55	Y	2	-0.56	0.91	Y
27	-0.02	0.57	-0.08	0.55	Y	2	-0.10	0.91	Y
28	-0.21	0.98	-0.42	0.57	Y	2	-0.34	0.91	Y
30	0.10	0.44	0.19	0.56	Y	2	0.04	0.91	Y
33	0.11	0.50	0.65	0.79	N	2	0.65	0.91	Y
34	-0.03	0.58	-0.20	0.63	Y	2	-0.59	0.91	Y
36	0.03	0.35	0.26	0.61	Y	2	0.59	0.91	Y
41	0.06	0.39	0.39	0.89	Y	2	-0.35	0.91	Y
53	0.10	0.50	0.36	0.65	Y	3	0.73	1.01	Y
55	0.06	0.50	0.57	0.90	N	3	0.45	1.01	Y
63	-0.06	0.64	-0.08	0.70	Y	4	-0.35	0.88	Y
67	-0.40	1.00	-0.66	0.71	Y	5	-0.46	0.89	Y
68	0.11	1.04	0.31	0.92	Y	5	0.23	0.89	Y
71	0.25	0.85	-0.07	0.85	Y	5	-0.03	0.89	Y
72	-0.20	1.20	-0.38	0.94	Y	5	-0.42	0.89	Y
73	-0.22	0.95	-0.24	0.81	Y	5	-0.26	0.89	Y
74	-0.09	0.86	-0.18	0.70	Y	5	0.15	0.89	Y
75	-0.07	0.89	-0.16	0.83	Y	5	-0.06	0.89	Y
76	-0.12	0.73	-0.20	0.61	Y	5	-0.18	0.89	Y
77	-0.04	0.79	-0.15	0.84	Y	5	-0.05	0.89	Y
78	-0.01	1.09	-0.19	0.91	Y	5	-0.02	0.89	Y
79	0.25	1.02	0.09	0.91	Y	5	0.13	0.89	Y
84	-0.21	0.79	0.23	0.96	Y	5	-0.08	0.89	Y
85	-0.09	0.98	-0.16	0.71	Y	5	-0.28	0.89	Y
86	0.01	0.96	0.25	0.74	Y	5	0.21	0.89	Y

Table 4.1 (cont'd)

N_2H^+ [a] #	N_2H^+ - $C^{18}O$ [a] Δ V (km s^{-1})	σ V (km s^{-1})	N_2H^+ - ^{13}CO point [b] Δ V (km s^{-1})	σ V (km s^{-1})	Good Fit?	Region[c] #	N_2H^+ - ^{13}CO region [d] Δ V (km s^{-1})	σ V (km s^{-1})	Good Fit?
87	0.00	0.41	-0.48	0.85	Y	5	-0.79	0.89	Y
90	-0.07	1.08	-0.19	0.94	Y	6	0.41	0.91	Y
91	0.05	0.56	0.68	0.87	Y	–	–	–	N
92	0.02	0.57	–	–	–	6	-0.44	0.91	Y
93	-0.23	0.60	–	–	–	6	-0.58	0.91	Y
94	-0.08	0.67	–	–	–	6	-0.62	0.91	Y
95	0.05	0.52	-0.07	0.39	Y	7	0.53	1.25	Y
96	0.01	0.71	-0.10	1.17	N	7	-0.08	1.25	Y
97	-0.01	0.49	-0.00	0.48	Y	7	-0.12	1.25	Y
98	0.08	1.05	-0.29	0.91	Y	7	-0.15	1.25	Y
99	0.01	0.39	-0.09	0.74	N	7	-0.08	1.25	Y
99	0.00	0.46	-0.72	0.74	N	7	-0.71	1.25	Y
100	-0.03	0.71	-0.14	0.81	Y	7	-0.10	1.25	Y
101	-0.14	1.42	0.27	1.15	Y	7	0.59	1.25	Y
102	0.12	1.11	0.18	1.04	N	7	0.22	1.25	Y
103	0.19	0.86	-0.58	1.22	Y	7	-0.83	1.25	Y
103	0.55	0.86	-0.22	1.22	Y	7	-0.47	1.25	Y
104	0.05	1.41	0.88	1.57	Y	7	0.97	1.25	Y
106	0.19	1.92	0.06	1.19	Y	7	-0.13	1.25	Y
107	0.25	0.41	-0.38	1.22	Y	7	-0.38	1.25	Y
109	-0.04	1.49	0.62	1.51	Y	7	0.86	1.25	Y
110	0.41	1.88	0.43	1.26	Y	7	0.35	1.25	Y
111	0.14	1.59	-0.52	1.25	Y	7	-0.80	1.25	Y
111	0.35	2.13	0.40	1.25	Y	7	0.12	1.25	Y
112	0.22	1.51	0.65	1.38	Y	7	0.78	1.25	Y
113	0.24	1.46	0.36	1.18	Y	7	0.35	1.25	Y
115	-0.30	1.53	-0.20	1.22	Y	7	-0.46	1.25	Y
116	-0.17	1.53	0.04	1.01	Y	7	0.21	1.25	Y
118	-0.28	1.31	-0.27	1.21	Y	7	-0.28	1.25	Y
118	0.12	1.31	0.13	1.21	Y	7	0.12	1.25	Y
121	-0.06	0.92	0.20	0.94	Y	7	-0.40	1.25	Y
122	-0.08	0.96	-0.29	0.74	N	7	0.36	1.25	Y
123	-0.15	0.94	-0.18	0.72	N	7	0.57	1.25	Y
124	0.13	1.57	0.06	0.98	Y	7	-0.58	1.25	Y
125	-0.07	0.70	-0.46	0.93	Y	7	-0.34	1.25	Y
126	-0.02	1.64	-0.17	1.12	Y	7	-0.78	1.25	Y
127	0.04	0.43	-0.02	0.46	Y	9	0.18	0.87	Y
128	0.07	1.40	-0.28	1.13	N	7	-0.41	1.25	Y
129	0.01	0.23	–	–	–	9	-0.80	0.87	Y
130	-0.01	0.67	–	–	–	9	-0.51	0.87	Y
131	0.05	0.38	–	–	–	9	-0.58	0.87	Y
132	-0.37	1.01	–	–	–	9	-0.59	0.87	Y

Table 4.1 (cont'd)

N_2H^+ [a] #	N_2H^+ - $C^{18}O$ [a] Δ V (km s^{-1})	σ V (km s^{-1})	N_2H^+ - ^{13}CO point [b] Δ V (km s^{-1})	σ V (km s^{-1})	Good Fit?	Region[c] #	N_2H^+ - ^{13}CO region [d] Δ V (km s^{-1})	σ V (km s^{-1})	Good Fit?
133	-0.16	1.07	–	–	–	9	-0.30	0.87	Y
134	-0.04	0.70	–	–	–	9	-0.49	0.87	Y
135	0.04	0.70	–	–	–	9	-0.64	0.87	Y
136	0.24	1.34	–	–	–	9	-0.72	0.87	Y
136	0.04	0.45	–	–	–	9	0.58	0.87	Y
138	-0.17	0.90	–	–	–	9	-0.29	0.87	Y
139	0.17	0.97	–	–	–	9	-0.27	0.87	Y
140	0.00	0.27	–	–	–	9	-0.02	0.87	Y
143	0.00	0.46	0.12	0.56	Y	9	-0.27	0.87	Y
145	-0.18	1.31	-0.42	0.60	N	10	-0.94	0.81	Y
146	0.15	0.88	0.06	0.71	Y	10	0.13	0.81	Y
147	0.09	0.86	0.05	0.70	Y	10	0.28	0.81	Y
148	-0.25	0.53	0.35	0.80	Y	10	0.75	0.81	Y
148	0.22	1.02	0.27	0.80	Y	10	0.67	0.81	Y
149	0.16	1.07	0.01	0.79	N	10	0.15	0.81	Y
150	-0.04	0.68	-0.20	0.74	N	10	-0.31	0.81	Y
151	0.11	0.56	0.08	0.47	Y	11	0.23	0.88	Y
152	0.03	0.74	-0.04	0.62	N	10	-0.28	0.81	Y
155	0.04	0.49	-0.20	0.45	N	11	-0.14	0.88	Y

[a] N_2H^+ core number, N_2H^+ to $C^{18}O$ relative velocity, and $C^{18}O$ velocity dispersion from Kirk, Johnstone & Tafalla (2007).

[b] N_2H^+ to ^{13}CO relative velocity and ^{13}CO velocity dispersion at the point of the N_2H^+ observation, and whether the ^{13}CO fit was deemed good. Only good fits were used in the analysis.Dashes denote regions where ^{13}CO data does not exist.

[c] Associated extinction region.

[d] ^{13}CO relative velocity and linewidth for the region and whether the ^{13}CO fit was deemed good. Only good fits were used in the analysis.

A second way to measure the relative motion between the species is to compare the difference in velocity to the velocity dispersion of the less dense species. This normalized velocity difference is written as:

$$\delta V_{norm} = \frac{V_A - V_B}{\sigma V_B} \tag{4.1}$$

This quantity indicates whether the dense core moves within the typical range of motions present in the lower density environment. Chapter 5 showed that the normalized velocity difference can provide strong discrimination between numerical simulations with varying input levels of turbulence and magnetic field strengths. The normalized velocity difference was also one of the most discrepant measurements between many of the simulations analyzed in Chapter 5 and the observations of Chapter 3. Figure 4.3 shows the normalized velocity difference between the three species. The normalized velocity difference also tends to be quite small – nearly always less than

one. The standard deviations of the normalized velocity differences are 0.22 (N_2H^+ - $C^{18}O$) and 0.39 (N_2H^+ - ^{13}CO). This indicates that the motions are coherent, but less so at larger scales.

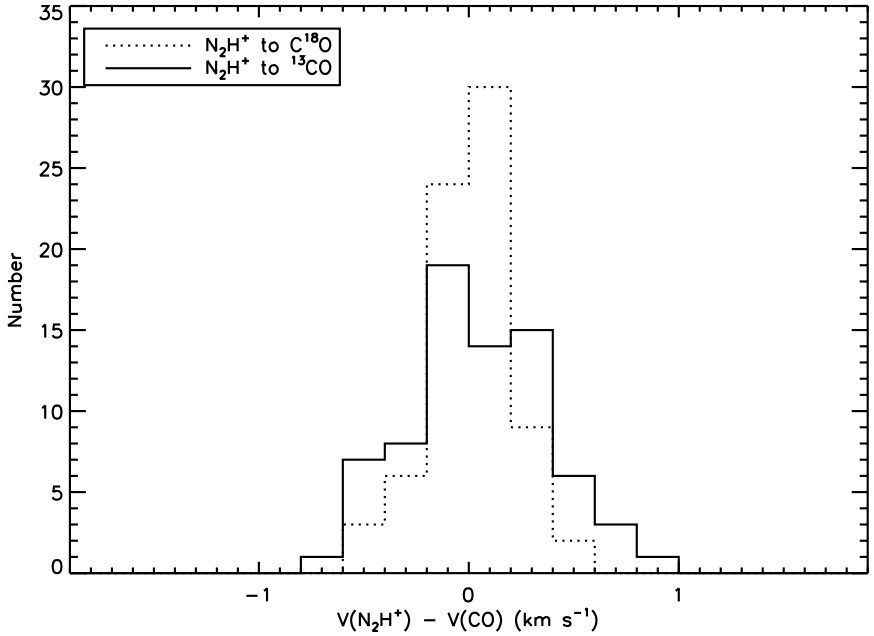

Figure 4.2 The distribution of relative motions between the dense cores (N_2H^+) and the surrounding lower density material traced in $C^{18}O$ (dotted line) and ^{13}CO (solid line).

A slight skew is apparent in both N_2H^+ - ^{13}CO distributions. We examined both distributions split up by region, and found slight skews in several of the regions (both in the same and opposite sense as the overall skew). At least some of these regional skews are likely due to small number statistics; a visual examination of the spectra did not reveal any obvious correlations.

4.4 DENSE CORES RELATIVE TO THE EXTINCTION REGIONS

4.4.1 Calculating Extinction Region Properties

Since a full map exists for the ^{13}CO data, it is also possible to quantify the motions of the dense cores within the larger extinction regions identified in KJD06, and summa-

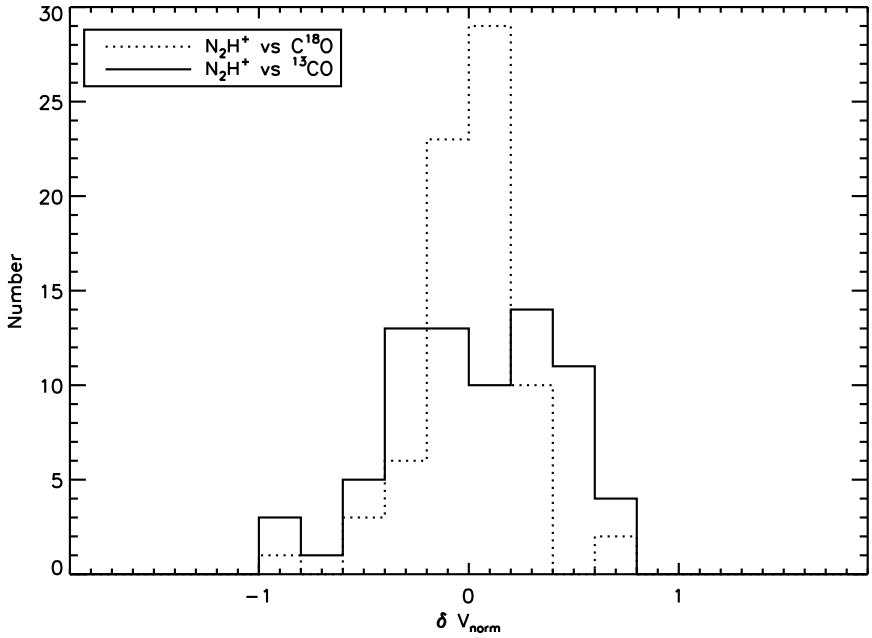

Figure 4.3 The distribution of the normalized velocity differences between the dense cores (N_2H^+) and the surrounding lower density material traced in $C^{18}O$ (dotted line) and ^{13}CO (solid line).

rized in Chapter 2. In order to more easily identify large-scale features in the regions for both this analysis and the velocity gradient analysis we present in Section 6, we first convolve and re-grid the ^{13}CO map to match the 2MASS extinction map angular resolution ($5'$) and grid. We create the mean ^{13}CO spectrum of the extinction region by summing all ^{13}CO spectra that lie within the contours of the extinction region boundaries of KJD06. We then calculate the centroid velocity and velocity dispersion of the spectrum using a single Gaussian fit. Several of the spectra are not well-fit by a single Gaussian; in Chapter 5, we found that the full width of emission was better characterized by the full width at quarter maximum (FWQM). To determine the reliability of the Gaussian fits to the spectra, we also measure the FWQM for the ^{13}CO region spectra, following the procedure outlined in Chapter 5, and convert the FWQM to the equivalent Gaussian sigma measure. Table 4.2 provides the values fit to the cumulative spectra for each region using both methods, while Figure 4.4 shows both results for all of the regions. Three of the eleven extinction regions have significantly incomplete ^{13}CO coverage. Regions that are not well-covered may not provide a good representation of the overall region kinematics, regardless of the method used

Table 4.2. Region Velocity Dispersions in ^{13}CO

Reg [a] #	Areal [a] Cov. (%)	σV_{Gauss} [b] (km s^{-1})	Good [b] Fit?	$\sigma V_{FWQM,equiv}$ [c] (km s^{-1})
1	100	0.62	Y	0.60
2	100	0.91	Y	0.88
3	95	1.04	N	0.98
4	55	0.94	N	1.18
5	100	0.87	Y	0.84
6	52	0.87	Y	0.80
7	100	1.22	N	1.20
8	100	0.83	Y	0.78
9	40	0.87	Y	0.84
10	100	0.79	N	0.74
11	84	0.76	Y	0.72

[a]Extinction region number and fractional coverage of ^{13}CO data over the extinction region.

[b]The Gaussian-fit ^{13}CO region velocity dispersion and whether the fit was judged to be good.

[c]The equivalent ^{13}CO region velocity dispersion as measured from the FWQM. See text for details.

to fit the total spectrum. We set a minimum value of 80% coverage in the ^{13}CO observations for all of our subsequent analysis. Figure 4.4 shows that when this cutoff is applied, both measures of the total velocity dispersion produce similar results. For the remainder of the analysis and for the normalized velocity difference between the N_2H^+ cores and their associated extinction regions provided in Table 4.1, only the Gaussian fit results are used.

4.4.2 Analysis

Figure 4.5 shows a histogram of the velocity differences found between the N_2H^+ centroid and the ^{13}CO centroid velocity for the extinction region in which the core resides using the fits to the region described above. The motions between the core and region again tend to be small, although larger than the difference using the ^{13}CO velocity at the location of the dense core. The standard deviation of the distribution

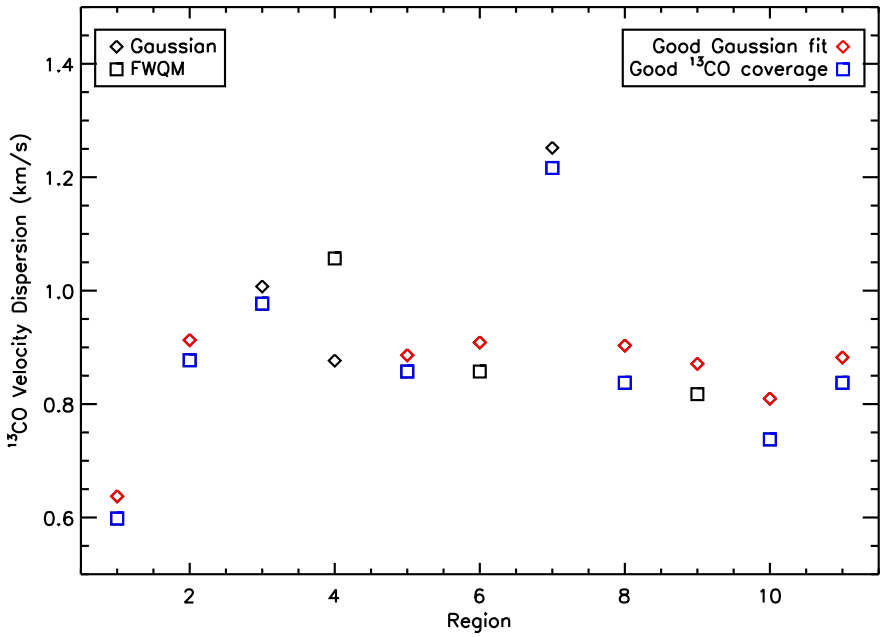

Figure 4.4 A comparison of the different measures of the velocity dispersion within each extinction region, illustrating that the measures are similar in regions where the ^{13}CO coverage is good. The ^{13}CO velocity dispersion is measured with both a single Gaussian (diamonds) and the equivalent Gaussian sigma derived from measuring the full width at quarter maximum (FWQM) of the spectra (squares). Red points denote the single Gaussian fits that were judged by eye to fit well, while blue points denote regions where the ^{13}CO data covers 80% or more of the extinction region, i.e., the spectrum is a good representation of that for the entire region. In all regions where there is good ^{13}CO coverage (blue points), both velocity dispersion measurements (diamonds and squares) are similar, regardless of whether the single Gaussian fits were judged to be good (red points) or not. The remainder of this chapter uses the single Gaussian fit measures, restricted to regions where there is good ^{13}CO coverage.

is 0.48 km s^{-1} (c.f. 0.33 km s^{-1} for ^{13}CO gas at the dense core location). Figure 4.6 shows the normalized velocity difference between the cores and regions; the standard deviation for this measure is 0.5 (c.f. 0.39 for ^{13}CO gas at the dense core location).

4.5 CORE KINEMATICS PER REGION

Most of the extinction regions contain multiple dense cores, thus the relationship between the ensemble of dense cores and the extinction region can also be examined. A reasonable question is how the relative motions of the dense cores compare to the

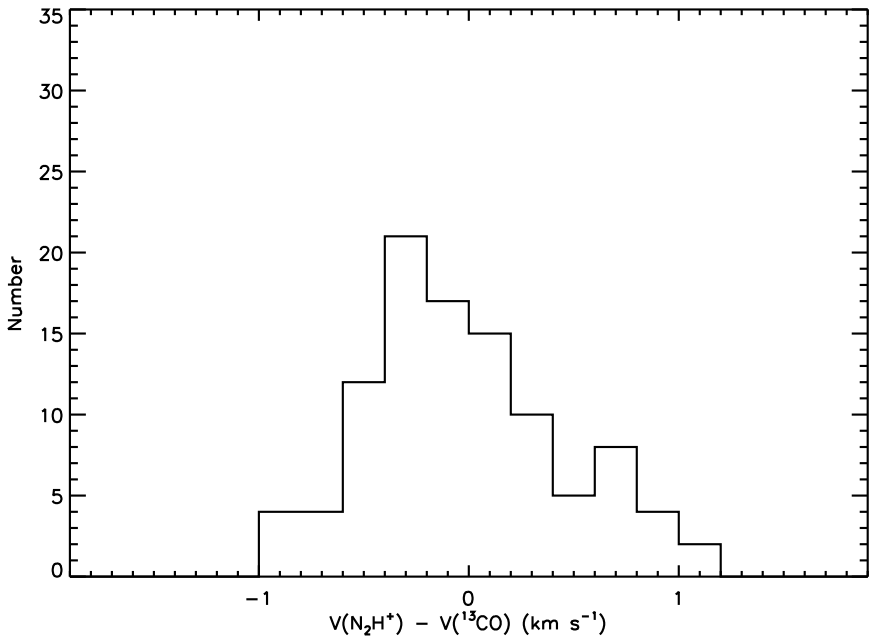

Figure 4.5 The distribution of the motions of the dense cores (N_2H^+) relative to the larger (^{13}CO) extinction regions they are found in.

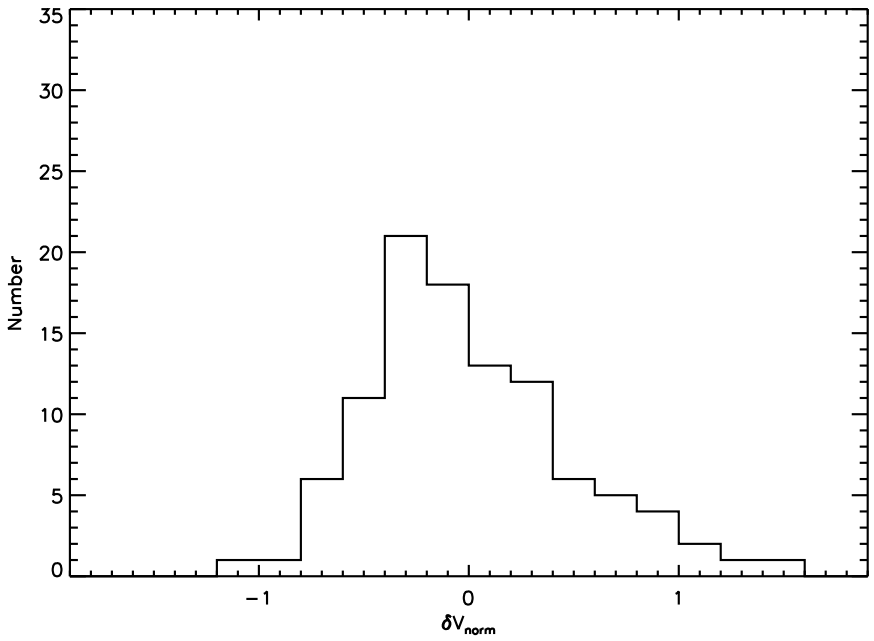

Figure 4.6 The distribution of the normalized velocity differences of the dense cores to the larger (^{13}CO) extinction regions they are found in.

motions within the region as a whole. This should reveal how connected the dense cores are to the lower density gas in the region. If the dense cores are connected to the large-scale turbulent motions, then the dispersion in the core-to-core motions would be expected to be similar to the global velocity dispersion of the region. If, however, the core-to-core motions are much smaller than the global velocity dispersion of the region, then this may be an indication that the dense cores have become detached from the large-scale turbulent flows within the cloud.

4.5.1 Method of Calculation

Section 4.1 describes the calculation of the extinction region velocity dispersions. There are several approaches that can be taken to quantify the core-to-core motions within each extinction region. The first, method A, is a purely statistical measure, which involves simply taking the standard deviation of the centroid velocities of all of the dense cores within each region. This is effective when the spectra of each core are well described by a single, relatively narrow, velocity component. In cases where these conditions do not hold, interpretation of the standard deviation can be more difficult. This method also does not account for individual core linewidths, which could represent a significant fraction of the total dense gas velocity dispersion of the core gas. The second method, method B, accounts for both the core-to-core motion and the internal velocity dispersion through summing all of the spectra and measuring the resultant total velocity dispersion. This method may be biassed if some cores are much brighter than others, and can be particularly challenging for molecules with hyperfine transitions, due to different components blending together in the summed spectrum. In Chapter 3, we adopted method A for measuring the N_2H^+ relative motions and method B for measuring the $C^{18}O$ relative motions; here, we again adopt method A for N_2H^+, but show that method B yields similar results. Note that any regional velocity gradients present are implicitly included in both measures and are not accounted for separately.

4.5.2 Results

Figures 4.7 through 4.12 qualitatively show our main result (examined in more detail below) – the dense cores have a much lower core-to-core velocity dispersion than the velocity dispersion of the ^{13}CO regions they reside in. In the top panel of each figure, a comparison is shown between the cumulative ^{13}CO spectrum across the entire region

with measures of the dispersion seen in all the N_2H^+ dense cores. The dashed light green line shows the result for N_2H^+ from method A above (the standard deviation of the N_2H^+ centroid velocities, centred on the mean centroid velocity), while the dark green line shows the result from method B above (the dispersion of the sum of the N_2H^+ spectra). As well, the dark blue line shows the result from method B applied to the $C^{18}O$ spectra in the region. All of these cumulative spectra are compared to the region as a whole in ^{13}CO (black). The figures show that the core-to-core velocity dispersion is similar when measured using either method A or method B, and that this velocity dispersion is significantly smaller than the velocity dispersion of the region as a whole.

We now determine the above result more rigorously. In Chapter 3, we preferred the use of method A to measure the N_2H^+ core-to-core velocity dispersion, due to the difficulties associated with method B for N_2H^+ outlined in Section 5.1. In that work, only starless cores were considered, due to the potential for protostars to have inherited more motion from surrounding sources. Here, we measure the standard deviation both for the starless cores only as well as the full sample of cores (the full sample was plotted in Figures 4.7 to 4.12). Table 4.3 provides the values derived for the core-to-core velocity dispersion for both method A (both starless cores and the full sample) and for method B (full sample only). Figure 4.13 shows a comparison of the core-to-core velocity dispersion measured by method A for the starless cores and all cores versus the velocity dispersion of the region. As can be seen in the figure, the core-to-core velocity dispersion tends to be similar in both samples; variations between the two may be partially attributed to small number statistics.

The difference in size between the core-to-core and ^{13}CO regional velocity dispersion is sufficiently larger that it cannot be attributed to the small number of cores within each region, however. We ran a set of simulations to determine the size of the error induced by using a small number of cores to measure the underlying total velocity dispersion. Scaling the regional velocity dispersion to a value of one, we selected a sample of N_{cores} objects with velocities randomly drawn from a normal distribution (using IDL's *randomn* function), and calculated the standard deviation of the object-to-object velocity. We ran 1000 simulations for each value of N_{cores}. Figure 4.14 shows the results of this calculation. The squares indicate the mean scaled velocity dispersion determined for the 1000 simulations for every value of N_{cores}, while the vertical lines indicate the standard deviation. Sampling very small numbers of cores tends to increase the difference between the measured and intrinsic velocity

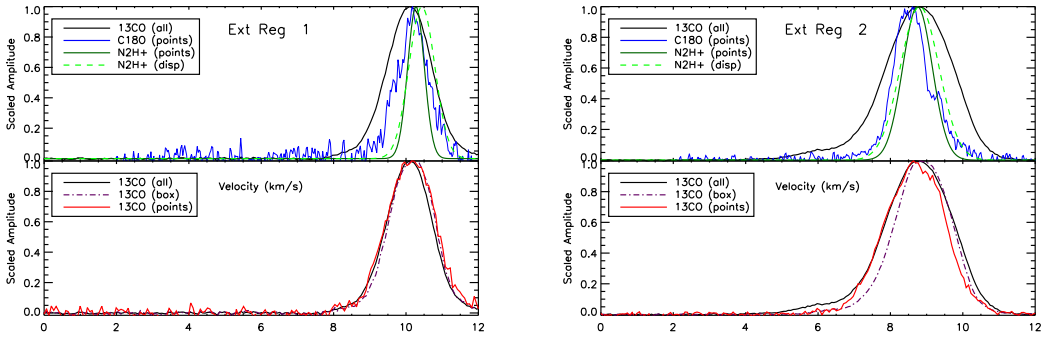

Figure 4.7 A comparison of cumulative spectra within extinction regions 1 and 2. Top panel: The ^{13}CO spectrum of the entire region from the top panel (black line), the C^{18}O spectrum summed over all locations in the region with C^{18}O detections ("method B", blue line), the resultant fit for a similar summation for N_2H^+ ("method B", dark green line), and the standard deviation of the centroid N_2H^+ velocities in each region ("method A"), centred on the mean value (light green dashed line). Bottom panel: ^{13}CO spectra derived from summing the spectra over the entire region (black line), summing over the box in which the N_2H^+ dense cores are found only (purple dot-dashed line), and summing over only the points where where N_2H^+ dense cores were detected (red line).

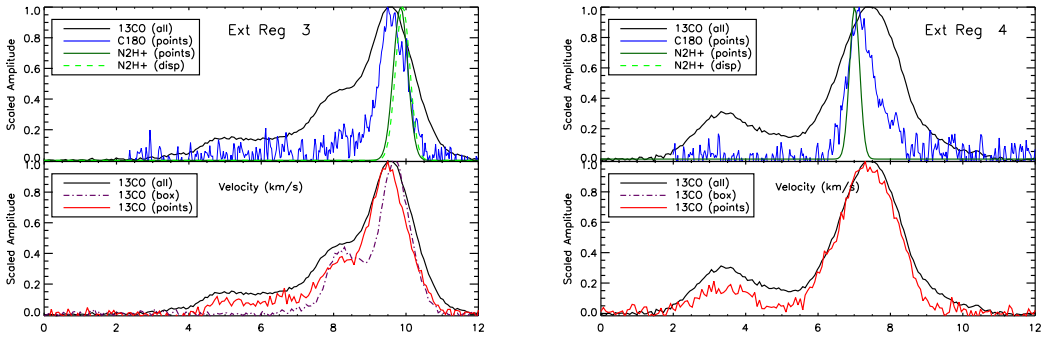

Figure 4.8 Cumulative spectra within extinction regions 3 and 4. See Figure 4.7 for the plotting conventions used.

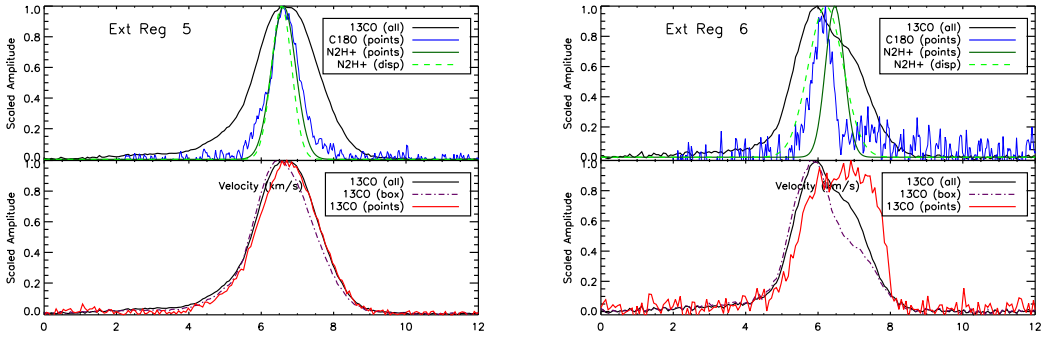

Figure 4.9 Cumulative spectra within extinction regions 5 and 6. See Figure 4.7 for the plotting conventions used. The offset in N_2H^+ centroids in extinction region 6 is caused by the small number of core (four) in the region, one of which is faint enough that it impacts the measurement from method A only.

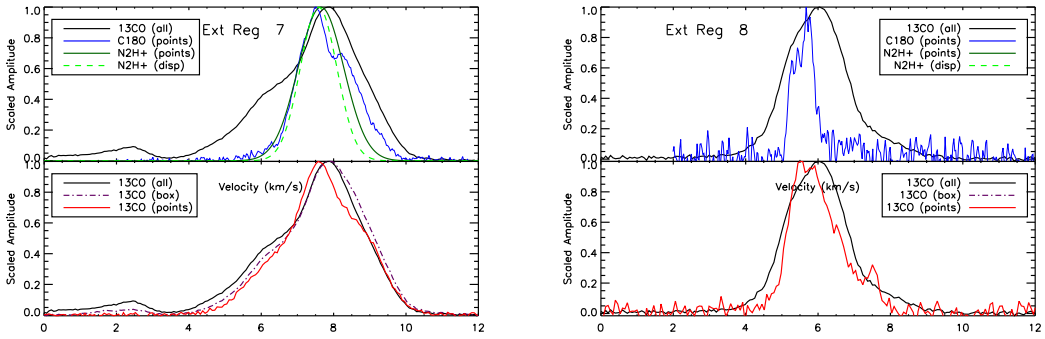

Figure 4.10 Cumulative spectra within extinction regions 7 and 8. See Figure 4.7 for the plotting conventions used.

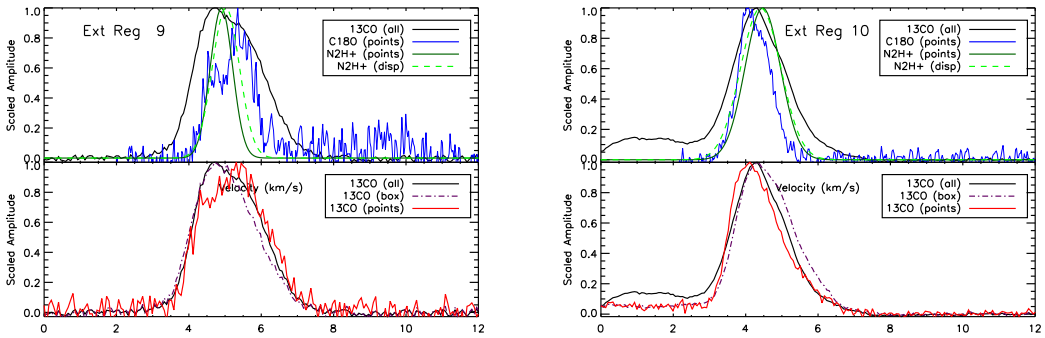

Figure 4.11 Cumulative spectra within extinction regions 9 and 10. See Figure 4.7 for the plotting conventions used.

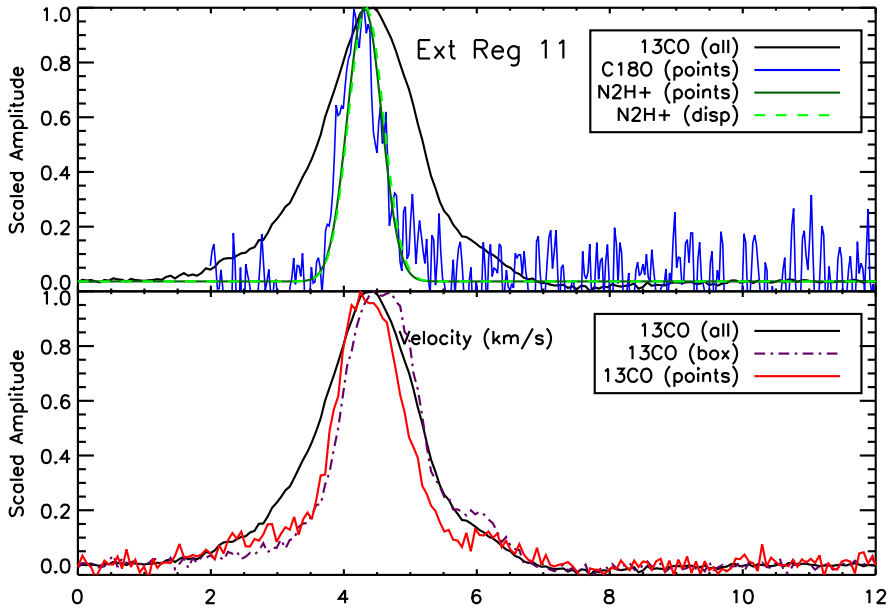

Figure 4.12 Cumulative spectra within extinction region 11. See Figure 4.7 for the plotting conventions used.

Table 4.3. Core-to-Core Velocity Dispersions

Region #	$\delta V_{sl,A}$ [a] (km s^{-1})	$\delta V_{all,A}$ [a] (km s^{-1})	$\delta V_{all,B}$ [b] (km s^{-1})
1	0.39	0.36	0.35
2	0.55	0.54	0.31
3	0.20	0.20	0.20
4	–	–	0.14
5	0.28	0.28	0.21
6	0.09	0.49	0.20
7	0.54	0.50	0.56
8	–	–	–
9	0.32	0.38	0.41
10	0.55	0.56	0.35
11	0.26	0.26	0.26

[a]Core-to-core velocity dispersion derived for starless cores and all cores using method A. Dashes denote regions with less than two cores. See text for details.

[b]Core-to-core velocity dispersion derived for all cores using method B. Dashes denote regions with no cores. See text for details.

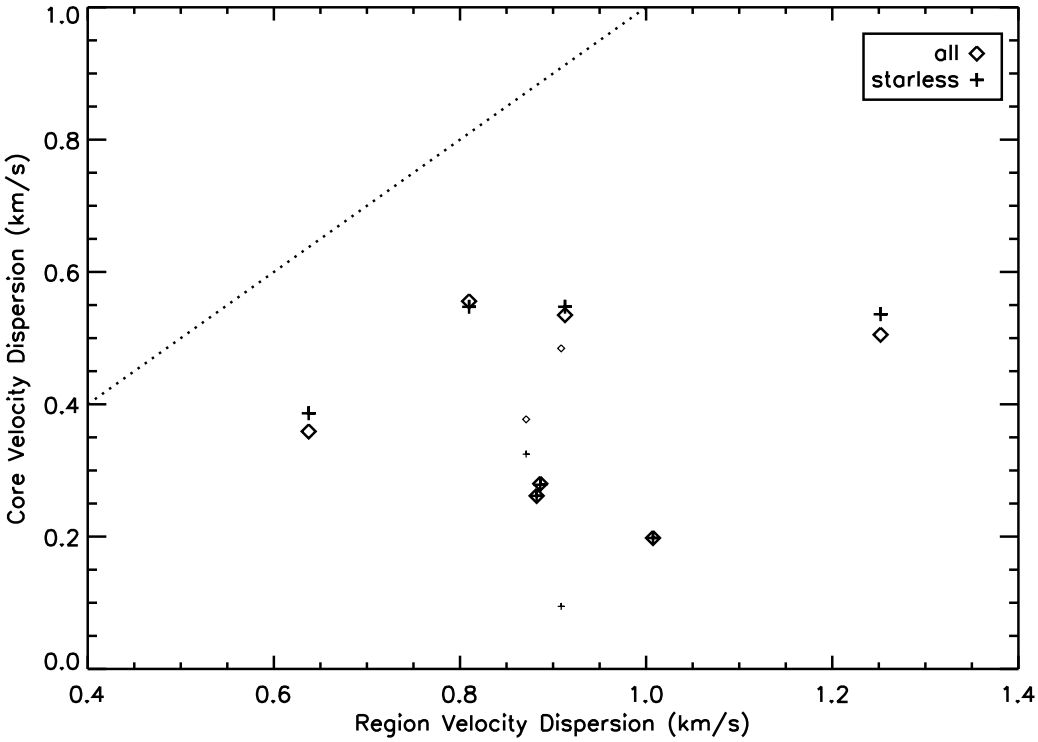

Figure 4.13 The spread in core-to-core velocity dispersions found in each extinction region versus the velocity dispersion of that region. The diamonds show the values derived using all of the dense cores within each region, while the asterisks show the values derived using only the starless cores within each region. The smaller symbols denote the values derived for the extinction regions with poor ^{13}CO coverage. The dotted line shows a 1-1 relationship.

dispersion, but does not systematically lower the measured velocity dispersion by a significant amount when more than two cores are present. The diamonds in Figure 4.14 show the observed values for our observed dense cores (including both the starless cores and protostars), with our core-to-core velocity dispersions measured scaled by the velocity dispersion of the region. The figure clearly shows that all of the observed core-to-core velocity dispersions lie well below the range of values expected for a population of objects sharing the same velocity dispersion as the parent ^{13}CO gas. By eye, the dashed line showing the simulated core-to-core velocity dispersion values multiplied by one half in Figure 4.14 provides a much better fit to the observations. This implies that if all regions have similar ratios of core-to-core versus regional velocity dispersions, a ratio of around one half is a reasonable estimate.

We conclude from this analysis that the dense cores tend to have a much smaller

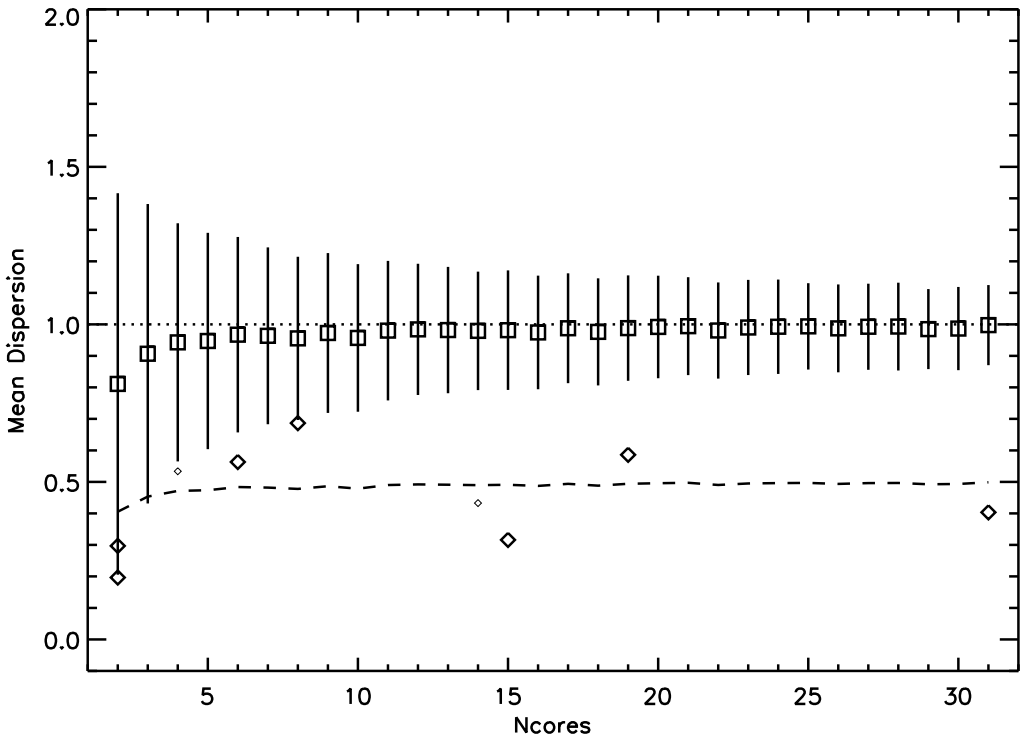

Figure 4.14 The expected range of observed core-to-core velocity dispersions relative to the distribution they were drawn from for a given number of cores. The boxes and vertical lines show the scaled mean and standard deviation of the core-to-core velocity dispersion for varying numbers of cores observed. The diamonds show our observed values scaled to the velocity dispersion of the region, with the small symbols denoting the extinction regions with poor ^{13}CO coverage. The dotted horizontal line indicates an observed velocity dispersion equal to that of the parent sample, while the dashed line shows the scaled mean core-to-core velocity dispersion values multiplied by one half.

core-to-core motion than is present in the mean ^{13}CO gas, roughly half the value, and that this result is not due to small number statistics.

4.5.3 Sampling

Since the dense cores tend to be preferentially found concentrated within a small portion of the extinction region, it is reasonable to ask whether the difference in size of the core-to-core and total region velocity dispersions is caused by spatial sampling rather than a physical difference between the two. For example, the dense cores could be at the centre of the potential well of the region and thus naturally be expected to

have a smaller velocity dispersion than the mean gas spanning the entire potential well. Here, we show that the core-to-core velocity dispersions are intrinsically smaller than the typical ^{13}CO velocity dispersions, even accounting for the difference in area sampled.

The bottom panel of Figures 4.7 through 4.12 show the total ^{13}CO spectrum for each extinction region with differing areas considered. The black line (identical to the one in the bottom panel) represents the sum of all ^{13}CO spectra within the region. The purple line shows the result that would be obtained if only the spectra within the area spanned by the cores were considered. In order to obtain this estimate, we summed only the spectra that lie within the minimal box (in RA and dec) containing all of the dense cores within the region. The resultant spectrum is similar to the total (black) spectrum, and certainly is not similar in width to the core-to-core result (green lines on the top panels).

We also considered an even more restrictive case – the red line in the bottom panel of Figures 4.7 through 4.12 shows the resultant spectrum if the ^{13}CO spectra *only at the locations of the dense cores* are used in the summation. This again shows marked similarity to the spectrum for the region as a whole, although with a lower signal to noise level.

The clustered locations of the dense cores therefore do not appear to have an impact on the measured velocity dispersions. The velocity dispersion measured for the region is similar across the region as a whole and when restricted to the area where the dense cores are located.

4.6 REGIONAL VELOCITY GRADIENTS

Finally, we analyze the large-scale features in the velocity structure of each extinction region. In order to more easily identify these features, the ^{13}CO map was convolved and re-gridded to match the 2MASS extinction map angular resolution ($5'$) and grid. We calculate the gradient of ^{13}CO centroid velocities across each extinction region by using the $5'$ colvolved ^{13}CO (see Section 4.1) and applying the gradient calculation method formulated in Goodman et al. (1993). Figures 4.15 and 4.16 show the centroid velocity measured for each cell in the convolved ^{13}CO map (colourscale) and the gradient measured (black arrows). The overall regional velocity gradient is shown in the bottom left corner of each plot. Table 4.4 provides the magnitude and orientation of the gradient measured in each region.

Table 4.4. ^{13}CO Gradients Across Each Extinction Region

Region [a] #	Gradient [b] (km s $^{-1}$ pc $^{-1}$)
1	0.15
2	0.11
3	0.18
4	0.81
5	0.23
6	0.67
7	0.32
8	0.83
9	0.93
10	0.42
11	0.63

[a]The extinction region number

[b]The velocity gradient measured across each extinction region See Section 6 for more details.

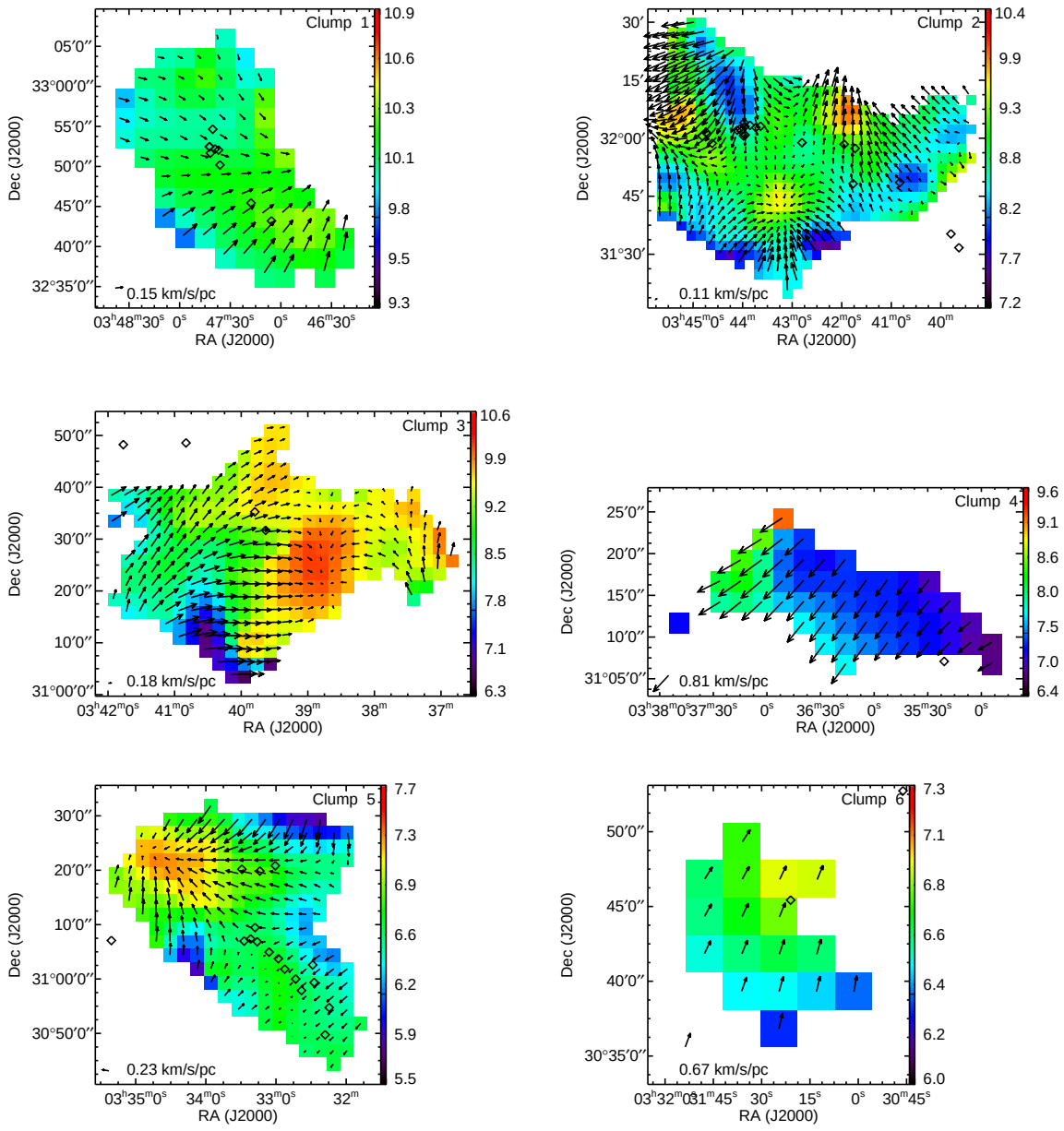

Figure 4.15 The overall velocity gradient measured for each extinction region in ^{13}CO for extinction regions 1-6. The colourscale indicates the centroid velocity of each cell, while the arrows indicate the direction of the local gradient. The overall gradient is indicated in the bottom left corner of each panel. Diamonds show the positions of the N_2H^+ cores in each region.

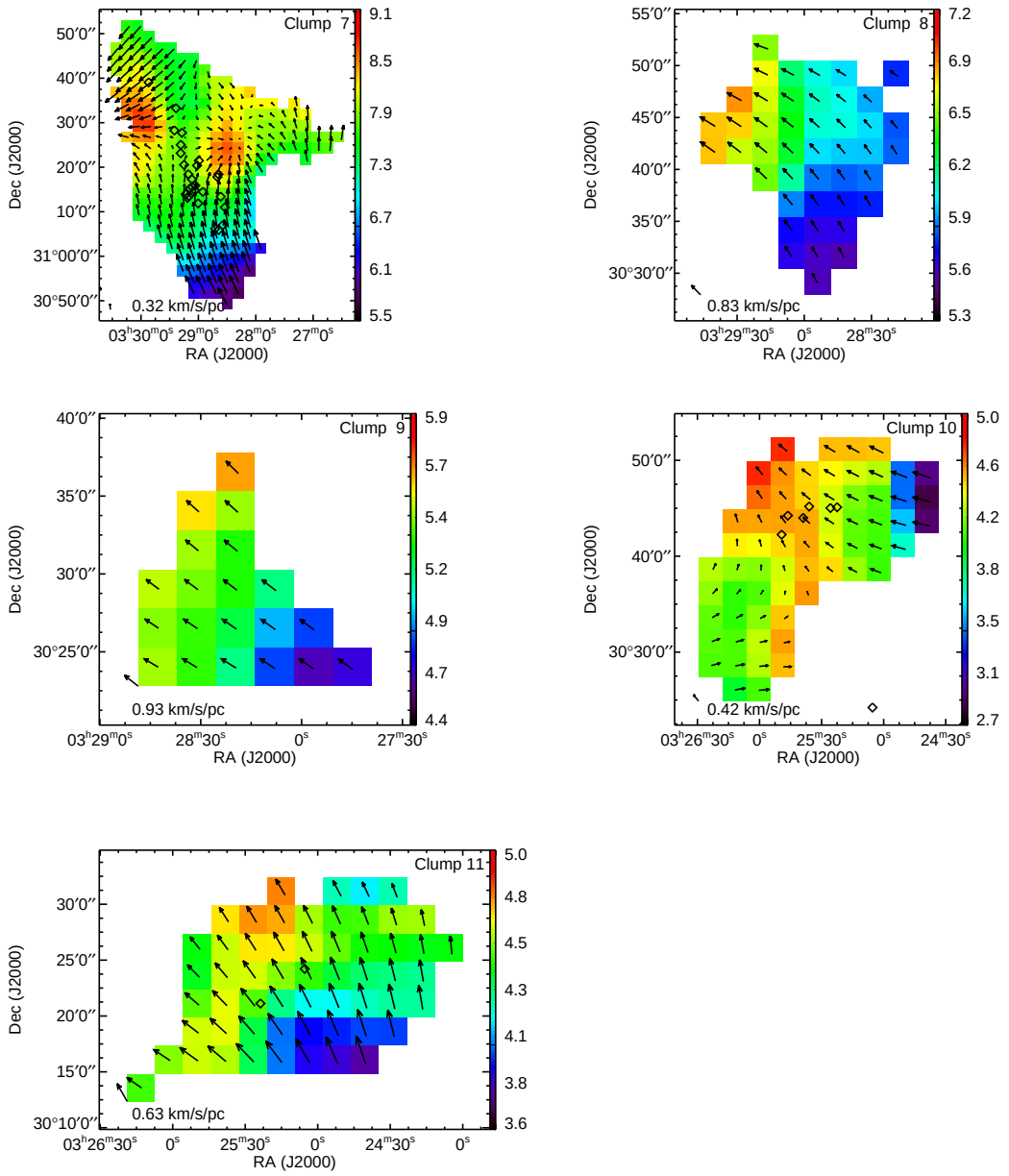

Figure 4.16 The overall velocity gradient measured for each extinction region in ^{13}CO for extinction regions 7 to 11. The colourscale indicates the centroid velocity of each cell, while the arrows indicate the direction of the local gradient. The overall gradient is indicated in the bottom left corner of each panel. Diamonds show the positions of the N_2H^+ cores in each region.

4.6.1 Cores Relative to the Gradient

If the dense cores are connected to the large-scale motions within each region, then they would be expected to follow the same large-scale gradient as is observed in ^{13}CO. We determine the velocity expected at each position in the region by using the velocity at the centre of the extinction region as a zero-point and extrapolating outwards using the gradient measured, i.e.,

$$V_{grad}(x,y) \quad = \quad V_c(x_c,y_c) + \nabla V \cdot \mathbf{d} \tag{4.2}$$

or

$$V_{grad}(x,y) \quad = \quad V_c(x_c,y_c) + \mid \nabla V \mid d_{\parallel} \tag{4.3}$$

where V_c is the velocity observed at the central position (x_c, y_c), *grad* is the gradient, and $d_{\parallel}$ is the distance from (x, y) to (x_c, y_c) in the direction parallel to the gradient's direction. Figure 4.17 shows the difference in core velocities to the velocity determined using the gradient measured in each region (red line). The deviation of individual ^{13}CO cells from the gradient-determined velocity is also shown (black line). While the cores do not perfectly follow the gradient-determined velocity, they tend to have a deviation similar to that of the typical ^{13}CO gas. There is no indication of a regional variation in this trend. Figure 4.18 shows the core velocities versus the velocities derived from the gradient extrapolation, illustrating that there is a similar relative scatter in the core velocities for every region (due to the overall gradient across Perseus, the cores from each region can be distinguished as the horizontal clusters of points).

4.6.2 Large-scale Energetics

The magnitude of the gradient across the region can be compared to the total velocity dispersion measured for the region. Regions dominated by large-scale motions such as shear or rotation, would be expected to have a high ratio of the velocity dispersion from gradient to the total velocity dispersion, whereas regions dominated by small-scale random motions would be expected to have a lower ratio.

Figure 4.19 shows a comparison of the velocity dispersion inferred from the gradient across each region (i.e., the gradient multiplied by the diameter of the region) versus the total dispersion observed in ^{13}CO. The ratio of large-scale versus total velocity dispersion is around 50% for the regions with well-determined measurements.

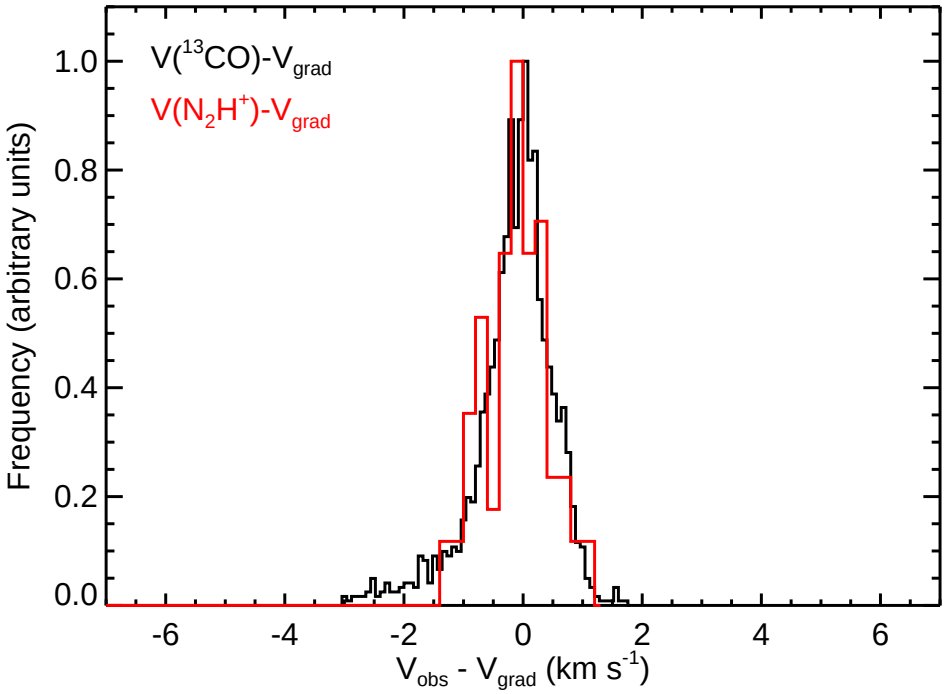

Figure 4.17 The scaled distribution of the difference between the dense core centroid velocities inferred from the extinction region (^{13}CO) velocity gradient is shown in red. The scaled distribution of the difference between the individual ^{13}CO cell centroid velocities and the velocities inferred from the extinction region (^{13}CO) velocity gradient is shown in black.

A few of the regions show ratios above 100%, which can be understood by the fact that our estimate of the large-scale velocity dispersion is crude. For example, a varying ^{13}CO column density across a region would tend to weight a limited range in velocities, and hence decrease the total velocity dispersion measured, while leaving the large-scale velocity dispersion determined from the gradient unchanged.

Turbulent motions that are dominated by large-scale modes can also produce an observable gradient. Burkert & Bodenheimer (2000) (hereafter BB00) investigated the magnitude of the gradient expected from large-scale turbulent modes for cores similar to the NH_3 cores observed in Goodman et al. (1993), Barranco & Goodman (1998), and Goodman et al. (1998). BB00 ran several thousand realizations of a 3D turbulent velocity field with power spectra of $P(k) \propto k^{-4}$ and $P(k) \propto k^{-3}$, where $P(k)$ is the power at wavenumber k; the oft-adopted Kolmogorov (incompressible turbulence) power spectrum falls within this range with $P(k) \propto k^{-11/3}$. Along with this

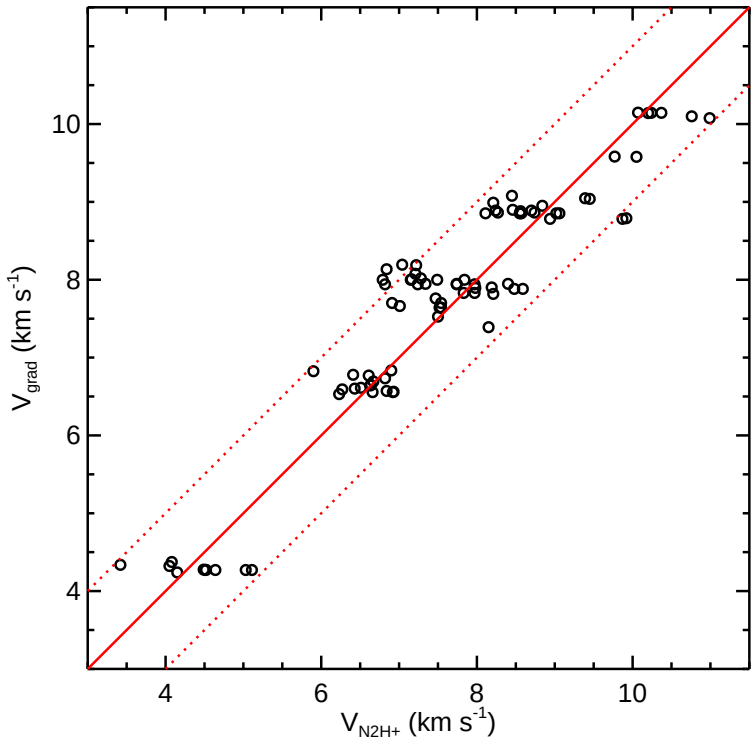

Figure 4.18 A comparison of the N_2H^+ dense core velocities with the velocity inferred from the extinction region velocity gradient. The solid line indicates a one-to-one relationship, while the dotted lines indicate a difference of 1 km s^{-1}.

turbulent velocity field, BB00 adopted a spherically symmetric, centrally-condensed density distribution. They then calculated the resultant spectra observable in 2D, and determined the gradient across the core using the same method as described in Goodman et al. (1993). The $P(k) \propto k^{-4}$ turbulent power spectrum has more power in the largest modes, and, as expected, was shown to generally produce larger observed gradients.

Although the BB00 models were run under the assumption of a single size scale (cores with a radius of 0.1 pc), BB00 assume a Larson-type scaling law with $\sigma V \propto R^{-0.5}$ to to compare their results to that of the entire Goodman et al. (1993) sample of NH_3 cores. Figure 4.20 shows the velocity dispersions and diameters of all of the extinction regions as well as the Goodman NH_3 cores. The extinction regions follow a similar trend to the Goodman cores, hence the BB00 models can be compared to the extinction regions in the same manner as was done for the Goodman cores. In Figure 4.21, we show the BB00 predictions for gradients resulting from turbulent

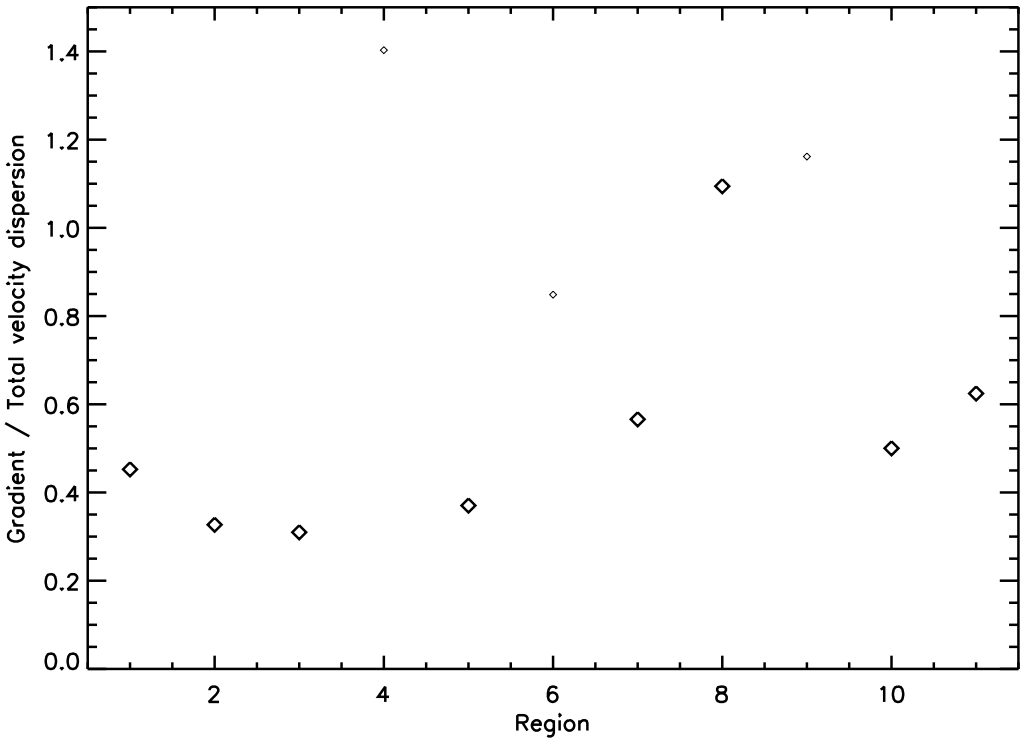

Figure 4.19 The ratio of large-scale to total velocity dispersion observed in each extinction region. The small symbols show the results for the three extinction regions where the ^{13}CO coverage was less than 80% and hence less reliable.

power spectra with $P(k) \propto k^{-4}$ and $P(k) \propto k^{-3}$ (diagonal lines), as well as the Goodman et al. (1993) data (asterisks) and our own ^{13}CO measurements (diamonds). For comparison, we also show a recent measurement of the size and velocity gradient of an embedded protostar (IRS 1) within the isolated Bok globule, BHR 71 (Chen et al., 2008). For plotting the Goodman et al. (1993) data, we adopt the same procedure as BB00 – the diameter used is the geometric mean of the Goodman et al. (1993) FWHM sizes of the major and minor axes, and updated gradient measurements for the seven sources in Barranco & Goodman (1998) replace those from Goodman et al. (1993). The thick diagonal lines indicate the most likely values of the gradient found in the BB00 simulations, while the thinner lines indicate the half maximum likelihood values. While the extinction regions we analyze are larger than the cores in Goodman et al. (1993), our observations clearly follow the same trend predicted by the BB00 model. Although the centrally concentrated density distribution adopted in the BB00 model is not a good representation of the density distribution in the regions

we analyze, BB00 state that their results are not strongly dependent on the density distribution – they found similar results when a constant density distribution was adopted. The extension of their predictions to the ^{13}CO gradients in the extinction regions measured here is therefore reasonable.

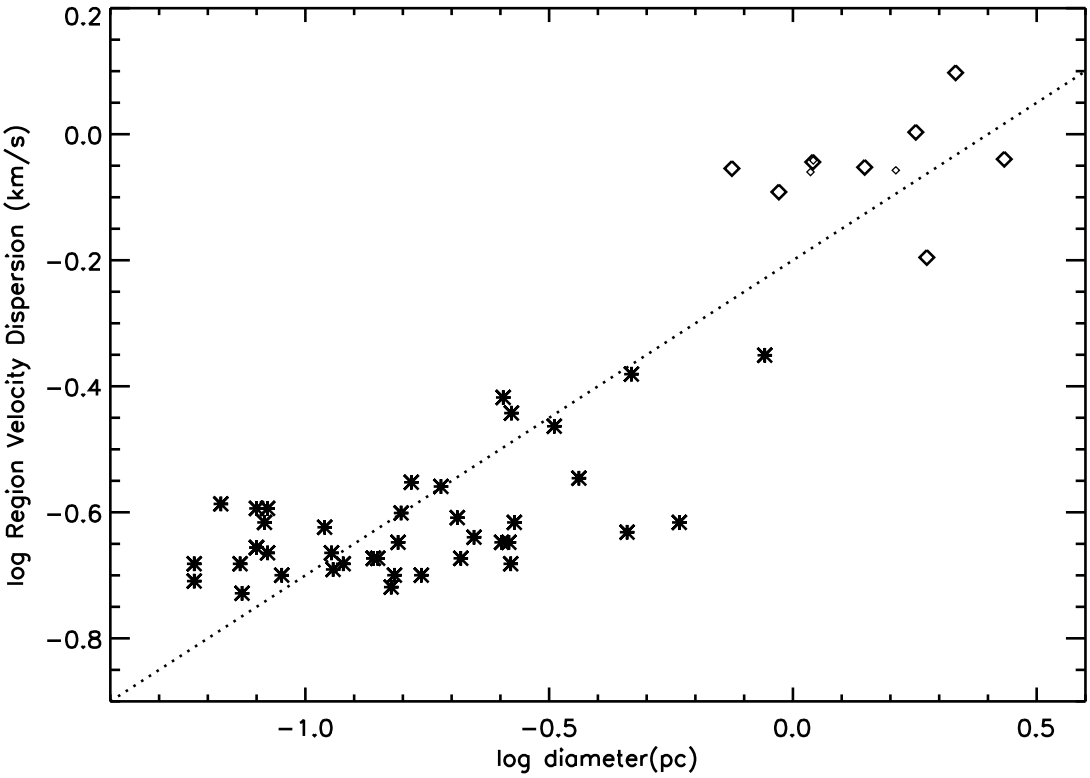

Figure 4.20 The observed velocity dispersion versus diameter for all of the extinction regions (diamonds) and NH_3 cores in Goodman et al. (1993) (asterisks). The small symbols show the results for the regions where the ^{13}CO coverage was less than 80%. The dotted line shows the slope of the scaling relationship assumed by Burkert & Bodenheimer (2000), $\sigma V \propto R^{-0.5}$. Note that a scale factor for the relationship is not given in Burkert & Bodenheimer (2000), so the line plotted is a guide to the slope only.

4.7 DISCUSSION – ENERGETICS

The above analyses all point towards a common picture of the energetics of dense cores within the context of the molecular clouds they inhabit. Previous work (e.g.,

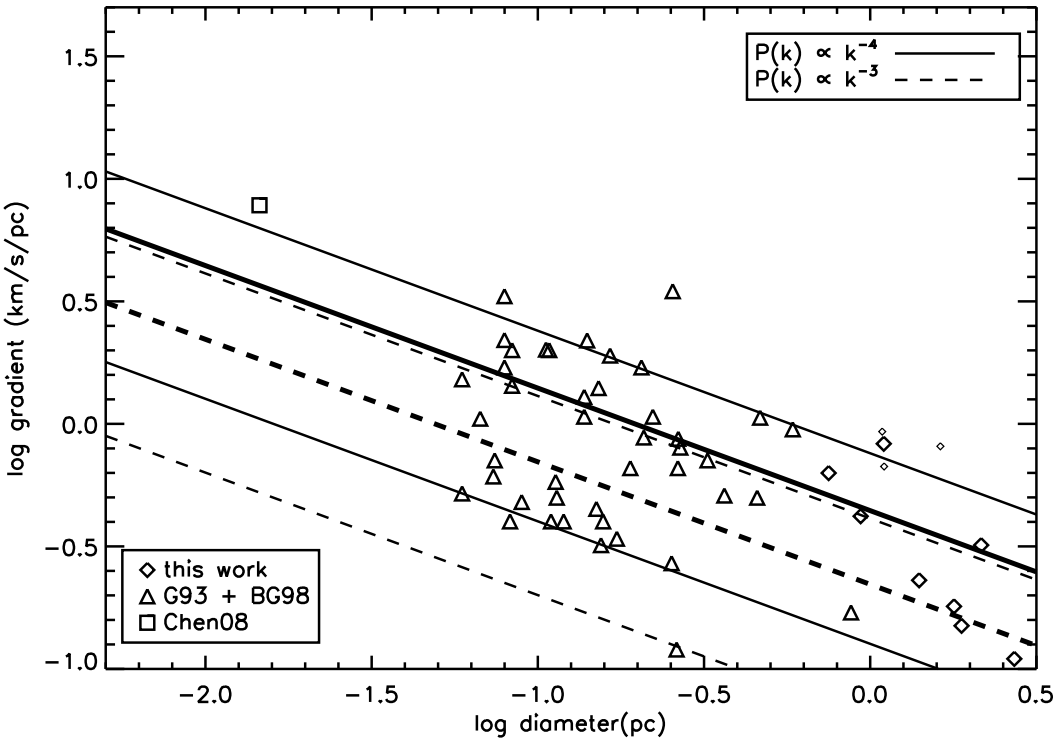

Figure 4.21 The gradient measured for each extinction region versus the diameter of the region (diamonds). The small symbols show the results for the three extinction regions where the ^{13}CO coverage was less than 80% and hence less reliable. The asterisks show the data from the NH_3 cores of Goodman et al. (1993), while the square shows data from Chen et al. (2008); see text for details. The solid diagonal lines show the range (thin) and most likely values (thick) predicted by BB00 for a k^{-4} turbulent power spectrum, while the dashed lines show the range (thin) and most likely values (thick) for a k^{-3} turbulent power spectrum.

Chapter 3) has shown that dense cores have little motion with respect to their immediate surrounding gas. This analysis has shown that the small motions continue to larger scales. Within the larger extinction regions that the cores inhabit, the cores have smaller velocities relative to the mean than the typical ^{13}CO gas. The virial velocity dispersion of the extinction regions can be estimated by two different methods – using the size and mass of the regions, or using the total ^{13}CO velocity dispersion as a proxy (see, for example, Larson, 1981). Using either estimate of the virial velocity dispersion of the region, the core-to-core velocity dispersion within each extinction region is found to be much smaller than the virial velocity dispersion (Chapter 5 and Chapter 3). This small core-to-core velocity dispersion is not due to either the

clustered locations of the dense cores within the region or the small number of cores present in each region. If all regions have the same intrinsic ratio of core-to-core versus total velocity dispersion, the ratio is roughly 0.5.

Despite the relative quiescence indicated by the dense core motions, the large-scale low density gas may be dominated by turbulent motions. Within the ^{13}CO gas, gradients were measured across each extinction region which appear to account for roughly half of the total velocity dispersion of the region. These gradients are the same size as those predicted to arise from large-scale modes of a turbulent power spectrum with $P(k) \propto k^{-4}$ (BB00).

4.8 CONCLUSIONS

We analyze the kinematic relationship between dense cores and the larger environments they inhabit using pointed N_2H^+ and $C^{18}O$ observations (Chapter 3) as well as a ^{13}CO spectral cube (Ridge et al., 2006; Pineda et al., 2008) of the Perseus molecular cloud. We find the dense cores have small motions with respect to the ^{13}CO gas at their location, with a standard deviation of 0.33 km s^{-1}, while the sound speed in the ambient medium is $\sim$ 0.23 km s^{-1}. Compared to the typical motions in the ^{13}CO gas (i.e., the velocity dispersion of the ^{13}CO), the N_2H^+ relative velocities are small, with a standard deviation of 0.39 times the ^{13}CO velocity dispersion at that location. This is an upper limit on the true value, since the ^{13}CO data have a beamsize roughly twice the size of the N_2H^+ data. The dense cores similarly have little motion with respect to the larger (extinction) regions that they inhabit, with a standard deviation of 0.46 km s^{-1}, or 0.5 times the velocity dispersion of the region. The core-to-core velocity dispersion within each of these regions is roughly half of the observed ^{13}CO velocity dispersion across the region and is also usually several times smaller than the virial velocity estimated using the mass and size of each region (Chapter 3). The dense cores tend to follow the overall velocity gradient of each extinction region to the same extent as the ^{13}CO gas. The gradients across each extinction region tend to account for roughly half of the total measured velocity dispersion, and are of the magnitude as expected by large-scale turbulent modes following a power spectrum of $P(k) \propto k^{-4}$ (Burkert & Bodenheimer, 2000). The kinematic measures presented in this chapter complement those presented in Chapter 3 and Chapter 5; jointly, these provide simple benchmarks by which to evaluate theoretical predictions and numerical simulations of star formation.

Chapter 5

The Interplay of Turbulence and Magnetic Fields in Star-Forming Regions: Simulations and Observations

5.1 ABSTRACT

We analyze a suite of thin sheet magnetohydrodynamical simulations based on the formulation of Basu, Ciolek, Dapp & Wurster. These simulations allow us to examine the observational consequences to a star-forming region of varying the input level of turbulence (between thermal and a Mach number of 4) and the initial magnetic field strength corresponding to a range of mass to flux ratios between subcritical ($\mu_0 = 0.5$) and supercritical ($\mu_0 = 10$). The input turbulence is allowed to decay over the duration of the simulation. We compare the measured observable quantities with those found from surveying the Perseus molecular cloud. We find that only the most turbulent of simulations (high Mach number and weak magnetic field) have sufficient large-scale velocity dispersion (at $\sim$1 pc) to match that observed across extinction regions in Perseus. Generally, the simulated core ($\sim$0.02 pc) and line of sight velocity dispersions provide a decent match to observations. The motion between the simulated core and its local environment, however, is far too large in simulations with high large-scale velocity dispersion.

5.2 INTRODUCTION

The study of star formation is no longer in its infancy. Both observational and theoretical advances have taken the field beyond simple descriptions and heuristic models toward a more critical examination of the physical processes involved in assembling a star within a molecular cloud. Indeed, perhaps the biggest advance in star formation studies has been the ability to connect the formation of a star with the physical properties of the molecular cloud. Theorists and simulators have thus begun to model the larger scale properties of the molecular cloud to attack the stellar Initial Mass Function (IMF) and the star formation efficiency (SFE) (see review by Bonnell et al., 2007). At the same time, observers have begun to investigate statistically meaningful samples of prestellar cores and protostars, often within a single star-forming region (see reviews by Di Francesco et al., 2007; Ward-Thompson et al., 2007).

Most stars are born in groups and associations (Lada & Lada, 2003), thus the traditional pursuit of how an isolated star forms requires either an interest in a small subset of all stars or a hope that the underlying physics of star formation is not dominated by conditions external to the local prenatal core. These investigations have nevertheless proved to be extremely useful, yielding a simple yet powerful five stage model (prestellar/Class0-III) for the collapse and ignition of an isolated stellar-mass core (Lada, 1987; André, Ward-Thompson, & Barsony, 1993). In this manner, the timescale for collapse, the evolution of the accretion luminosity, and the formation of disks and jets has been examined both theoretically and observationally (Terebey et al., 1984; Henriksen et al., 1997; Shu et al., 1994). It is hoped that if the initial physical conditions in the core can be characterized - mass, temperature, turbulent energy, angular momentum, magnetic field strength and geometry - the stellar (plus disk) properties can be inferred (at least probabilistically).

Once the simplifying assumptions of isolated collapse are removed, physical intuition becomes more difficult. Theoretical calculations become complex, and simulations take precedence in attempting to discern how a molecular cloud fragments into stars. The large discrepancy between the Jeans mass in the cloud, typically tens to hundreds of Solar masses, and the mass of either the total cloud (typically hundreds of thousands of Solar masses) or the average star formed (typically around half a Solar mass) provides incentive for studies which take star formation to be part of the evolution of the cloud itself. In this scenario, there may never be an equilibrium core stage and the final distribution of stars may be determined by the flow of mass,

energy, and magnetic fields within the evolving cloud. A large compendium of work on this topic is now available (e.g., MacLow & Klessen, 2004; Elmegreen , 2007).

Despite the complexity inherent in following the star formation process from the molecular cloud through dense core formation to the collapse to individual stars, the final outcome is quantifiable. Most simulations thus start with a particular set of initial conditions, evolve the cloud, and compare the outcome with observable quantities, primarily the IMF and SFE. The initial conditions usually attempt to recreate the observed physical conditions within the bulk cloud, concentrating on the additional support beyond thermal motion that keeps the bulk cloud from collapsing and fragmenting on a dynamical time. Thus supersonic turbulence and/or magnetic fields are utilized to provide partial support, at least initially, to the cloud. As the turbulence decays and the neutrals slip past the ions, gravity becomes dominant and the cloud collapses. Occasionally a suite of simulations with a range of initial conditions are computed and thus the variety in outcomes can be examined (e.g., Basu, Ciolek & Wurster, 2009; Basu, Ciolek, Dapp & Wurster, 2009, hereafter BCW09 and BCDW09 respectively).

Recent observations are providing new and more stringent conditions on the simulations. It is now possible to observe the dense gas and dust within an entire molecular cloud, revealing the manner in which structure forms - location, mass function, etc (e.g., Onishi et al. 1998; Johnstone, Di Francesco & Kirk 2004; Hatchell et al. 2005; KJD06 and also summarized in Chapter 2; Di Francesco et al. 2007; Ward-Thompson et al. 2007). As well, the kinematics of these dense cores and their surrounding envelopes can be detailed (e.g., Benson & Myers 1989; Jijina et al. 1999; Walsh et al. 2004, 2007; Chapter 3). It is thus time to consider how to utilize these additional constraints on star formation within the simulations.

In this chapter we consider how to appropriately 'observe' a molecular cloud simulation in order to compare the model output with the properties of real star-forming clouds. In §5.3 we describe the details of the numerical simulations. In §5.4 we introduce the observational data set used in this analysis. §5.5 discusses the manner in which the simulations are 'observed' while §5.6 discusses the results and compares with the observations. Finally, we relate the results back to the larger theoretical framework in §5.7 and conclude in §5.8. In Appendix 5.10 we furthermore show that the trends found in the preceding sections are robust.

5.3 SIMULATIONS

5.3.1 General Overview of Simulations

In order to analyze the interplay between the competing processes responsible for converting molecular cloud material into stars, along with the ensuing physical attributes, it is necessary to run (magneto)hydrodynamic simulations (see review by MacLow & Klessen, 2004). The purpose of the present chapter is to test which simulations show similarities with the observations of real molecular clouds and which observable measures provide the best discrimination between simulations with different initial conditions. We thus begin with a brief overview of the evolutionary implications of both turbulence and magnetic fields within molecular clouds, in order to set the stage for the results which follow.

In almost all simulations, the initial conditions begin with much more mass than can be supported under a simple thermal Jeans calculation. From the start of the calculation, the region is therefore inherently unstable to collapse unless additional processes are at play. Global gravitational collapse is typically delayed via the inclusion of initial supersonic turbulent motions. In keeping with both observations (e.g., Larson, 1981) and theoretical considerations, the largest length scales dominate the input turbulence. The simulated cloud therefore initially forms sheets and filaments with box crossing lengths, and it is within these over-dense regions that collapse takes place. Given the dynamic and fast evolution of these clouds, the applied initial conditions are extremely important and the explicit results should be taken with caution. The simulations provide instead an ideal laboratory for considering the time, length, and mass scales, and the efficiency of turbulent induced star formation.

An alternate mechanism which can significantly delay the global collapse of the simulated cloud is the inclusion of strong magnetic fields. The low density and moderate ionization fraction within molecular clouds leads to effective field freezing and thus magnetic fields act as an additional buoyant force opposing gravity. In sheet-like geometries, sufficiently strong magnetic fields are capable of overcoming gravity entirely and preventing collapse for an ambipolar diffusion time during which the neutral particles diffuse past the load-bearing, magnetic-field-coupled ions, eventually accumulating approximately a Jeans mass of material which is then capable of gravitational collapse.

While it is possible that either of these approaches alone may be responsible for de-

laying global cloud collapse, it is more likely that they are both present in which case the interplay between them is not at all straightforward. In addition to turbulence included in the initial conditions of a simulation, significant non-thermal motions can be generated through the gravitational collapse of non-uniformly distributed material (e.g., Burkert & Hartmann 2004). While magnetic fields oppose gravity by applying additional pressure support, supersonic turbulence both opposes gravity through enhanced kinetic energy in the gas and aids gravity through strongly compressive shocks. When both turbulence and magnetic fields are present, the turbulent shocks can be suppressed by magnetic fields. Even small enhancements in the density within these compressed regions, however, can significantly lower the ambipolar diffusion time. Meanwhile, shock compressions and rarefractions dissipate energy from the turbulent waves themselves, producing a competition between decaying turbulence and ambipolar diffusion.

Parameter studies following the evolution of molecular clouds with both magnetic fields and turbulence are greatly needed. The complicated numerical equations that must be solved in such cases make such simulations computationally expensive, however. Few large parameter studies have thus been carried out. Here, we utilize an extensive study (BCDW09) which followed the evolution of a sheet-like cloud in which significant simplifications are possible. The resolution of the simulations (128 by 128 cells) is modest, however, this is sufficient for our purposes – the simulations resolve the critical thermal length with a minimum of sixteen pixels and are stopped at an early enough stage that grid-scale fragmentation has not occurred. The analysis of BCDW09 further demonstrates the lack of impact that higher resolution has on the evolution of these simulations. As well, in Appendix B, we include our own analysis of higher resolution simulations (512 by 512 cells), which demonstrate that the coarser resolution simulations are adequate. We also note that while the geometry is simplified, and thus the turbulence and magnetic fields are idealized and unlike those expected in true three dimensional clouds, we are not attempting to prove any particular set of parameters as 'true'. Our goal is less ambitious: to determine the effect of the input parameters on observables.

We note that there are other aspects of the input parameters that still remain to be properly investigated. In particular, whether turbulent energy does indeed decay or is driven (see the recent analysis of simulated dense core observables by Offner et al., 2008). Other simulations have addressed this issue in order to determine the scale on which driving would need to occur to prevent collapse of cores (e.g., Klessen et

al., 2005). This remains, however, an open question to be considered with respect to the competition between magnetic fields and turbulence.

5.3.2 Details of the Simulations

Ciolek & Basu (2006, hereafter CB06) and BCW09 introduce and discuss in detail the setup and equations governing the evolution of the simulation with linear perturbations (see also Basu & Ciolek, 2004). The setup of simulations with turbulent initial conditions are discussed in BCDW09. Here, a few key details are highlighted. Note that the scalings applied to the simulation in order to convert from scale-free to observable quantities are given in Section 4.1. The simulations we analyze have a thin sheet geometry and are supported in the vertical direction by thermal pressure working against gravity and magnetic pinching. In the lateral direction, the evolution is governed by the interplay of thermal pressure, gravity, magnetic pinching and magnetic tension; see CB06 for a discussion on the physical justification and a detailed description of this geometry. The simulations start with uniform total (gas) column density and a constant vertical magnetic field. Velocity perturbations are added in Fourier space to wavenumbers k corresponding to wavelengths up to the simulation length in both the x and y direction. Velocity amplitudes are chosen from a Gaussian distribution scaled to the power spectrum $v_k^2 \propto k^{-4}$ (i.e., most of the power is on the largest scales). The turbulent energy in these simulations is not driven but is allowed to decay. Unlike some purely turbulent simulations, gravity is always "on"; there is no initial period where turbulence is driven without gravity.

The material in the simulation is bounded in the direction perpendicular to the sheet by external pressure and gravity, as well as smaller contributions from magnetic pressure and magnetic tension. The relative importance of the former two quantities is expressed by the dimensionless parameter $\widetilde{P}_{\rm ext}$, the initial ratio of the external pressure to the self-gravitational pressure of the sheet in the vertical direction. We analyze simulations where the external pressure is minimal and the sheets are gravitationally dominated ($\widetilde{P}_{\rm ext} = 0.1$), not unreasonable for the denser regions within molecular clouds. The other extreme, where the sheet is dominated by external pressure, would be appropriate in a situation where star formation is triggered by a supernova shock wave, for example. BCW09 analyzed a suite of simulations with both weak and strong external pressures ($\widetilde{P}_{\rm ext} = 0.1$ and 10) and found that high external pressure environments lead to the formation of much smaller cores that attain high column

density significantly faster than their low external pressure counterparts.

Considering only thermal support, the simulations begin with gravitationally unstable conditions. In the absence of external pressure, the simulations have a length of eight times the critical thermal length, or four times the lengthscale of maximum growth (see CB06 for further discussion), thus approximately sixteen objects would be expected to form. Additional support can be derived from both the input magnetic fields and turbulent velocity. We analyze simulations ranging from subcritical mass to magnetic flux ratios where there is no gravitational collapse possible without ambipolar diffusion ($\mu_0 = 0.5$ and 0.8), to critical ($\mu_0 = 1$), and supercritical ($\mu_0 = 2$ and 10)[1]. The turbulent velocity field input varies from having essentially no turbulent velocity (thermal Mach number of 0) to a Mach number of 4 in integer steps. Note that the simulations with higher Mach numbers, particularly Mach 4, showed significant qualitative differences from observations as discussed in Section 4.4, hence simulations with even higher Mach numbers were not run.

The simulations are evolved until a total (gas) column density of ten times the initial uniform value is reached. Figure 5.1 shows two sample total column density maps from the suite of simulations we analyzed. In simulations where the pressure from the magnetic field exceeds the pressure from the input turbulent motions, the magnetic field has a strong influence on the dynamics of the simulation. In particular, turbulent compressions are moderated by the restoring force of the magnetic field, hence density enhancements are smaller and tend to rebound rather than collapse due to gravity. When the magnetic fields are strong, the simulations thus require longer periods of time to reach a column density sufficient for the simulation to stop. The input turbulence is therefore able to decay to a much greater extent in these simulations than in turbulence-dominated ones. This causes the large-scale velocity dispersions to be smaller in the strongly magnetic simulations than their weakly magnetic counterparts, as seen in the analysis below. We postpone a full analysis of how the turbulent velocity field changes over the run of the simulation in these cases for a future chapter.

[1]We only analyze one simulation with $\mu_0 = 10$

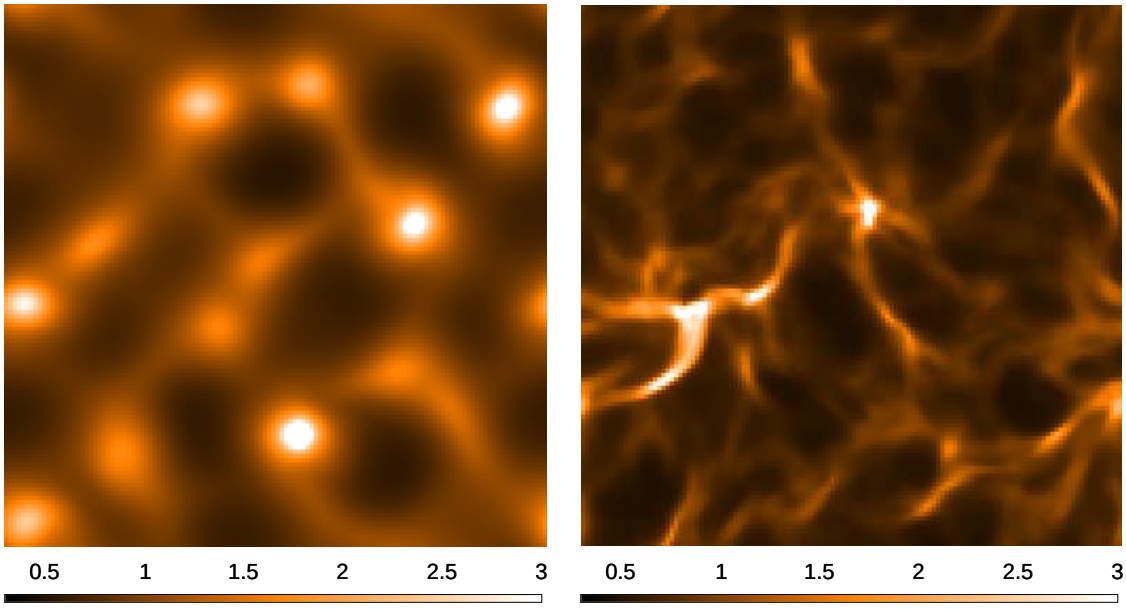

Figure 5.1 The final total gas column density in two simulations – with $\mu_0 = 0.5, M = 0$ (left) and $\mu_0 = 1.0, M = 3$ (right). The scale, in units of the initial total gas column density, is shown in the bar. Under the scalings we applied, a value of 1 corresponds to $3.5{\times}10^{21}$ cm^{-2}.

5.4 OBSERVATIONS

5.4.1 Summary of Previous Results

Previously, we conducted a large-scale pointed survey of cores and their dynamics in the Perseus molecular cloud (Chapter 3). As discussed in previous chapters, the Perseus molecular cloud is an intermediate mass star forming region located at a distance of ∼250 pc (e.g., Cernis, 1993) that displays more active and clustered star formation than seen in the low mass Taurus star forming region, but much less than seen in the high mass Orion star forming region. Our survey was thus ideal for probing the conditions of a more clustered mode of star formation without suffering from the complexity present in a region such as Orion. The dense core candidates were selected from cores observed in the submillimetre continuum using SCUBA (KJD06 and summarized in Chapter 2) and supplemented with visually-selected regions of higher extinction in the Palomar plates (and large-scale 2MASS extinction peaks). In our survey, we made single-point observations of dense core candidates simultaneously in N_2H^+(1-0) and $C^{18}O$(2-1), with beamsizes of 25″ and 11″ respectively, using the IRAM 30 m telescope in Spain. As discussed in Chapter 3, N_2H^+ is a good tracer of dense gas, with a critical density of $\sim 10^5$ cm^{-3} (Tafalla et al., 2002), while $C^{18}O$ traces lower density gas (critical density of $\sim 10^3$ cm^{-4} Schöier et al., 2005) and freezes out of the gas phase onto dust grains at $\sim 10^5$ cm^{-3} (Tafalla et al., 2002), hence the survey obtained information simultanenously about the dense core and the surrounding 'envelope' of material. We differentiated between protostars and starless cores on the basis of *Spitzer* data (Jørgensen et al., 2007). Supplemental information is also available from the COMPLETE Survey (Ridge et al., 2006) – large scale column density measures from stellar reddening observed with 2MASS (Alves & Lombardi in prep) using the NICER technique (Lombardi & Alves, 2001) as well as ^{12}CO and ^{13}CO FCRAO observations across the cloud (Ridge et al., 2006).

The survey presented in Chapter 3, based on submillimetre dust emission and optical / near-IR dust extinction - identified cores provides a useful set of dynamical constraints that simulations of star formation should match; we highlight several which are relevant to this work.

1) *Cores have little internal turbulence.* Starless cores have velocity dispersions which are dominated by thermal motions; protostars tend to have slightly larger (but still thermally-dominated) velocity dispersions. This result has been found by many

other surveys including Benson & Myers (1989) and Jijina et al. (1999).

2) *Material surrounding cores has a larger velocity dispersion.* The less-dense material (traced by $C^{18}O$ in our survey) surrounding the dense cores tends to display much larger non-thermal motions, also consistent with previous observations (e.g., Benson & Myers, 1989; Jijina et al., 1999).

3) *The relative velocity between the core and surrounding material is small.* The vast majority of dense cores (nearly 90%) have less than thermal motions with respect to their surrounding material. Previous observations (Walsh et al., 2004, 2007) concur with this result.

5.4.2 Additional Observations

In order to compare our previous results with the analysis of simulation data below, we must fold in a few additional pieces of information about larger scales. First, we note that the dense cores in Perseus are clustered within larger-scale regions, as seen in the 2MASS visual extinction map. We defined these regions in KJD06 (referred to there as 'extinction super cores' and here as 'extinction regions' for clarity); here we adopt the size and mass estimates of these regions from KJD06 (typically $10'$ and several hundred solar masses; see Table 5.1). These regions have roughly comparable sizes and masses to that found in the simulated box as discussed in the following section.

Additionally, we use the ^{13}CO data from COMPLETE (Ridge et al., 2006) to gather information on the dynamics of each extinction region. While the spatial resolution of this data cube is lower ($46''$) than our IRAM $C^{18}O$ data, it has the advantage of uniformly covering each extinction region rather than sampling a set of sparse and biased locations. We calculate the velocity dispersion along each line of sight by fitting a single Gaussian to each ^{13}CO spectrum. Additionally, we calculate the total velocity dispersion seen in each extinction region by summing all of the spectra within the extinction region and fitting the resultant spectrum with a single Gaussian. The ^{13}CO data cube has a smaller areal coverage than the extinction map thus we only consider the eight of eleven extinction regions that have $> 80\%$ coverage in the ^{13}CO data cube. For each extinction region, Table 5.1 gives the region number, the mass, the radius, the velocity dispersion required to prevent gravitational collapse (in Gaussian sigma units), the observed velocity dispersion in ^{13}CO (in Gaussian sigma units), the percentage of the region observed in ^{13}CO, and a descriptive location.

Table 5.1. Properties of Extinction Regions.

Number [a]	Mass[a] ($M_\odot$)	Radius[a] ($'$)	σV_{grav}[b] (km s^{-1})	σV_{CO}[c] (km s^{-1})	Coverage[c] (%)	Notes [d]
1	859.6	12.9	0.89	0.62	100	B5
2	1938.9	18.7	1.11	0.91	100	IC348
3	780.6	12.3	0.87	1.03	96	SW of IC348
4	560.5	11.2	0.77	0.94	56	E of B1
5	441.1	9.7	0.73	0.87	100	B1
6	257.6	7.6	0.63	0.87	52	SW of B1
7	973.3	14.8	0.88	1.22	100	NGC1333
8	246.2	7.6	0.62	0.83	100	S of NGC1333
9	240.1	7.5	0.62	0.87	40	L1455
10	173.7	6.4	0.56	0.79	100	L1448
11	107.4	5.2	0.50	0.76	84	S of L1448

[a]Extinction region number, mass and size from KJD06

[b]Velocity dispersion required for the region to be in virial equilibrium (measured using a Gaussian sigma), as calculated in Chapter 3.

[c]Velocity dispersion (using a Gaussian sigma) and fractional coverage of the extinction region observed in ^{13}CO COMPLETE data. Those regions with less than 80% coverage are not included in the analysis of this paper. See text for details.

[d]Descriptive location of extinction region.

Table 5.2. Observed Core Formation Statistics

Ext # [a]	$\sigma V_{tot}/c_S$ [b]	$N_{C,SCUBA}$ [c]	$N_{C,tot}$ [d]	$\mathrm{CFE}_{C,SCUBA}$ [c]	$\mathrm{CFE}_{C,tot}$ [d]
1	2.9	2	8	0.1	0.7
2	4.1	11	19	0.7	1.0
3	4.6	0	2	0.0	0.2
5	3.9	7	17	3.1	5.0
7	5.4	26	27	5.0	5.1
8	3.7	0	0	0.0	0.0
10	3.5	5	7	8.0	9.0
11	3.4	0	2	0.0	1.6

[a]Extinction region number as in Table 5.1. Only regions where ^{13}CO data coverage exceeds 80% are shown.

[b]Total velocity dispersion relative to the thermal value calculated from ^{13}CO data with the thermal component corrected to that expected for the mean gas.

[c]Number and percentage of the region's mass in SCUBA-associated N_2H^+ dense cores.

[d]Number of cores and core formation efficiency (CFE) as a percentage. See §5.6.4 for details.

For those extinction regions which have at least 80% coverage in the ^{13}CO data, Table 5.2 gives the observed ^{13}CO velocity dispersion relative to the sound speed (assuming a temperature of 15 K), the number of dense cores identified in the SCUBA data of KJD06, the number of dense cores observed in the IRAM data of Chapter 3, and the estimated percentage of the region's mass found in each set of dense cores (or core formation efficiency; the calculation of the number and mass of dense cores in each region is discussed in more detail in §5.4).

5.5 'OBSERVING' THE SIMULATIONS

5.5.1 Scalings

The simulations are scale-free, with units in terms of the mean density and sound speed. To convert to observable quantities, we adopt the nominal pressure scaling of

Ciolek & Basu (2006), a density scaling roughly three times their nominal density, plus the temperature and distance we previously adopted for our observations of the Perseus molecular cloud in KJD06 and Chapter 3, i.e., :

$$n_{n,0} = 10^4 \text{ cm}^{-3} \tag{5.1}$$

$$T = 15 \text{ K} \tag{5.2}$$

$$D = 250 \text{ pc} \tag{5.3}$$

Recall that we analyze simulations where the sheet is gravitationally dominated with minimal external pressure, i.e,

$$\widetilde{P}_{\text{ext}} = 0.1 \tag{5.4}$$

Using these scalings, the box length of the simulated region is 1.5 pc corresponding to an angular size of $21'$ at the distance of the Perseus molecular cloud. This is comparable to the sizes of the largest structures identified in the extinction maps of KJD06 (see Table 5.1). Each pixel in the simulation is 0.012 pc, corresponding to an angular size of $9.8''$, somewhat smaller than the beamsize of our SCUBA and IRAM observations. The mean initial total column density is 3.5×10^{21} cm^{-2}, corresponding to a value of 1 in the scale-free simulations. If we adopt a dust opacity of $\kappa_{850} = 0.02$ cm^2 g^{-1} and a dust temperature of 15 K (and assume a dust-to-gas ratio of 1:100) for our SCUBA observations, then 1 Jy bm^{-1} corresponds to $N_H = 6.37 \times 10^{22}$ cm^{-2} and the mean column density in the simulation corresponds to 55 mJy bm^{-1} [2].

The simulations are stopped when the maximum *column* density in the simulation reaches approximately a factor of 10 times the initial value, or $\sim 3.5 \times 10^{22}$ cm^{-2} (corresponding to a density of $\sim 10^6$ cm^{-3}). In simulations with strong turbulence and weak magnetic fields, this maximum is reached quickly, while in simulations with strong magnetic fields, more time is required to reach the maximum. The time each simulation runs is given in Table 5.3 in units of t_0 :

$$t_0 \equiv \frac{c_s}{2\pi G \sigma_{n,0}} \tag{5.5}$$

where c_s is the sound speed, G the gravitational constant, and $\sigma_{n,0}$ the initial column

[2]Note, however, that since the SCUBA maps are created from chopped observations, this constant component would not be seen in the data.

density in the simulation (see CB06). The unit of t_0 is related to the sound crossing time of the sheet – when thermal pressure is the dominant term in determining the thickness of the sheet, we can write

$$t_0 = \frac{Z_0}{2c_s} \tag{5.6}$$

(using eqn 13 of CB06), where Z_0 is the initial half-thickness of the sheet. Thus t_0 is approximately one quarter the sound crossing time of the entire thickness of the sheet. In their linear analysis, CB06 found that away from the critical mass to magnetic flux ratio ($\mu_0 = 1$), the lengthscale for maximum growth of instabilities was $2\lambda_T$ where λ_T is the critical thermal length scale given by

$$\lambda_T = \pi\Big(\frac{1 + 3\widetilde{P}_{\rm ext}}{1 + \widetilde{P}_{\rm ext}}\Big) Z_0 \tag{5.7}$$

(CB06 eqn 40), or $\lambda_T \simeq \pi Z_0$ for a low external pressure environment. Thus the sound crossing time across the lengthscale of maximum growth is $4\pi t_0$. Table 5.3 shows that in the non-turbulent simulations, the run-time for the weakest magnetic field cases is roughly equal to this timescale. In the highly turbulent simulations, the run-time can reach a few tenths of t_0, much shorter than even the turbulent crossing timescale of the linear lengthscale of maximum growth. This implies that in these highly turbulent simulations, the resultant peaks are due to compressions directly from the input initial conditions, as there has not been sufficient time for gravitational information to have propagated across the relevant lengthscales. Note that the entire length of the simulated box is $16\pi c_s t_0$ or 8 πZ_0, corresponding to four times the lengthscale of maximal growth for a low pressure environment with a mass to magnetic flux ratio away from critical. All of the turbulent simulations are therefore stopped well before the thermal crossing time of the box, $16\pi t_0$.

Figure 5.2 shows several examples of well-known star forming regions in Perseus observed in the submillimetre while Figure 5.3 shows the same example simulations as shown in Figure 5.1 but scaled to the same flux range and size as the observations. White noise has been added to the simulations at approximately the same level as is present in the observations.

Table 5.3. Simulation Timescales.

M [a] (c_s)	Time (t_0) [b] $\mu_0 = 0.5$[c]	$\mu_0 = 0.8$[c]	$\mu_0 = 1.0$[c]	$\mu_0 = 2.0$[c]	$\mu_0 = 10$[c]
0	204	167	121	23	12
1	49.6	31.6	4.3	2.5	–
2	28.7	10.8	2.5	1.1	–
3	36.0	0.9	0.8	0.8	–
4	2.1	1.0	0.7	0.5	–

[a]Input turbulence (in sound speed units).

[b]Time for a point in the simulation to reach a column density of roughly ten times the mean in units of t_0 (eqn 5). Note that the sound crossing time of the length scale of maximum growth is 4π (see §4.1 for more details).

[c]Input mass to magnetic flux ratio.

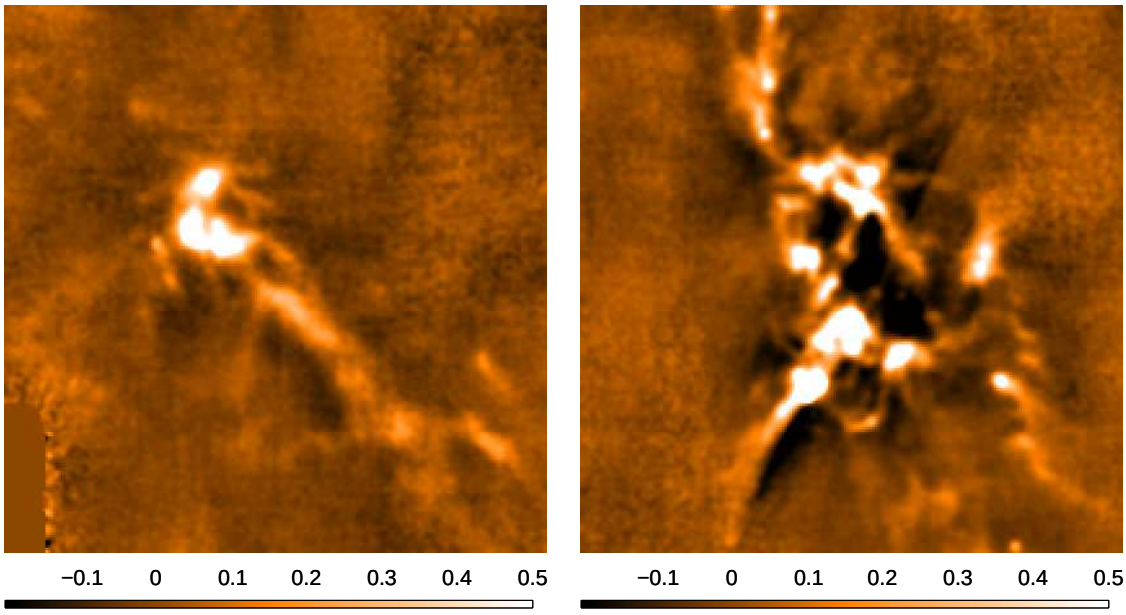

Figure 5.2 SCUBA submillimetre maps of two well-known star forming regions – B1 and NGC1333. Each image spans 21′ (∼1.5 pc) and the scale bar is in units of Jy bm^{-1}.

5.5.2 Identification of Simulated Cores

Direct comparison can be made between the column density structure found in the simulations and observations, since both are two-dimensional projections. This is not, however, the case for comparing dynamics. Since the velocity is only calculated in the two dimensions of the simulation, the simulations must be considered in a one dimensional projection along x or y in order to obtain the motion towards or away from an observer. We first project the column density map in the x and y directions to identify density peaks. Since the simulated sheet is thin, we do not account for changes in the projected column density due to variations in the thickness of the sheet. Note that the locations of peaks in the one dimensional projections tend to have good correspondence with overdensities in the original two dimensional column density map, although there can be differences where two structures lie along the same line of sight (particularly for filamentary structures seen in the highly turbulent simulations). Figure 5.4 shows examples of the projected 1D column density.

To identify cores, we find all the peaks in the projected column density which lie above a specified threshold and are separated by at least one IRAM N_2H^+ beam. We set the minimum peak threshold to a value corresponding to the typical column

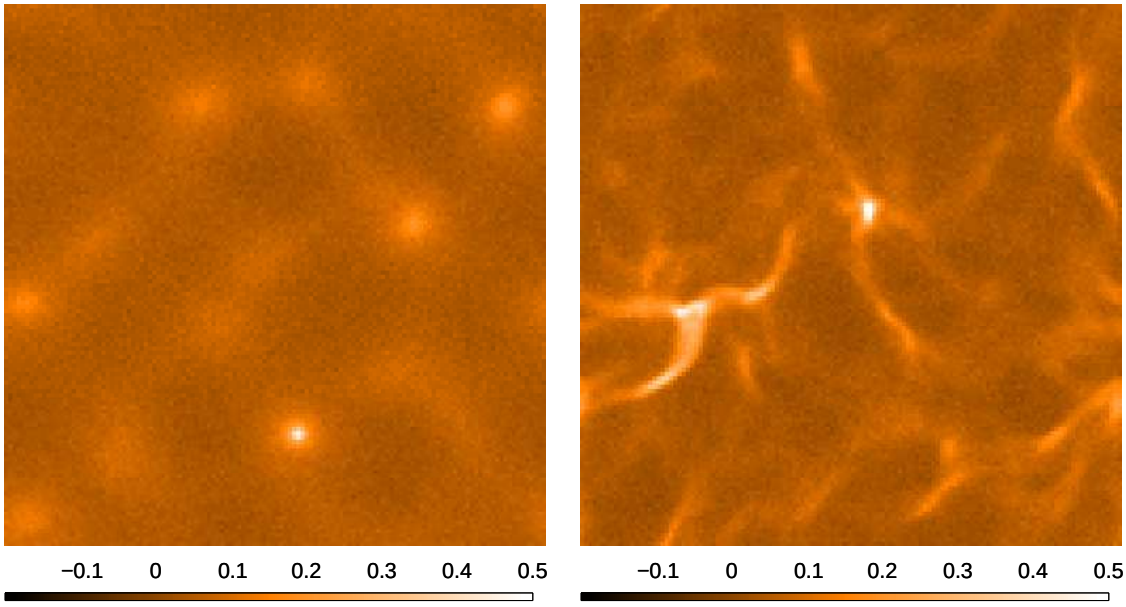

Figure 5.3 The same simulations shown in Figure 1, with the column density converted to equivalent SCUBA flux. White noise has been added at approximately the same level as the noise in the SCUBA observations. The linear size and scale bar are the same as in Figure 2.

density threshold we would expect in two dimensions – assuming a typical core spans little more than an IRAM N_2H^+ beam (3 pixels), and has a minimum column density threshold of 3 times the mean (which, for particles uniformly distributed along the column corresponds to a density of 9×10^4 cm^{-3}, roughly the critical density of N_2H^+), then the minimum 1D column density is $(N - 3) \times 1\sigma_0 + 3 \times 3\sigma_0$, where σ_0 is the mean column density (1) and N is the number of pixels in the simulation in 1D (128). This core identification is designed to mimic our observational method as best as is possible (N_2H^+ targets in KJT07 were based on dust column density measurements, primarily from SCUBA data). Note that the results in our later analysis show little variation with any changes in the peak identification parameters (see Appendix 5.10 for further details).

5.5.3 Calculation of Simulated Spectra

As described in §2, our IRAM survey consisted of pointed observations of dense cores in two molecules – N_2H^+, which traces the dense gas, and $C^{18}O$ which only traces the less dense gas. For every peak identified in the simulations, we can calculate spectra

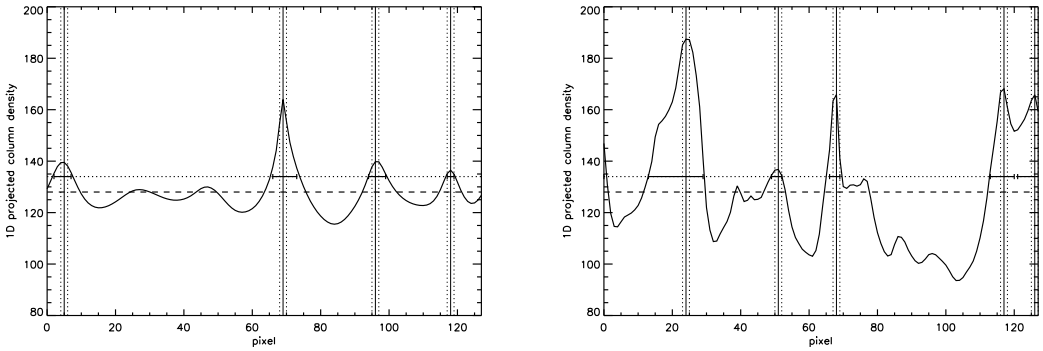

Figure 5.4 Projected 1D column density distribution (in the x direction) for the simulations shown in Figure 5.1 ($\mu_0 = 0.5$, $M = 0$ on the left and $\mu_0 = 1.0$, $M = 3$ on the right). Using our assumed scalings, a 1D column density value of 100 corresponds to 3.5×10^{23} cm^{-1}. Cores are identified as peaks above a specified threshold and separated by at least three pixels corresponding to roughly 29″or one IRAM N_2H^+ beam. The dashed horizontal line indicates the mean projected column density while the dotted horizontal line indicates the threshold for core identification. The solid horizontal lines indicate the extent of each core identified while the solid and dotted vertical lines indicate the core centres and width respectively.

corresponding to both of these tracers. For each projected 1D peak, we consider the material along the corresponding line of sight and split it into the dense material (cells with values above 3 times the mean column density), corresponding to the material which N_2H^+ traces, and less dense material (cells with values less than 3 times the mean column density), corresponding to the material which $C^{18}O$ traces. This threshold corresponds to a mean density of 9×10^4 cm^{-3} or nearly 10^5 cm^{-3}. We then calculate the spectra by assuming that each cell emits a thermally broadened Gaussian centred on the velocity of that cell and weighted by the amount of material (column density) present in that cell. For clarity, we term the two spectra calculated for every 1D column density peak as the core (high density gas) spectrum, which corresponds to the N_2H^+ dense core spectrum, and the LOS LDG (line of sight low density gas) spectrum, which corresponds to the $C^{18}O$ 'envelope' spectrum. Figure 5.5 shows two example sets of core and LOS LDG spectra.

As an aside, we note that the LOS LDG spectra are little affected by the exclusion of material above a column density threshold, rather than all material along the line of sight. The physical basis for this is that the majority of the mass is found in the lower density material, so the behaviour of the high density material has very little effect on a cumulative spectrum. This is demonstrated in Figure 5.6 which shows spectra of

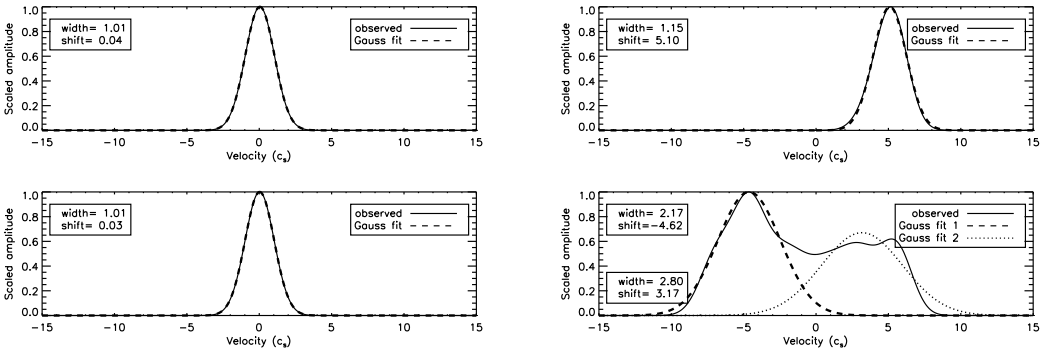

Figure 5.5 Two examples of spectra calculated for the core and LOS LDG material. The solid lines show the calculated ('observed') spectra while the dashed and dotted lines show the model (Gaussian) spectral fit. The top panels show the core spectra while the bottom panels show the LOS LDG material spectra. The left figure shows an example from a non-turbulent simulation with a subcritical mass to magnetic flux ratio ($\mu_0 = 0.5$, $M = 0$) where the spectra are well-described by a single Gaussian. The right figure shows an example from a highly turbulent simulation with a critical mass to flux ratio ($\mu_0 = 1$, $M = 3$) where the LOS LDG spectrum is less well-fit by even a two Gaussians.

the core (top panel), the LOS LDG material used in our regular calculations (middle panel), and all material along the LOS (bottom panel). This is one of many cases we found where the simulated core spectral peak lies roughly in the minimum between two spectral peaks in the associated LOS LDG material. Clearly, the addition of the extra material in determining the LOS spectrum (bottom panel) has very little effect on the LOS LDG spectrum. This is important, as it demonstrates that our choice of column density threshold for the LOS LDG material has little effect on the measure of core to LOS LDG velocity difference (see also Appendix 5.10).

In our IRAM survey, the beamsize of the N_2H^+ observations is more than twice as large as the $C^{18}O$ observations ($25''$ and $11''$ respectively), as mentioned in §5.4. In our calculation of the simulation 'observables', we similarly consider cells within the appropriate beamsize (3 pixels for the core, 1 pixel for the LOS LDG) for their contribution to each spectrum. An odd number of pixels is necessary to allow an equal sampling on either side of the core's peak.

A few peaks identified in the 1D projection have no cells within the beam above the (column) density threshold set for the core material. This occurs where two lower density structures, e.g. filaments, lie along the same line of sight, usually in the high turbulence simulations where the structure is less regular. We use data from these

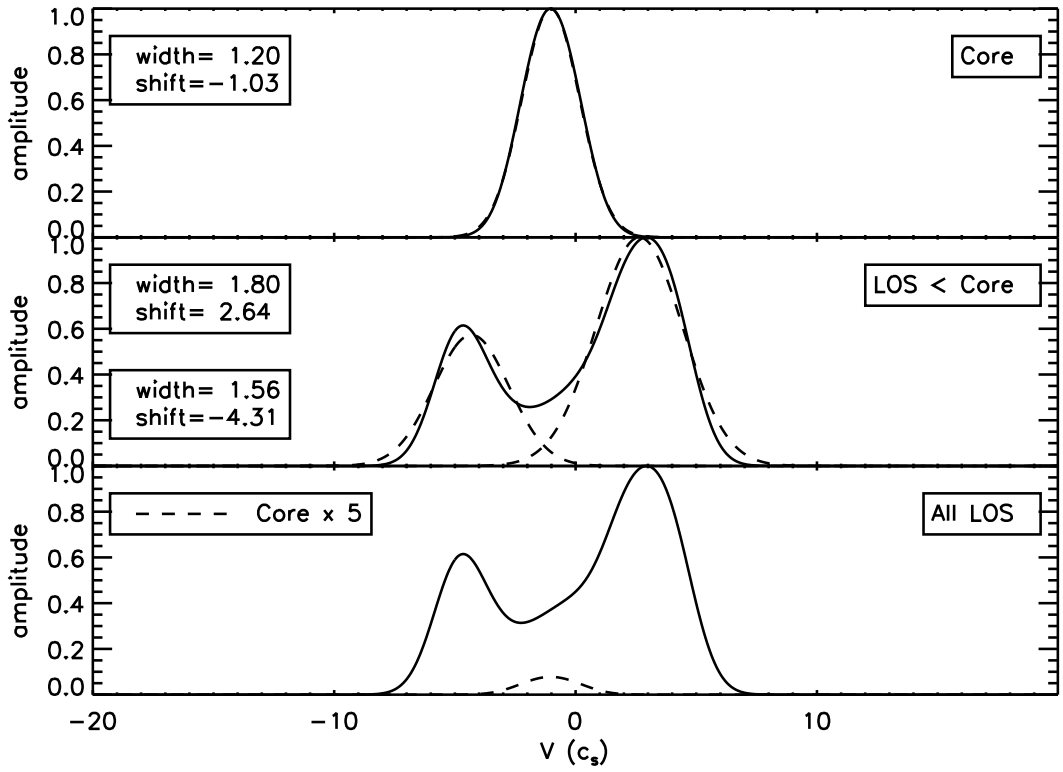

Figure 5.6 The spectrum calculated for a core identified in a simulation with a sub-critical mass to magnetic flux ratio (μ_0=0.8) and high input turbulence (M=3). This core was found to have supersonic motion between the core and LOS LDG material. The top panel shows the normalized spectrum of the core, with the best fit Gaussian shown by the dashed line (the fit parameters are given in the legend). The middle panel shows the normalized spectrum for the LOS LDG material around the core, with the two Gaussian fits indicated by the dashed lines. The lowest panel shows the normalized spectrum that would have been calculated for the LOS LDG material had all of the material along the LOS been used (rather than excluding that above the core detection threshold), as well as the core spectrum multiplied by a factor of five for visibility. There is little difference between this spectrum and the one used in our analysis (middle panel), indicating that our analysis is little effected by the inclusion of the core material in the LOS LDG spectrum (as also discussed in §5.5.3).

points only in our analysis of the distribution of LOS LDG velocity dispersions. This is analagous to our IRAM data, for which we had a few more detections in $C^{18}O$ than in N_2H^+ of candidate dense cores.

We also create spectra to compare with the ^{13}CO FCRAO observations. Like $C^{18}O$, the ^{13}CO observations trace the lower density material, however, we have ^{13}CO observations across the entire Perseus cloud (albeit at a lower resolution than our $C^{18}O$ observations). These observations allow us to gain a more global understanding of the dynamics of lower density material on larger scales. We therefore calculate LDG spectra along every LOS of the simulations using a beamsize of 5 pixels to correspond to the 46″ beam of the ^{13}CO data (i.e., 26 = 128/5 spectra for each x and y projection of a simulation). These simulated spectra can be thought of as arising from a chord across the projected centre of the star-forming region, and thus we compare these spectra with ^{13}CO spectra that run across the approximate centre (in right ascension and declination) of each extinction region. Comparison with all observed ^{13}CO spectra in the extinction region instead of only the central chord would include a larger fraction of lines of sight that pierce only the small edge of the 3D cloud, whereas the simulations trace the mid-plane of the cloud only.

5.5.4 'Observed' Properties

We fit the resultant core and associated LOS LDG spectra with Gaussians – a single Gaussian where possible, and two Gaussians where the fit is significantly improved; this method was also used in our IRAM survey. Figure 5.5 shows some examples of the spectra generated.

Simulations with strong turbulence tend to produce spectra which are more irregular and not well-fit even with a double Gaussian. In Chapter 3, we found that N_2H^+ dense core spectra were well fit by single (and occasionally double) Gaussians, and the $C^{18}O$ spectra were mostly well fit by single or double Gaussians. The poorer fits in the simulated spectra for the high input turbulence suggests that these simulations are qualitatively different than the observed regions.

We used our Gaussian fits of the simulated spectra to identify the relevant dynamical properties of each core and associated LOS LDG material – linewidth and centroid velocity. In the following sections, we analyze these results and compare them with the observational analyses in Chapter 3. Note that while a small number of cores are identified in a given simulation, small number statistics are not a major

concern, i.e., similar properties are measured across multiple simulations run with the same input Mach number and magnetic field strength[3].

For the larger-scale LDG LOS simulated spectra corresponding to our ^{13}CO observations, we found that both the simulated and observed spectra were less well described by a Gaussian fit. Since our analysis of these spectra requires only a measurement of the linewidth, we found that measuring the full width of the emission at one quarter of the peak (FWQM) was effective. Figure 5.7 shows an example of a simulated larger-scale LOS LDG spectrum in one of the most turbulent simulations. As seen in the figure, we found the width of the emission at half of the peak (FWHM) often picked out narrow emission peaks while missing underlying wide emission, while the FWQM was sensitive to the wider emission underneath. Measurement at levels lower than the quarter maximum sometimes presented a problem for the ^{13}CO observations where these levels became too close to the noise level. Where multiple peaks were found to be separated even at the quarter maximum, we only counted regions above the quarter max for our width measurement. This was especially important in our ^{13}CO observations to prevent bias from large noise spikes. (Note we also smoothed our ^{13}CO spectra to five spectral channels, or 0.33 km s^{-1} to reduce errors introduced by noise.) For a single Gaussian, the FWQM can be converted to a Gaussian σ through division by $4\sqrt{\ln 2}$ or ~ 3.3. We refer to the Gaussian σ corresponding to the measured FWQM as the "effective" velocity dispersion.

Finally, we created a composite spectrum describing the whole of each simulation (in both projections), and similarly summed all of the ^{13}CO spectra within each extinction region. To estimate the velocity dispersion of the entire region, we fit these spectra with a single Gaussian, which provides reasonable agreement. Note that in the simulations with weak magnetic fields, the velocity dispersion measured is nearly identical to what would be expected from the input turbulence level; simulations with

[3]We analyze data from three additional simluation runs with a μ_0 of 0.5 and a Mach number of 2 to determine the magnitude of statistical uncertainty in the derived core and LOS LDG properties. Qualitatively, we find that the column density maps of the additional $\mu_0 = 0.5$, $M = 2$ simulations reveal structures similar to the one we analyzed in the bulk of the chapter. We find a similar result quantitatively – comparison of the mean value (and where appropriate, standard deviation) of all of the 'observables' analyzed in this chapter shows these are consistent with the mean and standard deviation of the observables found in the extra three runs of the simulation. We also analyzed a single simulation run which again has $\mu_0 = 0.5$, $M = 2$ but an input turbulent velocity spectrum with $v_k^2 \propto k^{-3}$ where k is the wavenumber. This simulation also showed observables consistent with the additional runs with $\mu_0 = 0.5$ and $M = 2$ and our standard $v_k^2 \propto k^{-4}$. We therefore conclude that our results are not severely affected by small number statistics and furthermore that the results are somewhat insensitive to the power spectrum of the input turbulent velocity field. Further discussion of the latter point can be found in BCDW09.

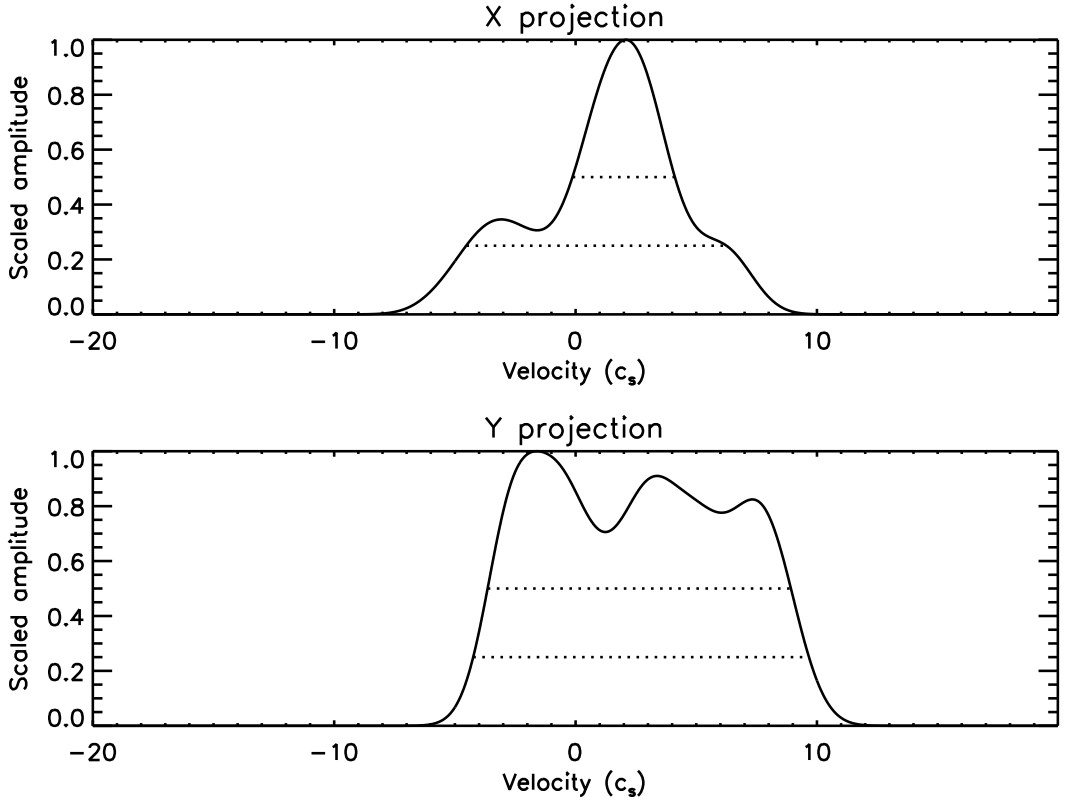

Figure 5.7 Calculated ^{13}CO spectra for one of the LOS's in the most turbulent simulation, with the weakest magnetic field (μ=2) and highest input turbulence ($M = 4$). The spectrum's amplitude has been normalized to the maximum intensity. The dotted horizontal lines indicate the extent of the spectrum at half- and quarter- maximum intensity. Note how it is necessary to measure the width well below the half-maximum mark in order to be sensitive to low-lying large scale modes.

stronger magnetic fields tend to have lower measured dispersions due to damping of the turbulence. Figure 5.8 shows the velocity dispersion found across the simulation as a whole versus the level of input turbulence. In our observations, we only include 8 of the 11 extinction regions identified in KJD06, as the other 3 have poor coverage ($< 80\%$) in the ^{13}CO map which prevents proper measurement of the dynamics.

Table 5.4 provides the overall statistics for all of the 'observed' dynamic quantities in the simulation – the mean and standard deviation of the velocity dispersion of the LDG material along all lines of sight (corresponding to the ^{13}CO observations), the velocity dispersion of the LDG material along lines of sight where dense cores were identified (corresponding to the C^{18}O observations), the velocity dispersion of the dense cores (corresponding to the N_2H^+ observations), and the difference in centroid

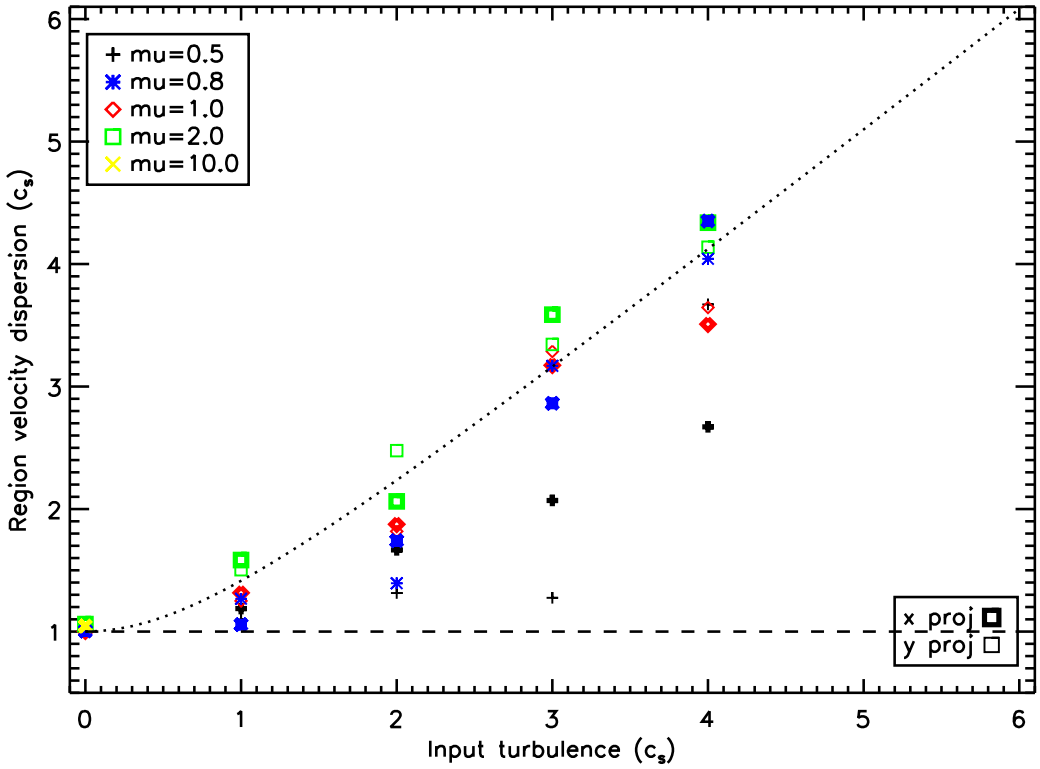

Figure 5.8 The velocity dispersion of the material in the entire simulated region measured at the end of the simulation versus the input level of turbulence. The dashed line indicates a thermal velocity dispersion while the dotted line shows the relationship for a velocity dispersion equal to the input turbulence. Thick and thin symbols show the results for the x and y projections of the simulations respectively. The simulations with strong magnetic fields show much smaller velocity dispersions than would be expected from the original input turbulence.

velocity between the core and LOS LDG material. Table 5.5 shows the number of cores found in each simulation and the percentage of mass found within the cores (core formation efficiency, or CFE). Note that Appendix B includes the analysis of several higher resolution simulations and demonstrates that the resolution does not affect the 'observable' dynamic quantities reported here.

Table 5.4. Simulation Dynamic Observables

M[a]	μ_0[a]	Projection[a]	$\sigma V_{LOSLDG,all}$[b]		$\sigma V_{LOSLDG,cores}$[c]		σV_{core}[c]		Core to LOS LDG[c]	
			mean	stddev	mean	stddev	mean	stddev	mean	stddev
0	0.5	X	1.00	0.00	1.00	0.00	1.00	0.00	0.07	0.05
0	0.5	Y	1.00	0.00	1.00	0.00	1.00	0.01	0.08	0.06
1	0.5	X	1.10	0.10	1.12	0.13	1.03	0.03	0.40	0.34
1	0.5	Y	1.07	0.05	1.09	0.04	1.01	0.00	0.58	0.05
2	0.5	X	1.12	0.06	1.16	0.01	1.02	0.00	0.23	0.01
2	0.5	Y	1.17	0.11	1.29	–	1.02	–	0.45	–
3	0.5	X	1.24	0.19	1.25	0.16	1.17	0.15	0.38	0.05
3	0.5	Y	1.13	0.07	1.13	0.02	1.05	0.03	0.55	0.34
4	0.5	X	2.22	0.43	1.37	0.32	1.34	0.13	1.68	0.22
4	0.5	Y	1.95	0.83	1.54	0.55	1.68	0.17	1.39	0.61
0	1.0	X	1.00	0.00	1.01	0.00	1.02	0.03	0.02	0.01
0	1.0	Y	1.00	0.00	1.01	0.01	1.03	0.03	0.04	0.04
1	1.0	X	1.08	0.07	1.19	–	1.07	–	0.74	–
1	1.0	Y	1.16	0.11	1.27	–	1.03	–	0.76	–
2	1.0	X	1.85	0.54	1.17	0.31	1.23	0.33	1.48	0.13
2	1.0	Y	1.73	0.49	1.49	0.50	1.34	0.42	1.46	1.01
3	1.0	X	2.59	0.97	1.77	0.76	1.16	0.16	1.06	0.69
3	1.0	Y	2.18	0.37	1.31	0.14	1.52	0.45	1.31	0.60
4	1.0	X	3.28	0.97	2.09	0.90	1.48	0.26	1.35	1.02
4	1.0	Y	3.00	0.81	1.70	0.44	1.31	0.25	1.95	1.80
0	2.0	X	1.06	0.04	1.10	–	1.05	–	0.17	–
0	2.0	Y	1.04	0.03	1.10	0.00	1.10	0.05	0.13	0.00
1	2.0	X	1.55	0.22	1.35	0.34	1.23	0.18	0.36	0.23
1	2.0	Y	1.34	0.09	1.27	0.08	1.05	0.04	0.58	0.26
2	2.0	X	1.92	0.73	1.61	0.54	1.32	0.25	0.63	0.99
2	2.0	Y	1.86	0.21	1.22	0.18	1.56	0.15	1.32	0.04
3	2.0	X	3.17	0.52	1.64	0.70	1.14	0.15	1.07	1.03
3	2.0	Y	2.41	0.65	1.50	0.22	1.60	0.84	1.54	1.24
4	2.0	X	3.02	0.70	2.14	1.02	1.52	0.14	1.46	0.90
4	2.0	Y	3.17	0.76	1.96	0.57	1.08	0.17	0.84	0.61
0	10.0	X	1.04	0.02	1.08	0.03	1.10	0.09	0.09	0.04
0	10.0	Y	1.03	0.03	1.05	0.03	1.06	0.07	0.09	0.06
0	0.8	X	1.00	0.00	1.02	–	1.04	–	0.11	–
0	0.8	Y	1.00	0.00	1.00	0.00	1.01	0.01	0.07	0.06
1	0.8	X	1.03	0.01	1.05	0.03	1.02	0.01	0.29	0.21
1	0.8	Y	1.05	0.05	1.08	0.05	1.03	0.03	0.34	0.15
2	0.8	X	1.37	0.24	1.16	0.20	1.09	0.07	0.54	0.73
2	0.8	Y	1.20	0.13	1.29	0.14	1.06	0.03	0.32	0.23
3	0.8	X	2.75	0.45	1.64	0.35	1.11	0.11	1.87	1.25
3	0.8	Y	2.25	0.66	1.72	0.75	1.45	0.08	1.06	1.00
4	0.8	X	2.75	0.44	1.48	0.52	1.05	0.09	0.89	0.99
4	0.8	Y	2.22	0.49	1.41	0.38	1.04	0.13	1.24	0.64

[a]Initial Mach number, mass to magnetic flux ratio, and projection for each simulation. See §5.3 for more detail.

[b]The LOS LDG velocity dispersion measured along every line of sight using the FWQM and converted into the equivalent Gaussian sigma measure. See §4.4 for more details.

[c]The mean and standard deviation of the LOS LDG velocity dispersion, core velocity dispersion, and absolute core to LOS LDG velocity difference for every core identified. (No standard deviation is listed where only one measurement exists).

Table 5.5. Simulation Core Formation Statistics

M[a]	σV_{box}[b]	μ_0[a]	Projection[a]	N_C[c]	CFE_C[c]
0	1.0	0.5	X	3	1.1
0	1.0	0.5	Y	0	0.0
1	1.2	0.5	X	3	1.9
1	1.1	0.5	Y	1	0.0
2	1.7	0.5	X	2	0.9
2	1.3	0.5	Y	1	0.2
3	2.1	0.5	X	4	4.0
3	1.3	0.5	Y	2	0.9
4	2.7	0.5	X	4	2.8
4	3.7	0.5	Y	2	1.4
0	1.0	1.0	X	2	0.9
0	1.0	1.0	Y	0	0.0
1	1.3	1.0	X	1	2.8
1	1.2	1.0	Y	0	0.0
2	1.9	1.0	X	2	1.6
2	1.8	1.0	Y	1	0.1
3	3.2	1.0	X	4	2.8
3	3.3	1.0	Y	2	1.6
4	3.5	1.0	X	5	4.9
4	3.6	1.0	Y	4	2.7
0	1.1	2.0	X	1	0.6
0	1.0	2.0	Y	1	0.3
1	1.6	2.0	X	4	2.3
1	1.5	2.0	Y	1	0.4
2	2.1	2.0	X	4	3.0
2	2.5	2.0	Y	1	0.4
3	3.6	2.0	X	6	3.9
3	3.3	2.0	Y	2	0.4
4	4.3	2.0	X	4	1.3
4	4.1	2.0	Y	3	0.5
0	1.0	10.0	X	5	1.6
0	1.0	10.0	Y	1	0.3
0	1.0	0.8	X	1	0.6
0	1.0	0.8	Y	1	0.1
1	1.1	0.8	X	2	1.2
1	1.3	0.8	Y	0	0.0
2	1.7	0.8	X	2	1.8
2	1.4	0.8	Y	0	0.0
3	2.9	0.8	X	4	2.0
3	3.2	0.8	Y	1	0.1
4	4.4	0.8	X	5	2.0
4	4.0	0.8	Y	4	0.6

[a]For simulation details, see §5.3.

[b]Velocity dispersion measured for the region in units of the sound speed; see §4.3 for further details.

[c]Number of cores and core formation efficiency (CFE) as a percentage.

5.6 RESULTS

5.6.1 Internal Velocity Dispersion

5.6.1.1 Across the Cloud

We first examine the behaviour of the larger-scale, less dense material in order to gain perspective on the environments in which the dense cores form. In Figure 5.9, we show the effective velocity dispersions observed in ^{13}CO along two central chords (in right ascension and declination) through each extinction region versus the velocity dispersion observed for the entire extinction region. (Note that the observational results do not change significantly if all lines of sight in the extinction region are used instead.) In Figure 5.10, we show the corresponding measurements for the simulations – the effective velocity dispersions of LDG along all LOSs compared to the velocity dispersion of the simulated region as a whole. (These values are included in Table 5.4.) Both Figures 5.9 and 5.10 show a range in LDG velocity dispersions along individual LOSs, ranging from small to larger than the mean for the cloud as a whole. Note that while the range in individual LOS LDG velocity dispersions are similar for both the observations and simulations, the extinction regions observed in Perseus tend to have higher velocity dispersions as a whole than within the simulations. Only simulations with the highest input turbulence (Mach number 3 or 4) show regional velocity dispersions similar to the lower end of the range spanned by our ^{13}CO observations. Since feedback is not included in the simulations, it may be more appropriate to compare the simulations only with regions in Perseus that do not appear to have formed previous generations of stars; the filled symbols in Figure 5.9 indicate the extinction regions which appear to have had less recent active star formation (i.e. excluding NGC1333, IC348, and B1). These regions do tend to have slightly lower regional velocity dispersions than their active star-forming counterparts.

5.6.1.2 LDG Along LOSs Associated with Dense Cores

We next examine the velocity dispersions seen in the LOS LDG material associated with the dense cores. As discussed above, the LOS LDG motion could provide hints for the scale of turbulence in the molecular cloud. There also may be a difference between lines of sight that contain cores and those that do not, if, for example, cores form at stagnation points in the velocity field. Our pointed IRAM C^{18}O observations are at higher spatial resolution than the ^{13}CO map, but still allow LOSs with cores

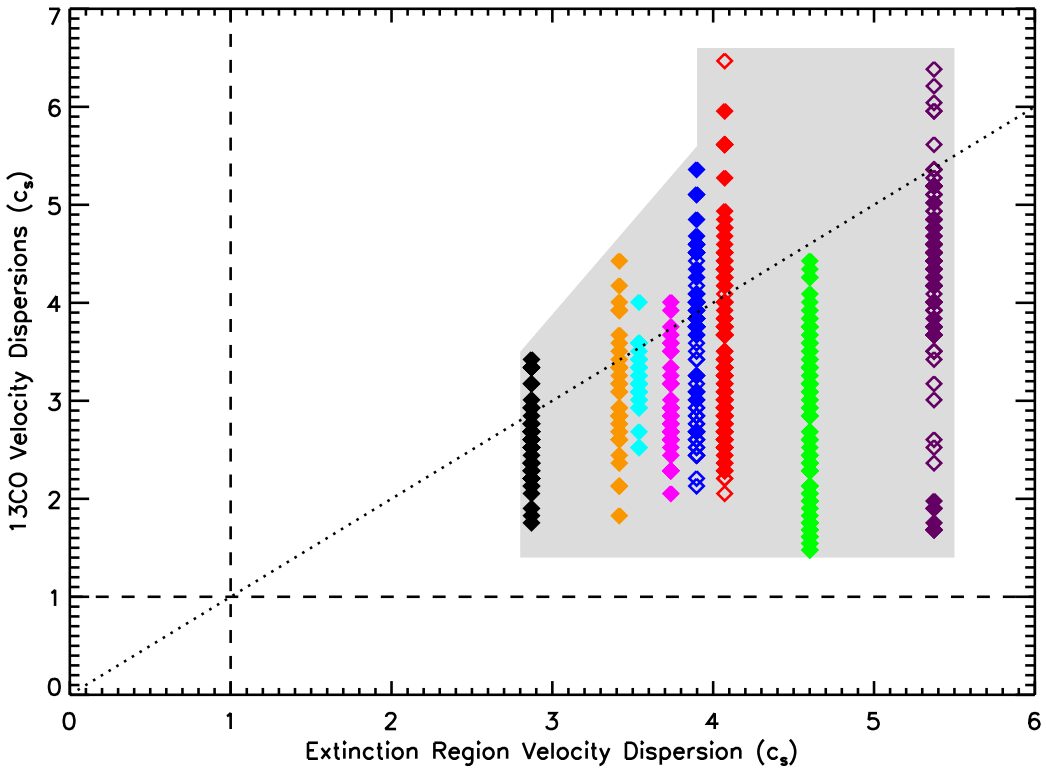

Figure 5.9 The velocity dispersion of low density material (^{13}CO) measured along the central chord through each extinction region versus the velocity dispersion seen across the region as a whole. The filled symbols indicate regions where star formation is more recent, while the shading indicates the region spanned by these observations.

to be compared with the overall distribution of LOS LDG dispersions.

Figures 5.11 and 5.12 show the distribution of velocity dispersions measured for LOS LDG material where cores were detected (points) for the observations and simulations (at the higher resolution of the IRAM survey) versus the velocity dispersion of the entire region. Each figure also shows the distribution of LDG velocity dispersions (mean plus and minus the standard deviation) for *all* line of sight material (at lower resolution / larger beamsize). Note that as in the previous section, the larger-scale LOS LDG linewidths are measured from the FWQM, with only the LOSs along the central right ascension and declination line of the extinction regions included in the observed plot. The dashed lines show the minimum expected observationally, i.e., the thermal width, while the dotted line shows a 1:1 relationship between the velocity dispersion of the larger environment (simulated region or extinction region) and the LOS LDG material. The figures illustrate that the bulk of the LOS LDG

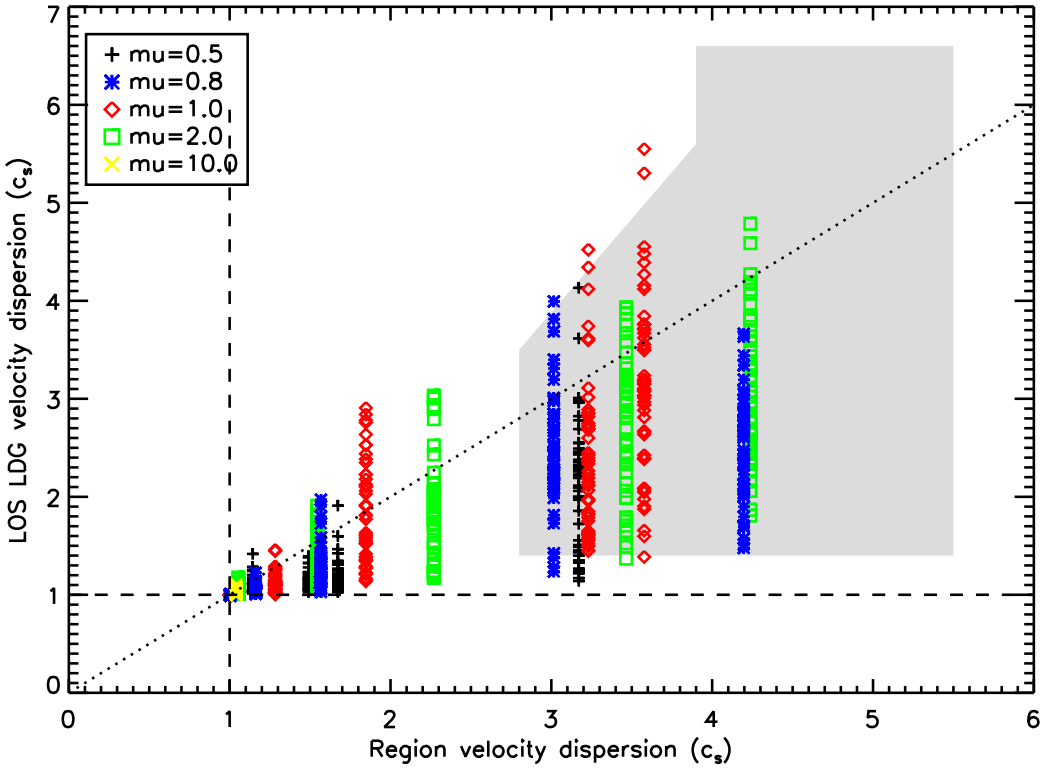

Figure 5.10 The velocity dispersion of low density material measured along all lines of sight in the simulation versus the velocity dispersion in the region as a whole. The shading indicates the region spanned by the observations (see Figure 5.9).

material has a similar velocity dispersion to the larger environment, while the LDG along LOSs that contain cores often have much lower velocity dispersions. Note the spectral line-fitting technique and resolution could play a role in this difference – the FWQM measure used for the bulk of the LOS LDG spectra is more sensitive to low levels of extended velocity dispersion than a single (or double) component Gaussian fit which may preferentially probe the local core environment.

5.6.1.3 Dense Cores

We next turn our attention to the cores. Recall that emission from the dense cores originates from relatively compact regions of overdensity. In some turbulent simulations, dense cores are transient features of overdensity formed by the intersection of two colliding streams of material (Ballesteros-Paredes et al., 2003). In such a case, one might expect to see a large internal velocity dispersion within the core for some

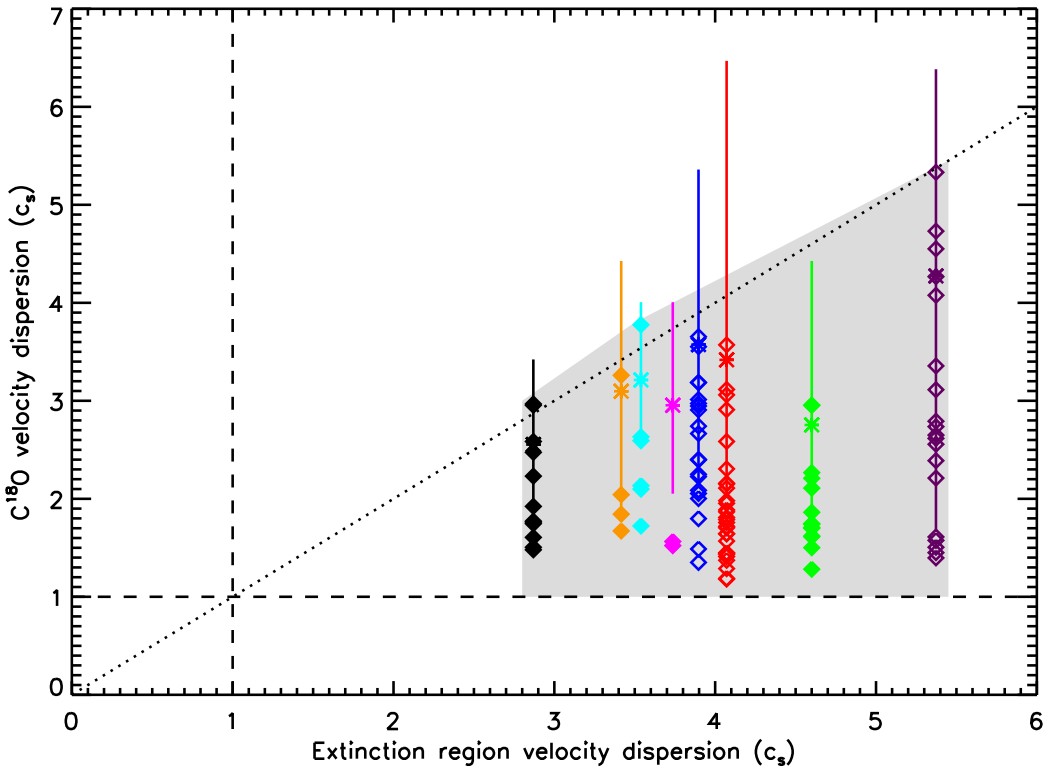

Figure 5.11 The velocity dispersion of low density material ($C^{18}O$) versus the velocity disperison measured in the larger extinction region (diamonds). The solid vertical lines indicate the range of velocity dispersions through the central chord of each extinction region, while the asterisk indicates the mean velocity dispersion. The dotted line indicates a 1-1 relationship while the dashed lines indicate thermal objects. The filled symbols indicate regions where star formation is more recent. The shaded region represents roughly the area spanned by our observations.

fraction of the population – although the centre of the turbulent compression typically has low velocity dispersion, the core as a whole can encompass a sufficiently large region so as to reveal a larger velocity dispersion. Indeed, in turbulent simulations for which the distribution of dense core internal velocity dispersions were calculated (Klessen et al., 2005; Ayliffe et al., 2007; Offner et al., 2008), a small but non-zero population of cores with supersonic internal velocity dispersions is present. In each case, the highest internal velocity dispersions in the simulations were larger than those seen in the observations of Chapter 3. On the other hand, cores which are bound and evolving more quiescently would be expected to have small internal velocity dispersions. As discussed in §5.4, previous dense core surveys (e.g., Ben-

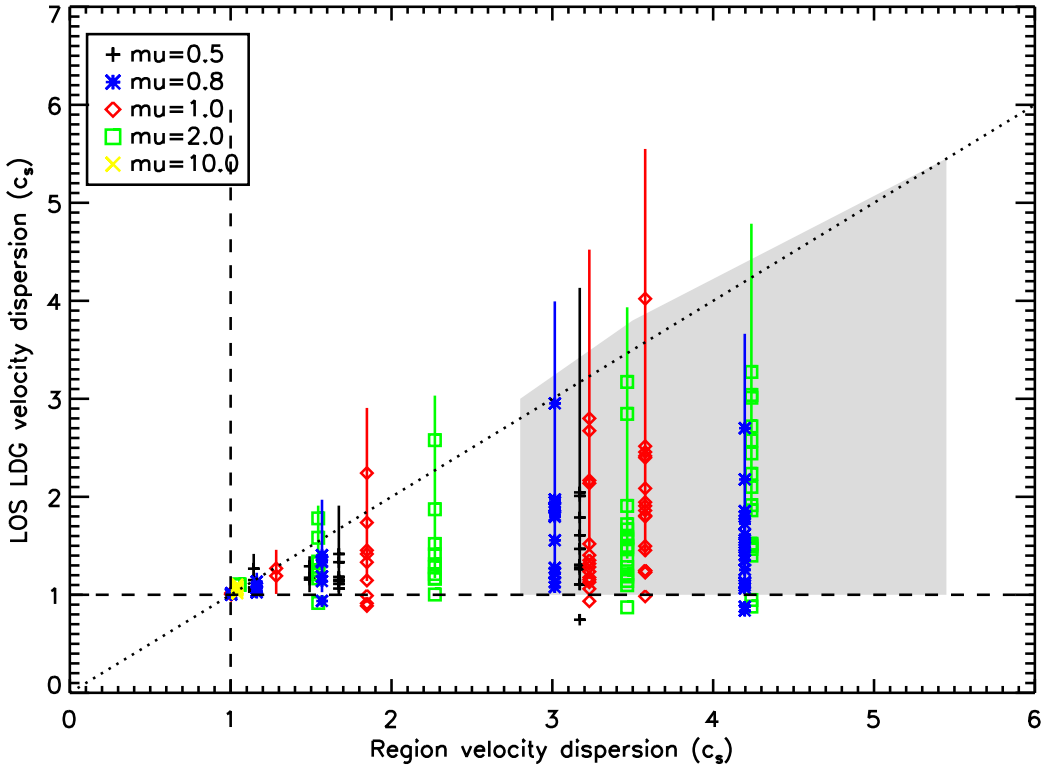

Figure 5.12 The velocity dispersion of low density material in the simulations versus the total velocity dispersion observed in the region (plus signs). The solid vertical lines indicate the full range of velocity dispersions that are seen along all lines of sight in the region within a 'beamsize' matching that of the ^{13}CO observations. The shaded region represents roughly the area spanned by our observations (see Figure 5.11).

son & Myers, 1989; Jijina et al., 1999) found that dense cores have small, thermally dominated internal velocity dispersions, although some turbulent motion may still be present, as discussed in §5.4.

Figures 5.13 and 5.14 show the internal velocity dispersion of the cores with respect to their larger environment (the extinction / simulation region) versus the velocity dispersion of the entire region. The cores have a similar range of velocity dispersions in both the simulations and observations, although as noted previously, the observed cores tend to inhabit large-scale environments with higher turbulent energy.

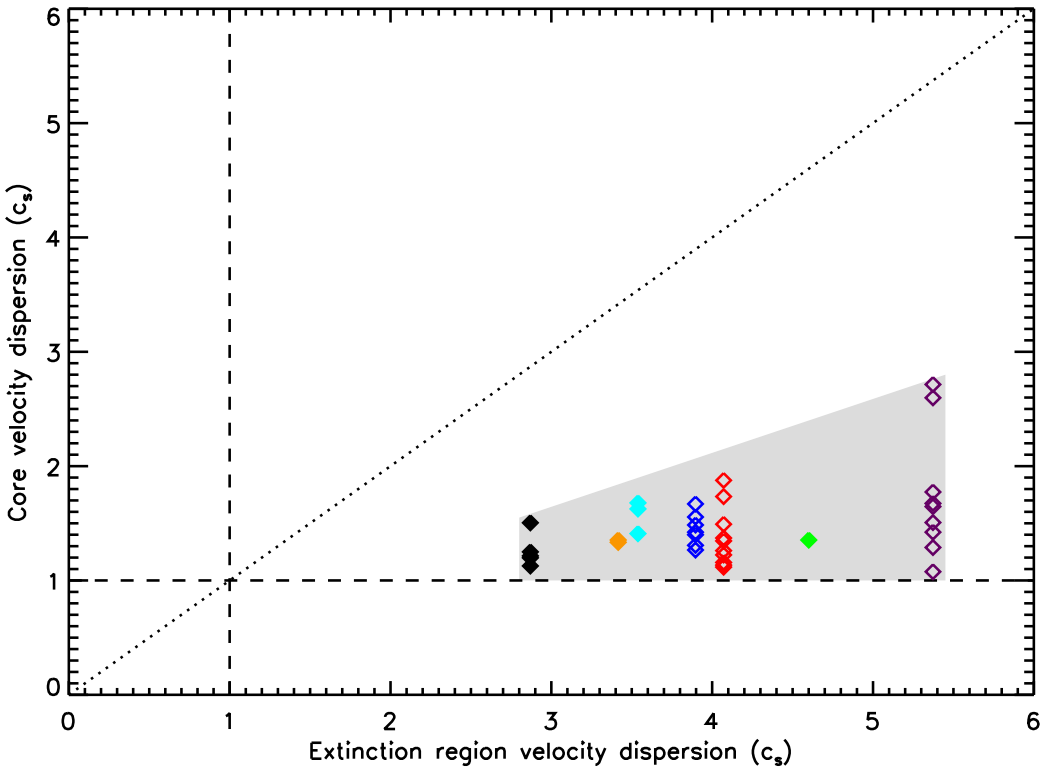

Figure 5.13 The internal velocity dispersion of the cores versus the velocity dispersion of their large-scale environment. The filled symbols indicate regions where star formation is more recent. The shaded region represents roughly the area spanned by our observations.

5.6.2 Core-to-LOS Motions

A second discriminant between the various simulations as well as the observations is the relative motion of the core and the surrounding LOS LDG material. Observations indicate that cores do not have significant motions within their local environment, with most displaying smaller motions than either the mean velocity dispersion of their local environment or the local sound speed (Walsh et al. 2004, 2007; Chapter 3). Walsh et al. (2004) have argued that in the turbulent framework of star formation, if cores form via competitive accretion, one might expect to see significant motion between the core and its local environment. Some simulators have since argued that competitive accretion simulations can display similarly small velocity dispersions (Ayliffe et al., 2007). It is unclear, however, whether these simulations are able to simultaneously meet all observational constraints (e.g., both the core to enve-

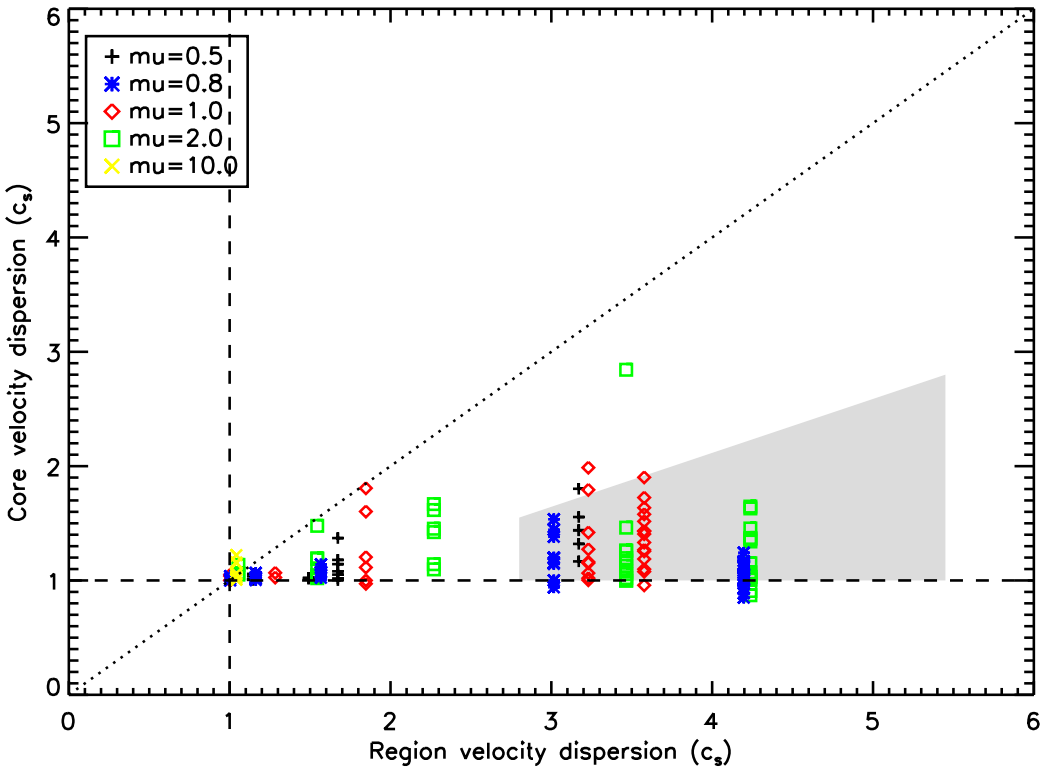

Figure 5.14 The internal velocity dispersion of the cores versus the velocity dispersion of their large-scale environment for the simulations. The shaded region represents roughly the area spanned by our observations (see Figure 5.13).

lope motions and core internal velocity dispersion; see Chapter 3). In any event, the motion between the core and its surrounding material is a useful measure to examine in the context of turbulent models.

Figures 5.15 and 5.16 show the relative motions of cores and their LOS LDG material versus the velocity dispersion of the entire region for the Perseus observations and the simulations respectively. What is striking about the two figures is that observations display a much greater connection between the core and LOS LDG material – the differences in velocity are quite small despite having more non-thermal motion on larger scales. In the simulations, the core-to-LOS LDG motion becomes large even for only moderate large-scale velocity dispersions.

A second way to measure the motion is to compare the core-to-LOS LDG motion to the typical motion found in the LOS LDG material, i.e., the LOS LDG internal velocity dispersion. The difference between the observations and simulations using

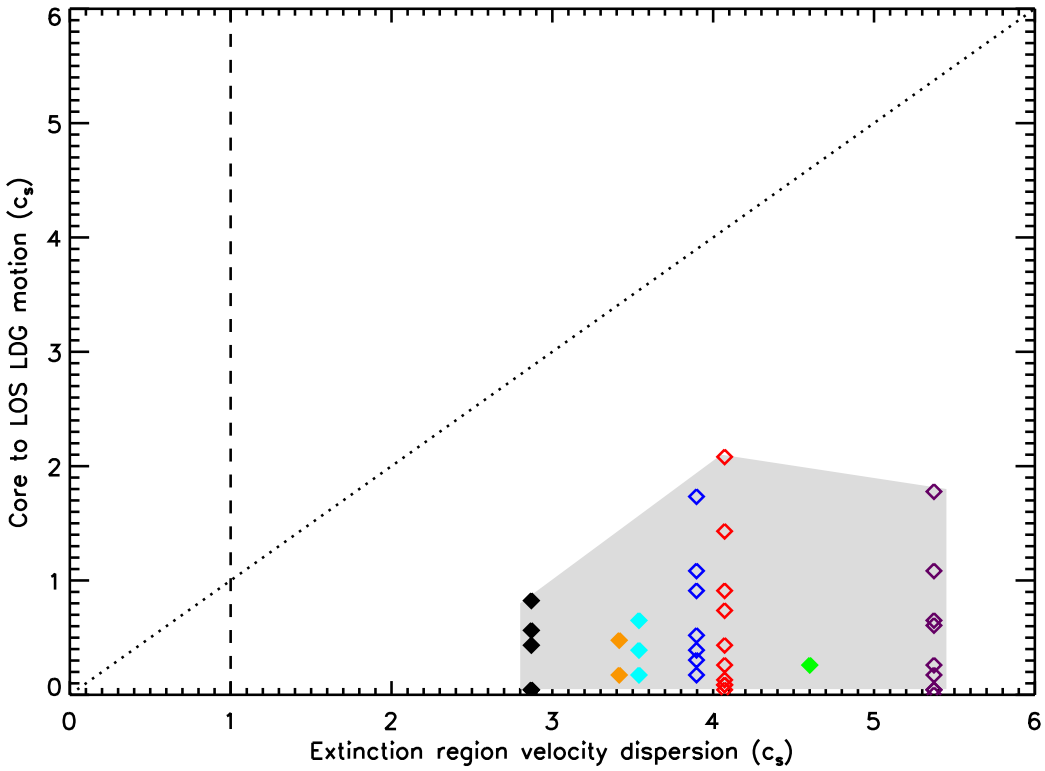

Figure 5.15 The observed relative motions of the core and its surrounding LOS LDG material versus the velocity dispersion of the extinction region. The filled symbols indicate regions where star formation is more recent. The shaded region represents roughly the area spanned by our observations.

this measure are even more pronounced. Observations show the cores are quite quiescent within their nearby surroundings, while the simulations show cores often have motions larger than the LOS LDG velocity dispersion. Figures 5.17 and 5.18 show the core-to-LOS LDG motion divided by the LOS LDG velocity dispersion versus the velocity dispersion of the region as a whole.

In the simulations with high input Mach numbers, the LOS LDG spectra often had complex structures and most required fits with two Gaussians. In instances of two Gaussian fits, we selected the velocity component with the closest centroid velocity to compare with the core centroid velocity. This was also the procedure used in our IRAM observations in Chapter 3, although in that work we found fewer spectra that required multiple Gaussian fits than in the turbulent simulations, where LOS LDG material spectra frequently displayed more than two peaks. We visually checked all core and LOS LDG spectra and fits to ensure the Gaussian fits to the more complex

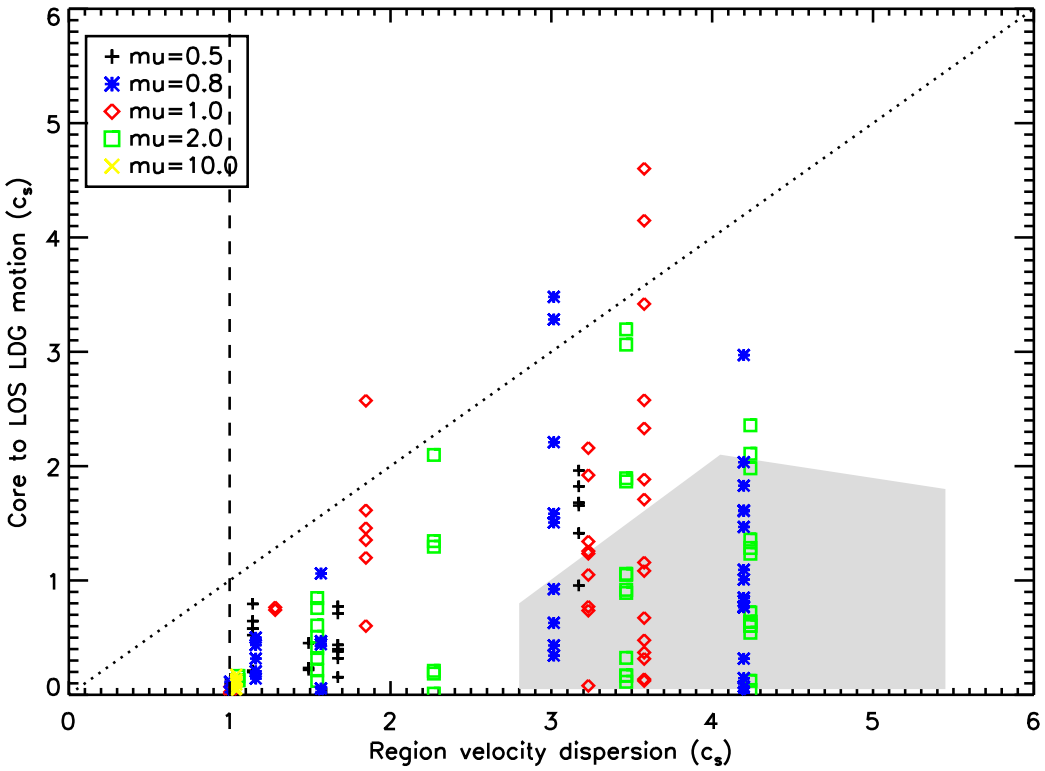

Figure 5.16 The relative motions of the core and its surrounding LOS LDG material in the simulations versus the velocity dispersion of the region. The shaded region represents roughly the area spanned by our observations (see Figure 5.15).

structure did not bias the fits to higher velocity differences. We found there are a few cores where somewhat smaller velocity differences would have been obtained had all of the peaks in complex LOS LDG spectrum been used for the spectral fitting, however, there were also several instances where the velocity differences would have been larger had all the peaks been used in the spectral fitting. We therefore conclude that the overall effect on the velocity difference from using only two Gaussian components is negligible. Note that for the observations, the selection of the closest $C^{18}O$ velocity component did not bias the results to smaller velocity differences (see Chapter 3 for more details).

5.6.3 Core to Region Motions

In order to further investigate the large motions between core and associated LOS LDG material in the most turbulent simulations, we examined the motion between

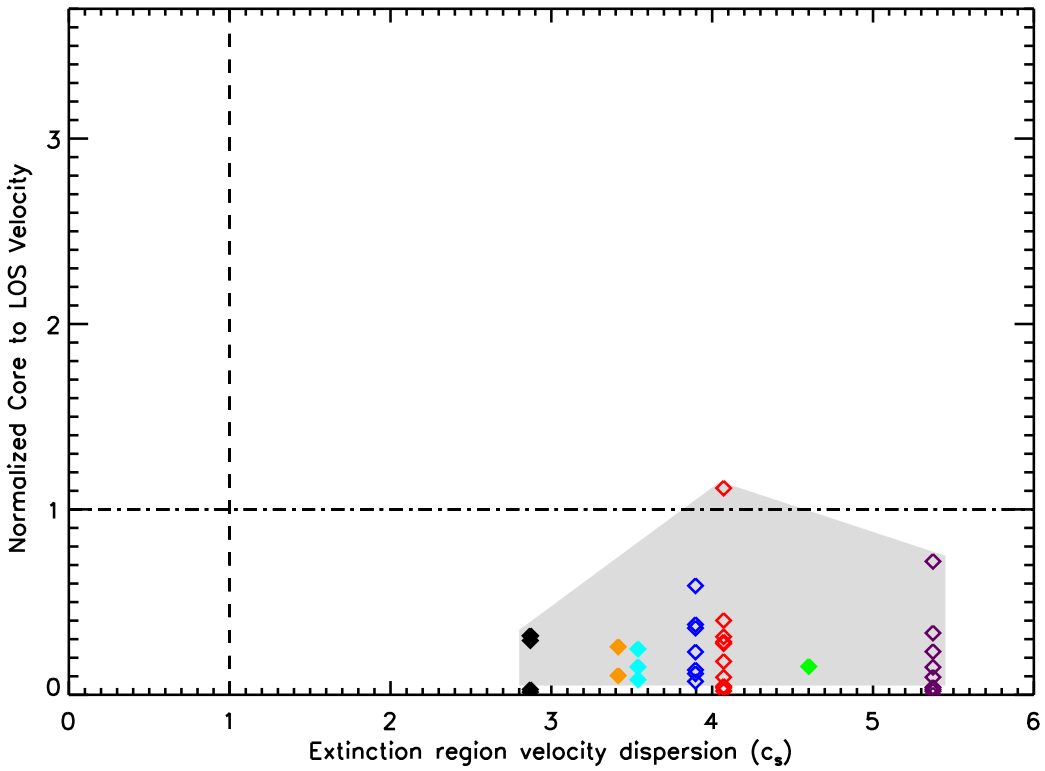

Figure 5.17 The ratio of observed core to LOS LDG motion and LOS LDG velocity dispersion versus the velocity dispersion of the extinction region. The dash-dot line indicates the point at which cores move faster than the velocity dispersion of the LOS LDG

with respect to their local environment (see §5.2). The filled symbols indicate regions where star formation is more recent. The shaded region represents roughly the area spanned by observations.

the core and the entire region. This provides an indication of whether the cores sit relatively unperturbed within the larger environment while the low density LOS material moves at high velocities, or whether both core and LOS LDG material move at (differing) high velocities.

Figure 5.19 shows the absolute difference in centroid velocity between the observed dense cores and the extinction region as a whole versus the velocity dispersion of the extinction region. While a significant fraction of the cores do display supersonic motions, nearly all have motions that are significantly smaller than the total velocity dispersion observed in the region. The velocity dispersion of each extinction region tends to be similar (within a factor of 1.5) to that required for the region to be in

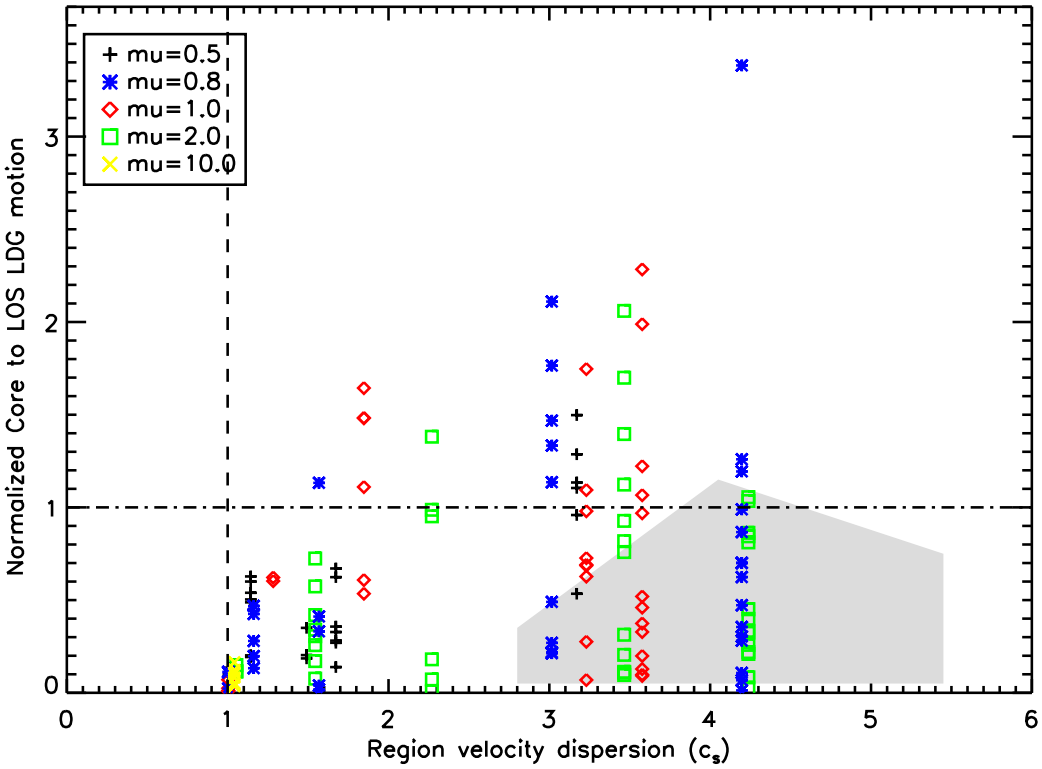

Figure 5.18 The ratio of core to LOS LDG motion and LOS LDG velocity dispersion in the simulation versus the velocity dispersion of the entire region. The dash-dot line indicates the line at which cores move faster than the velocity dispersion of the LOS LDG
with respect to their local environment (see §5.2). The shaded region represents roughly the area spanned by our observations (see Figure 5.17).

energy equipartition between gravitational and internal kinetic energy (Table 5.1) [4]. This implies that the dense cores observed tend to move with sub-virial velocities.

Such small velocities are not seen in the simulations, however. Figure 5.20 shows the absolute difference in centroid velocities between the dense core and the region as a whole versus the velocity dispersion of the region. This indicates that the dense cores can reach quite large velocities with respect to the simulated region as a whole (the centroid velocity of the region is nearly zero as one would expect). Figure 5.20 shows that the simulated cores often move much faster than the sound speed, and sometimes even in excess of twice that of the velocity dispersion of the region as a

[4]Note that this is often referred to being in virial equilibrium although it is not in the strict sense of the definition.

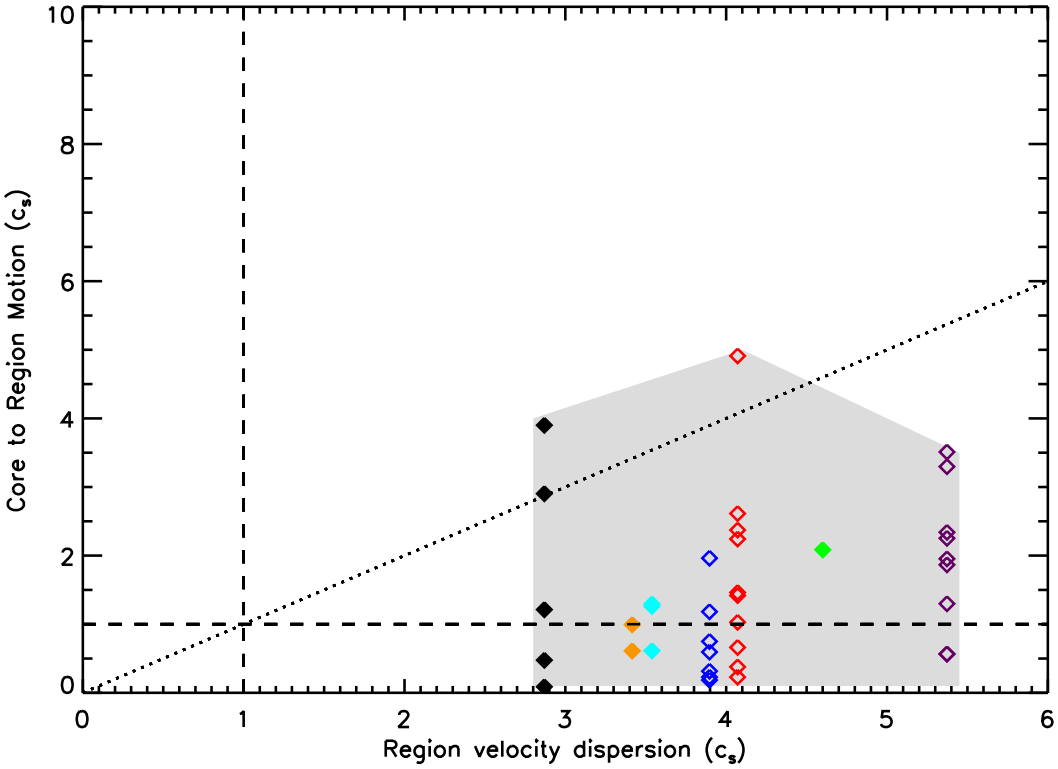

Figure 5.19 The motion of the observed N_2H^+ cores in Perseus within their parent extinction regions versus the velocity dispersion of the extinction regions they inhabit (as measured in ^{13}CO). The dotted line indicates a 1-1 relation. The filled symbols indicate regions where star formation is more recent. The shaded region represents roughly the area spanned by our observations.

whole! In these simulations, the timescale for the formation of the first high column density peak is very short – much less than a crossing time (see Table 5.3). The short timeframe before dense structure formation allows some of the cores to inherit the kinematics of material at the high end of the velocity tail of the input turbulence. (Note that for every high velocity core, there are several at lower velocities in the same simulation.) The short simulation timescale also originates from the high velocity tail – high velocities lead to strong turbulent compressions which quickly compresses the column density to ten times the mean, at which point the simulation is stopped.

The observations therefore paint a picture of cores moving slowly with respect to their turbulent surroundings, whilst in the simulations, compressed density enhancements can be formed with a much greater velocities than their surroundings.

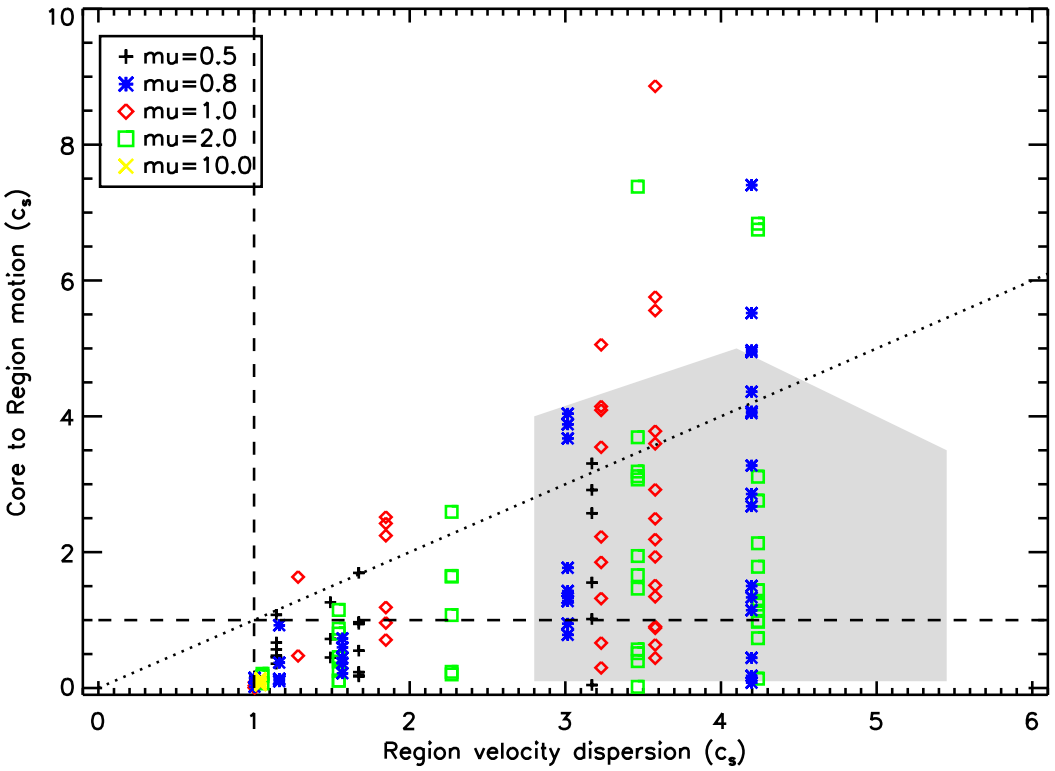

Figure 5.20 The difference between core and region centroid velocity versus the velocity dispersion of the region for the simulations. The dotted line indicates a 1-1 relation. The shaded region represents roughly the area spanned by our observations (see Figure 5.19).

5.6.4 Formation Efficiency

The final quantities that can be compared between the simulations and the observations are the number and total mass of the cores formed within each region. Star formation is known to be an inefficient process, with the fraction of mass ending up in stars ranging from a few percent to a few tens of percent in clustered environments (Lada & Lada, 2003). Within the size scale probed by the simulation, the fraction of mass in dense cores is expected to be on the order of 10%, since this is a more clustered environment than the cloud as a whole. Jørgensen et al. (2008) found that protostars make up 17% of the mass within the clustered regions of Perseus and 3% of the mass of the cloud as a whole. Similarly, KJD06 found that dense cores make up roughly 1% of the entire cloud mass in Perseus.

Our observations, unfortunately, do not lend themselves to a straightforward com-

putation of either the number of dense cores or the mass within them. Our IRAM N_2H^+ survey, which is the basis for the calculations of dense core properties, was based on a target list created using several methods. The majority of targets were based on cores found in the SCUBA dust continuum map of the cloud, while a still significant fraction was based on visual selection of targets from Palomar plates. The SCUBA observations spanned roughly the entire Perseus molecular cloud (to $A_V \sim 5$) so the list of N_2H^+ dense cores that have an associated SCUBA source should be complete and unbiased. The Palomar plate targets, however, were explicitly drawn from areas with no SCUBA detections. We anticipate that our total list of dense cores detectable in N_2H^+ is mostly (but not fully) complete, and may have slight biases in certain regions. We therefore provide *two* estimates of the number of cores observed per extinction region – the first being the number of N_2H^+ cores associated with a SCUBA source, and the second being the total number of N_2H^+ cores in our IRAM survey. The latter should provide a closer estimate of the total number, but different regions may have different fractions of cores missed. Table 5.2 provides both of these numbers for the eight extinction regions analyzed. The table shows that the number of cores varies between a few to nearly thirty, with only a small difference between the two estimates. Regions where star formation appears to have initiated more recently have less than ten cores per region.

The observed total mass of the cores within each extinction region provides a further challenge in calculation, and provides a second motivation for separating dense cores associated with SCUBA sources from the total population. The mass of the dense cores cannot be determined from our N_2H^+ observations. The SCUBA observations, however, allow the mass to be determined (making assumptions about the dust opacity, temperature, etc) but the Palomar cores do not. We use our estimates of SCUBA masses from our $3''$ map analysis (included in Table 6 of Chapter 3) and assume that the N_2H^+ cores without an associated SCUBA source each have the median mass of the SCUBA sources (0.8 $M_\odot$). Since these N_2H^+ cores were not detected with SCUBA, one might argue they are likely to have smaller masses than those with associated SCUBA sources, thus the reader is urged to treat the total core mass estimates for every extinction region as approximate. The fraction of mass in dense cores within every extinction region is calculated using the mass of the extinction regions found in KJD06. Table 5.2 shows the fraction of mass (core formation efficiency) found using both the N_2H^+ SCUBA cores only and all N_2H^+ cores. The fraction of mass in the dense cores tends to be on the order of a few percent using

either measure, somewhat lower than in Lada & Lada (2003), however, that measure includes already-formed stars.

In the simulations, both the number of dense cores and the fraction of mass contained within the dense cores (core formation efficiency) are straightforward to calculate. Table 5.5 shows these values for the various simulations. As can be seen from the table, the simulations tend to form a small number of cores (<10), with the fraction of mass contained within them being of order a few percent. Since the simulations are stopped at a relatively early time-step (when a column density of ten times the mean has been reached), it is possible that further accretion and / or fragmentation could significantly alter these results.

5.7 DISCUSSION – INTERACTION OF THE MAGNETIC FIELD AND TURBULENCE

We take a step back from the simulations here to discuss some general trends and behaviors which arise from the combination of input turbulence and magnetic field.

The purely isothermal simulation ($M = 0, \mu_0 = 10$) reveals the scales expected from gravitational instability (eqn 7), since the only other physical parameter, the external pressure, provides merely a small perturbation. The simulation thus produces mostly round, dense cores each with approximately a critcal mass, forming out of a regular velocity field and undergoing gravitational collapse after about a sound crossing time of the critical length, or $\sim 12t_0$.

When turbulence is added to the isothermal scenario, there is the addition of a non-regular velocity field, with the largest kinematic modes found on the largest spatial scales. These supersonic velocity fields lead to shocks which create significant density enhancements – the ram pressure is $\sim \rho_0 M^2 c_s^2$, which produces compressions of $\sim M^2$ in the post-shocked, isothermal gas. The strongest density enhancements originate from the largest turbulent modes, forming long filaments in less than a turbulent crossing time across the region. For highly turbulent simulations, the initial conditions of the highly supersonic velocity field can produce column density enhancements strong enough to stop the simulations extremely quickly. The dense objects formed in these simulations tend to be more elongated than in the isothermal case due to non-uniform compressions, and the sizes of the cores formed are smaller since the Jeans length decreases with the higher density.

When magnetic fields are added without turbulence, the relevant size scale for collapse varies significantly as a function of the initial mass to flux ratio μ_0 (CB06). The formed objects are mildly elongated (see BCW09, for a detailed discussion of the shapes), with a smooth velocity field. Strong magnetic fields, however, delay the formation of dense structures and gravitational collapse for an ambipolar-diffusion time, during which the neutrals slip past the load-bearing ions. For the conditions assumed here, the time to runaway collapse of the first core is about a factor of ten longer than in the isothermal nonmagnetic case.

When magnetic fields and turbulence are both present, the situation becomes much more complicated. For strong magnetic fields the magnetic pressure is sufficient to effectively prevent strong compressions even in turbulent velocity fields and evolution occurs only slowly via ambipolar diffusion. (Note that since we are analyzing thin sheet models with the magnetic field initially perpendicular to the sheet, compressions cannot act along the direction of the magnetic field lines.) In these cases, the final outcome will be similar to the case where only the magnetic field was present. For somewhat weaker magnetic fields, the turbulence is able to create significant compressions but the ram pressure is balanced by a post-shock enhanced magnetic field pressure in which the density increases by only $\sim M$ (Stahler & Palla, 2004) rather than by a post-shock thermal pressure at an enhanced density. In these compressed zones, the magnetic field enhancement effectively overwhelms gravity and collapse cannot occur until ambipolar diffusion removes the magnetic support. Given the higher density and shorter length scales involved, the ambipolar diffusion is nevertheless significantly shortened. Finally, when the magnetic fields are insignificant, even in the turbulently compressed regions, the simulation proceeds as in the purely turbulent case. Back of the envelope calculations show that the simulations we analyze fall in the regime of turbulent compression leading to significant magnetic field pressure; none have sufficiently weak fields to fall into the purely turbulent regime.

Will our results and conclusions differ dramatically if we consider three-dimensional simulations within the same physical parameter space? This is not likely, as demonstrated by the recent results of Kudoh & Basu (2008), who performed three-dimensional simulations of strongly and moderately magnetized clouds with initial turbulent fluctuations, including the effect of ambipolar diffusion. Their results are in general agreement with the thin-sheet calculations of Li & Nakamura (2004) and BCDW09. A large parameter study in three-dimensions, however, remains prohibitively expensive computationally. The special feature of our current work is that we are able to

sample a large range of parameter space. Nevertheless, we do anticipate performing a similar study with three-dimensional simulations in the future, as broad parameter surveys become available.

Despite the above point, we note that different conclusions may yet be possible if we consider the case of continually driven turbulence or global (non-periodic) cloud models, in either the thin-sheet or three-dimensional cases.

5.8 CONCLUSIONS

Although the simulations we analyze have a thin sheet geometry, their relative simplicity provide the advantage of taking a relatively short amount of time to run, and hence easily allow a parameter study. While we do not expect the quantities measured here to be identical with a more complex, three-dimensional study, we do expect the trends we observe to be generally valid in the three-dimensional case as well.

From our analysis of the simulations we find the following:

- *The large-scale (regional) low density gas velocity dispersions in the simulations tend to be lower than found in our observations.* Simulations with strong magnetic fields tend to cause input turbulence to significantly damp by the time the simulation is halted for analysis (column overdensity of ~ 10).

- *The velocity dispersions of the simulated dense cores tend to be low, in agreement with observations.* The low density material along the same line of sight (LOS) tends to have larger velocity dispersion, as is also observed.

- *The motion of the simulated core within its local environment (difference in core and LOS low density material centroid velocities) is large in simulations with high turbulence.* This contradicts our observations that show cores have little motion with respect to their local environment, even in the clustered environment of Perseus.

It therefore appears that reconciling turbulence on large scales and quiescence on small scales (both within the core and between the core and envelope material) requires additional forces to soften the small-scale dynamics while allowing turbulent motions to remain on the large scales. Magnetic fields are a promising avenue to provide the small-scale damping of motions, however, in the simulations we analyzed, the large-scale turbulent motions also decayed, hence a mechanism would be required

to renew large-scale turbulence. In the simulations we analyzed, the input turbulence is neither long-lived nor refreshed through the global evolution of the cloud or the formation of the first protostars, etc. The inclusion of further turbulent input after the start of the simulation thus might allow for supersonic motions to be observed on the large scale while preserving small scale quiescence.

The nature of the simulations themselves are also important to keep in mind – the simulations are done in the thin-sheet approximation and have periodic boundaries in the horizontal directions. This has some limitations, for example, magnetic field lines and turbulent vorticity can become tangled in three-dimensions in a manner that they cannot in thin-sheet models. The periodic boundaries can influence the coupling of turbulence on different scales, and also impose a rather arbitrary largest scale of turbulence in the simulation. We believe that the problem of maintaining very turbulent motions on large scales, while keeping cores relatively quiescent, may not be addressible in any periodic box model, whether thin-sheet or three dimensional, and may require a global approach to cloud modelling.

This study illustrates the power of utilizing kinematic 'observables' in simulations to discriminate between simulations with different initial conditions and to compare with observations, rather than limiting the analysis to quantities such as the mass function and star formation efficiency. This is an era where large (degree) -scale surveys are becoming more feasible (the COMPLETE Survey data used in part here will be eclipsed by more than an order of magnitude by the next generation of surveys, including the JCMT Gould's Belt Legacy Surey (Ward-Thompson et al., 2007b) and the *Herschel* Gould's Belt Legacy Survey (André & Saraceno, 2005)). Soon observers will be able to provide information on a statistically significant set of dense cores and their environment over the extent of many molecular clouds, which will provide much-needed information to constrain simulations of star formation. Simulators should start to prepare to take advantage of this vast increase in information when it arrives.

5.9 ACKNOWLEDGEMENTS

We thank the anonymous referee for the thorough review which improved our paper. HK would also like to acknowledge valuable discussions with people at the CfA, in particular Alyssa Goodman, Charles Lada, and Phil Myers, and Wolf Dapp (UWO) for a careful reading of our manuscript.

For the duration of this research, HK was supported by a Natural Sciences and

Engineering Research Council of Canada (NSERC) CGS Award and a National Research Council of Canada (NRC) GSSSP Award. DJ and SB are supported by NSERC Discovery grants.

5.10 APPENDIX A: EFFECT OF SCALINGS

The simulations we analyze are scale-free, which leads to the reasonable question of how dependent the results we find above are on the values of the scale factors (temperature, external pressure and mean density) we adopted in order to compare the simulations to observations. In this section, we address this question and demonstrate that a change in the scale factors has a minimal impact on the 'observables' derived and hence the results of our analysis. We start with a discussion of our motivation in choosing the values of the scale factors used in the above analysis, which gives a sense of the range that could have been applied. Next we show how modifications to the scale factor would effect our results.

5.10.1 Physical Motivation For Scalings

Converting the simulations into observable units requires one to assume a temperature, external pressure, and mean density. (Comparison to our observations requires a further assumption of the distance to the Perseus molecular cloud to convert the size observed from angular to physical.)

The temperature is constrained to a fairly small range by observations of star-forming regions, and hence does not tend to play a significant role in comparisons. Our previous observational results assumed that the temperature is 15 K everywhere. Recent ammonia observations have shown that dense cores in Perseus have a mean temperature of ∼12 K with a spread of only a few Kelvin (Rosolowsky et al., 2008); as discussed in Chapter 3, assuming a temperature of 15 K rather than 12 K does not have a large effect on our observational results. For ease of comparison with our previous work, we assume this temperature for the simulations as well.

The mean density, on the other hand, can be considered over a wider range of values, since star formation regions have a hierarchical structure in size and density. The dense cores we observed in our IRAM N_2H^+ survey require densities of greater than or equal to $\sim 10^5$ cm^{-3}, in order to be observable. Thus the simulation must reach similar peak densities in order to be 'observable'. Since the simulations are

stopped when the maximum column density is ten times the mean column density, the corresponding mean (three-dimensional) density cannot be too low for N_2H^+ to be detectable. The mean density also cannot be too large, as this would lead to a large fraction of the material in the simulation being at relatively high densities, while observations show that this is not the case (§5.6.4). Also note that a higher assumed mean density implies a smaller size for the region simulated (eqn 26 of CB06).

While the above physical arguments place some boundaries on the adopted scaling parameters, it is clear that there is an allowable range. A different choice in the adopted scaling parameters would lead to a different set of appropriate scale-free parameters we adopted to 'observe' the simulations (e.g., the beamsize in pixels). In order to determine the magnitude of the effect on our results that this would cause, we re-analyze the simulations using different scale-free parameters.

5.10.2 Beamsize

We first re-analyze the simulations using a larger beamsize (in pixels) with everything else identical to our standard method. Assuming a mean density ∼5 times higher than our nominal value and keeping the other constants fixed, for example, would shrink the physical size of each pixel and thus the beamsize would change to 7 pixels for N_2H^+ (and 3 pixels for $C^{18}O$). The observable quantities which we are interested in are the velocity dispersion of the core and LOS LDG material and the relative motion of the core and LOS LDG material. It would be difficult to compare these quantities on a core-to-core basis, since different cores could be identified in each (a larger beamsize increases the minimum separation required between cores). Instead, we use the mean and standard deviation of these quantities to represent the full span of values found for each simulation. (We use the absolute value for the relative motion of the core and LOS LDG material.)

Figures 5.21, 5.22, and 5.23 (left hand panels) show the variation of 'observables' (the core velocity dispersion, LOS LDG velocity dispersion, and core to LOS LDG velocity difference) versus the velocity dispersion of the region as a whole for the nominal beamsize (plus signs) and the larger beamsize (squares). In most cases, the larger beamsize has relatively little effect on the 'observables'.

The highly turbulent simulations tend to display filamentary structure in the 2D column density, which translates to clustered peaks in the 1D projected column density distribution which we use to identify cores. A larger beamsize tends to slightly

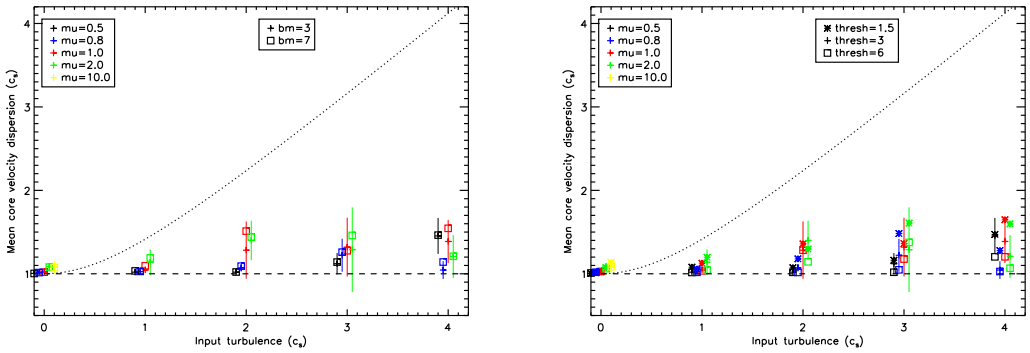

Figure 5.21 The variation in core velocity dispersion for cores identified with a differing beamsize (left) and minimum core column density threshold (right) versus the input turbulence. The plus signs and vertical lines indicate the mean and standard deviation of the velocity dispersion found for each simulation using our nominal values. The squares and asterisks indicate the mean found for the simulations with a differing beamsize (left) or core threshold (right). Note the data points have been slightly offset from the input turbulence to allow better visibility (μ increases from the left to the right).

decrease the number of cores identified, particularly in the highly turbulent simulations. The filamentary structure also leads to a larger amount of higher (column) density material in the core's vicinity; hence the core velocity dispersion in particular, and the LOS LDG velocity dispersion to a lesser extent tend to increase with an increasing beamsize, while the core-to-LOS LDG motion is less affected.

The fraction of mass in dense cores and number of cores detected (not plotted) show little to no variation with the varying beamsize, with differences in values no more than a few percent of the mass and one or two in number of cores.

5.10.3 Core Threshold

We next re-analyze the data using a higher and lower minimum core column density threshold (relative to the mean). A lower chosen physical mean density, for example, would require a higher minimum core column density relative to the mean in order to keep the same absolute value. The simulations have a relatively small dynamic range (less than two orders of magnitude in column density), so we test a minimum core column density threshold of twice and half our nominal value (i.e., 6 and 1.5 times the mean).

Figures 5.21, 5.22, and 5.23 (right hand panels) show the effect of varying the

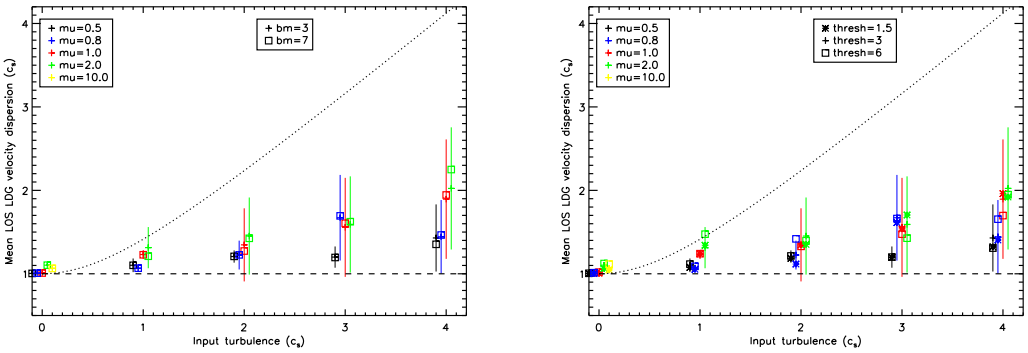

Figure 5.22 The variation in LOS LDG velocity dispersion for cores identified with a differing beamsize (left) and minimum core colum density threshold (right) versus the input turbulence. See Figure 5.21 for the plotting conventions used.

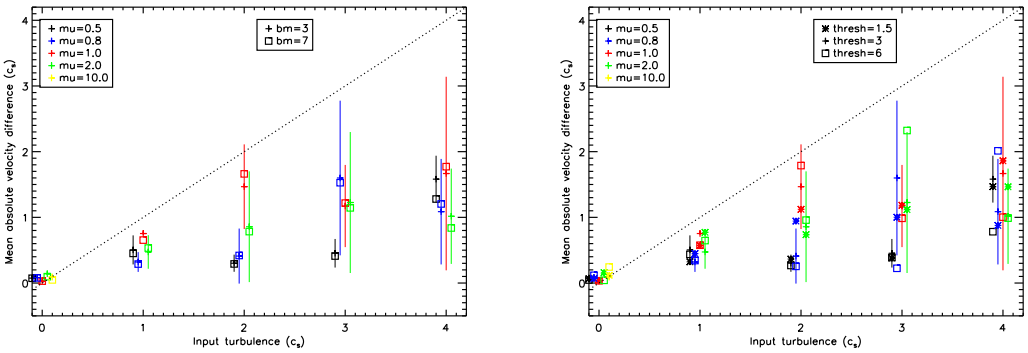

Figure 5.23 The variation in core to LOS LDG velocity difference for cores identified with differing beamsize (left) and minimum core column density threshold (right) versus the input turbulence. See Figure 5.21 for the plotting conventions used.

core identification threshold using the same plotting scheme as the left hand panels described above. As is found for the beamsize, the majority of 'observables' do not vary significantly with a different core identification threshold. As is also found for the variation in beamsize, the fraction of mass in the cores varies at most by a few percent and the number of cores varies by at most a few.

The greatest effect of a higher core identification threshold is that fewer cores are identified. As mentioned above, the dynamic range of the simulations is not large (the simulations are stopped when the peak column density exceeds roughly 10 times the mean), hence even the factor of two increase in the minimum core column density can significantly reduce the number of cores identified, in many cases to only one or two cores per simulation. The very small number statistics drawn from this appears

to be the largest contributor to the variations seen between the two thresholds.

At the lower core identification threshold, more cores are identified, although usually not substantially more than the nominal case. Here, the main differences originate from a larger fraction of material being included as part of the 'core' and a smaller fraction as the 'LOS LDG'. The amount of material excluded from the LOS LDG is a small fraction of the total, hence the LOS LDG velocity dispersions tend to decrease by only a small amount. This material makes up a larger fraction of the total core mass, hence the increase in core velocity dispersions tend to be somewhat larger. There is no obvious trend in the relative motions determined.

5.10.4 LOS LDG Upper Threshold

The other physical property which plays an implicit rather than explicit role is a chemical one – the density range in which N_2H^+ and $C^{18}O$ are sensitive. The minimum density at which N_2H^+ is sensitive sets the value for the core identification threshold and folds into the core identification threshold discussed above. The maximum density before $C^{18}O$ becomes significantly depleted sets the threshold for which material is considered to contribute to our LOS LDG measures. We nominally consider these two values to be identical, so that all of the material in the simulation is traced either by N_2H^+ or $C^{18}O$, but this might not be the case. Here, we consider cases where $C^{18}O$ is sensitive to half and twice the minimum density for N_2H^+ emission.

The left hand panels of Figures 5.24 and 5.25 show the LOS LDG velocity dispersion (Figure 5.24) and core to LOS LDG velocity difference (Figure 5.25) versus the velocity dispersion of the region as a whole for three different maximum $C^{18}O$ threshold values. (Note the core velocity dispersion remains unchanged, hence is not shown.) The change in LOS LDG column density threshold has little effect on the LOS LDG velocity dispersion (Figure 5.24), as one would expect given that most of the mass is found at the lower column densities which are included in all cases. There is a slightly larger change in the core-to-LOS LDG motion since the higher column density material tends to have a similar velocity to that of core material. Although the width of the spectral feature is little affected by the inclusion of higher column density material in the LOS LDG spectrum, the position of the peak tends to be pushed towards velocities nearer to that of the core. This is clearly illustrated in Figure 5.25 which shows the lower LOS LDG column density threshold results in larger relative core-to-LOS LDG motions while a higher threshold leads to smaller

relative motions. While the change in the core-to-LOS LDG motion is larger than the change in the LOS LDG velocity dispersion, both changes are relatively small. This result could have been anticipated from the brief discussion in Section 4.3 and Figure 5.6, where it was demonstrated that the LOS LDG spectra look very similar to the spectrum that would result from contributions due to *all* of the material along the line of sight, since only a small fraction of the material has high column density.

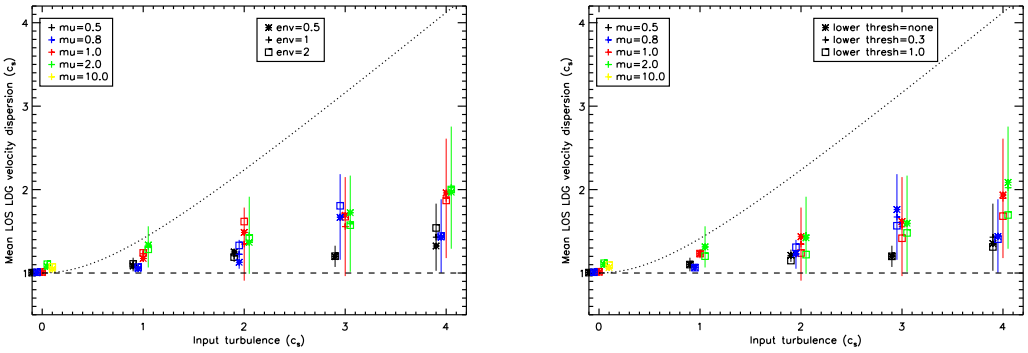

Figure 5.24 The variation in LOS LDG velocity dispersion for a differing LDG column density range. The left hand panel shows the effect of changing the maximum LDG column density threshold while the right hand panel shows the effect of changing the minimum LDG column density threshold. See Figure 5.21 for the plotting conventions used.

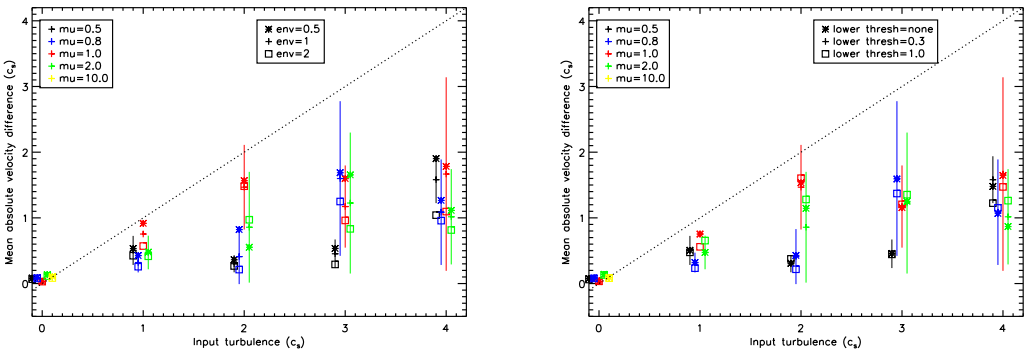

Figure 5.25 The variation in absolute core to LOS LDG velocity difference for a differing LDG column density range. The left hand panel shows the effect of changing the maximum LDG column density threshold while the right hand panel shows the effect of changing the minimum LDG column density threshold. See Figure 5.21 for the plotting conventions used.

5.10.5 LOS LDG Lower Threshold

Like any molecular tracer, $C^{18}O$ also has a minimum density to which it is sensitive. In our analysis above, we assume that the minimum density reached in the simulation is sufficiently high that $C^{18}O$ will trace all of of the low density material, but this might not be the case. Here, we consider cases where $C^{18}O$ is sensitive to only material above one third and one times the mean column density while keeping the maximum column density the same as our standard analysis (three times the mean column density).

The right hand panels of Figures 5.24 and 5.25 show the LOS LDG velocity dispersion (Figure 5.24) and core to LOS LDG velocity difference (Figure 5.25) versus the velocity dispersion of the region as a whole for three different maximum $C^{18}O$ threshold values. (Note the core velocity dispersion remains unchanged, hence is not shown.) The change in the minimum LOS LDG column density has little effect on the LOS LDG velocity dispersion, except in a few of the highly turbulent simulations where the LOS LDG velocity dispersion becomes somewhat lower when only material between one and three times the mean column density is considered. Similarly, the change in the core to LOS LDG motion calculated using different minimum LDG column density thresholds is small, with higher thresholds tending to slightly reduce the velocity difference. This illustrates the fact that most of the mass in the simulations is at moderately low column densities and that even using a greatly reduced range of column densities for the LOS LDG calculations has very little effect on our results.

5.11 APPENDIX B: RESOLUTION

As discussed in §2.1, the simulations we analyze here have 128 by 128 cells, in order for a large parameter study to be performed. To test whether resolution influenced the results of our calculations, we have also analyzed a subset of four times higher linear resolution models (512 by 512 cells). The results show that the original simulations are sufficient for our purposes. Here, we demonstrate that our results are not affected by the resolution adopted. We analyzed additional simulations with a Mach number of 4 and both weak ($\mu_0 = 2$) and strong ($\mu_0 = 0.5$) magnetic fields. The high Mach number simulations are the most likely to be affected by resolution since stronger turbulence has a greater ability to compress material to smaller scales.

We computed all of the 'observable' properties of the two additional simulations

Table 5.6. Comparison Between $\mu_0 = 2.0$, Mach 4 Simulations

Quantity [a]	N=128 Mean	N=128 Std Dev	N=512 Mean	N=512 Std Dev
Region Velocity Dispersion	4.24	0.14	4.21	0.04
All LOS Vel Disp X (matching ^{13}CO observations)	2.90	0.94	2.66	0.62
All LOS Velocity Dispersion Y Projection	3.28	1.16	2.64	0.65
LOS Vel Disp where Cores (matching C^{18}O observations)	2.02	0.73	1.89	0.67
Core Velocity Dispersion	1.21	0.26	1.26	0.41
Absolute Core-LOS Vel Difference	1.02	0.73	2.04	1.19
Absolute Core-LOS Vel Diff / LOS Vel Disp	0.49	0.34	0.92	0.45
Absolute Core Velocities	2.23	2.07	3.54	2.27
Number of Cores	3.5	0.7	6.5	2.1
Percentage of Mass in Cores	0.9	0.5	0.5	0.6

[a] All velocities in units of the sound speed.

Table 5.7. Comparison Between $\mu_0 = 0.5$, Mach 4 Simulations

Quantity [a]	N=128 Mean	N=128 Std Dev	N=512 Mean	N=512 Std Dev
Region Velocity Dispersion	3.17	0.71	3.90	0.73
All LOS Vel Disp X (matching ^{13}CO observations)	2.27	0.57	2.85	1.11
All LOS Velocity Dispersion Y Projection	1.96	0.79	2.16	0.92
LOS Vel Disp where Cores (matching C^{18}O observations)	1.43	0.40	1.53	0.33
Core Velocity Dispersion	1.45	0.22	1.28	0.21
Absolute Core-LOS Vel Difference	1.58	0.36	1.90	1.32
Absolute Core-LOS Vel Diff / LOS Vel Disp	1.09	0.33	0.91	0.27
Absolute Core Velocities	1.91	1.24	2.01	1.53
Number of Cores	2.5	1.4	3.0	0.0
Percentage of Mass in Cores	2.1	1.0	1.4	1.0

[a] All velocities in units of the sound speed.

and found them to be consistent with their lower-resolution simulation counterparts. Tables 5.6 and 5.7 show the mean and standard deviation of the 'observables' analyzed in the chapter at both the original and high resolution. As can be seen from these tables, there is no obvious change in any of the observables due to the higher resolution used. Note that identical results for the higher resolution simulations are not expected because the initial random distribution of turbulent velocities is different for each simulation run. Initial conditions, and in particular how these influence the time at which the simulation reaches a factor of 10 in column overdensity, have a much larger effect on the results than the change in resolution.

Chapter 6

Conclusion

6.1 Summary of Thesis

Stars form within large complexes of molecular gas and dust. While many advances in the field have been made, there is still debate over which physical processes (in particular, those associated with magnetic fields and turbulent motions) dominate the evolution of structure on each of the different size scales. This thesis consists of three interconnected projects which help address this question.

The first two components involve observational surveys across one entire nearby molecular cloud, Perseus. The Perseus molecular cloud is an ideal cloud to study – it is nearby (rougly 250 pc) and furthermore, offers a view into a relatively simple clustered star formation environment, where some processes (e.g., competitive accretion) are predicted to operate more strongly. A wealth of pre-existing complementary data further allows for deeper insight into the region than would otherwise be possible.

The third component of my thesis involves the analysis of a suite of numerical simulations of star formation with varying initial conditions, allowing for the effects of the interaction of differing magnetic field strengths and turbulence to be investigated.

The following sections summarize the results from the analysis of the observations and simulations in further detail.

6.1.1 Observations

First (for my MSc, also Kirk, Johnstone, & Di Francesco, 2006), I investigated the relationship between the large- and small-scale (column) density enhancements (extinction regions, extinction clumps, and dense cores) within the Perseus molecular

cloud. As well, the cores are divided into starless and protostellar cores based using *Spitzer* data (Jørgensen et al., 2007). These observations provide an important basis for my PhD thesis, where I conduct a kinematic survey of the same cloud. Kinematic information can often provide a greater discrimination between various models of star formation than (column) density information alone.

For the first survey (Chapter 3 and Kirk, Johnstone, & Tafalla 2007), I used single pointing observations from the IRAM 30 m telescope of N_2H^+(1–0) and $C^{18}O$(2–1) to measure the kinematics of dense cores (N_2H^+) and their lower density surroundings ($C^{18}O$) for all of the dense cores in the Perseus molecular cloud. The dense cores identified in my MSc (Kirk, Johnstone, & Di Francesco, 2006) form the basis of the locations targetted for the pointed spectral observations, enabling the use of this efficient observational technique. Internal velocity dispersions (linewidths) and relative motions (line centroids) are measured for both the dense cores and their surroundings, and properties are determined both for the sample as a whole as well as with the cores divided by whether they contain a central protostar (using the catalog of Jørgensen et al., 2007). The pre-existing column density observations further provide mass and size estimates for the dense cores and the extinction regions in which the cores reside.

For the second survey (Chapter 4 and Kirk, Pineda, & Johnstone, in prep), large-scale kinematic data of the low density gas across the entire Perseus cloud are obtained from FCRAO observations of ^{13}CO (1–0). The relationship between the motions of the dense cores and their larger lower-density environments are analyzed based on the combination of the data from Chapter 3 and the FCRAO data.

The key results from both of the above surveys are:

- The internal velocity dispersions of the cores are dominated by thermal motions, whilst the internal velocity dispersions of the surrounding material are somewhat larger.

- The internal velocity dispersions of the cores are roughly the size expected for the cores to be in virial equilibrium, so long as the surface pressure of the cores provided by the weight of the cloud is taken into account.

- The cores have little random motion with respect to the surrounding lower density gas – far less than the velocity dispersion of the surrounding material might suggest, and typically much less than the ambient sound speed of the medium.

- Once formed, protostars show little motion with respect to the dense core from which they form (this analysis appears in the related work of Jørgensen et al., 2007).

- Within the larger structures that they inhabit, dense cores have little motion – much smaller than the typical velocity dispersion in the region, or the estimated virial velocity dispersion of the region.

These results all point to quiescence on the scale of dense cores and their immediate surroundings, despite the large-scale non-thermal motions observed within molecular clouds. Successful theories of star formation must be able to explain how these two dynamical regimes are able to arise.

6.1.2 Simulations

For the third part of my thesis (Chapter 5 and Kirk, Johnstone, & Basu 2009), I analyzed a suite of thin-sheet magneto-hydrodynamical simulations of star formation with magnetic field strengths varying between weak ($\mu_0 = 10$) and strong ($\mu_0 = 0.5$) and initial turbulence levels varying between a Mach number of 0 and 4. The predicted behaviour of material under different magnetic field strengths and turbulence levels for a simplified version of the simulation setup (perpendicularly colliding flows in a 2D sheet) is provided in Appendix A. All of the simulations analyzed fall into the 'magneto-turbulent' or 'thermal' regimes. I create synthetic observations of the simulations which mimic the kinematic observations of the first two parts of my thesis. A variety of measurements are applied to the simulations, and analysis of these reveal which measurements are able to best discriminate between the various initial conditions applied to the simulations. The measurements are also compared to the actual observational results, showing that it is difficult to simultaneously match all of the observed kinematic properties of dense cores and their environments, regardless of the initial cloud properties. The major results from this analysis are:

- The small internal velocity dispersion of dense cores can be reproduced reasonably well in most simulations; even when overdensities are formed due to the collision of turbulent flows, the centre of the compressed region tends to have a low velocity dispersion.

- The velocity dispersion of the large-scale structures ('extinction regions') can only be matched by highly turbulent simulations with weak magnetic fields.

Strong magnetic fields delay the onset of dense core formation until the initial turbulence has decayed significantly.

- The small observed motion between the dense cores and their surrounding low density gas can only be reproduced in simulations with weak initial turbulence and / or strong magnetic fields. In all of these simulations, the velocity dispersion of the large-scale structures is also small.

The simulations I analyze are not able to match the combination of small-scale quiescence and large-scale turbulence that is found in observations. One possible solution is to include additional turbulence generated as the dense cores evolve (e.g., due to the formation of outflows). In such an instance, strong magnetic fields might allow the dense cores and their environments to remain coupled, while an initially high turbulence level is maintained through the additional energy input.

The simulations analyzed have a thin-sheet geometry and utilize periodic boundary conditions. This setup may also influence the results, since the effect of both magnetic fields and turbulent flows are dependent on geometry. Modification of these properties, however, does not appear likely to be sufficient to provide the desired observables – analysis of a clustered star formation simulation which had an initial spherical geometry and no periodic boundary conditions (Ayliffe et al., 2007) also resulted in larger motions between the dense cores and their surroundings than is observed (or else large dense core internal motions).

6.2 Future Directions

The kinematic survey of dense cores and their local environments presented in Chapter 3 (and Kirk, Johnstone & Tafalla, 2007) represents a new and efficient technique to characterize statistically significant populations of dense cores. These measurements have the additional advantage of being both relatively easy to interpret and simple to measure in numerical simulations. Currently, there are few clouds with the wealth of supplementary data that exist for the Perseus cloud which allow for the rich analysis presented. The Ophiuchus molecular cloud is a nearby molecular cloud which does have such data already, and also displays a very different mode of clustered star formation (the majority of stars form in a single large cluster). IRAM observations have been applied for to undertake such a survey. In the longer term,

there are numerous other opportunities for extending the analysis presented here, some of which are discussed in the following two sections.

6.2.1 Observations – Legacy Surveys

Several surveys are planned or in progress with a range of telescopes including *Spitzer*, *Herschel*, and the JCMT that will map the complete census of dense cores within all nearby molecular clouds (the Gould's Belt). These surveys include full continuum mapping (identification of the dense cores) and limited spectal mapping of the CO gas. While not directly included in these surveys, spectral observations of the dense cores will be possible to achieve in follow-up surveys. A pointed N_2H^+ (or NH_3) survey such as the one presented here would provide an efficient manner in which to measure the properties of the many hundreds of dense cores that are anticipated to be identified in the Gould's Belt surveys. Necessary ancillary data such as the classification of starless cores and more evolved protostars will also be available from the Legacy Survey data. The Legacy Survey data themselves will provide large statistical measurements of dense core continuum properties (such as those analyzed in my MSc thesis), while the follow-up spectral surveys will provide the complementary kinematic information. The combination of these two datasets should allow for various models of star formation to be tested over a variety of environments and will likely rule out at least some of the currently proposed models.

6.2.2 Simulations

While most simulations presented in the literature consist of one (or at most a few) different runs, the analysis presented in Chapter 5 (and Kirk, Johnstone & Basu, 2009) has shown that parameter studies of simulations are valuable. Parameter studies have the ability to provide insight into the effects of the complex interactions between physical processes which are difficult or impossible to predict analytically. As we showed with our mock observations of the simulations, some observational measures provide greater discrimination between various simulations than others and therefore provide a better test to how well the simulation matches reality. We found that pointed observations measuring the motion between dense cores and their surroundings provides one such strong discrimination between simulations and is particularly difficult to match to our observations. Now that statistically significant observational characterizations of dense cores within a single molecular cloud are becoming available,

our hope is that simulators will begin to provide similar predictions from their simulations in their future work. I plan to analyze one set of simulations in collaboration with Fabian Heitsch (Universitiy of Michigan) on some of his 3D non-periodic box simulations of colliding flows in the near future.

Appendix A

Dynamic Regimes Within MHD Simulations

A.1 Introduction

This short appendix introduces a simple theoretical framework in which to consider the effects of both turbulence and magnetic fields acting on a thin slab of material with initially uniform surface density. Although this is a simplification even of the simulations analyzed in Chapter 5 (Kirk, Johnstone & Basu, 2009), it does provide some insight into those simulations.

A.2 Physical Setup

Consider a plane wave moving at Mach number M perpendicular to a magnetic field B_0 in a medium with an initial density of ρ_0 and sound speed of c_s. In the preshock region, the pressure support is:

$$P_0 = \rho_0 c_s^2 + M^2 \rho_0 c_s^2 + B_0^2/8\pi \tag{A.1}$$

where the first term is the thermal pressure, the second is the ram pressure, and the third the magnetic pressure. In the post-shock region, the total pressure is:

$$P_1 = \rho_1 c_s^2 + B_1^2/8\pi \tag{A.2}$$

where $B_1 = (\rho_1/\rho_0)B_0$ due to the compression of the magnetic field by the wave. Equating the two pressures, we can derive an equation for the ratio of pre- and post-shock density (i.e., the compression factor):

$$(\rho_1/\rho_0)^2\frac{B_0^2}{8\pi} + (\rho_1/\rho_0)\rho_0 c_s^2 - \Big(\rho_0(M^2+1)c_s^2 + \frac{B_0^2}{8\pi}\Big) = 0 \tag{A.3}$$

Solving for (ρ_1/ρ_0) and substituting the Alfven velocity ($v_{A_0} = B_0\ /\sqrt{4\pi\rho_0}$) and defining a 'magnetic Mach number', $M_{B_0} = v_{A_0}/c_s$, we find:

$$(\rho_1/\rho_0) = \frac{1}{M_{B_0}^2}\Big(-1 + \sqrt{1 + 2(M^2+1)M_{B_0}^2 + M_{B_0}^4}\Big) \tag{A.4}$$

A.3 Compression Regimes

Using equation A.4 we can examine several regimes in turbulent/magnetic space which have different compressional behaviours.

A.3.1 Thermal - $M << 1$ and $M_{B_0} << 1$

When the Mach number is zero (i.e. thermal motions only), the compression reduces to $(\rho_1/\rho_0) = 1$, i.e., no compression. The timescale over which dense objects can form and evolve is thus dominated by the thermal (Jeans) timescale since the magnetic field is weak and has little effect on the evolution.

A.3.2 Ambipolar Diffusion $M << M_{B_0}$ and $M_{B_1} >> 1$

Here, the compression equation reduces to:

$$(\rho_1/\rho_0) \simeq \frac{1}{M_{B_0}^2}\Big(-1 + M_{B_0}^2\Big) \simeq 1$$

In this instance, the magnetic fields dominate the evolution of cores – there is no initial compression, and dense objects build up mass over an ambipolar diffusion timescale.

A.3.3 Turbulent $M >> M_{B_0}$ and $(M^2+1)M_{B_0}^2 << 1$

Here we find the compression goes roughly as

$$(\rho_1/\rho_0) \simeq \frac{1}{M_{B_0}^2}\Big(-1 + 1 + (M^2+1)M_{B_0}^2\Big) \simeq (M^2+1)$$

For a large Mach number, this reduces to the familiar $(\rho_1/\rho_0) = M^2$. Note that in this case, the condition $(M^2+1)M_{B_0}^2 << 1)$ is equivalent to $M_{B_1} << 1$.

A.3.4 Magneto-Turbulent $M >> M_{B_0}$ and $(M^2+1)M_{B_0}^2 >> 1$

Here the compression goes roughly as

$$(\rho_1/\rho_0) \simeq \frac{1}{M_{B_0}^2}\Big(\sqrt{2(M^2+1)M_{B_0}^2}\Big) \simeq \sqrt{2}\frac{\sqrt{M^2+1}}{M_{B_0}}$$

For high Mach numbers, this reduces to $(\rho_1/\rho_0) = \sqrt{2}M/M_{B_0}$. Within the compressed region, magnetic fields dominate:

$$\frac{M_{B_1}}{M_{B_0}} = \frac{B_1}{B_0}\sqrt{\frac{\rho_0}{\rho_1}}\frac{M_{B_1}}{M_{B_0}} = \sqrt{\frac{\rho_1}{\rho_0}}$$

so the compression can be re-written as

$$\Big(\frac{M_{B_1}}{M_{B_0}}\Big)^2 \simeq \sqrt{2}M/M_{B_0}$$

or

$$M_{B_1}^2 \simeq \sqrt{2}MM_{B_0}$$

which we know must be much greater than one. Since the turbulent Mach number within the compression is zero by assumption, this implies that the material within the compression evolves by a similar scheme to the ambipolar diffusion scenario (albeit with a different density and length scale than found in the initial region).

A.4 Timescales

The compressions are only part of the story of the evolution of material; the other necessary piece is the timescale of each of the physical processes which may be involved

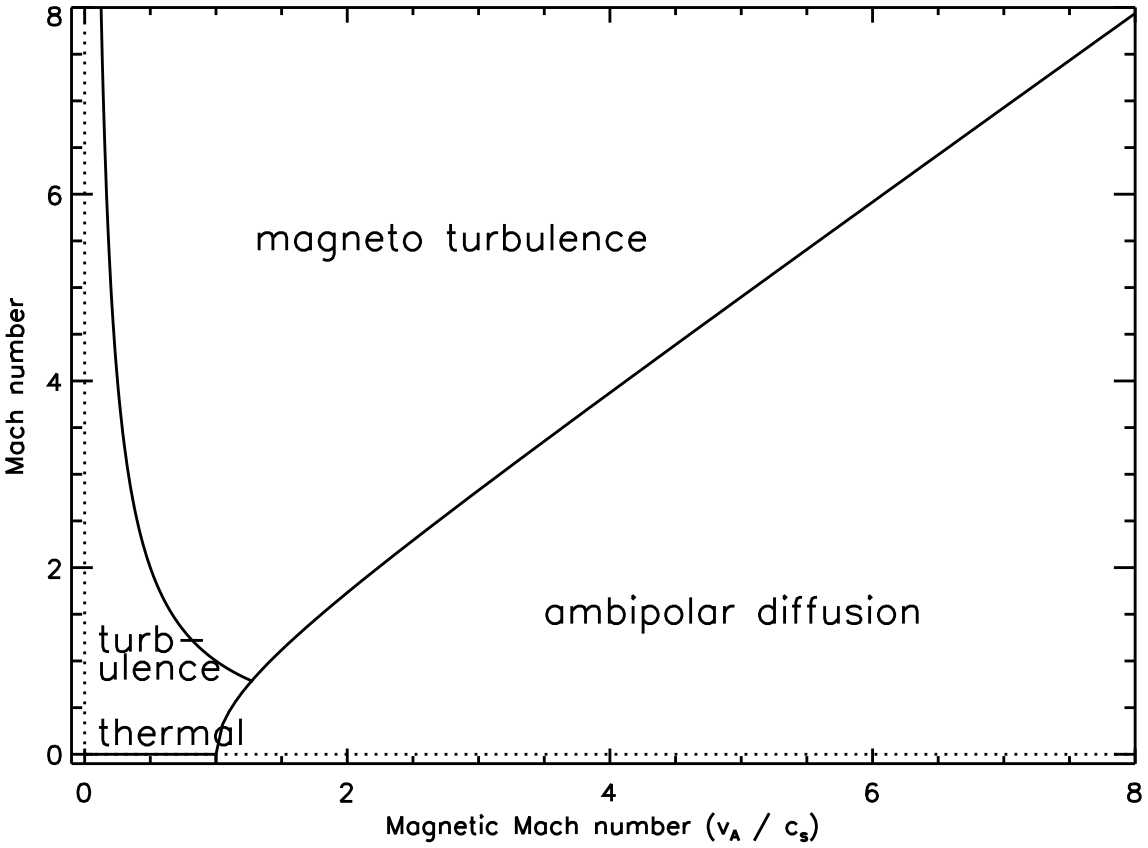

Figure A.1 The four dynamical regimes resulting from 2D compression as a function of turbulent and magnetic Mach numbers.

– the build-up of material (in a compression), re-expansion, gravitational collapse, and ambipolar diffusion. The relative size of each of these provides an estimate of how long it takes to form dense objects and whether the first compression is sufficient to force the object into (immediate) gravitational collapse.

A.4.1 Build-up of Material

Within a turbulent compression, material builds up at a rate of $Mc_s\rho_o$ per cross-sectional area of the flow. The compressed region will become gravitationally unstable when roughly a Jeans mass of material is built up within an area equal to the Jeans

length squared. This gives us

$$Mc_s\rho_0 R_{J_1} t_{\rm build} = \rho_1 R_{J_1}^3$$

which then gives

$$t_{\rm build} = \frac{(\rho_1/\rho_0)^{1/2}}{M}\frac{R_{J_0}}{c_s} \tag{A.5}$$

In the purely turbulent regime, this reduces to $t_{\rm build} = R_{J_0}/c_s$ which is the thermal expansion time of a non-compressed region:

$$t_{\rm therm} = \frac{R_{J_0}}{c_s} \tag{A.6}$$

A.4.2 Turbulent Crossing Time

Turbulent simulations tend to have most of the turbulent power input on the largest scales; the length of time for this large scale mode to cross the simulated box (and form a large filament) is given by $t_{\rm cross} = L_{\rm box}/Mc_s$ which can be re-written as

$$t_{\rm cross} = N_{RJ} R_{J_0}/Mc_s \tag{A.7}$$

where N_{RJ} is the number of Jeans lengths across the simulated box.

A.4.3 Gravitational Collapse

The gravitational collapse time is given by $t_{\rm grav} = 1/(\sqrt{G\rho})$ which for a compression of (ρ_1/ρ_0) decreases to

$$t_{\rm grav} = (\rho_1/\rho_0)^{-1/2} t_{\rm grav_0} \tag{A.8}$$

A.4.4 (Thermal) Expansion

In a thermal, non-magnetized medium, compressions rebound on the initial gravitational collapse time, $t_{\rm grav_0}$ or also $t_{exp} = R_{J_0}/c_s$ where R_{J_0} is the Jeans length. In a magnetized medium, information propogates via the Alfven speed rather than the sound speed, so the expression would become $t_{exp} = R_{J_0}/v_{A_0}$. In a strong compression, one must also note that the Jeans length is smaller and the Alfven speed larger

due to the enhanced density:

$$R_{J_1} = (\rho_1/\rho_0)^{-1/2} \times R_{J_0} \quad \text{and} \quad v_{A_1} = (\rho_1/\rho_0)^{1/2} \times v_{A_0}$$

Therefore we arrive at:

$$t_{exp} = (\rho_1/\rho_0)^{-1/2}\ t_{\mathrm{grav}_0} \quad \text{for } M_{B_1} < 1 \tag{A.9}$$

$$t_{exp} = (\rho_1/\rho_0)^{-1}\ (1/M_{B_0})\ t_{\mathrm{grav}_0} \quad \text{for } M_{B_1} > 1 \tag{A.10}$$

A.4.5 Ambipolar Diffusion

For strongly magnetic cases, the ambipolar diffusion timescale is also important. Following Shu (p364, Gas Dynamics), this can be written as

$$t_{\mathrm{AD}} \simeq L^2/v_A^2\tau_{ni}$$

where τ_{ni} is the interaction timescale between neutrals and ions. We are interested in the ambipolar diffusion timescale over a compressed region, i.e.,

$$L = (\rho_1/\rho_0)^{-1}\ R_{J_0}$$

From CB06 the neutral-ion interaction timescale is given by

$$\tau_{ni} = 1.4\Big(\frac{27}{25}\Big)(1.69\times10^{-9})^{-1}(3\times10^{-3})^{-1}\Big(\frac{n_n}{10^5\ cm^{-3}}\Big)^{-1/2} sec$$

where n_n is the number density of neutral particles. Taking n_{n_0} to be the number density corresponding to ρ_0, we can define τ_{ni_0} to be the neutral-ion interaction timescale for a number density of n_{n_0}. For the compressed region we thus get

$$t_{\mathrm{AD}} = (\rho_1/\rho_0)^{-5/2}\Big(\frac{R_{J_0}}{v_{A_0}}\Big)^2\tau_{ni_0}^{-1} \tag{A.11}$$

A.5 Evolution

Putting together the results of the previous sections, we can now discern the evolution of dense material in each of the regimes.

A.5.1 Thermal

There are initially no compressions in the gas; the lengthscale of interest for forming objects is the Jeans scale or larger (the fastest growing mode may be larger than the Jeans scale). The timescales for the formation and evolution of dense objects are governed by the thermal or Jeans timescale, $t_{\rm therm}$.

A.5.2 Ambipolar Diffusion

Again, there are initially no compressions in the gas. Here, the lengthscale of interest is the Jeans length as the magnetic field prevents the growth of larger scale modes. Dense objects build up mass over an ambipolar diffusion timescale, $t_{\rm AD_0}$. This is usually significantly longer than the thermal timescale. Once a Jeans mass of material has been built up, gravitational collapse occurs on roughly the same timeframe, $t_{\rm grav_0}$ or $t_{\rm therm}$.

A.5.3 Turbulent

Compression does occur in the turbulent regime and result in the formation of higher density filaments which have a reduced Jeans length. Material builds up in a turbulent compression over a timescale $t_{\rm build}$ roughly equal to the $t_{\rm therm}$. The gravitational collapse time of this object is then $(1/M)t_{\rm therm}$ (a factor of M faster than the thermal case). The largest scale compressions (long filaments) require a timescale of $(N_{RJ}/M)t_{\rm therm}$ to form. Depending on the relative values of N_{RJ} and M, the large scale compression may not have formed before the gravitational collapse of smaller scale compressions.

A.5.4 Magneto-Turbulent

Again, compression does occur, and results in higher density filaments which have a reduced Jeans length. Magnetic fields, however, reduce the amplitude of turbulent compressions, causing the timescale for material to build up to be $\sim \sqrt{2}(M\ M_{B_0})^{-1/2}t_{\rm therm}$ for high Mach numbers. In the compressed region, the magnetic field dominates, thus in order for gravitational collapse to occur, ambipolar diffusion is necessary to overcome the magnetic fields. This occurs at an enhanced rate due to the increased density in the compression: $\sim (2M/M_{B_0})^{-5/4}t_{\rm AD_0}$ for high Mach numbers. If this timescale is faster than the thermal expansion time $\sim (2M/M_{B_0})^{-1/4}\ (c_s/v_A)\ t_{\rm therm}$

then gravitational collapse can occur. Gravitational collapse would then occur over a timescale of $\sim (2M/M_{B_0})^{-1/2} t_{\rm therm}$ for high Mach numbers.

A.6 Discussion

The simulations analyzed in Chapter 5 (Kirk, Johnstone & Basu, 2009) with non-zero initial turbulence all fall into the magneto-turbulent regime. In the literature, it is often assumed that in highly turbulent scenarios, a weak magnetic field has little effect in either pre- or post-shock material. The equations above demonstrate in a simplistic manner that given the appropriate geometry, such as in these simulations, the compression of even a very weak magnetic field within a shock front can be significant – enough to fall into the magneto-turbulent regime rather than the purely turbulent regime. Realistic molecular clouds are three-dimensional and would be expected to have shocks occuring at oblique angles likely without an idealized magnetic field orientation, hence the formulae derived here are meant only as an approximate guide rather than an absolute rule to subsequent evolution. The results do suggest, however, that caution should be used before ignoring the effect of even weak magnetic fields within regions that harbour turbulent compressions.

Bibliography

Aikawa, Y., Ohashi, N., Inutsuka, S., Herbst, E., & Takauwa, S. 2001, ApJ, 552, 639

Aikawa, Y., Ohashi, N. & Herbst, E. 2003, ApJ, 593, 906

Alves, J., Lada, C. J., & Lada, E. A. 2001, Nature, 409, 159

Alves, J.& Lombardi, M. in preparation

André, P., Ward-Thompson, D., & Barsony, M. 1993, ApJ, 406, 122

André, P. & Saraceno, P. 2005, Proceedings of the dusty and molecular universe: a prelude to Herschel and ALMA, A. Wilson (eds), ESA Publications, Noordwijk, Netherlands, p179-184

Ayliffe, B. A., Langdon, J. C., Cohl, H. S., & Bate, M.R. 2007, MNRAS, 374, 1198

Ballesteros-Paredes, J. Klessen, R. S. & Vázquez-Semadeni, E. 2003, ApJ, 592, 188

Bally, J., Walawender, J., Johnstone, D., Kirk, H., Goodman, A., Porras, A. & Ridge, N. Handbook of Star Forming Regions Vol. I. The Northern Sky (ed. Reipurth), 2008

Barranco, J. A. & Goodman, A. A. 1998, ApJ, 504, 207

Basu, S. & Ciolek, G. E. 2004, ApJ, 607, 39L

Basu, S., Ciolek, G. E., & Wurster, J. 2009, NewA, 14, 221

Basu, S., Ciolek, G. E., Dapp, W. B. & Wurster, J. NewA, 14, 483

Bate, M. R., Lubow, S. H., Ogilvie, G. I. & Miller, K. A. 2003, MNRAS, 341, 213

Benson, P. J. & Myers, P. C. 1989, ApJS, 71, 89

Bergin, E. A., Alves, J., Huard, T., & Lada, C. J. 2002, ApJ, 570L, 101

Bergin, E. A. & Tafalla, M. 2007, ARA&A, 45, 339

Bertoldi, F. & McKee, C. F. 1992, ApJ, 395, 140

Bonnell, I. A., Larson, R. B., & Zinnecker, H. 2007, in Protostars and Planets V, ed. B. Reipurth, D. Jewitt, & K. Keil (Tucson: Univ. Arizona Press), 149

Bonnor, W. B. 1956, MNRAS, 116, 351

Burkert, A. & Bodenheimer, P. 2000, ApJ, 543, 822

Burkert, A. & Hartmann, L. 2004, ApJ, 616, 288

Caselli, P., Myers, P. C., Thaddeus, P. 1995, ApJ, 455L, 77

Caselli, P. & Myers, P. C. 1995, ApJ, 446, 665

Caselli, P., Benson, P. J., Myers, P. C., &Tafalla, M. 2002, ApJ, 572, 238

Černis, K. 1993, BaltA, 2, 214

Chen, X., Laundhardt, R., Bourke, T. L., Henning, T., & Barnes, P. J. 2008, ApJ, 683, 862

Ciolek, G. E. & Basu, S. 2006, ApJ, 652, 442

Cohen, M. &Kuhi, L. V. 1979, ApJS, 41, 743

Crapsi, A., Caselli, P., Walmsley, C. M., Myers, P. C., Tafalla, M., Lee, C. W., & Bourke, T. L. 2005, ApJ, 619, 379

Crutcher, R. M. 1988, LNP, 315, 105

Crutcher, R. 1999, ApJ, 520, 706

de Gregorio-Monsalvo, I., Gómez, J. F., Suárez, O., Kuiper, T. B. H., Rodríguez, L. F., Jiménez-Bailón, E. 2006, ApJ, 642, 319

Dapp, W. B. & Basu, S. 2009, MNRAS, 395, 1092

Di Francesco, J., Evans, N. J. II, Caselli, P., Myers, P. C., Shirley, Y., Aikawa, Y., & Tafalla, M. 2007, in Protostars and Planets V, ed. B. Reipurth, D. Jewitt, & K. Keil (Tucson: Univ. Arizona Press), 33

Di Francesco, J., Johnstone, D., Kirk, H., Ledwosinksa, E. & MacKenzie, T. 2008, ApJS, 175, 277

Dib, S., Vazquez-Semadeni, E., Kim, J., Burkert, A. & Shadmehri, M. 2007, ApJ, 661, 262

Ebert, R. 1955, Z. Astrophys., 37, 217

Elmegreen, B. G. 1998, ASPC, 148, 150

Elmegreen, B. G. 2007, ApJ, 668, 1064

Enoch, M. L. et al. 2006, ApJ, 638, 293

Enoch, M. L., Evans, N. J. II, Sargent, A. I., Glenn, J., Rosolowsky, E, & Myers, P. 2008, ApJ, 684, 1240

Enoch, M. L., Evans, N. J. II, Sargent, A. I., & Glenn, J. 2009, APJ, 692, 973

Evans, N. J. et al. 2003, PASP, 115, 965

Evans, N. J. et al. 2009, ApJS, 181, 321

Gammie, C. F. & Ostriker, E. C. 1996, ApJ, 466, 814

Girart, J. M., Rao, R., & Marrone, D. P. 2006, Science, 313, 812

Goodman, A. A., Benson, P. J., Fuller, G. A. & Myers, P. C. 1993, ApJ, 406, 528

Goodman, A. A., Barranco, J. A., Wilner, D. J. & Heyer, M. H. 1998, ApJ, 504, 223

Hartmann, L. 1998, Accretion Processes in Star Formation (Cambridge: Cambridge University Press)

Hatchell, J., Richer, J. S., Fuller, G. A., Qualtrough, C. J., Ladd, E. F., & Chandler, C. J. 2005, A&A, 440, 151

Hatchell, J., Fuller, G. A., Richer, J. S., Harries, T. J., & Ladd, E. F. 2007, A&A, 468, 1009

Hatchell, J., Fuller, G. A., & Richer, J. S. 2007, A&A, 472, 187

Heitsch, F., Hartmann, L. W., Slyz, A. D., Devriendt, J. E. G., & Burkert, A. 2008, ApJ, 674, 316

Heitsch, F., Hartmann, L. W., & Burkert, A. 2008, ApJ, 683, 786

Henriksen, R., André, P., & Bontemps, S. 1997, A&A, 323, 549

Herbst, W. Handbook of Star Forming Regions Vol. I. The Northern Sky (ed. Reipurth), 2008

Holland, W. S., et al. 1999, MNRAS, 303, 659

Jijina, J., Myers, P. C., Adams, F. C. 1999, ApJS, 125, 161

Johnstone, D., Wilson, C.D., Moriarty-Schieven, G., Giannakopoulou-Creighton, J., & Gregersen, E. 2000, ApJ, 131, 505

Johnstone, D., Fich, M., Mitchell, G.F. & Moriarty-Schieven, G. 2001, ApJ, 559, 307

Johnstone, D., Di Francesco, J., & Kirk, H. 2004, ApJ, 611L, 45

Johnstone, D., Matthews, H., & Mitchell, G. F. 2006, ApJ, 639, 259

Johnstone, D. & Bally, J. 2006, ApJ, 653, 383

Jørgensen, J. K., Harvey, P. M., Evans, N. J II, Huard, T. L., Allen, L. E., Porras, A., et al. 2006, ApJ, 645, 1246

Jørgensen, J. K., Johstone, D., Kirk, H., & Myers, P. C. 2007, ApJ, 656, 293

Jørgensen, J. K., Johnstone, D., Kirk, H., Myers, P. C., Allen, L. E., & Shirley, Y. L. 2008, ApJ, 683, 822

Johnstone, D., Rosolowsky, E. W., Kirk, H., & Tafalla, M. in prep

Kirk, H., Johnstone, D., & Di Francesco, J. 2006, ApJ, 646, 1009

Kirk, H., Johnstone, D., & Tafalla, M. 2007, ApJ, 668, 1042

Kirk, H., Johnstone, D., & Basu, S. 2009, ApJ in press

Klessen, R. S., Ballesteros-Paredes, J., Vázquez-Semadeni, E. & Durán-Rojas, C. 2005, ApJ, 620, 786

Kramer, C., Stutzki, J., Rohrig, R., & Corneliussen, U. 1998, A&A, 329, 249

Kudoh, T., Basu, S. 2008, ApJ, 679, L97

Lada, C. J. 1987, Proceedings of the Symposium, Tokyo, Japan, Dordrecht, D. Reidel Publishing Co., p1-17

Lada, C. J., Lada, E. A., Clemens, D. P., & Bally, J. 1994, ApJ, 429, 694

Lada, C. J. & Lada, E. A. 2003, ARA&A, 41, 57

Larson, R. B. 1981, MNRAS, 194, 809

Lee, C. W., Myers, P. C., & Tafalla, M. 2001, ApJS, 136, 703

Li, Z.-Y., & Nakamura, F. 2004, ApJ, 609, L83

Lombardi, M. & Alves, J. 2001, A&A, 377, 1023

Lombardi, M., Alves, J., & Lada, C. J. 2006, A&A, 454, 781

MacLow, M-M. & Klessen, R. 2004, RvMP, 76, 125

Matthews, H. E., McCutcheon, W. H., Kirk, H., White, G. J., & Cohen, M. 2008, AJ, 136, 2083

McKee, C. 1989, ApJ, 345, 782

McKee, C. F. & Tan, J. C. 2003, ApJ, 585, 850

Mestel, L. & Spitzer, L., Jr 1956, MNRAS, 116, 503

Mouschovias, T. C. 1976, ApJ, 207, 141

Morata, O., Girart, J. M., Estalella, R. 2005, A&A, 435, 113

Motte, F., André, P., & Neri, R. 1998, A&A, 336, 150

Müller, H. S. P., Thorwirth, S., Roth, D. A. & Winnewisser, G. 2001, A&A, 370, L49

Myers, P. C., Dame, T. M., Thaddeus, P., Cohen, R. S., Silverberg, R. F., Dwek, E., & Hauser, M. G. 1986, 301, 398

Nakamura, F. & Li, Z.-Y. 2008, ApJ, 687, 354

Offner, S. S. R., Klein, R. I., & McKee, C. F. 2008, AJ, 136, 404

Olano, C. A. 1982, 112, 195

Onishi, T., Mizuno, A., Kawamura, H. O., & Fukui, Y. 1998, ApJ, 502, 296

Ossenkopf, V. & Henning, T. 1994, A&A, 291, 943

Pineda, J. E., Caselli, P., & Goodman, A. A. 2008, ApJ, 679, 481

Pineda, J. E., Rosolowsky, E. W., & Goodman, A. A. 2009, ApJ, 699L, 134

Rebull, L. et al., 2007, ApJS, 171, 447

Reid, M. A. & Wilson, C. D. 2005, ApJ, 625, 891

Ridge, N. A., Di Francesco, J., Kirk, H., Li, D., Goodman, A. A., et al. 2006, AJ, 131, 2921

Rosolowsky, E. W., Pineda, J. E., Foster, J. B., Borkin, M. A., Kauffmann, J., Caselli, P., Myers, P. C., Goodman, A. A. 2008, ApJS, 175, 509

Salpeter, E. E. 1955, ApJ, 121, 161

Schleuning, D. A. 1998, ApJ, 493, 811

Schöier, F. L., van der Tak, F. F. A., van Dishoeck, E. F., & Black, J. H. 2005, A&A, 432, 369

Shirley, Y. L., Nordhaus, M. K., Grcevich, J. M., Evans, N. J. II, Rawlings, J. M. C. & Tatematsu, K. 2005, ApJ, 632, 982

Shirley, Y. L. 2007, Molecules in Space And Laboratory, eds. J. L. Lemaire & F. Combes ,14

Shu, F., Adams, F., Lizano, S. 1987, ARA&A, 25, 2

Shu, F. H. 1992, Gas Dynamics Vol. II (University Science Books)

Shu, F., Najita, J.,Ostriker, E., Wilkin, F., Ruden, S., & Lizano, S. 1994, ApJ, 429, 781

Spitzer, Lyman Jr., 1978, Physical Processes in the Interstellar Medium (John Wiley & Sons)

Stahler, S. W. & Palla, F. 2004, The Formation of Stars (Wiley-VCH)

Tafalla, M., Myers, P. C., Caselli, P., Walmsley, C. M., Comito, C. 2002, ApJ, 569, 815

Tafalla, M., Myers, P. C., Caselli, P., & Walmsley, C. M. 2004, A&A, 416, 191

Tafalla, M., Kumar, M. S. N., & Bachiller, R. 2006, A&A, 456, 179

Tereby, S., Shu, F. H., & Cassen, P. 1984, ApJ, 286, 529

Ungerechts, H., Bergin, E. A., Goldsmith, P. F., Irvine, W. M., Schloerb, F. P. & Snell, R. L. 1997, ApJ, 482, 245

Vá zquez-Semadeni, E., Gó mez, G. C., Jappsen, A. K., Ballesteros-Paredes, J., Gonzá lez, R. F., & Klessen, R. S. 2007, ApJ, 657, 870

Walawender, J., Bally, J., Reipurth, B., & Aspin, C. 2004, AJ, 127, 2809

Walawender, J., Bally, J., Kirk, H., Johnstone, D. 2005, AJ, 130, 1795

Walawender, J., Bally, J., Kirk, H., Johnstone, D., Reipurth, B., & Aspin, C. 2006, AJ, 132, 467

Walawender, J., Bally, J., Di Francesco, J., Jørgensen, J., Getman, K. Handbook of Star Forming Regions Vol. I. The Northern Sky (ed. Reipurth), 2008

Walsh, A. J., Myers, P. C. & Burton, M. G. 2004, ApJ, 614, 194

Walsh, A. J., Myers, P. C., Di Francesco, J., Mohanty, S., Bourke, T. L., Gutermuth, R., & Wilner, D. 2007, ApJ, 655, 958

Ward-Thompson, D., Nutter, D, Bontemps, S, Whitworth, A, & Attwood, R. 2006, MNRAS, 369, 1201

Ward-Thompson, D., André, P., Crutcher, R., Johnstone, D., Onishi, T. & Wilson, C. 2007, in Protostars and Planets V, ed. B. Reipurth, D. Jewitt, & K. Keil (Tucson: Univ. Arizona Press), 33

Ward-Thompson, D., et al. 2007, PASP, 119, 855

Williams, J.P., de Geus, E.J., & Blitz, L. 1994, ApJ, 428, 693

Zeeman, P. 1897, ApJ, 5, 332